Phase formation, hydration behavior, and pressure response of sulfide and thiophosphate solid electrolytes

Christian Schneider

München 2023

Dissertation zur Erlangung des Doktorgrades
der Fakultät für Chemie und Pharmazie
der Ludwig–Maximilians–Universität München

Phase formation, hydration behavior, and pressure response of sulfide and thiophosphate solid electrolytes

Christian Schneider

aus

Ingolstadt, Deutschland

2023

Erklärung

Diese Dissertation wurde im Sinne von § 7 der Promotionsordnung vom 28. November 2011 von Frau Prof. Dr. Bettina V. Lotsch betreut.

Eidesstattliche Versicherung

Diese Dissertation wurde eigenständig und ohne unerlaubte Hilfe erarbeitet.

Stuttgart, den 22.01.2023

Christian Schneider

Dissertation eingereicht am:	24.01.2023
1. Gutachterin:	Prof. Dr. Bettina Valeska Lotsch
2. Gutachter:	Prof. Dr. Konstantin Karaghiosoff
Mündliche Prüfung am:	28.02.2023

Danksagung

An aller erster Stelle gilt mein Dank Prof. Dr. Bettina Lotsch für die Möglichkeit am Max-Planck-Institut für Festkörperforschung meine Dissertation anfertigen zu können. Danke auch für die Unterstützung, Betreuung, Geduld und die gewährte wissenschaftliche Freiheit.
Des Weiteren danke ich Prof. Dr. Konstantin Karaghiosoff, Prof. Dr. Pieremanuele Canepa, Prof. Dr. Armin Hartschuh, Prof. Dr. Jennifer Rupp und Prof. Dr. Andreas Kornath für die Begutachtung meiner Arbeit und für ihre Bereitschaft, ein Teil des Prüfungskommitees zu sein.
Danke auch an alle Co-Autoren, allen voran Dr. Tanja Scholz, Dr. Markus Joos, Dr. Maxwell Terban, Roland Eger, Christoph Schmidt, Anton Neumann, Moritz Clausnitzer, Marcel Sadowski, Dr. Sascha Harm und Dr. Zeyu Deng.
Bedanken möchte ich mich auch bei Viola Duppel, Jürgen Nuss, Igor Moudrakovski, Armin Schulz und Marie-Luise Schreiber für SEM und TEM, SCXRD, NMR, Raman und ICP-OES Messungen. Danke auch an Stefan Höhn und Willi Hölle für die technische Unterstützung. Insbesondere möchte ich auch der Servicegruppe Röntgenographie am MPI-FKF danken.
Ich will mich auch bei Claudia Camella und Sigrid Fuhrman bedanken, die beide so oft organisatorische und bürokratische Aspekte übernommen hatten. Danke für die vielen schönen Gespräche (schwätzen: [ˈʃɛt͡sn̩]) und die Dialekt-Bereicherung.
Mein Dank gilt auch Dr. Sourav Laha und Dr. Manisha Samanta. Die Zeit in einem indisch-deutschen Büro hat mich in vielerlei Weise sehr bereichert. ধন্যবাদ. Für das Korrekturlesen der Arbeit möchte ich neben Sourav und Manisha auch Dr. Marcel Maslyk danken.
Ich bedanke mich auch bei allen (ehemaligen) Kollegen der Arbeitsgruppe für ihre Hilfe im Labor, die stets harmonische Arbeitsatmosphäre und die vielen Freundschaften die im Laufe der Jahre entstanden sind. Ich werde diese Zeit nicht vergessen.
Ein großes Danke auch an alle *CdD*-Freunde , die auf humoristische Weise diesen Weg mit mir gegangen sind.

Mein Dank geht auch an Julia Bihr. Für ihre Inspiration, Kreativität, Motivation, ihren Rückhalt und ihre Liebe.
Mein größter Dank gilt meiner Familie. Meine Eltern, Gertrud und Helmut, meine Schwester Simone und meine Großeltern haben mich immer in all meinen Zielen unterstützt und an mich geglaubt, auch in Zeiten, in denen ich Zweifel hatte. Vielen Dank.

The whole strenuous intellectual work of an industrious research worker would appear, after all, in vain and hopeless, if he were not occasionally through some striking facts to find that he had, at the end of all his criss-cross journeys, at last accomplished at least one step which was conclusively nearer the truth.

Max Planck
Nobel Lecture, June 2, 1920

Abstract

Rechargeable lithium ion batteries (LIB) have become an essential part of our daily lives in recent decades, powering mobile phones, laptops, cordless power tools, and even automobiles. While LIB technology currently dominates the battery market for these mobile applications, its physicochemical power and energy density limit will be reached soon. The use of a solid electrolyte instead of a liquid electrolyte in LIBs promises higher energy density, safer operation, and faster charging. Although the benefits of an all-solid-state battery (ASSB) are enormous, certain prerequisites for solid electrolyte application must be met in order for ASSBs to be technologically and commercially competitive. Ionic conductivity is arguably the most important performance indicator of a solid electrolyte. In Chapter 1, this thesis introduces the concept of LIBs and ASSBs, as well as fundamentals of battery performance and ion conduction in solids, as well as an overview of material classes with a focus on sulfide- and thiophosphate-based solid electrolytes. Furthermore, in Chapter 2, the techniques used to characterize the solid electrolytes presented in this thesis are introduced. Furthermore, this work presents several design strategies for improving the ionic conductivity of solid electrolytes based on sulfides and thiophosphates. Bottom-up and top-down post-synthetic modification approaches, thermally and chemically induced phase transitions, and microstructure modifications cover a wide range of length scales.
After defining the research objectives in Chapter 3, Chapter 4 demonstrates the importance of cationic disorder for lithium ion conduction in $Li_{4-3x}Sc_xP_2S_6$. While the ionic conductivity in trigonal and monoclinic $LiScP_2S_6$ is low due to fully occupied lithium positions, partial lithium occupation by aliovalent substitution of scandium significantly improves the ionic conductivity as measured by EIS. Furthermore, the crystal structures of these three compounds are presented, as well as possible ion migration pathways and comprehensive characterization of the $P_2S_6^{4-}$ anion, which contributes to a better understanding of structure-property relationships in ionic solids.
Currently, the academic and commercial focus is on lithium-based batteries due to their high energy benefits. However, lithium is a limited and expensive resource. By substituting sodium for lithium, supply chain risks are avoided, and a lower-cost alternative to lithium-based energy storage devices is provided. Chapter 5 presents the effect of cation disorder on the sodium ion conductor $Na_4P_2S_6$, which is controlled by synthesis and phase formation. Solid-state synthesis or wet chemical precipitation can be used to

prepare the two monoclinic $Na_4P_2S_6$ polymorphs, α and β. The synthesis determines the occupancy of interlayer sodium ions, the crystallinity, and the symmetry of $P_2S_6^{4-}$, which has been thoroughly investigated using single crystal and powder X-ray diffraction (SCXRD and PXRD), transmission electron microscopy (TEM), nuclear magnetic resonance spectroscopy (NMR), and Raman spectroscopy. The redistribution of one interlayer sodium position in α-$Na_4P_2S_6$ into two lower occupancy positions in β-$Na_4P_2S_6$ increases ionic conductivity and flattens the energy landscape. The phase transition $\alpha \longrightarrow \beta$ is also observed upon heating above 160 °C, which is confirmed by Raman spectroscopy, PXRD and DSC.

Chapter 6 presents the transition of β-$Na_4P_2S_6$ into a third, high-temperature polymorph (T >580 °C), γ-$Na_4P_2S_6$. While the molecular structure of the translationally fixed anions in γ-$Na_4P_2S_6$ is preserved, they dynamically reorient, leading to a time-averaged cubic symmetry, as confirmed by PXRD and pair distribution function (PDF) analysis. *Ab initio* molecular dynamics simulation (AIMD) and bond valence sum (BVS) calculations show high sodium ion mobility and a flat potential energy surface, confirming the high ionic conductivity and low activation energy, as measured by high-temperature impedance spectroscopy. For the first time, we report a cubic plastic crystal phase for a thiophosphate-based solid electrolyte containing the elongated, complex $P_2S_6^{4-}$ anion. This work highlights how the rapid anion reorientation facilitates cation dynamics by increasing the available volume and thus relaxing the structural constraints on ion migration.

The potential energy surface for ion migration can also be manipulated by screening the attractive Coulomb interactions of cations and anions. The concept of tuning the transport properties of two-dimensional $Li_2Sn_2S_5$ by water intercalation is introduced in Chapter 7. While maintaining the overall layered structure, reversible water intercalation into the interlayer space increases the interlayer distance and solvates the interlayer lithium ions. As a result, the effective attraction between the negatively charged layers and lithium is weakened so that lithium ion transport in $Li_2Sn_2S_5 \cdot xH_2O$ becomes comparable to liquid electrolytes as measured by electrochemical impedance spectroscopy (EIS) and pulsed field gradient (PFG) NMR. This environmentally benign, post-synthetically obtained layered material bridges the gap between solid and liquid electrolytes and sheds light on how ion transport properties can be tuned in confined two-dimensional materials.

Under pressure, a similar confinement effect is observed in solid electrolytes . In Chapter 8, the effect of stacking and pelletizing pressure on the ultrafast solid electrolyte Li_7SiPS_8 is investigated using *operando* EIS. For the first time, the Heckel analysis for granular powder compression is applied to a thiophosphate solid-state electrolyte, allowing to link the mechanical response to ionic conductivity. For two samples with different particle distributions, this multiscale study shows the effect of pressure on microstructure formation as well as the atomistic effect of unit cell compression. Computational discrete element method (DEM) simulation generates an accurate microstructure model, which is then analyzed with finite volume analysis (FVA) to determine the effective ionic conductivity at various compression stages. The model accurately captures the effects of microstructure and unit cell compression, emphasizing the importance of microstructure, particle size, and pressure control in polycrystalline samples.

Contents

CHAPTER 1

Introduction

Batteries have been an integral part of our society for many centuries. To understand how batteries work and what materials are needed to build a battery, this chapter presents historical developments of electrochemical energy storage systems, introduces general battery performance indicators, and gives an overview of today's lithium and sodium ion battery technology. It also introduces the concept of the all solid-state battery as a potential successor to the lithium-ion battery, focusing on electrode materials, the basic physics of ion conduction, and promising solid electrolyte materials and compounds as separators.

Contents of Chapter 1

1.1 Motivation

The world population consumed around 11112 PWh ($4.05 \cdot 10^{20}$ J) of primary energy in 2000, four times as much as in 1950.[1,2] Since 2000, demand for primary energy has increased by 47% to 16532 PWh ($5.95 \cdot 10^{20}$ J) in 2021.[2] This rapid development illustrates the central importance of energy worldwide. The lion's share of primary energy still comes from fossil fuels such as coal, oil, and natural gas, which accounted for 82.3 percent of total primary energy production in 2021.[2] Alternative energy sources, ranked by their contribution from high to low, include hydroelectric, renewables, such as biomass, biofules, wind and solar, and nuclear.[2]

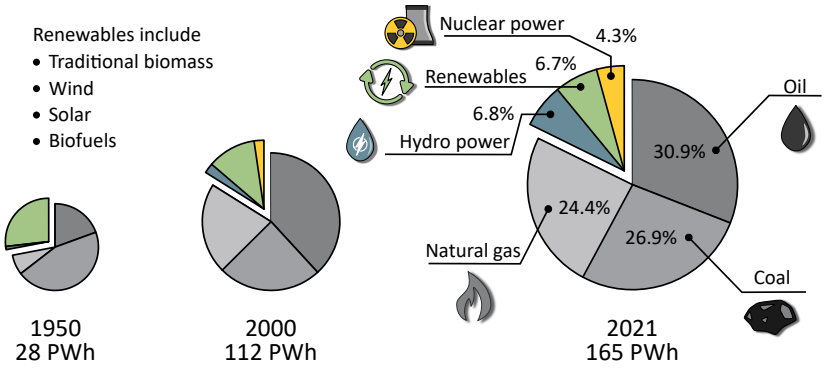

Figure 1.1: Pie-chart scheme of worldwide primary energy consumption for 1950, 2000 and 2021.

A major advantage of conventional energy sources, including fossil and nuclear, is that they can be used regardless of annual or daily time variations because they are relatively easy to store and transport. As a result, these energy-rich and powerful resources are constantly available, guaranteeing an almost uninterrupted supply of energy in the form of heat and electricity to industry and domestic consumers. With the Paris Agreement of 2015, 195 countries worldwide have committed to drastically reducing their CO_2 emissions to keep global warming below 1.5 °C compared to pre-industrial levels. This, of course, means that the world will have to shift its primary energy demand from fossil fuels to renewables. As a result, the primary energy demand currently needed for process heat or heating buildings will increasingly have to be met by electricity generated from large renewable sources such as wind and solar. In addition to storing electrical energy by converting it into chemical products such as hydrogen or methane, electrochemical storage systems are particularly advantageous because they offer the possibility of uninterrupted power supply, as they can make the stored energy immediately available without major efficiency losses. With the expansion of renewable energy in the power supply, battery storage is becoming an indispensable component for grid stability and can help close hours of supply gaps.[3] Electrochemical storage systems are also becoming increasingly important in the transportation sector, especially for personal transportation in the form of battery electric vehicles (BEV), electric bicycles (e-bikes), and electric scooters (e-scooters). In 2020 the global market for electronic mobility was estimated at USD 230

billion, and one year later in 2021 at USD 279 billion.[4] For 2028 the e-mobility market is expected to grow to around USD 1500 billion, translating to an annular growth rate of approximately 27.2%.[4] To achieve this potential market growth, BEVs must become competitive to internal combustion engines. This requires BEVs to offer long range and the ability to be recharged quickly. These demanding requirements are currently met in part almost exclusively by lithium-ion batteries (LIBs), since they have both high gravimetric and volumetric energy density and can be charged quickly. However, there is a physicochemical limit to the cell architecture of LIBs, which is expected to be reached in the next few years.[5] To further increase the capacities of lithium ion based batteries, the all solid-state (lithium ion) battery (ASSB) has been proposed. This type of battery uses a solid electrolyte instead of a liquid electrolyte, which in principle allows lithium metal to be used as the negative electrode material, thus increasing the energy density.[6] As a side benefit, replacing the flammable liquid electrolyte with a much more inert solid promises to prevent battery ignition in the event of a thermal runaway, making the ASSB a safer option compared to traditional LIB technology. The key component of an ASSB is the solid electrolyte, which acts as a separator and internal ion conductor to counteract the external current. From the perspective of a solid-state chemist or material scientist, there are many materials with ion-conducting properties, but few meet the main requirement of high ionic conductivity for ASSBs. In this work, the relationship between the (micro-) structural properties of sulfide- and thiophosphate-based solids and their ionic conductivity is investigated.

1.2 A brief history of electrochemical storage devices

Electrochemical storage devices have been known for more than 200 years. The Italian scientist Allessandro Volta invented the first historically documented battery, known today as the "voltaic pile."[7] This device uses the electrochemical potential between zinc and hydrogen. Paper discs soaked in brine serve as electronic insulation to prevent a short circuit between the copper and zinc metal plates. The voltaic pile is capable of providing a relatively constant current and voltage over a reasonable period of time (hours), which is the basic definition of a battery as we understand it today. Volta's understanding of the origin of the current was incorrect, however, as he believed that the current generated came from the metal plates touching[8] rather than from a chemical degradation reaction of the zinc, also known as corrosion.
The next major step toward modern batteries was approached in 1836, when English chemist John F. Daniell invented a cell based on the same metals that Volta used, but with a different architecture and chemistry.[9] By using separate solutions of zinc and copper sulfate connected only by a salt bridge acting as a barrier, Daniell took advantage of the electrochemical potential between copper and zinc. This resulted in a higher voltage in a single cell and prevented hydrogen evolution at the copper electrode, as observed in the voltaic piles. The success of the Daniell cell and its improved variants soon led to the use of this technology for telegraphy. The Volta cell and the Daniell cell are considered the first working batteries to convert chemical energy into electrical energy.
However, the conversion of chemical to electrical energy in these cells, which we now call primary cells, is possible only in one way. In other words, they lack the ability to be charged with electrical energy to restore the battery back to its original, ready-to-use state. This inherent deficiency was addressed by Gaston Planté in 1859 with the invention of the lead-acid battery.[10] This cell uses metallic lead as the anode and lead dioxide as the cathode. The electrodes are immersed in sulfuric acid, and lead sulfate forms on both electrodes when the battery is discharged. The chemical reaction is reversible when the current flow is reversed, making this type of battery a secondary battery. The lead-acid batteries and improved variants are still used today as an integral part of vehicles with internal combustion engines. There, the battery is usually used to start the engine and is later recharged by an alternator. The high weight of the battery, the large amount of stored sulfuric acid, and the specific charge and discharge characteristics make the lead-acid battery rather unattractive for applications other than in the automotive and transportation sectors.

The first dry cells that functioned without leaking or spilling liquid were based on the cell chemistry proposed by Georges Leclanché in 1866.[11] Originally, the Leclanché wet cells contained a zinc anode and a manganese dioxide cathode immersed in an ammonium chloride solution. In 1886, German scientist Carl Gassner "solidified" the cell by mixing the ammonium chloride with gypsum.[12] Other cell designs used zinc chloride instead of ammonium chloride as the electrolyte, but still relied on the same redox reaction. These cells became known as dry cells or zinc-carbon cells because the current collector is made of carbon.
The zinc-carbon cell was popular as a primary battery until the 1950s, when it was

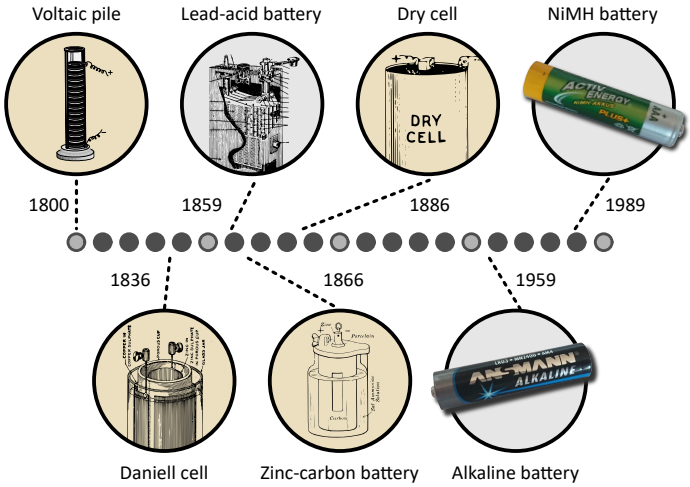

Figure 1.2: Timeline of historically important battery inventions and innovations from 1800 until 2000. The colored backgrounds indicate if a certain battery is technologically outdated (beige) or is still used in large quantities (gray) as of 2022.

eventually replaced by the alkaline batteries still used today. While the electrode active materials are the same as in the Leclanch'e and Gassner cells (Zn and MnO_2), potassium hydroxide is used in these alkaline batteries instead of ammonium chloride or zinc chloride, hence the name.[13] Because of its much higher energy density and longer shelf life compared to zinc-carbon cells, the alkaline battery quickly became the battery type of choice for most consumer electronics. Although alkaline batteries are often sold and used as primary batteries, they can be recharged up to 10 times. Another (secondary) cell that has made its way into the consumer market is the nickel-metal hydride (NiMH) battery. This battery uses an intermetallic compound as the hydrogen storage material and anode, and nickel hydroxide as the cathode.[14] The NiMH secondary batteries are used primarily in high power consumption devices that would otherwise require frequent replacement of a primary alkaline cell.

1.3 Batteries and their performance indicators

A battery converts chemical energy into electrical energy and vice versa. The electrochemical process in a battery can be described using oxidation and reduction equations, which describe the chemical reactions at the anode and cathode of the discharge cell, respectively. The sum of the oxidation and reduction equations gives the total redox reaction of the system. Discharge of the cell by a load results in an external direct current of electrons, which must be countered by an internal current of positively charged ions to ensure charge neutrality of the cell. An ion-conducting separator spatially and electronically separates the anode from the cathode, creating the half-cells of a full-cell battery. Figure 1.3 schematically shows the operating principle of a battery based on the Daniell cell chemistry.

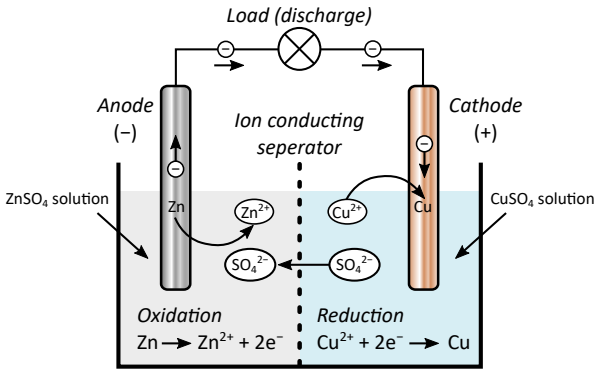

Figure 1.3: Schematic setup of a Daniell cell, illustrating the working principle of a conversion-type battery.

The discharge of a battery is a spontaneous process when the anode and cathode are electrically connected. The driving force of this process is related to the (reversible) cell voltage E_{rev}, which in turn is related to the chemical potential between anode and cathode:

$$E_{\mathrm{rev}} = \frac{\mu_{\mathrm{anode}} - \mu_{\mathrm{cathode}}}{n \cdot F} \ , \tag{1.1}$$

where μ, n, and F are the chemical potential, the number of involved electrons, and the Faraday constant (96 485.332 C/mol), respectively. The maximum electrical work $W_{\mathrm{e,max}}$ that an electrochemical cell can provide is a function of the cell potential and the charge transferred during the discharge reaction:

$$W_{\mathrm{e,max}} = n \cdot F \cdot E_{\mathrm{rev}} \ . \tag{1.2}$$

Since the change in Gibbs free enthalpy $\Delta_{\mathrm{R}}G$ is a measure of the amount of provided work, Equation (1.2) can be expressed as:

$$\Delta_{\mathrm{R}}G = n \cdot F \cdot E_{\mathrm{rev}} \ . \tag{1.3}$$

With the relationship $\Delta_R G = \Delta_R G^\circ + RT \cdot \ln Q_r$, the reversible cell voltage at any condition can be calculated with Equation (1.4):

$$E_{rev} = E^\circ_{rev} - \frac{RT}{nF} \cdot \ln Q_r = E^\circ_{rev} - \frac{RT}{nF} \cdot \ln \prod_{i=1}^{k} a_i^{\nu_k} \ , \tag{1.4}$$

with R, T, Q_r, a_i, and ν_k being the ideal gas constant ($8.314\,47\,\mathrm{J\,mol^{-1}\,K^{-1}}$), the absolute temperature, the reaction quotient, the standard activity, and stoichiometric coefficient of component i (negative for products, respectively). The zero denotes standard conditions. Equation (1.4) holds for a reaction equation of k components C:

$$\nu_1 \mathrm{C}_1 + \nu_2 \mathrm{C}_2 + \ldots \rightarrow \ldots + \nu_{k-1} \mathrm{C}_{k-1} + \nu_k \mathrm{C}_k \ . \tag{1.5}$$

Equation (1.4) is commonly known as the Nernst equation and permits the calculation of half-cell and full-cell potentials of electrochemical cells.
In practice, the full cell potential E_{rev} is measured without any load and is therefore referred to as the open cell voltage $V_{OC} = E_{rev}$. The open cell voltage depends solely on the electrode materials and their thermodynamic behavior during the redox reaction. In a real cell, additional factors such as internal transfer resistances (ohmic IR drop) at the various interfaces and junctions, as well as non-ohmic polarization effects reduce the measured cell voltage. The goal must therefore be to reduce these effects in order to use as much as possible of the potential provided by the thermodynamics of the system.
The stored energy E of a battery can be quantified by how long it can deliver a certain current I with a potential V. This is expressed by the time-integral of current times potential, as these quantities usually change over time:

$$E = \int_0^{\Delta t} I \cdot V dt \ . \tag{1.6}$$

Today, it is common to give the capacity C of a battery, which is a measure of the stored charge. Formally it can be calculated by:

$$C = \int_0^{\Delta t} I dt \ . \tag{1.7}$$

Knowing the battery's capacity and voltage, Equation (1.6) for the stored energy can be simplified to:

$$E = C \cdot V \ , \tag{1.8}$$

while the power P that the battery delivers is the product of the drawn discharging current I and the cell voltage V:

$$P = I \cdot V \ . \tag{1.9}$$

The battery capacity depends on the amount of electrode material in the cell, whereas the cell voltage is a function of the Nernst potential (open cell voltage) minus ohmic and non-ohmic losses. Both anode and cathode contribute to the total capacitance and must be balanced to access the maximum theoretical capacity C_{theo} of each electrode.

The electrode capacity is specific to a particular material because it is determined by the number of electrons transferred during the oxidation or reduction reaction and the molecular weight M_w of the electrode material.

$$C_\mathrm{theo} = \frac{nF}{M_\mathrm{w}} \quad . \tag{1.10}$$

Since the specific capacity is usually given in units of [mA h g^{-1}], a conversion from [C] to [mA h] requires multiplying Equation (1.10) by $\frac{1}{3.6}$. Specific capacity describes the upper limit of the usable capacity, which varies with the discharge current. The conversion of chemical energy into electrical energy is associated with the kinetics of the chemical reactions. If the current, which is proportional to the reaction rate, is too high, the usable capacity decreases due to diffusion limitations at the interfaces.
To quantify how fast a battery is charged or discharged, the C-rate [/hour] is used. It is defined as the ratio of discharge or charging current and battery capacity. (Dis-)charging a battery in one hour refers to a rate of 1C, while the process at 10C only takes $\frac{1}{10}$h = 6min. This quantity is of particular interest for applications such as battery electric vehicles, which require fast charging to compete with internal combustion engine cars that take only a few minutes to refill. For secondary batteries, the Coulombic efficiency CE determines how efficiently a charge is transferred in batteries. It is the ratio between the amount of electrons removed and the number of electrons originally introduced over the course of a complete charge/discharge cycle:

$$CE = \frac{C_\mathrm{discharge}}{C_\mathrm{charge}} \quad . \tag{1.11}$$

For a fully reversible system, the CE is 100%, while in practice it is less than 100%. The "lost" electrons can be consumed by the formation of by-products or transported from the anode to the cathode *via* the separator, eventually bypassing the external load. If the bypassed electrons are accompanied by ions, or if neutral species are transferred internally, the battery will self-discharge over time.[15] Self-discharge further limits the available capacity of a battery after some time in storage. However, self-discharge is not permanent and can be prevented by recharging the battery from time to time.
At any point during discharge, the percentage of remaining capacity relative to maximum capacity is indicated by the State of Charge (SoC). This quantity, often expressed as a percentage, is a valuable indicator of how far the battery has been drained of its energy. From the Equation (1.8), we know that battery energy is the product of stored capacity and voltage. To determine the SoC, we can use this relationship by either integrating the current over time (which gives the charge) or measuring the cell voltage, if it varies with the SoC. Since these methods have their shortcomings, more accurate SoC estimates can be made by combining them or implementing Kalman filters that iteratively estimate the state of a system using multiple external measurements.[16] While state of charge is useful to determine the current state of the battery, state of health (SoH) refers to the state after cycling and aging. SoH is defined as the ratio between the maximum available battery capacity and the rated capacity when the battery was new. A SoH of 50% means a loss of 50% of the original rated capacity.

1.4 Lithium and sodium ion batteries

Although lithium and sodium are homologous elements that share many physical and chemical properties, lithium and sodium ion batteries (LIB and SIB) differ in many aspects. First, this section reviews the historical LIB development, including prominent battery materials and outstanding contributions by researchers. Second, the SIB technology is shortly introduced and later the two battery types, LIB and SIB, are compared in terms of their key indicators such as energy density, safety, application, and cost. The section concludes with a short discussion of the critical aspects of the LIB and SIB technology.

1.4.1 Developing the lithium ion battery

Since the capacity and voltage determine the energy of a battery, the focus in improving battery technology consequently shifted to lighter elements and compounds with low (anode) and high (cathode) electrode potential. Researchers soon recognized the potential of lithium, as its low density of $0.534\,\mathrm{g\,cm^{-3}}$ yields a high specific capacity of $3860\,\mathrm{mA\,h\,g^{-1}}$.[17,18] Moreover, the standard electrode potential of $-3.04\,\mathrm{V}$ *versus* standard hydrogen electrode (SHE)[17] makes lithium metal an excellent choice for a high voltage battery. However, lithium is very reactive and causes many problems when used in its metallic form. Despite difficult chemistry, some primary LIBs such as the lithium-sulfur dioxide battery[19] or the lithium-manganese oxide battery[20] have been commercialized. Others such as the lithium-iodine-polyvinylpyridine battery in pacemakers are still used today.[21]

The first steps toward a secondary lithium-ion battery were made in the 1970s when the intercalation chemistry of transition metal dichalcogenides was studied.[22–25] For TiS_2, a layered compound, reversible lithium intercalation in a lithium-titanium disulfide battery[26] was demonstrated by Stanley Whittingham in 1973 and soon patented. A few years later, in 1976, Whittingham finally proved the patent claims with a reversible battery.[27] Whittingham's battery, based on a lithium metal anode and a TiS_2 intercalation cathode, provided a cell voltage of $2.5\,\mathrm{V}$.[27] A solution of $LiPF_6$ in propylene carbonate (PC) served as the liquid electrolyte. This battery provided the impetus for developing new cathode materials with higher potential *versus* Li/Li^+. A key breakthrough was made when John Goodenough *et al.* proposed the layered cathode material $LiCoO_2$ (LCO), which had a potential of $3.9\,\mathrm{V}$ *versus* Li/Li^+.[28–30] Goodenough's findings paved the way for developing layered oxides with a lower amount of costly and toxic cobalt, such as NMC ($LiNi_xMn_yCo_zO_2$, $x+y+z\approx 1$) and NCA ($LiNi_{0.8}Co_{0.15}Al_{0.05}O_2$) cathode materials. Other structure types, such as spinels like LMO ($Li_{1-x}Mn_2O_4$) and LNMO ($LiNi_{0.5}Mn_{1.5}O_4$) or olevins like LFP (Li_xFePO_4), also gained a significant share in the LIB market over time.[31] At the time Whittingham proposed his lithium metal-based LIB, Besenhard *et al.* reported the intercalation of lithium in graphite to form LiC_6.[32–34] The crystalline graphite acts as a layered host structure that accepts lithium in its vacancies in the van der Waals gap, similar to the intercalation of lithium ions into the layered LCO-type cathodes. At the time, the idea of implementing LiC_6 as a safer option compared to lithium anodes seemed promising, as the lithium ions could be shifted back and forth between two intercalation electrodes without the risk of dendrite formation during lithium plating, as observed in lithium metal batteries.[35,36] However, co-intercalation of

the liquid electrolyte molecules between the layers leads to the exfoliation of the graphite and eventual destruction of the electrode. Akira Yoshino mitigated the disadvantages of crystalline graphite by using petroleum coke,[37,38] a carbonaceous material with crystalline domains embedded in non-crystalline ones. The latter protected the graphite domains from exfoliation while still providing high specific capacitance. Finally, the LIB with a

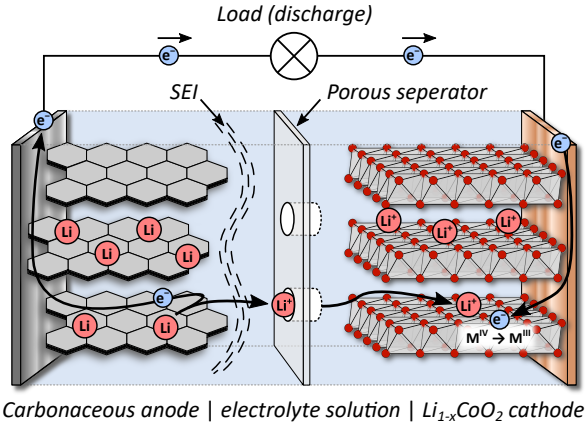

Figure 1.4: Schematic representation of a lithium ion battery based on the C|LCO chemistry with a liquid electrolyte an porous polymer separator.

carbon-based anode, an LCO cathode, and a $LiPF_6$/PC electrolyte was commercialized by the Japanese company SONY in 1991.[39] Concurrent with the commercialization of the LIB, researchers found new electrolyte solvents[40] that reacted with the formerly unusable graphite to form a solid electrolyte interface (SEI) layer.[41] The SEI layer consists of degradation products at the anode-electrolyte interface and protects the graphite from exfoliation. In addition to the carbonaceous anode materials, Li_xM (M = Al, Sn, Mg, Ag, Sb) alloys, Si-based materials, and oxides such as LTO ($Li_4Ti_5O_{12}$) have been intensively researched.[42] LIBs with LTO anodes excel in high C-rate applications[43] and are already being used commercially in BEVs and e-bikes.
Although the road to lithium-ion batteries has been paved with many obstacles, research groups in academia and industry have found creative solutions that enable the highly selective redox chemistry that a long cycle life battery requires. The outstanding contributions of Whittingham, Goodenough and Yoshina were recognized with the 2019 Nobel Prize in Chemistry "for the development of lithium-ion batteries."[44]

1.4.2 Beyond lithium - the sodium ion battery

When the LIB entered the market in 1991, the price of LIBs was USD 7500 per kWh.[45,46] Since then, the price per kWh has dropped by more than 97% to USD 181 in 2018.[45,46] A recent study found that about 50% of the cost reduction was due to improvements in research and development, particularly increases in cell energy density.[47] The study also found that a large portion of the total cost of LIBs is due to the price of the cathode

material. Along with transition metals such as Ni, Co, Mn, and Fe, Li_2CO_3 is the most important starting material for the synthesis of LIB cathode materials. While the price of nickel and especially cobalt has long dominated the cost of NMC-based active materials, the price of a ton of Li_2CO_3 increased from USD 6750 in January 2021 to USD 74725 in October 2022.[48] Given the recent price increase of critical materials and the resulting supply chain risks in some lithium refining countries, the (geopolitical) price of lithium could become a significant risk factor or even bottleneck for future LIB production, especially in Western countries.[49–51] As a promising alternative to lithium-based batteries, chemical intuition points to the use of sodium as a substitute. Although sodium has a lower standard potential (−2.71 V *versus* SHE) and does not form graphite intercalation compounds such as LiC_6, sodium ion batteries (SIBs) have recently received increasing interest. In principle, LIBs and SIBs share the common chemistry of intercalation electrodes immersed in a liquid electrolyte containing lithium or sodium salts. As with LIBs, layered transition metal oxides $NaMO_2$ (M = Fe, Ni, Cr, V, Ti) can be used as cathodes for SIBs, as well as mixed metal oxides $NaM'M''O_2$ (M = Fe, Co, Ni, Mn), similar to NMC materials for LIBs.[52–58] Compared to the often used $LiCoO_2$ cathode material, the sodium counterpart $NaCoO_2$ exhibits a distinct step-like charge-discharge profile (voltage *versus* capacity) caused by the phase transitions in the case of sodium (de)intercalation. The average voltage *versus* Na/Na^+ is about 3 V for $NaMO_2$ cathodes. Other possible cathode materials include metal phosphates and fluorophosphates such as $Na_3V_2(PO_4)_2F_3$[59] with an average half-cell voltage of 3.8 V, as well as Prussian blue analogs such as $Na_{1.92}Fe_2(CN)_6$[60] (3 - 3.5 V *versus* Na/Na^+). Although graphite is rather unsuitable as an anode material, with the exception of solvent co-intercalation,[61] many studies have successfully used hard carbon (HC, 0.25 V *versus* Na/Na^+) as a substitute.[55,62] Besides hard carbon, $Na_2Ti_3O_7$,[63,64] $NaTiO_2$,[65] $Na_3Ti_2(PO_4)_3$,[66] and some sodium alloys and conversion materials[67,68] were identified as suitable low potential anode materials. The choice of electrolyte salts and solvents is quite similar for LIBs and SIBs, to the obvious difference that they contain Na-containing salts.

1.4.3 LIB *versus* SIB

Although lithium and sodium-ion batteries share many similarities in terms of the basic concepts of their chemistry, their performance data differ. This is also true for the different LIB cell types. In this section, we summarize some of the most important key performance indicators (KPIs) and the applications of various commercial LIBs and compare LIBs with a new SIB introduced by CATL. An overview of KPIs for LIBs/SIBs is presented in Table 1.1. The LIB data was sourced from reference [69] and [70], and the data on SIB is taken from the 2021 press release[71] of CATL. The range of specific energy density is quite large for LIBs with carbon-based anodes and depends mainly on the cathode material used. It ranges from 90 Wh/kg for lower power LIBs based on LFP cathode to 260 Wh/kg for LIBs based on NCA. The "oldest" but also most mature cell chemistry, C|LCO, can still compete with newer cells such as HC|NMC or HC|NCA in terms of energy density. High specific energy is especially important for high-performance, long-range BEVs like the Tesla Model S, or for consumer devices like smartphones and laptops that need to last long while being lightweight. The choice of "right" cell chemistry depends

not only on performance KPIs, but is also influenced by price. Despite the low specific energy of LFP-based LIBs, Tesla has already started to use them in its entry-level models because the price of 90 USD/kWh is much lower compared to 130 USD/kWh for the NCA alternative. This development is mainly due to the recent price increase in cobalt and nickel. LFP, which obviously does not require expensive materials (except Li), is often chosen for large stationary energy storage or other applications such as buses where weight is less important. LFP exhibits higher safety because the tendency to thermal runaway is much lower compared to LCO and NMC-based batteries. It also exhibits a very high cycle life compared to most other batteries. Another cell chemistry that is considered very safe and enduring is the LTO | LMO or LTO | NMC configuration. Unfortunately, this cell type has a low specific energy and is one of the more expensive batteries.

Table 1.1: Comparison of commercially available LIB and soon available SIB cells. Abbreviations: *TR*: thermal runaway, *C*: graphite, *HC*: hard carbon, *LCO*: $LiCoO_2$, *NMC*: $LiNi_xCo_yMn_zO_2$, *NCA*: $LiNi_{0.8}Co_{0.15}Al_{0.05}O_2$, *LMO*: $LiMn_2O_4$, *LTO*: $Li_4Ti_5O_{12}$, *LFP*: $LiFePO_4$, *PB*: Prussian Blue analougue.

Type	Chemistry	E_{cell} [V]	Energy [Wh/kg]	Cycle life	Charge [C-rate]	Discharge [C-rate]	Safety TR [°C]
LIB	C | LCO	3.6-3.9	150-200	500-1000	0.7-1	1	150
LIB	HC | NMC	3.6-4.0	150-220	1000-2000	0.7-1	1	210
LIB	HC | NCA	3.6-3.65	200-260	500	0.7	1	150
LIB	HC | LMO	3.7-4.0	100-150	300-700	0.7-1	1	250
LIB	LTO | LMO LTO | NMC	2.3-2.5	50-85	3000-7000	1	10	NA
LIB	HC | LFP	3.2-3.3	90-130	2000+	1	1-25	270
SIB	HC | PB	2.75-3.25	165-200	–	–	–	–

Both academic and industrial research over the past 20 to 30 years has focused on the development and improvement of LIBs rather than SIBs. Recently, however, interest in SIBs has increased as risks in the supply of lithium and typical cathode raw materials are increasingly discussed. In 2020, Abraham compared two proposed SIBs, an 18650 cell (18 mm diameter, 65 mm height, (0) indicates a round cell) from the French research agency CNRS CEA and one from Washington University /PNNL. While the CEA cell holds 90 Wh/kg, the author calculated a specific energy of 150 Wh/kg for the WSU/PNNL cell.[72] Recently, the Chinese company CATL announced a "first generation" SIB with 160 Wh/kg and 15 min fast charging capability (80% SoC) for 2023.[71] They promised high cycling stability even at −20 °C, a temperature at which most LIBs struggle to operate. The company is targeting a specific energy of more than 200 Wh/kg for the second-generation SIB. Assuming that the announced CATL SIB cells deliver the specified energy, LFP- and LMO-based LIBs could face serious competition in the medium term because their specific energies are comparable. The higher natural abundance of sodium (23600 ppm) compared to lithium (20 ppm) in the Earth's crust brings a potential cost

advantage for SIBs in the long term. Another cost-reducing factor for SIBs could be the use of aluminum foil as an anodic current collector. In LIBs, copper foil must be used as a current collector on the anode side because aluminum will alloy with lithium at low potentials. No such alloying reaction with aluminum is known for sodium, making aluminum a viable and cheaper option for SIBs. Currently, the overall cost of LIB is low due to economic scaling effects and high capacity utilization.[45,47] If SIB technology follows the same trajectory as LIB technologies in terms of improving capacity and reducing overall processing costs, SIBs could become cost competitive with LIBs.[72,73] Therefore, sodium ion conducting compounds are highly interesting as potential electrode or electrolyte materials.

1.4.4 Critical aspects of LIBs and SIBs

Despite the progress that LIBs and, most recently, SIBs have made, some critical aspects of the current technology must be mentioned. Apart from the environmental criticisms of raw material mining and production, which are by far the most important, LIBs and SIBs are often criticized for their safety risk. The origin of the safety concern with LIBs is often the use of liquid electrolytes. The solvents used pose a safety concern if the cell is shorted either by internal lithium/sodium dendrite formation, external penetration, or mechanical abuse.[74] Short-circuiting results in the rapid discharge of the cell and subsequent thermal runaway of the battery. This process is characterized by self-sustaining energy generation due to thermal decomposition. Once the temperature is high enough, the liquid electrolyte catches fire, usually resulting in the destruction of the entire device and release of toxic fumes. Overcharging, rapid charging and even simple aging can also cause thermal runaway.[74] These safety concerns have long been in the public eye, but have yet to be fully addressed. Another problem with current LIB technology is the poor chemical compatibility of lithium metal with liquid electrolyte solvents. When a lithium metal anode is used, side reactions consume large amounts of lithium over time, reducing the overall Coulombic efficiency of the battery. To compensate for the lithium loss, a larger amount of up to 300% excess lithium metal was initially added to the battery.[75] However, this practice increases costs and lowers energy density.[75] Considering all the disadvantages of lithium metal anodes, such as dendrite formation and dead lithium, side reactions, and volume change during charging/discharging, the use of lower capacity carbonaceous anodes has become the standard for LIBs.

The drive to increase safety and energy density has inevitably brought the use of lithium metal anodes back into focus. Finding less flammable or better replacing liquid electrolytes is seen as one of the next major steps in improving LIBs. Ideally, novel electrolytes for LIBs and SIBs will have high ionic conductivity and chemical stability (relative to Li), be processable on a larger scale, and be made from cheap and abundant elements.

1.5 All solid-state batteries and solid electrolytes

New technologies must offer an advantage over existing technology to achieve a profitable market share. The high energy density of LIBs has always been the selling point for the use of this special electrochemical cell design in energy- and power-intensive applications. A possible successor to the LIB is the all-solid-state battery (ASSB). This section presents possible active materials for ASSBs and compares the new cell architecture and processing challenges with current LIBs. It also discusses the fundamental physics of ion-conducting solids and introduces relevant solid-state electrolyte classes that are at the heart of ASSBs. Finally, the section focuses on the class of sulfide- and thiophosphate-based solid electrolytes.

1.5.1 Electrode materials and fabrication challenges for ASSBs

In principle, the choice of active materials for solid-state batteries can be derived from LIBs. However, the change from liquid to solid electrolytes does not automatically lead to an immediate increase in the performance of ASSBs. The energy density of an ASSB with intercalation-based active materials might even be lower compared to LIB cells.[6] One of the main issues preventing higher energy densities in lithium-based batteries is the long-term incompatibility of the lithium metal with most (solid) electrolytes. For many years, the selling point of ASSBs was the use of lithium metal, as this promised an increase in gravimetric energy density of about 40 % compared to LIBs.[6] This is mainly due to the high specific capacity of lithium, but also to the higher cell voltage. However, the same problems arise with lithium metal anodes in ASSBs as with LIBs. The high chemical reactivity and the tendency for dendrite growth along the grain boundaries of the solid electrolyte in ASSB make the use of lithium one of the biggest challenges for solid-state batteries. A recent expert survey on the technological and market potential (i.e. the latent capacity for a technology to contribute to societal or economic progress) of various ASSB anode materials concluded that the market potential for lithium metal anodes is considered critically low, while the technological potential is considered high.[18] The study also concluded that silicon-based anodes could have similar (high) technological potential to Li-metal while, in addition, achieving high market potential.[18] Silicon has a high theoretical capacity of more than $3500\,\mathrm{mA\,h\,g^{-1}}$ (depending on the Li_xSi composition), but also exhibits a volume change of more than 300 %. This poses a challenge to the mechanical stability of the battery, as the volume change during cycling leads to contact loss, particle pulverization, and destruction of the protective layer.[76] Approaches to limit the harmful effects of volume change include nanosizing, encapsulating Si in graphite, patterning silicon by introducing pores or cavities, and even using multifunctional binders to help with binning and bonding the particles.[76]

In terms of material selection for the cathode side, there are no major differences between ASSBs and LIBs. Layered oxides such as LCO, NMC and NCA, as well as spinel and olevine-like materials such as LMNO and LFP, are considered suitable in terms of their technological potential.[18] As with LIBs, cathode cost could become more and more of a limiting factor in the battery production. For example, the higher capacity of NMC/NCA cathodes could be offset by the lower cost of LFP-based systems. In particular, LFP cathodes in ASSBs could be successful in low-cost, short-range BEVs

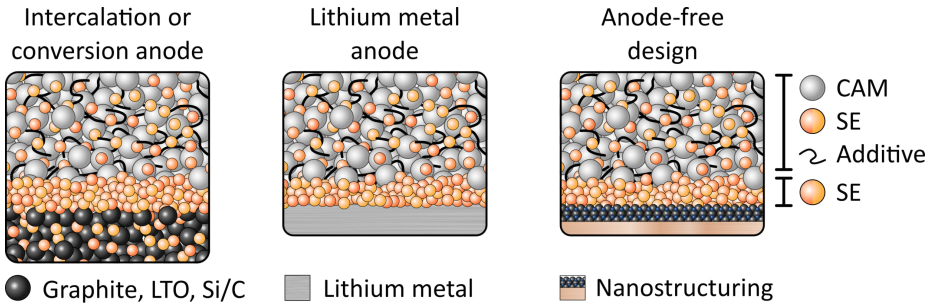

Figure 1.5: Schematic ASSB designs based on a intercalation cathode and solid electrolyte separator and different anode types. Left for right: Intercalation anode, lithium metal anode, anode-free or nanostructured anode.

or stationary applications.[18] The processing of the battery materials, the manufacturing of the components and finally the production of the ASSBs differ in many ways from the LIBs. The electrodes in LIB cells are porous to soak up the lithium ion conducting liquid electrolyte. This solvent infiltration ensures that the large surface area of both electrodes is fully wetted, allowing efficient ion transport through and into the active material. A similar strategy is being explored for the fabrication of ASSB cathodes, using a solution or dispersion of SE in an organic solvent for infiltration. Alternatively, the cathode active material (CAM) and solid electrolyte (SE) are dispersed together in a solution of solvent and (polymeric) binder and then applied to the current collector. For both processing techniques, a drying and pressing step (calendering) is mandatory. If solvents must be or can be avoided, melt extrusion of CAM, SE, binder and additives is an option. This dry processing can be combined with extrusion of the solid electrolyte in a co-extruder to obtain a cathode-separator laminate.[77,78] The type of processing, wet or dry, is mainly determined by the type of solid electrolyte used.[18] All of these processing steps for cathode composites require extensive knowledge of the chemical and thermal stability of the individual components, the rheology of the slurry or melt, and the influence of microstructure on performance after calendering.[18] The fabrication of anodes can be similar to cathodes if graphite-, LTO-, or silicon-based active anode materials are used. In the case of lithium metal anodes, some unique but undesirable properties of lithium further complicate the cell fabrication process. The surface of fresh lithium metal foils reacts quickly with many atmospheric constituents, forming highly resistive products on the surface. Additionally, lithium metal adheres to many materials, making it difficult to calender or press without ripping the foil apart. The soft nature of lithium is also problematic, as it tends to creep and flow plastically.[79]
The anode-free cell design, as shown in Figure 1.5, avoids lithium foil handling challenges by *in situ* lithium deposition during the first discharge cycle. Therefore, a structured anode is used to deposit lithium metal uniformly.[80] In this configuration, lithium is introduced exclusively through the fully lithiated cathode active material. Although this cell design is promising, lithium-consuming side reactions reduce the effective cathode capacity because no excess lithium is available. During cell assembly, the cathode, separator and anode are brought together to finally build the cell. To achieve this, the sheets must be cut

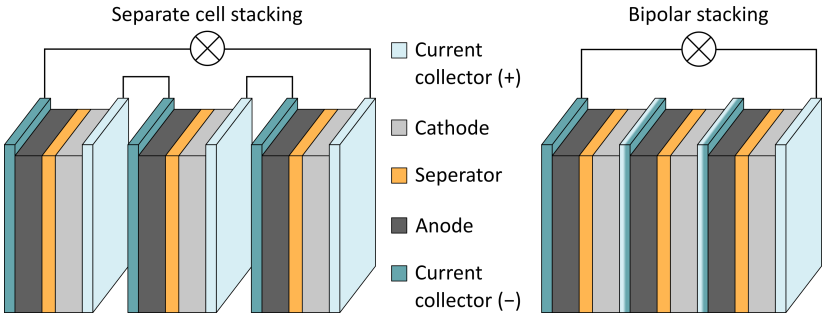

Figure 1.6: Left: Scheme of separate cell stacking and serial electric connection. Right: Bipolar stacking configuration.

(by laser), stacked on top of each other, joined by pressing, and finally enclosed in a cell housing.[18,77] For ASSBs, these individual steps may differ from those of LIB production due to the mechanical properties of the solid electrolyte and the possibility of bipolar stacking. Typically, the individual cells are stacked and connected in series, resulting in the typical LIB cell architecture shown in Figure 1.6. However, ASSBs can also be realized in a bipolar stacking configuration. This is achieved by connecting two or more cells in directly series, bypassing the need of additional electric connections, resulting in a higher single cell voltage and potentially higher energy density.[18] A schematic representation of single and bipolar cell stacking is shown in Figure 1.6. However, bipolar stacking is considered a major challenge for ASSB production, as the electrodes must be almost perfectly matched in terms of capacity (areal loading) to achieve the promised benefit.
The solid electrolyte poses another challenge for cell manufacturing, as the often brittle nature of the SE hinders certain steps in manufacturing and assembly.[77] In terms of industrially relevant cell designs, three cell types stand out for LIBs: cylindrical, pouch, and prismatic. While cylindrical cells have the cathode/separator/anode laminate rolled up and enclosed in a metal cylinder, pouch and prismatic cells use flat laminate plates. The latter two cell types are preferred for ASSBs because they can be pressurized to maintain tight interfacial contact between the components during cycling.[77] For ASSBs with very soft and flexible electrolytes, cylindrical cells may be an option.[77]

1.5.2 Fundamental physics of solid electrolytes

Assuming that the above problems are solved, the performance of a solid-state battery depends to a large extent on the solid electrolyte. Therefore, understanding the fundamental physics that govern the ion migration in solids is paramount. In a crystalline solid, the atoms or ions are densely packed in an ordered manner. For ions to move, this order must be temporarily and locally disrupted by creating intrinsic defects. These defects are divided into Schottky and Frenkel defects, where an anion-cation pair is removed from the bulk and relocated to the surface (Schottky), or the ions occupy interstitial sites instead of their lattice sites (Frenkel). While intrinsic defects are relevant for near perfect single crystals at high temperatures, extrinsic defects play a dominant role in most "real" samples. Extrinsic defects are introduced either by (intentional) doping of the

material or by a non-stoichiometric composition, which is an elemental ratio not represent by natural numbers, resulting in an excess or deficiency of the migrating ion. Prominent examples of non-stoichiometric ion conductors are CeO_2 based systems, in which the ionic conductivity can be tuned by surface reduction at low oxygen partial pressure to produce highly conductive $CeO_{2-\delta}$.[81] Doping can be achieved by aliovalent substitution of atoms or ions, which is compensated by more or less available (mobile) charge carriers in the solid to guarantee charge neutrality. A discussion on substitutions in solid electrolytes and some prominent examples are given in later sections.
The random (Brownian) motion of ions in the lattice of a solid is thermally activated.[82] The coordination sphere around a mobile ion creates a potential well in which the ion resides in its equilibrium position. To move from the starting site to a neighboring site, the ion must cross the potential barrier between the two sites. The hopping model attempts to explain ionic conduction as a series of hopping processes based on the random walk theory for uncorrelated motion. At any nonzero temperature, a mobile ion attempts to jump from its potential well at a frequency ν (jump rate of successful jumps) to a neighboring site at a distance r (hopping distance). This jump attempt is described by the random walk diffusion coefficient D_r:[82,83]

$$D_\mathrm{r} = \frac{r^2 \nu}{z} \ . \tag{1.12}$$

The dimensionality is considered by the geometrical factor z that equals 2, 4 or 6 for one-, two-, or three-dimensional geometries, like in channels, planes or networks. The microscopic random walk diffusion coefficient is connected to the macroscopic (long-range), or sometimes called *charge* or *conductivity* diffusion coefficient D_σ that is accessible *via* conductivity measurements, by the tracer correlation factor f and the Haven ratio H_R:[84]

$$D_\sigma = \frac{f}{H_\mathrm{R}} D_\mathrm{r} \ . \tag{1.13}$$

While f considers single ion correlations (directional ion movement does not influence the consecutive movement of the very same ion, for pure interstitial diffusion $f = 1$), H_R includes many-ion correlations. H_R does not bear a direct physical meaning but includes any deviation from a complete random and uncorrelated ion migration. This means that the directional movement of one ion influences consecutive movements of other ions[84,85] For $H_\mathrm{R} = 1$, the ion diffusion is uncorrelated; values smaller than one indicate a correlated motion.[82] For most materials, f and H_R take values between zero and one.[82,86] The tracer correlation factor and the Haven ratio are mathematically defined as:[84]

$$f \equiv \frac{D_\mathrm{tr}}{D_\mathrm{r}} \ , \quad H_\mathrm{R} \equiv \frac{D_\mathrm{tr}}{D_\sigma} \ . \tag{1.14}$$

The (macroscopically defined) tracer diffusion coefficient D_tr can be obtained by pulsed field gradient nuclear magnetic resonance spectroscopy (PFG NMR) measurements,[84] allowing to calculate the ionic conductivity from PFG NMR, as shown later. The diffusion coefficient D_σ depends on the mobility μ_i of the ion i and the ion's charge q_i (in terms of

elemental charge).

$$D_\sigma = \frac{\mu_i k_\mathrm{B} T}{q_i} \ , \tag{1.15}$$

with k_B and T being the Boltzmann constant and absolute Temperature. Equation (1.15) relates to *dc* ionic conductivity *via* Equation (1.16):[83]

$$\sigma = c_i q_i \mu_i \ , \tag{1.16}$$

with c_i being the concentration of charge carriers. Hence, the ionic conductivity of a solid is calculated by:

$$\sigma = \frac{c_i q_i^2 D_\sigma}{k_\mathrm{B} T} \ , \tag{1.17}$$

which in solid-state electrolyte literature is often called the the Nernst-Einstein relation.[83] Diffusion *via* interstitials is a thermally activated process,[82,83] so that the jump frequency ν (see Equation (1.12)) can be expressed as:

$$\nu = \nu_0 \exp\left(\frac{-\Delta G_\mathrm{m}}{k_\mathrm{B} T}\right) \ , \tag{1.18}$$

with ν_0 and ΔG_m being the attempt frequency (on the order of the Debye frequency)[83] and the Gibbs free energy of ion migration. Equation (1.18) allows to rewrite Equation (1.12) for the diffusion coefficient D_r to:[84]

$$D_\mathrm{r} = g r^2 \nu_0 \exp\left(\frac{-\Delta G_\mathrm{m}}{k_\mathrm{B} T}\right) \ , \tag{1.19}$$

with g being a geometric factor[84] that includes lattice geometry and interstitial type (octahedral or tetrahedral site). With the relation $\Delta G_\mathrm{m} = \Delta H_\mathrm{m} - T\Delta S_\mathrm{m}$ for the free Gibbs energy for ion migration, (1.19) can be rewritten as:

$$D_\mathrm{r} = g r^2 \nu_0 \exp\left(\frac{-\Delta H_\mathrm{m}}{k_\mathrm{B} T}\right) \exp\left(\frac{\Delta S_\mathrm{m}}{k_\mathrm{B}}\right) \ . \tag{1.20}$$

Finally, the ionic conductivity can be expressed by:

$$\sigma = \frac{g f c_i q_i^2 r^2 \nu_0}{H_\mathrm{R}\, k_\mathrm{B} T} \exp\left(\frac{-\Delta H_\mathrm{m}}{k_\mathrm{B} T}\right) \exp\left(\frac{\Delta S_\mathrm{m}}{k_\mathrm{B}}\right) \ . \tag{1.21}$$

As described before, ion diffusion is thermally activated, hence, follows an Arrhenius-type power law:

$$\sigma = \frac{\sigma_0}{T} \exp\left(\frac{-\Delta H_\mathrm{a}}{k_B T}\right) = \frac{\sigma_0}{T} \exp\left(\frac{-\Delta H_\mathrm{m}}{k_\mathrm{B} T}\right) \exp\left(\frac{-\Delta H_\mathrm{f}}{2 k_\mathrm{B} T}\right) \ , \tag{1.22}$$

where ΔH_m and ΔH_f are the migration and formation enthalpy of the charge carrier. Only at high temperature, where significant intrinsic defect formation happens, ΔH_f plays a role. If the concentration of extrinsic defects exceeds the amount of intrinsic

defects, Equation (1.22) simplifies to (1.23) with ΔH_m being the activation energy E_a, an expression that it is mostly referred to as the Arrhenius equation for ionic conductivity (in solids) in the literature:

$$\sigma = \frac{\sigma_0}{T} \exp\left(\frac{-E_\mathrm{a}}{k_B T}\right) \quad . \tag{1.23}$$

The pre-exponential factor σ_0 includes the contribution of jump distance and frequency, possible ion-ion correlation and geometric factors, as well as entropy effects (see Equation (1.20)):

$$\sigma_0 = \frac{q_i^2 c_i f g r^2 \nu_0}{H_\mathrm{R}\, k_\mathrm{B}} \exp\left(\frac{\Delta S_\mathrm{m}}{k_\mathrm{B}}\right) \quad . \tag{1.24}$$

Many inorganic solid ionic conductors follow the Arrhenius law of Equation (1.23). Therefore, correlated or uncorrelated ion hopping *via* point defects can be assumed to be the predominant conduction mechanism in these solids.[87]
Of course, also some ionic conductors exhibit a different ion transport mechanism. In particular, very fast ionic conductors such as $RbAg_4I_5$ or β-AgI exhibit an almost liquid-like conductivity, hence the term "superionic conductors". This is thought to be due to the partially molten cation sublattice in these compounds. This high disorder results in a nearly flat potential energy surface for facile ionic motion.
Another uncommon mechanism involves the rotational freedom of some anions, namely the paddle-wheel effect. This effect is based on the idea that the rotational disorder of complex, globular-shaped anions drives nearby cations in a concerted manner, much like a revolving door leads someone in a particular direction. The entropy-driven paddle-wheel effect has been described for many classes of materials and has recently gained more attention due to the high ionic conductivities found in plastic crystal phases.[88] However, the exact mechanism is still controversial as it raises the classical chicken-egg dilemma of cation-anion coupling interactions.

1.5.3 Optimization strategies for solid electrolytes

The previous section has introduced the fundamentals of ion migration based on the ion hopping mechanism. Furthermore, correlated motion and the paddle-wheel mechanism for ionic conduction were shortly introduced. In this section, different strategies to improve the ionic conductivity of crystalline solids is presented. Some of these strategies can be derived from the fundamentals, presented in the previous section by identifying parameters that can be changed by chemical modification of the material. From Equation (1.21) we can draw the following conclusion: The ionic conductivity depends on several factors, including geometrical factors, correlations, the valency of the mobile ion, and the potential well it resides in. Some of these factors are easily influenced by chemical doping of the system (changing c_i), softening of the lattice (changing ν_0), and expansion or contraction of the lattice (changing r). Of course, changing the dimensionality of the system also affects the ionic conductivity. Thus, the solid-state chemist has a useful set of tools and guidelines for optimizing structures for higher ionic conductivity, which are presented below.

Changing carrier concentration and introducing defects

The ionic conductivity is directly proportional to the charge carrier concentration c_i (see Equation (1.21)). If one increases the concentration of the mobile ion, one would assume that the conductivity would also increase. However, this is not always the case, since structures in which all available sites are occupied by "mobile ions" usually exhibit little to no ionic conductivity. Regulating the carrier concentration by introducing defects serves to keep ions mobile since the so formed vacancies are required for ions to migrate without Coulomb repulsion. For perfect crystals, these (intrinsic) defects were introduced in Section 1.5.2 as Schottky and Frenkel defects. Extrinsic defects arising from intentional aliovalent substitution or ubiquitous impurities dominate in most samples. Prominent examples of substitution in solid electrolytes are given in a later section. Changing the composition by the incorporation of other elements not only changes the charge carrier concentration, but can also affect the bond distances and thus the hopping distance r.

Concerted ion migration

As briefly mentioned in section 1.5.2, concerted ion migration, captured by the Haven ratio H_R, can facilitate ion migration over long distances by lowering the energy barrier for hopping. It describes a process in which multiple neighboring ions jump to their respective adjacent sites within a short time frame. The simultaneous movement of many ions in close distance reduces the overall activation barrier, as ions jumping from high to low-energy sites lower the activation barrier that applies to ions jumping from low to high-energy sites. The origin of this "pushing" or "pulling" phenomenon has been attributed to Coulomb interactions between cations and is often observed in structures with high mobile cation concentrations, such as $Li_{10}GeP_2S_{12}$,[89] $Li_7La_3Zr_2O_{12}$,,[89,90] $Li_{1.3}Al_{0.3}Ti_{1.7}(PO_4)_3$,[89] β-Li_3PS_4,[91] and $Na_3Zr_2Si_2PO_{12}$.[92] In these structures, more lithium ions are available as low energy sites, which forces the excess lithium ions to occupy vacant higher energy sites. Tuning the carrier concentration to force correlated ion migration has the potential to improve ionic conductivity for many structures that allow aliovalent substitution.

Crystal structure

For lithium ions, a tetrahedral (coordination number CN = 4) or octahedral (CN = 6) coordination environment is most common.[93] The coordination polyhedra, spanned by the anion sublattice, form a potential well for the cation. During the migration from its initial site to its final site, the mobile ion overcomes the energy barrier between two adjacent potential wells. In a computational study, Wang investigated the influence of three different sulfide sublattice packings, body-centered cubic (bcc), face-centered cubic (fcc), and hexagonal close-packing (hcp), on the energy barrier for the ion jump (see Figure 1.7.[94] While structures with bcc-type anion packing have face-sharing tetrahedra (T), fcc-type packing has adjacent tetrahedra connected by a common face-sharing octahedron (O). The connectivity of low energy tetrahedral sites in bcc lattices is associated with a low energy barrier to the T-T jump, while in fcc lattices, the necessary jump into an octahedral site, which has a higher energy, results in an overall higher barrier to the corresponding T-O-T jump.[94] Structures with an hcp-like sulfide arrangement have both T-T and T-O-T pathways, but the latter are required for lithium diffusion over long

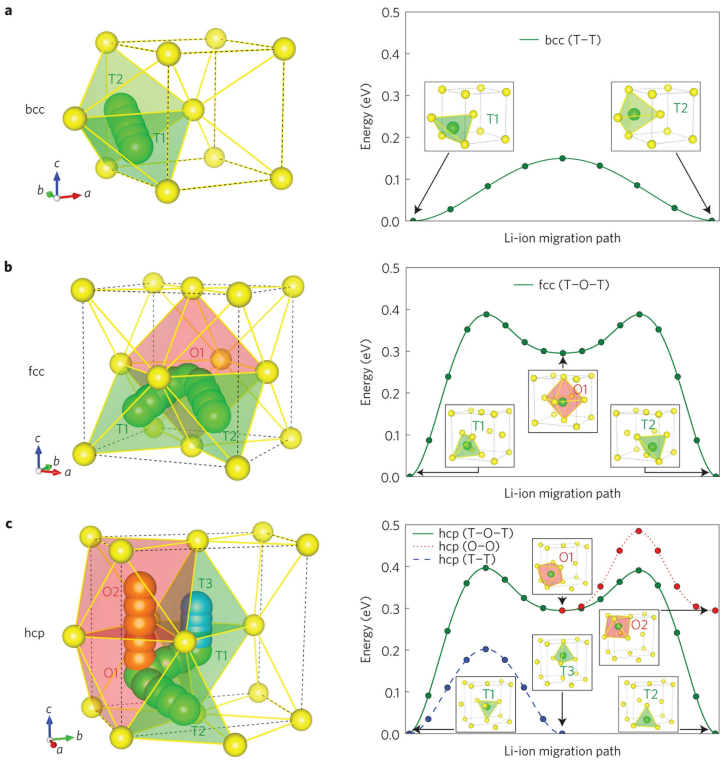

Figure 1.7: Lithium ion migration pathways in (a) bcc, (b) fcc, and (c) hcp anion packing (sulfur depicted as yellow) as calculated by DFT. The corresponding migration barriers are depicted next to the unit cells. The figure was reproduced from Wang *et al.*[94]

distances, which increases the overall barrier compared to the energies obtained for fcc packing. The increased activation barrier decreases ionic conductivity according to the Arrhenius relationship in Equation (1.23). This demonstrates the influence of anion packing types for 3D ionic conductors and provides an explanation for the high ionic conductivities observed for compounds such as $Li_{10}GeP_2S_{12}$ and $Li_7P_3S_{11}$ with a predominantly tetrahedral coordination network for lithium.[94]

In addition to anion packing, dimensionality is an important factor for ionic conductivity, which - in a simple picture - is reflected not only in the geometric factor z (1D: $z = 2$, 2D: $z = 4$, 3D: $z = 6$) in the Equation (1.12), but more importantly in possible clogging of the paths. In a 3D ionic conductor, ions can move freely in all three spatial dimensions. In 2D and 1D ionic conductors, ion movement is restricted to planes or channels along a particular crystallographic direction. While point defects or disorder, for example due to impurities, do not play a major role in 2D ionic conductors, the path in 1D ionic conductors can be blocked simply by the presence of an immobile cation.[95–97] Another aspect of dimensionality is the behavior at grain boundaries. The more isotropic ion migration in 3D ionic conductors favors migration between grains, while the probability of an unfavorable arrangement of grains leading to clogging of the conduction path is

higher with lower dimensionality of the conduction path. Although this simplified picture does not acknowledge more complex grain boundary behaviors, it demonstrates why solid electrolytes with two- or three-dimensional paths are preferred.

Structural frustration and disorder

Structural frustration in solids refers to atoms occupying positions that do not fully satisfy their geometric and/or electrostatic requirements; in other words, atoms located in rather unusual or distorted coordination polyhedra. Distorted coordination polyhedra are energetically less favorable to lithium ions and therefore flatten the potential energy landscape experienced by lithium ions during migration.[93] This is because the lack of a well-defined and geometrically constraining position forces the lithium ion to occupy positions that are energetically closer (and higher), as the formation energy for distorted lithium coordination polyhedra as in $[LiS_4]$ tetrahedra in $LiTi_2(PS_4)_3$ is higher than for more regular tetrahedra.[93] In $LiTi_2(PS_4)_3$, the frustration of the energy landscape and thus an entropically stabilized transition state for lithium ion migration leads to a high pre-exponential factor together with a low energy barrier.[93] Moreover, the higher pre-exponential factor in $LiTi_2(PS_4)_3$ is due to a larger hopping distance defined by the lithium-titanium distance rather than the lithium-lithium distance. A similar effect of the frustrated structure and energy landscape is thought to account for the much higher ionic conductivity of $Na_{8.5}(AlS_4)_{0.5}(SiS_4)_{1.5}$ compared to other members of the Na_5AlS_4-Na_4SiS_4 solid solution series.[98]
Structural frustration is observed not only in cation-anion coordination polyhedra, but also in cation-cation interactions. For the garnet $Li_xLa_3Zr_2O_{12}$ ($3 < x < 7$, LLZO), strong lithium-lithium interactions have been observed for half-integer (x) compositions, leading to a disordered and frustrated lithium ion sublattice.[99] The ionic conductivity is expected to be higher for $x = 5.5$ and $x = 6.5$ compared to other compositions.
Disorder in the anion sublattice is best known for argyrodites, which will be discussed in a later section. There, the disorder between S^{2-} and X^- ($X =$ Cl, Br, I) anions has been shown to affect the ionic conductivity of lithium ions.[100] Introducing frustration and disorder through the application of novel synthetic routes or the search for structure types with inherently disordered coordination polyhedra for alkaline cations represent an additional design strategy for solid electrolytes.

Lattice softness and anion lattice dynamics

When considering rather static potential wells, in which ions oscillate around their equilibrium, low-energy site to eventually jump to an adjacent site, the influence of lattice dynamics on ion motion is neglected. Selectively tuning the depth and width of the potential wells by reducing the interaction between cations and the anion sublattice can improve ionic conductivity by many orders of magnitude. Several design principles discussed in this section have been proposed.
First, the bonding interaction between the host lattice and the mobile ion can be weakened by what is known as softening of the lattice. This is achieved by increasing the polarizability of the lattice by isovalent substitution of, e.g. O^{2-} with S^{2-} or S^{2-} with Se^{2-}. Elements with a larger ionic radius are more polarizable because they are more capable of forming

spontaneous dipoles. The combination of less polarizable cations with more polarizable anions results in an overall more covalent bonding character, which effectively reduces the electrostatic penalty for ionic motion of otherwise ionic compounds.[101] This basic principle was recognized by applying the principle of hard and soft acids and bases (HSAB) for solid electrolytes, leading to the discovery of many new solid ion conductors. The effect of lattice softening is best observed in argyrodites and thio-LISICON compounds, which will be discussed in a later section.

Second, changing the anion lattice to a softer lattice not only affects the covalency of the cation-anion interaction, but also reduces the total lattice vibrations, directly affecting the attempt frequency ν_0 of ion jumps.[102–104] Several physical quantities have been identified that correlate well with total lattice vibrations. These include the Debye frequency, which is accessible *via* sound velocity measurements (acoustic phonons), the optical phonon frequency, and the average phonon frequency, often referred to as the phonon band center.[104] The latter can be computed, as well as measured by inelastic neutron scattering, making the phonon band center a useful descriptor for lattice vibrations and their effect on migration enthalpy and entropy.

Third, the lattice dynamics involving the rotation of polyanionic motifs should not go unmentioned. Normally, in an inorganic solid, the relaxation time of a mobile cation, i.e., the time it stays in its equilibrium position, is much shorter than the "sublattice motion." Therefore, the anion sublattice is often considered to be immobile and rigid. In this configuration, the anion sublattice does provide a host structure through which cations can move, but it also leads to strong anion-cation interactions during ion migration. In some structures, rapid anion rotation is observed, which has become known as the paddle-wheel effect (see above). The paddle-wheel effect is also known as the revolving door effect. It is characterized by a translationally fixed but rotationally free sublattice,[105,106] as schematically shown in Figure 1.8. The characteristic rapid reorientation of the anions

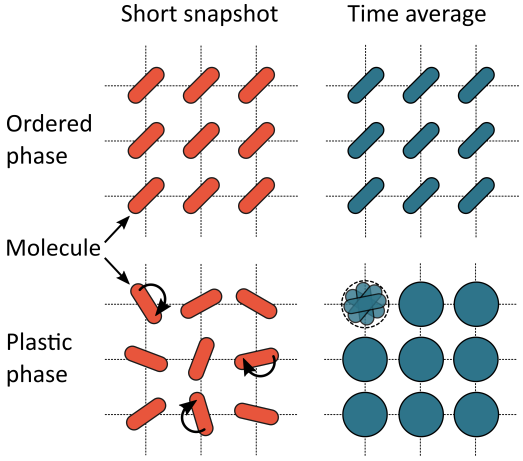

Figure 1.8: Scheme of an ordered and plastic phase. The short snapshot and time average picture illustrate the rotation of the molecule on a short timescale and after longer observation time. Parts of the graphic are loosely adapted from Zhang *et al.*[107] and Lunkenheimer *et al.*[108]

has some unique effects on the material properties of the so-called plastic crystals or rotor phases. First, the heat of fusion is significantly lower compared to chemically similar compounds because the anion sublattice already exhibits a state of high degree of rotational freedom.[109] However, the transition from the solid to the plastic phase is accompanied by a large change in entropy and enthalpy to free these very degrees of rotational freedom. Second, plastic crystal transitions are usually accompanied by a large volume expansion, which is sometimes explained by a larger space requirement for the reorientation of anions, leading to a less densely packed cell.[110–112] Third, plastic crystals often adopt high (cubic) symmetry,[107] like in *HT*-Li_2SO_4.[111] However, some exceptions like Na_3PS_4 exist, which transforms from cubic β-Na_3PS_4 to the orthorhombic γ-Na_3PS_4 rotor phase.[110] This is particularly evident in measurements where signals are accumulated over a long period of time (see Figure 1.8). Fourth, plastic crystals are malleable, which is sometimes considered a beneficial property of solid electrolytes, but can present a challenge for sample handling. Commonly found in organic plastic crystals having large globular shaped molecular motives, is still a rather rare phenomenon for solid ion conductors and is usually reported for high-temperature and high-entropy phases. Lowering the transition temperature is therefore necessary to access the paddle-wheel effect at a more practical temperature. Two recent reports demonstrate how substitution assists this objective. Partial substitution of P^{5+} with Si^{4+} in β-Li_3PS_4 stabilizes the high-temperature rotational phase at room temperature ($\sigma = 1.2 \cdot 10^{-3}\,S\,cm^{-1}$ for $Li_{3.25}[Si_{0.25}P_{.75}]S_4$) by increasing the entropy.[88] Substituting a boron atom in the sodium ion conductor *closo*-$Na_2B_{10}H_{10}$ for carbon ($NaCB_9H_{10}$, $\sigma = 3 \cdot 10^{-2}\,S\,cm^{-1}$ at 297 K) effectively lowers the transition temperature from an initial 373 K to 323 K, which is further stabilized to 285 K after heating above 310 K.[113] These two examples show how increasing entropy and decreasing formal polyanion charge help to facilitate rapid anion rotational disorder, effectively increasing conductivity and lowering activation energy.

1.5.4 Material classes of solid ion conductors

Crystalline, glass-ceramic, and glassy solid ionic conductors can be classified by many different characteristics, including conductivity, mobile ion type (anion *versus* cation, or H^+, Li^+, Na^+, ...) and ionic valence (M^+, M^{2+}, ...), structure type (garnets, spinels, rock salt-like, ...), and dimensionality (1D, 2D, 3D) or material class (oxide, sulfide, halide, ...). Although each classification category has its advantages, it is common for battery-relevant solid electrolytes (SE) to be classified according to their anion host structure. Three SE material classes are often mentioned: oxide-, polymer-, and sulfide-based electrolytes. However, there are also classes such as halides, borohydrides and phosphidometalates, but their importance for research and industrial applications is currently rather low. A schematic overview of the solid electrolyte classes presented below is depicted in Figure 1.9.

Oxide-based solid electrolytes

The term "oxide-based" can be misleading, as this class includes not only oxides but also sulfates, phosphates, or other complex O-containing structures and anions. This class of materials typically offers high mechanical, thermal, and chemical stability, a wide

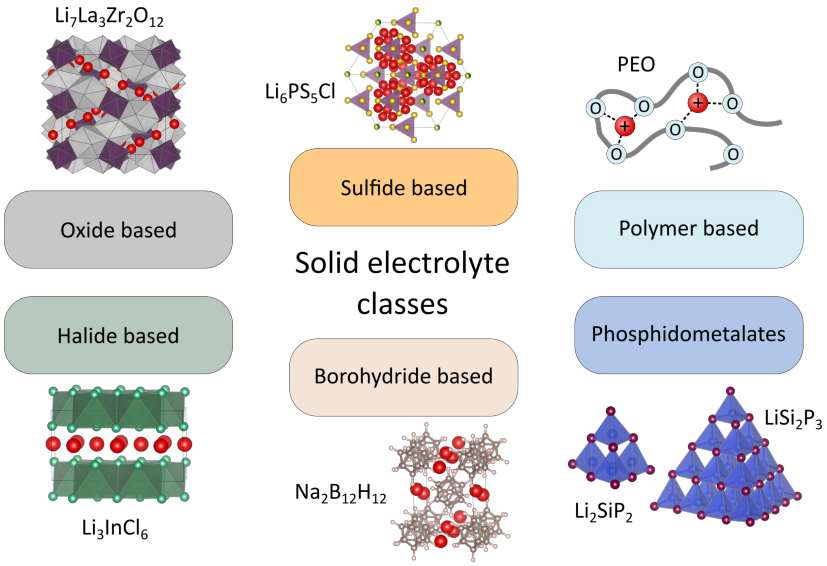

Figure 1.9: Material classes of solid electrolytes with a prominent example.

electrochemical stability window (some are even stable to Li metal) and does not require a special atmosphere for fabrication, storage, and handling. Despite these advantages, oxide-based SEs have the disadvantage of being brittle and requiring sintering at high temperatures. This costly production step is necessary to lower the disadvantageous grain boundary resistance to achieve the high ionic conductivities required in an ASSB. However, the temperature sensitivity of many active cathode materials makes co-sintering oxide-based SEs with CAM another challenge. It can be concluded that oxide-based SEs have potential as separators in high-voltage ASSBs, but require special processing and operational measures due to their brittleness.

Polymer-based solid electrolytes

Although polymer electrolytes are often categorized as solid electrolytes, they differ significantly from their inorganic counterparts. Typically, a polymer backbone, a lithium salt, and additives form a polymer SE. The ionic conductivity is understood as the result of the movement of the polymer backbone above the glass transition temperature. The lithium salt is dissolved in the polymer matrix and serves as an ion source, since the polymer itself does not contain lithium. Additives, like inorganic ceramics, are usually used to improve certain properties, such as dendrite suppression or mechanical strength. Polymeric SEs offer some advantages over ceramic SEs, namely, ease of processing, scalable synthesis, low cost, and soft mechanical properties. However, the low conductivity of simple polyethylene oxide (PEO)-based polymers hinders their mass commercialization. Polymeric SEs with more sophisticated monomers or crosslinks can achieve higher ionic conductivities, but at the expense of increased complexity and cost. In summary, polymer-based SEs offer many desirable properties for an ASSB separator, but their low conductivity

and resistance to dendrite intrusion remain their Achilles heel.

Sulfide-based solid electrolytes

The term "sulfide-based" solid electrolytes includes not only sulfides with free S^{2-} anions, but is usually used for thiophosphates (P-S), thioborates (B-S), and other thiometalates (M-S, M = Si, Ge, Sn, As, Sb, transition metals). However, due to the plethora of thiophosphate compounds in this class, thiophosphate are often mentioned separately, as in this thesis, or as a substitute for "sulfide-based". The rich chemistry of this class of materials has produced many structures with different dimensionalities, exhibiting a wide range of properties and ionic conductivities. Since this work focuses on the synthesis and characterization of thiostanate- and thiophosphate-based Li and Na ionic conductors, Section 1.5.5 is devoted to this class of materials and provides a broader overview of the various structures and their respective properties.

Niche solid electrolytes

Although many research articles and reviews mention only the three SE material classes presented above, a whole range of ionic conductors have been reported that do not fit into the "triumvirate" classification of solid ionic conductors. In this section, emerging solid electrolytes that have drawn a lot of attention in recent years, as well as some often overlooked SEs will be briefly introduced.
First, solid electrolytes based on halides should be mentioned here, as they include some of the most promising candidates as separators for ASSBs. Some halide-based SEs reach ionic conductivity values well above the ASSB-relevant threshold of $1 \cdot 10^{-3}\,\mathrm{S\,cm^{-1}}$,[114,115] for example, Li_3InCl_6 ($2.0 \cdot 10^{-3}\,\mathrm{S\,cm^{-1}}$)[116] synthesized from aqueous solution, or ball mill synthesized $Li_3YBr_3Cl_3$ ($7.2 \cdot 10^{-3}\,\mathrm{S\,cm^{-1}}$).[117] The low valence of the halide sublattice reduces the Coulombic interaction with the lithium (or sodium) ions, thus facilitating ion migration.[118] In addition, the anion sublattice is highly polarizable, especially for the heavier halides, and the materials are generally soft.[118] In terms of their compatibility with high and low potential active materials, halide-based SEs with F^- and Cl^- frameworks are considered superior due to their large electrochemical stability window. However, the metal in Li_3MX_6 type SEs (M = Al, Ga, In, Sc, Er, Y, Ho, Zr, La, ... , X = F, Cl, Br, I) can be redox active, which narrows the electrochemical stability window compared with binary LiX compounds.
Another class of solid-state lithium and sodium ion conductors are borohydrides. This class of materials is characterized in part by the ability of electron-deficient boron to form large molecular structures called clusters. The inclusion of carbon in these clusters is also quite unique among inorganic solid ionic conductors. The simplest borohydride, $LiBH_4$, has an ionic conductivity on the order of $10^{-3}\,\mathrm{S\,cm^{-1}}$, which is suitable for ASSBs.[119] The family of sodium *closo*-borohydrides ($[B_{10}H_{10}]^{2-}$ and $[B_{12}H_{12}]^{2-}$) and their carba-borohydride analogs ($[CB_9H_{10}]^-$ and $[B_{11}H_{12}]^-$) have attracted much attention recently, as their sodium ion conductivities also reach quite high values due to their plastic crystal properties ($>10^{-3}\,\mathrm{S\,cm^{-1}}$).[120–123] Despite their soft nature and advantageous low density, which allows good contact and high gravimetric energy density, borohydrides are difficult to handle and require high temperatures to achieve high conductivity. The high

conductivity of some sodium borohydrides may be of interest for sodium ASSBs in the future.

A completely new class of ion-conducting materials are phosphidometalates, $A_xM_yP_z$ (A = Li, Na, K, M = Al, Si, Ge), which arose from the idea of replacing S^{2-} in $A_xM_yS_z$ with P^{3-}. Some compounds worth mentioning are $Li_{14}SiP_6$ and Li_9AlP_4, showing high lithium ionic conductivity of $1 \cdot 10^{-3}\,S\,cm^{-1}$[124] and $3 \cdot 10^{-3}\,S\,cm^{-1}$,[125] respectively. A fast sodium ion conductor is the high-temperature polymorph $HT-NaSi_2P_3$ with a conductivity of $4 \cdot 10^{-4}\,S\,cm^{-1}$.[126] This highlights the potential of this emerging class of materials. However, further studies are needed to quantify other important parameters for potential use in ASSBs.

1.5.5 Sulfide-based solid ion conductors

As mentioned earlier, sulfide-based electrolytes include different types of structures with different types of anions. In this section, the main subclasses of thio-pnictide-based electrolytes are introduced and their advantages, perspectives, and challenges are briefly discussed. Additionally, thioborates are mentioned as emerging sulfide-based electrolytes.

Thio-LISICON and thio-NASICON

The thio-LISICON and thio-NASICON structures (*LI*thium *S*uper *I*onic *CON*ductor) are the thiophosphate equivalents of their phosphate-based counterparts LISICON and NASICON. The LISICON and NASICON families are derived from the general sum formula $AM_2(PO_4)_3$ ($A =$ Li, Na, $M =$ tri-/tetravalent metal ions). The change from oxide to sulfide sublattices softens the anion sublattice and weakens the interaction of the mobile cation with its host structure, thus increasing the ionic conductivity. An important breakthrough in this class was achieved by stabilizing the metastable β-Li_3PS_4 phase and then optimizing the synthesis to increase the conductivity of $3 \cdot 10^{-7}\,S\,cm^{-1}$ in γ-Li_3PS_4[127] to eventually about $2 \cdot 10^{-4}\,S\,cm^{-1}$ in nanoporous β-Li_3PS_4.[128] The iso- and aliovalent substitution of P in Li_3PS_4 gave rise to many new (moderate) ionic conductors by introducing vacancies or increasing the charge carrier density. In 2011, Kamaya *et al.* reported that the substitution of P by Ge leads to a new thio-LISICON-like conductor. This new compound, $Li_{10}GeP_2S_{12}$ (LGPS), was the first lithium ion-conducting solid with a conductivity value ($1.2 \cdot 10^{-2}\,S\,cm^{-1}$) that outperformed liquid organic electrolytes, and was soon considered the founder of a new class of sulfide-based ion conductors, which are often categorized according to their symmetry. LGPS crystallizes in a tetragonal structure[129] rather than in orthorhombic cells like the original end members of the thio-LISICON family, β-Li_3PS_4 and Li_4GeS_4.[130,131] The LGPS-class will be discussed later. Although LGPS has emerged as a thio-LISICON-related compound, thio-LISICON materials have not demonstrated the high conductivity required for ASSBs. Despite the plethora of oxide-based NASICONs, thio-NASICONs are still rare. A recent example with a moderate ionic conductivity of $1.7 \cdot 10^{-5}\,S\,cm^{-1}$ for $x = 0.4$ is $Na_{1+x}Ti_{2-x}Ga_x(PS_4)_3$.[132]

Na_3PnS_4 (Pn = P, Sb)

The class of SEs of the type Na_2PnS_4 (Pn = P, As, Sb) must be mentioned separately despite their compositional similarity to thio-LISICON and thio-NASICON phases. The best known compound of this class is Na_3PS_4. It crystallizes as either a (low temperature) tetragonal or (high temperature) cubic polymorph. While t-Na_3PS_4 has a low conductivity of about $10^{-6}\,S\,cm^{-1}$,[133] the room temperature stabilized c-Na_3PS_4 has a conductivity of $2 \cdot 10^{-4}\,S\,cm^{-1}$.[134] Phosphorus can be completely replaced by antimony, resulting in a more air-stable Na_3SbS_4 with a high conductivity of $1 \cdot 10^{-3}\,S\,cm^{-1}$.[135,136] Air stability can also be achieved by As substitution.[137] The ionic conductivity of Na_2PnS_4 (Pn = P, Sb) can be further increased to $1.3 \cdot 10^{-2}\,S\,cm^{-1}$ ($Na_{2.9}P_{0.9}W_{0.1}S_4$) or $4.1 \cdot 10^{-2}\,S\,cm^{-1}$ ($Na_{2.9}Sb_{0.9}W_{0.1}S_4$) by aliovalent substitution of Pn with W.[138,139] This sodium ion-exclusive class is very promising due to high conductivity values and low-cost starting materials.

LGPS-type

As described earlier, LGPS-type solid electrolytes form a class of their own, despite their historical association with thio-LISICONs. This class includes some of the record holders for fast lithium ion conductivity, such as $Li_{10}GeP_2S_{12}$ ($1.2 \cdot 10^{-2}\,S\,cm^{-1}$)[129] or $Li_{9.54}Si_{1.74}P_{1.44}S_{11.7}Cl_{0.3}$ ($2.5 \cdot 10^{-2}\,S\,cm^{-1}$).[140] Structurally similar to LGPS and its analogs are $Na_{10}SnP_2S_{12}$ ($4 \cdot 10^{-4}\,S\,cm^{-1}$) and $Na_{11}Sn_2PS_{12}$ ($3.7 \cdot 10^{-3}\,S\,cm^{-1}$).[141,142] The LGPS-like structure consisting of LiS_6–$(M/P)S_4$ (M = Si, Ge, Sn) chains along the c direction that are connected *via* PS_4 tetrahedra, provides a very favorable (flat) energy landscape for ion conduction. The tetragonal crystal structure of $Li_{10}GeP_2S_{12}$, along with the different coordination polyhedra of Li, Ge and P is depicted in Figure 1.10. The dimensionality of ionic conduction in LGPS is quasi-isotropic (3D), with a slight

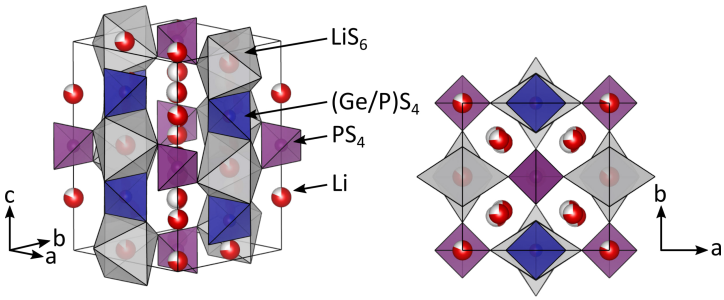

Figure 1.10: Crystal structure of $Li_{10}GeP_2S_{12}$ in different orientations.

preference for conduction along the chains in c direction (1D, see Figure 1.10),[143–147] making this class an excellent choice for potentially high conductivity. Despite the very high conductivity values reported for this class (see Figure 1.11, the LGPS family has some shortcomings. First, some of the highest performing LGPS-type SEs rely on germanium. This metalloid is expensive due to its low abundance in the Earth's crust (about 1.7 ppm), which is problematic for large-scale battery production. The cost of LGPS-type SE can be reduced by replacing Ge with its higher and lower homologues Si and Sn.[145,148–150] Prominent example for silicon-based LGPS-type SE are tetragonal Li_7SiPS_8 and $Li_{11}Si_2PS_{12}$, exhibiting a fast ion conductivity of at least $2 \cdot 10^{-3}\,S\,cm^{-1}$ for t-Li_7SiPS_8[150] and high ion diffusivity of $3.5 \cdot 10^{-12}\,cm\,s^{-2}$ for $Li_{11}Si_2PS_{12}$[145] (LGPS:[151] $D_{exp} = 2.2 \cdot 10^{-12}\,cm\,s^{-2}$). Second, the electrochemical stability window of LPGS-type SEs is low due to the presence of reducible elements (P, Si, Ge, Sn).[152] When in contact with lithium metal, these elements form a mixed ion and electron conducting (MIEC) interface.[153,154] Ultimately, the electrically conductive interface grows until the solid electrolyte or lithium metal anode (LMA) is completely consumed, making it difficult to use an LMA. Strategies to extend the stability window are therefore essential for LGPS-type SEs.

Argyrodites

The class of argyrodites is unique because of its structure. The eponym and first argyrodite to be discovered is the mineral Ag_8GeS_8. In 2008, Deiseroth *et al.* reported a

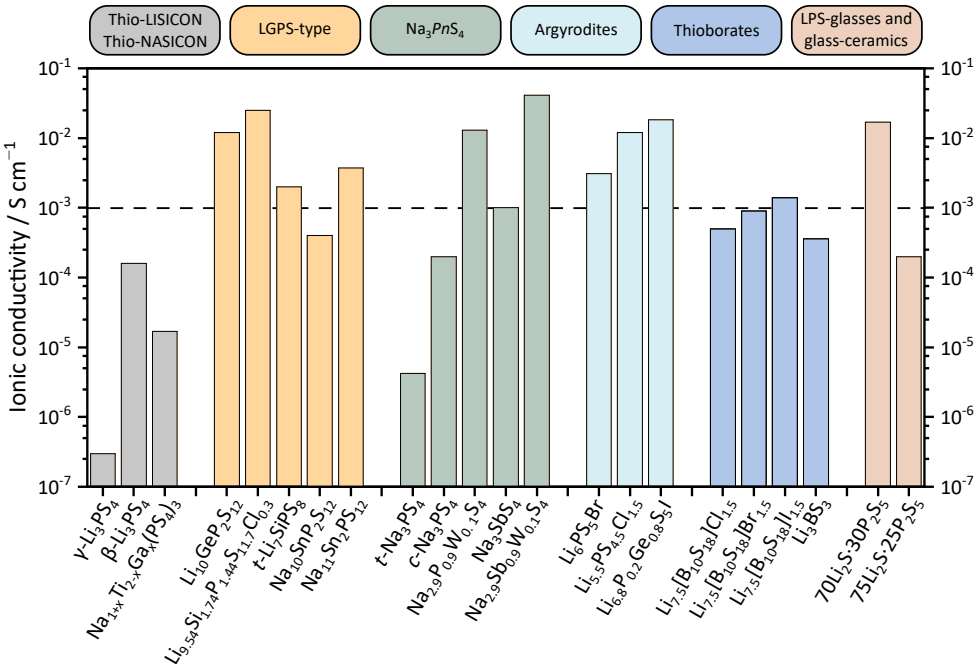

Figure 1.11: Reported ionic conductivities of prominent lithium and sodium solid electrolytes, as mentioned in this section. The dashed line indicates the threshold of the ASSB relevant ionic conductivity of $1 \cdot 10^{-3}\,\mathrm{S\,cm^{-1}}$.[114,115]

lithium analog, Li_6PS_5X (X = Cl, Br, I),[155] which triggered a remarkable development of new metal-free lithium ion conductors with exceptionally high conductivity. Generally, argyrodites are highly tunable because the structure allows substitutions at the P, S, and X sites.[156] In this way, different argyrodite SEs have been identified.[157] The cubic argyrodite structure consists of MCh_4 units (M = P, As, Ge, Si, Sn, Sb, Ch = O, S, Se) filling half of the tetrahedral cavities of the fcc halide packing, while S^{2-} occupies the other half. The lithium ions are scattered in a cage-like arrangement around the S^{2-} anions and can jump from cage to cage, resulting in the long-range ionic conductivity. Additionally, argyrodites exhibit a characteristic halide/sulfide site disorder that can be controlled by the cooling rate of the sample.[100] A higher site disorder is favorable for ionic conduction and lowers the action energy. Tuning the proper X^-/S^{2-} disorder and replacing P with Ge resulted in one of the highest reported ionic conductivities of $1.8 \cdot 10^{-2}\,\mathrm{S\,cm^{-1}}$ in $Li_{6.6}P_{0.2}Ge_{0.8}S_5I$.[158] If metals are to be avoided, $Li_{5.5}PS_{4.5}Cl_{1.5}$ with a conductivity of $1.2 \cdot 10^{-2}\,\mathrm{S\,cm^{-1}}$ is a promising option for ASSBs.[159] Argyrodites with high ionic conductivity of $3.1 \cdot 10^{-3}\,\mathrm{S\,cm^{-1}}$ (Li_6PS_5Br) are also accessible *via* liquid-phase synthesis, thus offering a significant advantage over other sulfide-based SEs.[160] Overall, argyrodites are considered one of the best performing SEs for ASSB applications due to their high conductivity, low cost, and partially scalable synthesis in liquid media. Site disorder must be adjusted and, most importantly, maintained during the battery operation to ensure high performance.

Thioborates

Although thioborates are often not considered part of the sulfide-based solid electrolyte family, they exhibit similar properties to their lithium thiophosphate counterparts. Recently, this subclass has received more attention. Kaup *et al.* reported three new lithium thioborate halides with the composition $Li_{7.5}[B_{10}S_{18}]X_{1.5}$ ($X = $ Cl, Br, I).[161] These form supertetrahedral structures, similar to some phosphidosilicates,[126,162] but additionally contain halide ions that occupy the large channel-like cavities together with lithium ions. The high ionic conductivities of $0.5 \cdot 10^{-3}\,S\,cm^{-1}$ ($X = $ Cl), $0.9 \cdot 10^{-3}\,S\,cm^{-1}$ ($X = $ Br), and $1.4 \cdot 10^{-3}\,S\,cm^{-1}$ ($X = $ I) are attributed to the weak cation-anion interactions within the disordered Li/X sublattice in the large channels. Another fast lithium thioborate ion conductor is the glass (ceramic) Li_3BS_3 with an ionic conductivity of $3.6 \cdot 10^{-4}\,S\,cm^{-1}$.[163] These examples illustrate the potential of thioborate-based solid electrolytes for ASSBs. However, this class needs to be studied in more detail for their phase space, stability, and structure-transport property relationship to be able to draw a conclusion about their suitability as ASSB separators.

Other sulfide- and thiophosphate-based solid electrolytes

Glasses, glass-ceramics, and some other ceramic thiophosphates not included in any of the above classes are discussed here. Glasses are characterized by the absence of long-range order, but can contain structural motifs known from ceramic compounds. In the case of lithium thiophosphate (LPS) glasses, these motifs include *ortho*-thiophosphate ($[PS_4]^{3-}$) as well as condensed thiophosphate anions such as *pyro*-thiophosphate ($[P_2S_7]^{4-}$, edge-sharing tetrahedra), *meta*-thiodiphosphate ($[P_2S_6]^{2-}$, corner-sharing tetrahedra), or *hypo*-thiodiphosphate ($[P_2S_6]^{4-}$), which contains $P^{IV}-P^{IV}$ bond. The molecular structure of the P-S polyanions is depicted in Figure 1.12. While some thiophosphate polyanions, like $[P_2S_7]^{4-}$ form more stable glasses, others like $[P_2S_6]^{4-}$ tend to rather form stable crystalline compounds.[164] Despite the low conductivity (Li_3PS_4 glass: $2 \cdot 10^{-4}\,S\,cm^{-1}$)[166]

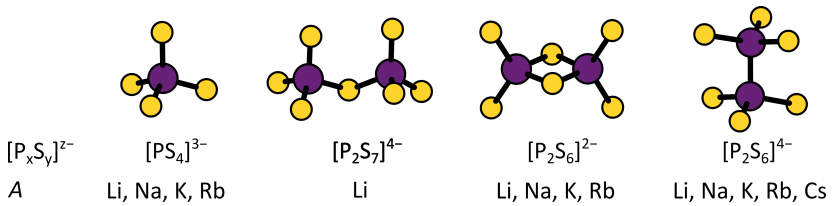

Figure 1.12: Thiophosphate polyanions species commonly observed in ternary ceramic, glass-ceramic and glassy A-P-S compounds (A = alkaline metal).[165] Known A - thiophosphate combinations are indicated by listing the alkaline metals below respective anions.

compared to some SEs presented above, glasses are advantageous due to several properties.[167] First, glasses do not have inter-particle grain boundaries. Grain boundaries have been identified as gateways for lithium dendrite growth, especially in oxide ceramic solid electrolytes,[168,169] and may exhibit resistive behavior[149] for ion conduction. Second, glasses have an isotropic character, as there are no crystalline domains pointing in one

direction or the other. Third, the higher plasticity of glasses can improve the cycling behavior in ASSBs. Furthermore, since LPS glasses are metal-free SE, their decomposition products are unlikely to be electron conducting at the anode interface. Therefore, glasses can be a competitive option as solid electrolytes for separators.

During heat treatment of glasses, portions of the glass may crystallize to form a glass ceramic. This process can either decrease ionic conductivity by forming less conductive phases such as $Li_4P_2S_6$[170] or increase conductivity by precipitating highly conductive phases like $Li_7P_3S_{11}$.[171] In the LGPS-like material Li_7SiPS_8, the ionic conductivity is also affected by the presence of an amorphous side phase, rendering this ionic conductor a glass-ceramic. Various glass-ceramic compositions are known (crystalline counterpart in parentheses): $50\,Li_2S:50\,P_2S_5$ ($Li_2P_2S_6$), $67\,Li_2S:33\,P_2S_5$ ($Li_4P_2S_6$), $70\,Li_2S:30\,P_2S_5$ ($Li_7P_3S_{11}$), $75\,Li_2S:25\,P_2S_5$ (Li_3PS_4), and $88\,Li_2S:12\,P_2S_5$ (Li_7PS_6).[172] Generally, the microstructure of glass-ceramics can be quite complex due to the distribution of crystalline domains embedded in the amorphous glass matrix. As in LPS glasses, different thiophosphate anions are found in the crystalline and glassy parts of glass-ceramics. However, the composition of glass-ceramics is strongly dependent on the temperature treatment and involves redox reactions of different thiophosphate moieties.[167] Overall, LPS glass-ceramics are quite diverse, as the original glass composition and heat treatment affect the transport properties and local structures of the resulting glass-ceramics. The glass ceramic $Li_7P_3S_{11}$ seems to be promising thanks to its high ionic conductivity and low cost.[171]

So far, the various thiophosphate-based ionic conductors have been classified according to their structure or structural similarity within a class. However, some ionic conductors, studied as part of this work, can hardly be classified into one of the classes presented above.

The first material, $Li_2Sn_2S_5$, is a part of the solid solution series $Li_{4x}Sn_{1-x}S_2$ ($\frac{1}{x} = \frac{1}{2}, \frac{1}{3}, \frac{1}{4}, \frac{1}{5}, \frac{1}{9}$).[173] While the $\frac{1}{x} = \frac{1}{2}$ member, Li_4SnS_4,[174] crystallizes isostructurally (orthorhombic unit cell) to Li_4GeS_4 in a three-dimensional structure with lone SnS_4 polyhedra (see Figure 1.13), the other solid solution members are layered materials and crystallize in monoclinic or rhombohedral unit cells, depending on the Li/Sn ordering. In monoclinic Li_2SnS_3 ($\frac{1}{x} = \frac{1}{3}$) the edge-sharing LiS_6 and SnS_6 octahedra build cation ordered honeycomb-type lattice with the addition lithium ions residing in the interlayer space.[173,175] Cation disorder or translational stacking faults can cause an increase in symmetry to an average rhombohedral structure.[173] For the $\frac{1}{x} = \frac{1}{5}$ member—$Li_2Sn_2S_5$—the negatively charged layers consist of edge-sharing $(Li/Sn)S_6$ polyhedra and are held together by Coulomb interactions with lithium ions occupying the interlayer space. Compared to Li_4SnS_4 and Li_2SnS_3, $Li_2Sn_2S_5$ is characterized by the high amount of vacancies, as well as Li occupied tetrahedral sites in the interlayer space.[176] The ionic conductivity is predominantly two-dimensional and runs within the van der Waals gap of this material, as depicted by the bond valence energy landscape in Figure 1.13. The high covalency of the Li/Sn-S layers allows exfoliation and restacking of this material without losing much of the original structure and properties.[173,178] The hydration behavior of $Li_2Sn_2S_5$ will be subject of Chapter 7.

In contrast, the second compound, $Na_4P_2S_6$, can be considered part of the LPS-type ceramic materials and can be synthesized similarly to $Li_4P_2S_6$ by a solid-state reaction or by dehydration of $Na_4P_2S_6 \cdot 6\,H_2O$. While the hydrate is three-dimensional, dry $Na_4P_2S_6$

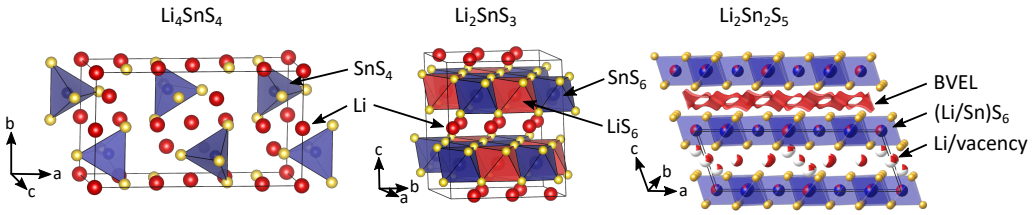

Figure 1.13: Crystal structures of orthorhombic Li_4SnS_4,[174] monoclinic Li_2SnS_3,[173,175,177] and monoclinic $Li_2Sn_2S_5$.[176]

has a two-dimensional character in terms of structure and transport properties. The structure is composed of layers of sodium ions and $P_2S_6^{4-}$ dumbbells, with additional sodium ions in the interlayer space, and is unique to the $A_4P_2S_6$ (A = Li, Na, K, Rb) family.[179,180] The synthesis and electrochemical characterization of $Na_4P_2S_6$ is discussed in Chapter 5.

References

(1) Smil, V., *Energy Transitions: Global and National Perspectives, 2nd Edition*, accessed: 07.09.2022; ABC-CLIO: 2016.

(2) Dale, S. bp Statistical Review of World Energy 2021, https://www.bp.com/en/global/corporate/energy-economics/statistical-review-of-world-energy/primary-energy.html, Electronic Article, accessed: 07.09.2022, 2022.

(3) Tong, D.; Farnham, D. J.; Duan, L.; Zhang, Q.; Lewis, N. S.; Caldeira, K.; Davis, S. J. *Nat. Commun.* **2021**, *12*.

(4) Fortunate Business Insight Electric Mobility Market Size, Share & COVID-19 Impact Analysis, https://www.fortunebusinessinsights.com/infographics/electric-mobility-market-106485, Electronic Article, accessed: 20.01.2023, 2022.

(5) Janek, J.; Zeier, W. G. *Nat. Energy* **2016**, *1*, 16141.

(6) Janek, J.; Zeier, W. G. *Nat. Energy* **2016**, *1*, 16141.

(7) Trasatti, S. *J. Electroanal. Chem.* **1999**, *460*, 1–4.

(8) Cecchini, R.; Pelosi, G. *IEEE Antennas Propag. Mag.* **1992**, *34*, 30–37.

(9) Jensen, W. B. The Daniell Cell, https://drc.libraries.uc.edu/bitstream/handle/2374.UC/702761/The-Daniell-Cell.pdf?sequence=1, accessed: 27.10.2022, 2013.

(10) Kurzweil, P. *J. Power Sources* **2010**, *195*, 4424–4434.

(11) Leclanché, G. Quelques observations sur l'emploi des piles électriques, https://catalogue.bnf.fr/ark:/12148/cb33560795b, accessed: 27.10.2022, 1867.

(12) Gassner, C. GALVANIC BATTERY, US patent no. 373064, 1887.

(13) Marsal, P. A.; River, R.; Kordesch, K.; Lakewood; Urry, L. F. Dry cell, US patent no. 2960558, 1960.

(14) Sapru, K.; Reichman, B.; Reger, A.; Ovshinsky, S. R. Rechargeable battery and electrode used therein, US patent no. 4623597, 1985.

(15) Huggins, R., *Advanced Batteries: Materials Science Aspects*; Springer US: 2008.

(16) Rzepka, B.; Bischof, S.; Blank, T. *Energies* **2021**, *14*, 3733.

(17) Wiberg, N., *Lehrbuch der Anorganischen Chemie*; De Gruyter: 2008.

(18) Schmaltz, T.; Wicke, T.; Weymann, L.; Voß, P.; Neef, C.; Thielmann, A. Solid-State Battery Roadmap 2035+, https://www.isi.fraunhofer.de/content/dam/isi/dokumente/cct/2022/SSB_Roadmap.pdf, accessed: 08.09.2022, 2022.

(19) Meyers, W. F.; Simmons, J. W. Electric current-producing cell with anhydrous organic liquid electrolyte, US patent no. 3 423 242, 1961.

(20) Garche, J.; Dyer, C.; Moseley, P.; Ogumi, Z.; Rand, D.; Scrosati, B., *Encyclopedia of Electrochemical Power Sources*; Elsevier Science: 2013.

(21) Holmes, C. *ECS Transactions* **2007**, *6*, 1–7.

(22) Rüdorff, W. *Chimia* **1965**, *19*, 489–499.

(23) Bichon, J.; Danot, M.; Rouxel, J. *C.R. Acad. Science* **1973**, *276*, 1283–1286.

(24) Whittingham, M. S. *J. Chem. Soc., Chem. Commun.* **1974**, 328.

(25) Whittingham, M. S.; Gamble, F. R. *Mater. Res. Bull.* **1975**, *10*, 363–371.

(26) Whittingham, M. S. Batterie à Base de Chalcogénures, Belgian patent no. 819672, 1975.

(27) Whittingham, M. S. **1976**, *192*, 1126–1127.

(28) Goodenough, J. B.; Mizushima, K. Fast Ion Conductors, US patent no. 4 357 215, 1982.

(29) Mizushima, K.; Jones, P. C.; Wiseman, P. J.; Goodenough, J. B. *Mater. Res. Bull.* **1980**, *15*, 783–789.

(30) Karthikeyan, D.; Sikha, G.; White, R. *J. Power Sources* **2008**, *185*, 1398–1407.

(31) Zhao, Y.; Pohl, O.; Bhatt, A. I.; Collis, G. E.; Mahon, P. J.; Rüther, T.; Hollenkamp, A. F. *Sustain. Chem.* **2021**, *2*, 167–205.

(32) Besenhard, J. O.; Fritz, H. P. *J. electroanal. chem. interfacial electrochem.* **1974**, *53*, 329–333.

(33) Guerard, D.; Herold, A. *Carbon* **1975**, *13*, 337–345.

(34) Besenhard, J. O. *Carbon* **1976**, *14*, 111–115.

(35) Yazami, R.; Touzain, P. *J. Power Sources* **1983**, *9*, 365–371.

(36) Mauger, A.; Julien, C. M.; Goodenough, J. B.; Zaghib, K. *J. Electrochem. Soc.* **2020**, *167*, 070507.

(37) Yoshino, A.; Sanechika, K.; Nakajima, T., Japanese patent no. 1989293, 1985.

(38) Yoshino, A.; Sanechika, K.; Nakajima, T. Secondary Battery, US patent no. 4 668 595, 1987.

(39) Nishi, Y. *Chem. Rec.* **2001**, *1*, 406–413.

(40) Fong, R.; Von Sacken, U.; Dahn, J. R. *J. Electrochem. Soc.* **1990**, *137*, 2009–2013.

(41) Peled, E. *J. Electrochem. Soc.* **1979**, *126*, 2047–2051.

(42) Nzereogu, P. U.; Omah, A. D.; Ezema, F. I.; Iwuoha, E. I.; Nwanya, A. C. *Appl. Surf. Sci. Adv.* **2022**, *9*, 100233.

(43) Jin, X. et al. *Adv. Mater.* **2022**, *34*, 2109356.

(44) Press release: The Nobel Prize in Chemistry 2019, `https://www.nobelprize.org/prizes/chemistry/2019/press-release/`, accessed: 18.08.2022, 2019.

(45) Ziegler, M. S.; Trancik, J. E. *Energy Environ. Sci.* **2021**, *14*, 1635–1651.

(46) Ritchie, H., `https://ourworldindata.org/battery-price-decline`, accessed: 22.08.2022, 2021.

(47) Ziegler, M. S.; Song, J.; Trancik, J. E. *Energy Environ. Sci.* **2021**, *14*, 6074–6098.

(48) German Lithium Participation, `https://germanlithium.com/language/en/`, accessed: 10.11.2022, 2022.

(49) Mining.com, https://www.mining.com/lithium-supply-chain-threatened-by-east-west-geopolitical-tensions-report/, accessed: 22.08.2022, 2021.

(50) nouvelles, I. E., https://www.ifpenergiesnouvelles.com/article/what-level-criticality-lithium-electrification-global-automobile-fleet, accessed: 22.08.2022, 2018.

(51) Nygaard, A. *Circular Economy and Sustainability* **2022**, DOI: 10.1007/s43615-022-00181-x.

(52) Delmas, C.; Fouassier, C.; Hagenmuller, P. *Physica B+C* **1980**, *99*, 81–85.

(53) Braconnier, J. J.; Delmas, C.; Hagenmuller, P. *Mater. Res. Bull.* **1982**, *17*, 993–1000.

(54) Molenda, J.; Delmas, C.; Hagenmuller, P. *Solid State Ion.* **1983**, *9-10*, 431–435.

(55) Yabuuchi, N.; Kubota, K.; Dahbi, M.; Komaba, S. *Chem. Rev.* **2014**, *114*, 11636–11682.

(56) Kubota, K.; Komaba, S. *J. Electrochem. Soc.* **2015**, *162*, A2538–A2550.

(57) Mariyappan, S.; Wang, Q.; Tarascon, J. M. *J. Electrochem. Soc.* **2018**, *165*, OA status: green-published, A3714–A3722.

(58) Xiao, J.; Li, X.; Tang, K.; Wang, D.; Long, M.; Gao, H.; Chen, W.; Liu, C.; Liu, H.; Wang, G. *Mater. Chem. Front.* **2021**, *5*, 3735–3764.

(59) Yang, Z.; Li, G.; Sun, J.; Xie, L.; Jiang, Y.; Huang, Y.; Chen, S. *Energy Storage Mater.* **2020**, *25*, 724–730.

(60) Wang, L.; Song, J.; Qiao, R.; Wray, L. A.; Hossain, M. A.; Chuang, Y.-D.; Yang, W.; Lu, Y.; Evans, D.; Lee, J.-J.; Vail, S.; Zhao, X.; Nishijima, M.; Kakimoto, S.; Goodenough, J. B. *J. Am. Chem. Soc.* **2015**, *137*, 2548–2554.

(61) Escher, I.; Freytag, A. I.; López Del Amo, J. M.; Adelhelm, P. *Batter. Supercaps* **2023**, e202200421.

(62) Chen, X.; Zheng, Y.; Liu, W.; Zhang, C.; Li, S.; Li, J. *Nanoscale* **2019**, *11*, 22196–22205.

(63) Senguttuvan, P.; Rousse, G.; Seznec, V.; Tarascon, J.-M.; Palacín, M. *Chem. Mater.* **2011**, *23*, 4109–4111.

(64) Rudola, A.; Saravanan, K.; Mason, C. W.; Balaya, P. *J. Mater. Chem. A* **2013**, *1*, 2653.

(65) Wu, D.; Li, X.; Xu, B.; Twu, N.; Liu, L.; Ceder, G. *Energy Environ. Sci.* **2015**, *8*, 195–202.

(66) Li, Z.; Ravnsbæk, D. B.; Xiang, K.; Chiang, Y.-M. *Electrochem Commun.* **2014**, *44*, 12–15.

(67) Lao, M.; Zhang, Y.; Luo, W.; Yan, Q.; Sun, W.; Dou, S. X. *Adv. Mater.* **2017**, *29*, 1700622.

(68) Fang, L.; Bahlawane, N.; Sun, W.; Pan, H.; Xu, B. B.; Yan, M.; Jiang, Y. *Small* **2021**, *17*, 2101137.

(69) Zhang, R.; Xia, B.; Li, B.; Cao, L.; Lai, Y.; Zheng, W.; Wang, H.; Wang, W. **2018**, *11*, 1820.

(70) Of Lithium-ion, B.-2. T., `https://batteryuniversity.com/article/bu-205-types-of-lithium-ion`, accessed: 24.08.2022, 2021.

(71) Contemporary Amperex Technology Co., L. (p. r., `https://www.catl.com/en/news/665.html`, accessed: 24.08.2022, 2021.

(72) Abraham, K. M. *ACS Energy Lett.* **2020**, *5*, 3544–3547.

(73) Chayambuka, K.; Mulder, G.; Danilov, D. L.; Notten, P. H. L. **2020**, *10*, 2001310.

(74) Feng, X.; Ouyang, M.; Liu, X.; Lu, L.; Xia, Y.; He, X. *Energy Storage Mater.* **2018**, *10*, 246–267.

(75) Xu, W.; Wang, J.; Ding, F.; Chen, X.; Nasybulin, E.; Zhang, Y.; Zhang, J.-G. *Energy Environ. Sci.* **2014**, *7*, 513–537.

(76) Zhang, C.; Wang, F.; Han, J.; Bai, S.; Tan, J.; Liu, J.; Li, F. *Small Structures* **2021**, *2*, 2100009.

(77) Heimes, H. H.; Kampker, A.; Lienemann, C.; Locke, M. A.; Offermanns, C.; Michaelis, S.; Rahimzei, E., 3. Eddition; Produktionsprozess einer Lithium-Ionen-Batteriezelle; PEM der RWTH Aachen und VDMA Eigendruck: Frankfurt am Main, 2018.

(78) Boaretto, N.; Garbayo, I.; Valiyaveettil-SobhanRaj, S.; Quintela, A.; Li, C.; Casas-Cabanas, M.; Aguesse, F. *J. Power Sources* **2021**, *502*, 229919.

(79) Masias, A.; Felten, N.; Garcia-Mendez, R.; Wolfenstine, J.; Sakamoto, J. *J. Mater. Sci.* **2019**, *54*, 2585–2600.

(80) Lee, Y.-G. et al. *Nat. Energy* **2020**, *5*, 299–308.

(81) Wang, B.; Zhu, B.; Yun, S.; Zhang, W.; Xia, C.; Afzal, M.; Cai, Y.; Liu, Y.; Wang, Y.; Wang, H. *NPG Asia Mater.* **2019**, *11*.

(82) Gao, Y.; Nolan, A. M.; Du, P.; Wu, Y.; Yang, C.; Chen, Q.; Mo, Y.; Bo, S.-H. *Chemical Reviews* **2020**, *120*, 5954–6008.

(83) Mehrer, H., *Diffusion in solids: fundamentals, methods, materials, diffusion-controlled processes*; Springer Science & Business Media: 2007; Vol. 155.

(84) Heitjans, P.; Kärger, J., *Diffusion in Condensed Matter*, second; Springer: Berlin, Heidelberg, 2005.

(85) Vargas-Barbosa, N. M.; Roling, B. *ChemElectroChem* **2020**, *7*, 367–385.

(86) Julien, C.; Nazri, G., *Solid State Batteries: Materials Design and Optimization*; The Springer International Series in Engineering and Computer Science; Springer US: 2013.

(87) Kotobuki, M.; Song, S.; Chen, C.; Lu, L., *Ceramic Electrolytes for All-Solid-State Li Batteries*; World Scientific: 2017.

(88) Zhang, Z.; Li, H.; Kaup, K.; Zhou, L.; Roy, P.-N.; Nazar, L. F. *Matter* **2020**, *2*, 1667–1684.

(89) He, X.; Zhu, Y.; Mo, Y. *Nat. Commun.* **2017**, *8*, 15893.

(90) Jalem, R.; Yamamoto, Y.; Shiiba, H.; Nakayama, M.; Munakata, H.; Kasuga, T.; Kanamura, K. *Chem. Mater.* **2013**, *25*, 425–430.

(91) Forrester, F. N.; Quirk, J. A.; Famprikis, T.; Dawson, J. A. *Chem. Mater.* **2022**, *34*, 10561–10571.

(92) Zhang, Z.; Zou, Z.; Kaup, K.; Xiao, R.; Shi, S.; Avdeev, M.; Hu, Y.-S.; Wang, D.; He, B.; Li, H.; Huang, X.; Nazar, L. F.; Chen, L. *Adv. Energy Mater.* **2019**, *9*, 1902373.

(93) Di Stefano, D.; Miglio, A.; Robeyns, K.; Filinchuk, Y.; Lechartier, M.; Senyshyn, A.; Ishida, H.; Spannenberger, S.; Prutsch, D.; Lunghammer, S.; Rettenwander, D.; Wilkening, M.; Roling, B.; Kato, Y.; Hautier, G. *Chem* **2019**, *5*, 2450–2460.

(94) Wang, Y.; Richards, W. D.; Ong, S. P.; Miara, L. J.; Kim, J. C.; Mo, Y.; Ceder, G. *Nat. Mater.* **2015**, *14*, 1026–1031.

(95) Malik, R.; Burch, D.; Bazant, M.; Ceder, G. *Nano Lett.* **2010**, *10*, 4123–4127.

(96) Morkhova, Y. A.; Rothenberger, M.; Leisegang, T.; Adams, S.; Blatov, V. A.; Kabanov, A. A. *J. Phys. Chem. C* **2021**, *125*, 17590–17599.

(97) Wiedemann, D.; Islam, M. M.; Bredow, T.; Lerch, M. *Z. Phys. Chem.* **2017**, *231*, 1279–1302.

(98) Harm, S.; Hatz, A.-K.; Schneider, C.; Hoefer, C.; Hoch, C.; Lotsch, B. V. *Front. Chem.* **2020**, *8*, DOI: 10.3389/fchem.2020.00090.

(99) Kozinsky, B.; Akhade, S. A.; Hirel, P.; Hashibon, A.; Elsässer, C.; Mehta, P.; Logeat, A.; Eisele, U. *Phys. Rev. Lett.* **2016**, *116*, DOI: 10.1103/physrevlett.116.055901.

(100) Gautam, A.; Sadowski, M.; Prinz, N.; Eickhoff, H.; Minafra, N.; Ghidiu, M.; Culver, S. P.; Albe, K.; Fässler, T. F.; Zobel, M.; Zeier, W. G. *Chem. Mater.* **2019**, *31*, 10178–10185.

(101) Dimitrov, V.; Komatsu, T. *J. Solid State Chem.* **2012**, *196*, 574–578.

(102) Krauskopf, T.; Muy, S.; Culver, S. P.; Ohno, S.; Delaire, O.; Shao-Horn, Y.; Zeier, W. G. *J. Am. Chem. Soc.* **2018**, *140*, 14464–14473.

(103) Kraft, M. A.; Culver, S. P.; Calderon, M.; Bo, F.; Krauskopf, T.; Senyshyn, A.; Dietrich, C.; Zevalkink, A.; Janek, J.; Zeier, W. G. *J. Am. Chem. Soc.* **2017**, *139*, 10909–10918.

(104) Muy, S.; Schlem, R.; Shao-Horn, Y.; Zeier, W. G. *Adv. Energy Mater.* **2021**, *11*, 2002787.

(105) Jansen, M. *Angew. Chem. Int. Ed.* **1991**, *30*, 1547–1558.

(106) Lundén, A. *Solid State Ion.* **1988**, *28-30*, 163–167.

(107) Zhang, Z.; Nazar, L. F. *Nat. Rev. Mater.* **2022**, *7*, 389–405.

(108) Lunkenheimer, P.; Michl, M.; Loidl, A. In *J. Adv. Dielectr.* Springer International Publishing: 2018, pp 277–300.

(109) Timmermans, J. *J. Phys. Chem. Solids* **1961**, *18*, 1–8.

(110) Famprikis, T.; Dawson, J. A.; Fauth, F.; Clemens, O.; Suard, E.; Fleutot, B.; Courty, M.; Chotard, J.-N.; Islam, M. S.; Masquelier, C. *ACS Mater. Lett.* **2019**, *1*, 641–646.

(111) Nilsson, L.; Thomas, J. O.; Tofield, B. C. *J. Phys., C, Solid state Phys.* **1980**, *13*, 6441–6451.

(112) Meilander, B. E.; Nilsson, L. *Z. Naturforsch. A* **1983**, *38*, 1396–1399.

(113) Tang, W. S.; Matsuo, M.; Wu, H.; Stavila, V.; Zhou, W.; Talin, A. A.; Soloninin, A. V.; Skoryunov, R. V.; Babanova, O. A.; Skripov, A. V.; Unemoto, A.; Orimo, S.-I.; Udovic, T. J. *Adv. Energy Mater.* **2016**, *6*, 1502237.

(114) Xu, R.; Han, F.; Ji, X.; Fan, X.; Tu, J.; Wang, C. *Nano Energy* **2018**, *53*, 958–966.

(115) Ding, Z.; Li, J.; Li, J.; An, C. *J. Electrochem. Soc.* **2020**, *167*, 070541.

(116) Li, X.; Liang, J.; Chen, N.; Luo, J.; Adair, K. R.; Wang, C.; Banis, M. N.; Sham, T.-K.; Zhang, L.; Zhao, S.; Lu, S.; Huang, H.; Li, R.; Sun, X. *Angew. Chem.* **2019**, *131*, 16579–16584.

(117) Liu, Z.; Ma, S.; Liu, J.; Xiong, S.; Ma, Y.; Chen, H. *ACS Energy Lett.* **2021**, *6*, 298–304.

(118) Wang, C.; Liang, J.; Kim, J. T.; Sun, X. *Sci. Adv.* **2022**, *8*, eadc9516.

(119) Matsuo, M.; Nakamori, Y.; Orimo, S.-I.; Maekawa, H.; Takamura, H. *Appl. Phys. Lett.* **2007**, *91*, 224103.

(120) Skripov, A. V.; Babanova, O. A.; Soloninin, A. V.; Stavila, V.; Verdal, N.; Udovic, T. J.; Rush, J. J. *J. Phys. Chem. C.* **2013**, *117*, 25961–25968.

(121) Udovic, T. J.; Matsuo, M.; Unemoto, A.; Verdal, N.; Stavila, V.; Skripov, A. V.; Rush, J. J.; Takamura, H.; Orimo, S.-i. *Chem. Commun.* **2014**, *50*, 3750–3752.

(122) Kweon, K. E.; Varley, J. B.; Shea, P.; Adelstein, N.; Mehta, P.; Heo, T. W.; Udovic, T. J.; Stavila, V.; Wood, B. C. *Chem. Mater.* **2017**, *29*, 9142–9153.

(123) Udovic, T. J.; Matsuo, M.; Tang, W. S.; Wu, H.; Stavila, V.; Soloninin, A. V.; Skoryunov, R. V.; Babanova, O. A.; Skripov, A. V.; Rush, J. J.; Unemoto, A.; Takamura, H.; Orimo, S.-I. *Adv. Mater.* **2014**, *26*, 7622–7626.

(124) Strangmüller, S.; Eickhoff, H.; Müller, D.; Klein, W.; Raudaschl-Sieber, G.; Kirchhain, H.; Sedlmeier, C.; Baran, V.; Senyshyn, A.; Deringer, V. L.; Van Wüllen, L.; Gasteiger, H. A.; Fässler, T. F. *J. Am. Chem. Soc.* **2019**, *141*, 14200–14209.

(125) Restle, T. M. F.; Sedlmeier, C.; Kirchhain, H.; Klein, W.; Raudaschl-Sieber, G.; Deringer, V. L.; Wüllen, L.; Gasteiger, H. A.; Fässler, T. F. *Angew. Chem. Int. Ed.* **2020**, *59*, 5665–5674.

(126) Haffner, A.; Hatz, A.-K.; Moudrakovski, I.; Lotsch, B. V.; Johrendt, D. *Angew. Chem. Int. Ed.* **2018**, *57*, 6155–6160.

(127) Tachez, M.; Malugani, J.-P.; Mercier, R.; Robert, G. *Solid State Ion.* **1984**, *14*, 181–185.

(128) Liu, Z.; Fu, W.; Payzant, E. A.; Yu, X.; Wu, Z.; Dudney, N. J.; Kiggans, J.; Hong, K.; Rondinone, A. J.; Liang, C. *J. Am. Chem. Soc.* **2013**, *135*, 975–978.

(129) Kamaya, N.; Homma, K.; Yamakawa, Y.; Hirayama, M.; Kanno, R.; Yonemura, M.; Kamiyama, T.; Kato, Y.; Hama, S.; Kawamoto, K.; Mitsui, A. *Nat. Mater.* **2011**, *10*, 682–686.

(130) Matsushita, Y.; Kanatzidis, M. G. *Z. Naturforsch. B* **1998**, *53*, 23–30.

(131) Homma, K.; Yonemura, M.; Kobayashi, T.; Nagao, M.; Hirayama, M.; Kanno, R. *Solid State Ion.* **2011**, *182*, 53–58.

(132) Schlem, R.; Till, P.; Weiss, M.; Krauskopf, T.; Culver, S. P.; Zeier, W. G. *Chem. Eur. J.* **2019**, *25*, 4143–4148.

(133) Jansen, M.; Henseler, U. *J. Solid State Chem.* **1992**, *99*, 110–119.

(134) Hayashi, A.; Noi, K.; Sakuda, A.; Tatsumisago, M. *Nat. Commun.* **2012**, *3*, 856.

(135) Wang, H.; Chen, Y.; Hood, Z. D.; Sahu, G.; Pandian, A. S.; Keum, J. K.; An, K.; Liang, C. *Angew. Chem., Int. Ed.* **2016**, *55*, 8551–8555.

(136) Banerjee, A.; Park, K. H.; Heo, J. W.; Nam, Y. J.; Moon, C. K.; Oh, S. M.; Hong, S.-T.; Jung, Y. S. *Angew. Chem., Int. Ed.* **2016**, *55*, 9634–9638.

(137) Shang, S.-L.; Yu, Z.; Wang, Y.; Wang, D.; Liu, Z.-K. *ACS Appl. Mater. Interfaces* **2017**, *9*, 16261–16269.

(138) Fuchs, T.; Culver, S. P.; Till, P.; Zeier, W. G. *ACS Energy Lett.* **2020**, *5*, 146–151.

(139) Hayashi, A.; Masuzawa, N.; Yubuchi, S.; Tsuji, F.; Hotehama, C.; Sakuda, A.; Tatsumisago, M. *Nat. Commun.* **2019**, *10*, 5266.

(140) Kato, Y.; Hori, S.; Saito, T.; Suzuki, K.; Hirayama, M.; Mitsui, A.; Yonemura, M.; Iba, H.; Kanno, R. *Nat. Energy* **2016**, *1*, 16030.

(141) Richards, W. D.; Tsujimura, T.; Miara, L. J.; Wang, Y.; Kim, J. C.; Ong, S. P.; Uechi, I.; Suzuki, N.; Ceder, G. *Nat. Commun.* **2016**, *7*, 11009.

(142) Duchardt, M.; Ruschewitz, U.; Adams, S.; Dehnen, S.; Roling, B. *Angew. Chemie Int. Ed.* **2018**, *57*, 1351–1355.

(143) Fu, Z.-H.; Chen, X.; Zhao, C.-Z.; Yuan, H.; Zhang, R.; Shen, X.; Ma, X.-X.; Lu, Y.; Liu, Q.-B.; Fan, L.-Z.; Zhang, Q. *Energy Fuels* **2021**, *35*, 10210–10218.

(144) Iwasaki, R.; Hori, S.; Kanno, R.; Yajima, T.; Hirai, D.; Kato, Y.; Hiroi, Z. *Chem. Mater.* **2019**, *31*, 3694–3699.

(145) Kuhn, A.; Gerbig, O.; Zhu, C.; Falkenberg, F.; Maier, J.; Lotsch, B. V. *Phys. Chem. Chem. Phys.* **2014**, *16*, 14669–14674.

(146) Liang, X.; Wang, L.; Jiang, Y.; Wang, J.; Luo, H.; Liu, C.; Feng, J. *Chem. Mater.* **2015**, *27*, 5503–5510.

(147) Weber, D. A.; Senyshyn, A.; Weldert, K. S.; Wenzel, S.; Zhang, W.; Kaiser, R.; Berendts, S.; Janek, J.; Zeier, W. G. *Chem. Mater.* **2016**, *28*, 5905–5915.

(148) Bron, P.; Johansson, S.; Zick, K.; Der Günne, J. S. A.; Dehnen, S.; Roling, B. *J. Am. Chem. Soc.* **2013**, *135*, 15694–15697.

(149) Bron, P.; Dehnen, S.; Roling, B. *J. Power Sources* **2016**, *329*, 530–535.

(150) Harm, S.; Hatz, A.-K.; Moudrakovski, I.; Eger, R.; Kuhn, A.; Hoch, C.; Lotsch, B. V. *Chem. Mater.* **2019**, *31*, 1280–1288.

(151) Kuhn, A.; Duppel, V.; Lotsch, B. V. *Energy Environ. Sci.* **2013**, *6*, 3548–3552.

(152) Richards, W. D.; Miara, L. J.; Wang, Y.; Kim, J. C.; Ceder, G. *Chem. Mater.* **2016**, *28*, 266–273.

(153) Camacho-Forero, L. E.; Balbuena, P. B. *J. Power Sources* **2018**, *396*, 782–790.

(154) Riegger, L. M. et al. *Chem. Mater.* **2022**, *34*, 3659–3669.

(155) Deiseroth, H.-J.; Kong, S.-T.; Eckert, H.; Vannahme, J.; Reiner, C.; Zaiß, T.; Schlosser, M. *Angew. Chem. Int. Ed.* **2008**, *47*, 755–758.

(156) Ohno, S.; Banik, A.; Dewald, G. F.; Kraft, M. A.; Krauskopf, T.; Minafra, N.; Till, P.; Weiss, M.; Zeier, W. G. *Prog. Energy* **2020**, *2*, 022001.

(157) Bai, X.; Duan, Y.; Zhuang, W.; Yang, R.; Wang, J. *J. Mater. Chem. A* **2020**, *8*, 25663–25686.

(158) Kraft, M. A.; Ohno, S.; Zinkevich, T.; Koerver, R.; Culver, S. P.; Fuchs, T.; Senyshyn, A.; Indris, S.; Morgan, B. J.; Zeier, W. G. *J. Am. Chem. Soc.* **2018**, *140*, 16330–16339.

(159) Adeli, P.; Bazak, J. D.; Park, K. H.; Kochetkov, I.; Huq, A.; Goward, G. R.; Nazar, L. F. *Angew. Chem. Int. Ed.* **2019**, *58*, 8681–8686.

(160) Yubuchi, S.; Uematsu, M.; Hotehama, C.; Sakuda, A.; Hayashi, A.; Tatsumisago, M. *J. Mater. Chem. A* **2019**, *7*, 558–566.

(161) Kaup, K.; Assoud, A.; Liu, J.; Nazar, L. F. *Angew. Chem. Int. Ed.* **2021**, *60*, 6975–6980.

(162) Haffner, A.; Hatz, A.-K.; Zeman, O. E. O.; Hoch, C.; Lotsch, B. V.; Johrendt, D. *Angew. Chem. Int. Ed.* **2021**, *60*, 13641–13646.

(163) Kimura, T.; Inoue, A.; Nagao, K.; Inaoka, T.; Kowada, H.; Sakuda, A.; Tatsumisago, M.; Hayashi, A. *ACS Appl. Energy Mater.* **2022**, *5*, 1421–1426.

(164) Sadowski, M.; Albe, K. *J. Power Sources* **2020**, *478*, 229041.

(165) Dietrich, C.; Weber, D. A.; Culver, S.; Senyshyn, A.; Sedlmaier, S. J.; Indris, S.; Janek, J.; Zeier, W. G. *Inorg. Chem.* **2017**, *56*, 6681–6687.

(166) Hayashi, A.; Hama, S.; Morimoto, H.; Tatsumisago, M.; Minami, T. *J. Am. Ceram. Soc.* **2004**, *84*, 477–79.

(167) Dietrich, C.; Weber, D. A.; Sedlmaier, S. J.; Indris, S.; Culver, S. P.; Walter, D.; Janek, J.; Zeier, W. G. *J. Mater. Chem. A* **2017**, *5*, 18111–18119.

(168) Ren, Y.; Shen, Y.; Lin, Y.; Nan, C.-W. *Electrochem. commun.* **2015**, *57*, 27–30.

(169) Cheng, E. J.; Sharafi, A.; Sakamoto, J. *Electrochim. Acta* **2017**, *223*, 85–91.

(170) Mizuno, F.; Hayashi, A.; Tadanaga, K.; Tatsumisago, M. *Solid State Ion.* **2006**, *177*, 2721–2725.

(171) Seino, Y.; Ota, T.; Takada, K.; Hayashi, A.; Tatsumisago, M. *Energy Environ. Sci.* **2014**, *7*, 627–631.

(172) Zhang, Q.; Cao, D.; Ma, Y.; Natan, A.; Aurora, P.; Zhu, H. *Adv. Mater.* **2019**, *31*, 1901131.

(173) Kuhn, A.; Holzmann, T.; Nuss, J.; Lotsch, B. V. *J. Mater. Chem. A* **2014**, *2*, 6100–6106.

(174) MacNeil, J. H.; Massi, D. M.; Zhang, J.-H.; Rosmus, K. A.; Brunetta, C. D.; Gentile, T. A.; Aitken, J. A. *J. Alloys Compd.* **2014**, *586*, 736–744.

(175) Brant, J. A.; Massi, D. M.; Holzwarth, N. A. W.; Macneil, J. H.; Douvalis, A. P.; Bakas, T.; Martin, S. W.; Gross, M. D.; Aitken, J. A. *Chem. Mater.* **2015**, *27*, 189–196.

(176) Holzmann, T.; Schoop, L. M.; Ali, M. N.; Moudrakovski, I.; Gregori, G.; Maier, J.; Cava, R. J.; Lotsch, B. V. *Energy Environ. Sci* **2016**, *9*, 2578–2585.

(177) Kaib, T.; Haddadpour, S.; Kapitein, M.; Bron, P.; Schröder, C.; Eckert, H.; Roling, B.; Dehnen, S. *Chem. Mater.* **2012**, *24*, 2211–2219.

(178) Hatz, A.-K.; Moudrakovski, I.; Bette, S.; Terban, M. W.; Etter, M.; Joos, M.; Vargas-Barbosa, N. M.; Dinnebier, R. E.; Lotsch, B. V. *Chem. Mater.* **2021**, *33*, 7337–7349.

(179) Mercier, R.; Malugani, J. P.; Fahys, B.; Douglande, J.; Robert, G. *J. Solid State Chem.* **1982**, *43*, 151–162.

(180) Kuhn, A.; Eger, R.; Nuss, J.; Lotsch, B. V. *Z. Anorg. Allg. Chem.* **2014**, *640*, 689–692.

CHAPTER 2

Selected analytical methods

The transport property of a crystalline solid electrolyte is closely linked to its structure. Therefore, it is paramount to investigate the structure-transport property relationship to not only understand how ions migrate but more so to further improve the material for higher conductivity and stability. In order to do so, solid-state chemists can choose from broad tool box of characterization methods to analyze their samples. In this chapter, the characterization methods for the solid electrolytes studied in this thesis are presented phenomenologically. Experimental and instrumental details are presented in the chapters 4, 5, 6, 7, and 8, as well as in the respective appendices A, B, C, D, and E. Details about the various experimental and computational contributions from co-authors to the individual projects is presented in Appendix F. Some details are also given in this chapter.

Contents of Chapter 2

2.1 Diffraction

Diffraction refers to the constructive and destructive interference of waves with matter. This physical principle is used in X-ray diffraction, where X-rays interfere with the electron charge density of the matter subjected to the beam. In this section, three techniques based on the scattering of X-rays by (crystalline) solids are presented.

Single crystal X-ray diffraction

X-ray diffraction patterns contain information about the electron density in a unit cell and thus information about the unit cell dimensions, crystal system, and symmetry. Single crystal X-ray diffraction (SCXRD) is particularly useful for determining crystal structures and is based on gathering diffraction data of a multitude of single crystal orientations with regard to the incident beam, allowing to access the information about the (almost complete) reciprocal space of the sample. This allows accurate determination of bond lengths and angles as well as site occupancy. However, suitable single crystals are often difficult to synthesize at a reasonable size, otherwise poorly represent the bulk sample.

Powder X-ray diffraction

The one-dimensional powder X-ray diffraction (PXRD) pattern is a representation of the Debye-Scherrer rings formed by the superposition of the diffraction patterns of countless scattering domains. The position, intensity, and shape of the reflections provide information about the unit cell parameters, atomic parameters (electron density as a measure of atomic number), and crystallinity of the sample. Information about the crystallize size can be obtained by analyzing the peak broadening using the Scherrer equation. XRD can be used to qualitatively compare and quantitatively determine many structural properties of the sample. Defects in the form of stacking faults in 2D materials appear as so-called Warren-type peaks,[1] where the reflection exhibits an asymmetric skew toward higher diffraction angles. It is also possible to determine the crystal structure from PXRD, although some ambiguity remains for structures with non-centrosymmetric space groups. Additionally, PXRD is an excellent tool for qualitatively determining the phase purity of a powder sample by inspecting characteristic reflections of the sample and comparing it to a reference pattern. Another advantage of PXRD over SCXRD is the ability to quantify the phase fractions in a multiphase sample by quantitative phase analysis. This is done by Rietveld analysis of the whole diffraction pattern, where the total intensity is fitted as a function of the contributing phases, more precisely the structure factor of the different unit cells. By using an internal crystalline standard for Rietveld analysis, it is possible to determine residual amorphous side phases that would otherwise go unnoticed because X-ray diffraction is more sensitive to crystalline domains. PXRD samples can also be measured under different biases, such as high temperature, pressure, electrical potentials and in different gas or humidity environments. This opens up the possibility to study temperature, pressure or reaction-related phase transitions and possibly draw conclusions on kinetics or limitations of phase formation and phase stability.

Total scattering pair distribution function analysis

SCXRD and PXRD are excellent for crystalline samples. However, they are unsuitable for amorphous samples without long-range periodicity, such as glasses, and, hence, lack information on samples with amorphous side phases. Glasses and glass-ceramics typically exhibit a (wave-like) background pattern, which in the case of glass-ceramics is superimposed by reflections from crystalline domains. The background pattern is caused by diffuse scattering from amorphous or disordered matter. Pair distribution function (PDF) analysis allows to obtain information about short-range correlations, as in clusters or molecular motifs, based on the Fourier transformation of the diffuse scattering part of (X-ray) diffraction data. The result is a weighted histogram of atom-to-atom distances, effectively describing all correlations in the sample. This technique is very advantageous because the data acquisition is similar to X-ray diffraction and can even be performed on laboratory diffractometers. Additionally, PDF calculations are computationally inexpensive and yield a 1D function that is intuitive to interpret. For solid electrolytes with molecular motifs, as in thiophosphates, or layers, as in many electrode active materials and solid electrolytes like $Li_2Sn_2S_5$, PDF can identify the molecular units or turbostratic disorder.[2] Like PXRD, PDF measurements can also be performed under various measurement conditions to understand different structural correlations as a function of temperature, pressure, or dynamics of a possible reaction.

2.2 Spectroscopy

By definition, spectroscopy derives information about the materials through the interaction of solid matter with electromagnetic waves and interprets it as a function of wavelength, frequency, or other derived measures. This section presents three spectroscopy methods that have been used in different research projects described in this work to identify phases and compositions.

Engery dispersive X-ray spectroscopy

Polycrystalline samples may contain side phases with compositions different from the nominal composition. While elemental analysis uses a larger amount of material to determine the elemental composition, energy-dispersive X-ray (EDX) spectroscopy can chemically characterize individual particles due to its high spatial resolution. This technique uses the characteristic X-ray emission spectra of elements produced by the interaction of the incident high-energy electron beam with the electron density of the solid sample. The EDX spectrum of a multi-element sample contains the characteristic emission peaks of each element present. Since the peak intensity is proportional to the atomic fraction of each element present in the investigated region of interest, the local composition can be calculated. However, lighter elements such as lithium or hydrogen are often not detected in EDX due to their low electron counts. In solid electrolytes, this technique is, for example, used to identify thiophosphate phases based on the P/S ratio or to verify element substitutions with similar electron numbers (isoelectronic configuration as in S^{2-} and Cl^{-}) that could not be distinguished by XRD.

Raman spectroscopy

Another useful spectroscopic method for identifying phases is Raman spectroscopy. This characterization technique uses the inelastic scattering of monochromatic photons by matter. The absorbed photon energy excites different vibrational modes of a lattice or molecule, producing a short-lived excited state that emits a photon with lower (Stokes) or higher (anti-Stokes) energy than the incident one. In Raman active modes, the polarizability of the molecule changes.[3] The intensity of the Raman band is proportional to the squared change in polarizability.[3] Thiophosphate anions fulfill this requirement and show a characteristic Raman spectrum with defined Raman band positions. This helps in the identification of minor phases by assigning the Raman bands to the characteristic bending or stretching vibrations at specific wavenumbers. In addition, Raman spectra can help to identify the point group symmetry of thiophosphate anions with different configurations, like $P_2S_6^{4-}$, which exists in an ethane-like (D_{3d}) and 1,2-dichloroethane-like (C_{2h}) configuration.

Solid state nuclear magnetic resonance spectroscopy

Unlike most other spectroscopic methods, nuclear magnetic resonance (NMR) spectroscopy probes the nucleus rather than the electrons. When a nucleus is exposed to a (strong) magnetic field, the magnetic moment of the nucleus causes a splitting of nuclear energy states proportional to the strength of the external magnetic field, which is commonly

known as the Zeeman-splitting. The magnetization vector of the nucleus tries to align with the external field. A radio frequency pulse excites the nucleus to an excited state and flips the magnetization vector out of parallel alignment. The excited nucleus then relaxes by realigning with the external field. This characteristic process is detected, amplified, and Fourier transformed to obtain a frequency-dependent signal, that is then recalculated to a chemical shift by referencing to an external or internal standard. The chemical environment of an atom in a sample affects the shielding ability towards the local magnetic field, resulting in peaks at different chemical shifts. While in liquid media the NMR peaks are sharp, solid-state NMR produces broad signals with contributions from the anisotropic interactions of the nulcei within the solid. Magic angle spinning (MAS) circumvents this by artificially spinning the sample at a high frequency at 54.74° with respect to the external magnetic field. This angle is known as the magic angle at which anisotropic interactions are averaged out. The resulting spectrum contains the isotropic chemical shift (δ_{iso}) peak as well as spinning sidebands. For (thio-) phosphates, δ_{iso} for ^{31}P nuclei are characteristic and allow phase identification. Other NMR active nuclei that are relevant for solid electrolytes include ^{1}H, ^{6}Li and ^{7}Li, ^{23}Na, ^{27}Al, ^{29}Si, ^{77}Se, and ^{119}Sn. Since in direct excitation NMR experiments, the nuclei of a sample are probed, the peak area is directly proportional to the number of nuclei contributing to the signal. Therefore, in those NMR experiments is sensitive to atomic ratios and can be used to quantitatively determine phase fractions or occupations.
Furthermore, ion dynamics (for NMR: nuclei) can be studied using pulsed field gradient (PFG) NMR.[4] In this technique, the tracer diffusion coefficient D_{tr} is probed, which is related to the diffusion coefficient D_{σ} by $D_{\mathrm{tr}} = D_{\sigma} \cdot H_{\mathrm{R}}$ (H_{R} being the Haven ratio). An extended discussion about NMR probed diffusion coefficients can be found in Chapter 1.5.2. When the diffusion coefficient is sufficiently high at a given temperature, the normalized peak intensity as a function of gradient strength follows an exponential decay law. Fitting this decay gives D_{tr}. This allows (with some assumptions) the calculation of a PFG NMR-based ionic conductivity *via* equation (1.17) (see Section 1.5.2 in the Introduction). The time between gradient pulses, as well as the gradient strength can be modulated. This allows ion migration processes happening on different time and length scales to be studied.

2.3 Microscopy

Microscopy is the observation or imaging of objects that cannot be seen with the bare human eye. While imaging in optical (light) microscopy is limited by the wavelength of visible light, electron microscopy offers higher resolution down to the atomic level. In electron microscopy, a cathode electron gun emits a stream of electrons that are accelerated through a ring-shaped anode. The potential between the cathode and anode (tens to hundreds of kV) determines the energy of the electrons and is varied according to the needs of the experimenter. Magnetic lenses focus the high-energy electron beam to the desired focal point. Depending on the type of interaction between the sample and the electrons, various election microscopy techniques have been developed using this basic setup. This section presents two electron microscopy techniques commonly used to study solid electrolytes.

Scanning electron microscopy

Scanning electron microscopy (SEM) uses the focused, high-energy electron beam to scan the surface of a sample. The incident electrons penetrate the sample and produce element-specific X-rays, secondary electrons (SEs), back-scattered electrons (BSEs), and Auger electrons. While SEs are used to produce images with morphological information, BSE images contain compositional information. In BSE images, lighter elements appear darker and heavier elements appear lighter. SEM images combined with EDX can be used to study multiphase systems or samples with side phases. In addition, SEM images can be used to determine the particle size distribution and morphology of a sample. This information is valuable for the characterization of solid electrolytes, since microstructural aspects also influence the microscopically measured conductivity.

Transmission electron microscopy

In transmission electron microscopy (TEM), electrons penetrate a nanometer-thin sample, producing a direct image on a detection screen at the end of the beam path. For solid electrolytes, TEM enables the study of grain boundaries or defects, as sub-micron structures and even atomic arrangements can be resolved. Additionally, many TEMs are equipped with detectors for electron diffraction and EDX spectroscopy. Electron diffraction patterns, which are similar to X-ray diffraction patterns, can be used to determine the crystal orientation and space group symmetry of the sample. Stacking faults, commonly observed in layered materials, appear as diffuse scattering intensities between reflections/streaks in certain zonal planes, while sharp intensity spots can be observed in crystalline materials. Despite the many beneficial aspects for the study of thiophosphate-based solid electrolytes, TEM entails significant experimental challenges. Since the sample must be very thin (nanometers), brief exposure to air during sample transfer into the TEM can destroy the sample by oxidation. In addition, when the electronically insulating sample is exposed to a high-energy electron beam during imaging, it eventually leads to severe beam damage (specimen heating, mass-loss,...) and consequently to the destruction of the sample.[5]

2.4 Thermal analysis

When a solid is subjected to a non-ambient temperature, it can show different behaviors, like melting, decomposition, or phase transitions. This section introduces two well suited techniques for measuring the thermal properties of solid electrolytes.

Thermogravimetric analysis

Elevated temperatures are often problematic for thiophosphate-based compounds because of thermal decomposition and evaporation of volatile elements (P, S). Solid electrolytes may also contain water or solvents due to liquid medium synthesis or intercalation. Thermogravimetric analysis (TGA) is used to determine the thermal stability of a sample or the temperature required for drying. In TGA, the sample is heated with a constant heating rate (usually 5-20 $\mathrm{K\,min^{-1}}$ from room temperature up to 1500 °C) in a stream of a defined atmosphere (He, Ar, O_2/N_2, humid atmosphere, ...) while its weight is constantly recorded. From the weight loss, for example, the ratio of crystal water to solid electrolyte, the original composition can be calculated. Furthermore, the evolved gases can be analyzed by gas chromatography in conjunction with mass spectroscopy to identify the decomposed products, even in small amounts. Thermal stability is important for the application of thiophosphates as solid electrolytes, since the processing of the cathode or anode laminate usually requires some kind of thermal treatment.

Differential scanning calorimetry

When heated, solids exhibit a phase transition to the melt when the decomposition temperature exceeds the melting temperature. Additionally, some solids exhibit a solid-solid phase transition. The nature of such phase transitions can be measured using differential scanning calorimetry (DSC). As with TGA, the sample and additionally a reference are heated and the voltage difference between the sample and the reference thermocouple is recorded. Calibration measurements with known standards allow the exchanged heat to be calculated as the area integral of a peak. Exothermic and endothermic reactions and phase transitions show peaks in different directions with respect to the baseline. DSC is capable of detecting minute thermal events with small amounts of exchanged heat. Therefore, phase transitions with subtle structural changes that would otherwise go unnoticed can be identified in DSC. For crystalline thiophosphates, DSC is a suitable tool for identifying high-temperature phases with new structures and different transport properties. DSC can also help determine appropriate synthesis parameters or track the success of lowering the transition temperature of a desired high-temperature polymorph.

2.5 Electrochemical characterization

Undoubtedly, the transport property of a solid electrolyte is the most important physical property to be investigated. Hence, it is paramount to precisely determine the properties associated with ion and electron transport. This section introduces two electrochemical characterization methods for solid electrolytes. Considering the importance of these techniques, the fundamental theory—adapted from Orazem,[6] Huggins[7] and Macdonald[8]—is also discussed below.

Electrochemical impedance spectroscopy

Impedance is the electrical resistivity of a sample under alternating current (AC). It is composed of resistance and reactance. Resistance describes the property of opposing the flow of electric current, while reactance opposes the change of current. Electric components related to these properties are resistors (R), capacitors (X_C) and inductors (X_L). The total reactance is $X_\mathrm{t} = X_\mathrm{C} + X_\mathrm{L}$, whereas the total resistance is just R. While the time t dependant current response $\hat{I}$ to a sinusoidal excitation voltage $\hat{U}$ is in phase for a resistor ($I \propto U$), the responses of a capacitor ($I \propto \frac{\mathrm{d}U}{\mathrm{d}t}$) and an inductor ($I \propto -\frac{\mathrm{d}U}{\mathrm{d}t}$) are phase shifted by $\phi = -\frac{\pi}{2}$ and $\phi = \frac{\pi}{2}$, respectively. Similar to Ohm's law for direct current, the impedance $\hat{Z}$ for alternating current can be calculated by:

$$\hat{Z} = \frac{\hat{U}}{\hat{I}} = \hat{Z}_0 \frac{\sin(\omega t)}{\sin(\omega t + \phi)} \ , \tag{2.1}$$

with $\omega = 2\pi f$ being the angular frequency, where f is the frequency of AC response. Alternatively, the impedance can be expressed as a complex quantity using the Euler relationship:

$$\hat{Z} = |Z| e^{j\phi} = Z' + jZ'' \ , \tag{2.2}$$

where Z' and Z'' are the real and imaginary part of the impedance and j is the imaginary unit. The impedance of the isolated circuit elements: resistor ($\hat{Z}_\mathrm{R}$), capacitor ($\hat{Z}_\mathrm{C}$) and inductor ($\hat{Z}_\mathrm{L}$), are as follows:

$$\hat{Z}_\mathrm{R} = R \qquad \hat{Z}_\mathrm{C} = -\frac{j}{\omega C} \qquad \hat{Z}_\mathrm{L} = j\omega L \ , \tag{2.3}$$

where R, C, and L are the resistance, the capacitance and the inductance. While a resistor only contributes the real part, a capacitor or an inductor only contribute to the imaginary part. The (angular) frequency dependent impedance can be plotted in a complex plane representation, also called Nyquist plot. Schematic Nyquist plots of the three basic circuit elements discussed are depicted Figure 2.1. Additionally, a forth circuit element, the constant phase element (CPE) is also shown. As shown in Figure 2.1, a CPE can adopt different behaviors, depending on the constant phase ($-90° \cdot \alpha$) value. For $\alpha = 1$ and $\alpha = -1$ the CPE adopts the characteristics of a capacitor or an inductor, respectively. Values between 1 and -1 indicate a non-ideal behavior, which is

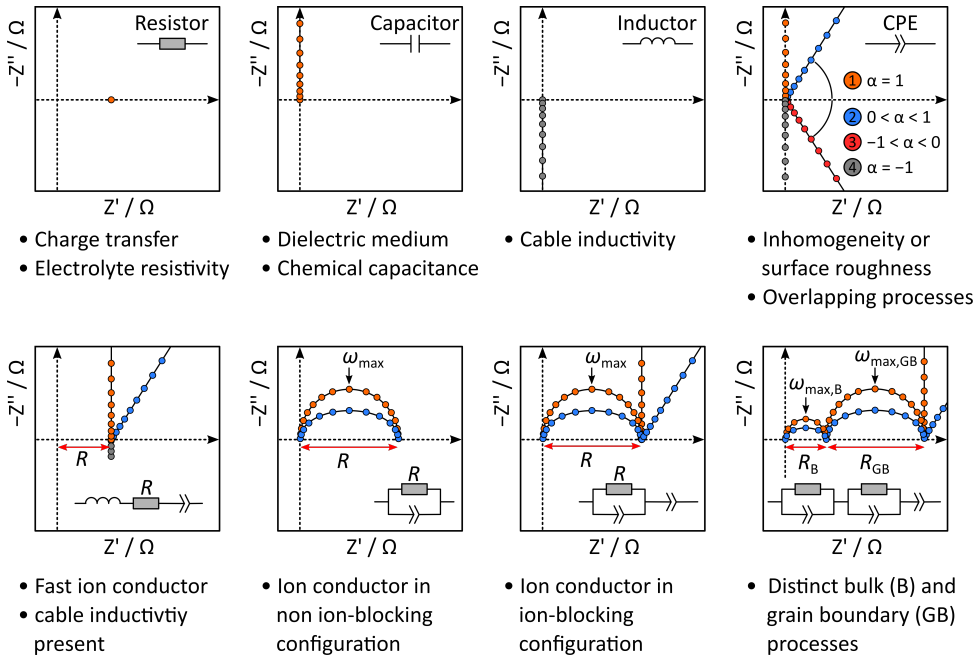

Figure 2.1: Top row: Schematic Nyquist plots of resistor, capacitor, inductor, and constant phase element circuit elements. A short description of physical processes described with the above circuit elements is given below the respective Nyquist plot.
Bottom row: Schematic Nyquist plots of exemplary equivalent circuits used to analyze impedance spectra of (thiophosphate-based) solid electrolytes. Equivalent circuits describing ideal ($\alpha = 1$) and non-ideal ($0 < \alpha < 1$) capacitive behavior of an assumed sample are depicted in orange and blue, respectively. The short description below indicates the kind of sample or configuration measured with typical EIS measurement parameters and assuming a ion-blocking configuration if not stated otherwise.

often observed for real samples. The impedance of a constant phase element is:

$$\hat{Z}_{\mathrm{CPE}} = \frac{1}{Q(j\omega)^{\alpha}} \ , \tag{2.4}$$

with Q being a numerical value without specific physical meaning. Circuit elements can be combined in series or parallel arrangements, to understand the behavior of different dynamics in different timescales. This gives a variety of possible configuration, that can be mathematically solved using Kirchhoff's laws:

$$\text{Serial:} \quad \hat{Z} = \sum_{n=1}^{N} \hat{Z}_n \qquad \text{Parallel:} \quad \hat{Z}^{-1} = \sum_{n=1}^{N} Z_n^{-1} \ . \tag{2.5}$$

In the following, equivalent circuit diagrams relevant for solid electrolytes, as they are shown in Figure 2.1, are discussed. For low impedance samples, e.g. very fast

ion conduction, experimental EIS data resemble an angled straight line with a positive intercept of the Z' axis. In the corresponding serial equivalent circuit, R-CPE (hyphen denotes a series connection), R describes sample resistance and CPE the polarization of ions at the ion-blocking sample-electrode interface. For ill-shielded measurements, cable inductance, L, can be observed at very high frequency. Samples with a more moderate conductivity often exhibit an arc-like behavior, that is explained by a parallel (R)(C) or (R)(CPE) arrangement (brackets denote parallel connection) . Here, R remains the sample resistance, while the C/CPE describes the chemical capacitance. The capacitance calculated from a CPE element (Equation 2.6) depends on the type of connection (serial/parallel), the α and Q value, as well as the resistance R of involved resistors:[9]

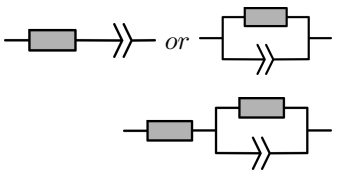

$$C = \left(\frac{Q}{R^{\alpha-1}}\right)^{\alpha^{-1}}$$

$$C = \left(\frac{Q}{\left(R_1^{-1} + R_2^{-1}\right)^{1-\alpha}}\right)^{\alpha^{-1}} . \tag{2.6}$$

Depending on the magnitude of the (apparent) capacitance, conclusions about the underlying physical processes can be drawn.[10] In an ion-blocking configuration the electrode polarization spike is present, translating to a (R)($\mathrm{CPE}_{\mathrm{sample}}$)-$\mathrm{CPE}_{\mathrm{electrode}}$ circuit, while for a non-ion-blocking configuration, (R)($\mathrm{CPE}_{\mathrm{sample}}$), it is absent. The CPE element is often introduced in the equivalent circuit because of its flexibility to describe non-ideal systems. As schematically shown in Figure 2.1, it suppresses the semicircle, observed for the (R)(C) element (with $\alpha = 1$), to a flatter arc in the (R)(CPE) circuit (with $0 < \alpha < 1$). The non-ideal behaviour of a sample can be caused by a superposition of processes with different time constants τ ($\omega_{\max} = \frac{1}{\tau} = \frac{1}{RC}$), that are not sufficiently separated. For processes with very different time constants, physical processes can be separated by fitting two (or more) (R)(C) or (R)(CPE) circuits in series. For solid electrolytes which show a distinct grain boundary (GB) behavior, a series connection is often chosen to fit such systems. Additionally, the distribution of relaxation times (DRT) analysis can be used to deconvolute more complex impedance spectra, giving an indication of how many different processes are present. Once the contributions to the impedance spectrum are analyzed, the ionic conductivity σ of the sample with sample thickness d and contact area A can be calculated:

$$\sigma = \frac{1}{R}\frac{d}{A} \tag{2.7}$$

Chronopotentiometry and chronoamperometry

Pure solid ion conductors exhibit solely ionic conductivity. However, most samples exhibit an additional partial electronic conductivity. While the partial electronic conductivity of a solid electrolyte impedes the application as a separator, because it accelerates the self-discharge of a cell, it is a beneficial property for electrode materials. Therefore, the electronic conductivity of a sample is an important quantity to determine. For this, chronopotentiomentric (CP) and chronoamperometric (CA) direct current (DC) measurements are performed. For CP measurements the current is kept constant and the voltage is recorded as a function of time, while for CA measurement a constant potential is applied and the time dependent current is recorded. Schematic CP and CA measurements are depicted in Figure 2.2.

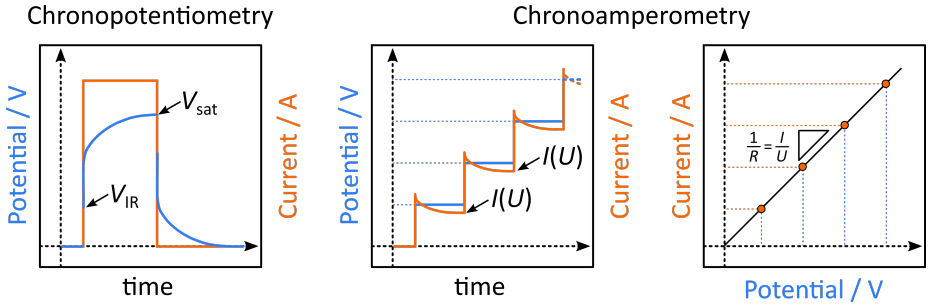

Figure 2.2: Left: Schematic chronopotentiomentry with IR-drop voltage V_{IR} and saturation voltage V_{sat}. Middle: Schematic chronoamperometry with excitation voltage steps in blue and current response in orange. Right: Schematic analysis of chronoamperometry data according to Ohm's law.

For CP measurements, the electronic (σ_{eon}) and total (σ_{tot}) conductivity can be calculated from the following equations:

$$\sigma_{\mathrm{eon}} = \frac{1}{R_{\mathrm{eon}}}\frac{d}{A} \quad \text{with} \quad R_{\mathrm{eon}} = \frac{V_{\mathrm{sat}}}{I} \qquad \sigma_{\mathrm{tot}} = \frac{1}{R_{\mathrm{IR}}}\frac{d}{A} \quad \text{with} \quad R_{\mathrm{IR}} = \frac{V_{\mathrm{IR}}}{I} \tag{2.8}$$

For CA measurements, the saturation (plateau) current is plotted as function of the excitation voltage. From this the electronic resistance R_{eon} can be calculated (see Figure 2.2, right) for samples that follow Ohm's law (U, I linearity). The transference number t_{ion}, a measure of how selective an ion conductor is towards ionic conductivity, can be calculated using the ionic conductivity from EIS and the electronic conductivity from DC measurements:

$$t_{\mathrm{ion}} = \frac{\sigma_{\mathrm{ion}}}{\sigma_{\mathrm{ion}} + \sigma_{\mathrm{eon}}} = \frac{\sigma_{\mathrm{ion}}}{\sigma_{\mathrm{tot}}} \tag{2.9}$$

2.6 Computational methods

Although experimental characterization methods yield many important properties of solid electrolytes, certain physical properties and phenomena are challenging to measure experimentally. Computational chemistry offers the possibility to study and predict such properties based on structure models of existing and predicted/modeled compounds. Larger scale simulations based on continuum mechanics and physical laws help to model and predict micro- and macroscopic properties of multi-element systems. This section phenomenologically introduces four computational methods that are part of this thesis, as a more extensive introduction discussion is better described in the appendices of this thesis and in textbooks.[11] The DFT and AIMD calculation were performed by F. Pielnhofer, T. Scholz, Z. Deng, and M. Sadowski, under the supervision of B. Lotsch, P. Canepa, and K. Albe. DEM and FVA were performed by C. Schmidt, A. Neumann, and M. Clausnitzer, under the supervision of W. Wall and A. Latz. BVS calculation were performed by C. Schneider and T. Scholz under the supervision of B. Lotsch. A more detailed description of project contributions is presented in Appendix F.

Density functional theory and *ab initio* molecular dynamics

The density functional theory (DFT) reduces the $3N$ coordinate problem of many-body systems, containing N electrons, by using the electron density instead. The first principle calculations based on DFT enables the computation of many physical properties (magnetic, electronic, optic, ...) of solid materials on a reasonable time scale. As an input, only information the crystal structure is needed. For solid electrolytes, DFT-based calculations are especially relevant to predict new structures, relax structures to their energetic minimum or calculate properties, like the thermodynamic stability in multi-phase systems, band gaps, and the stability towards lithium metal and allow interpretation of Raman bands and or interface behaviors.
Ab initio molecular dynamics (AIMD) simulations, used to simulate the molecular or ion dynamic movement in a solid within a set period of time, are of special relevance. Classic MD simulation numerically solves the dynamic interaction of atoms or molecules in a classic, (semi-)empirical potential force field. *Ab inito* MD acknowledges quantum mechanic aspects by calculating the atom-atom interactions based on DFT. With the advances in computation power, AIMD is able to simulate the dynamics of a complex system, consisting of many atoms ($\sim 10^2$) or unit cells over a sufficiently long period of time ($\sim 10^{-12}$ s) with a high time resolution (fs). From AIMD simulations, which are typically performed at different simulation temperatures, the mean squared displacement (MSD) of an ion/atom/molecule can be calculated, which indicates the type of motion (long- *versus* short-range) and the velocity of the mobile species in a certain direction. This helps to understand the ion dynamics in solid electrolytes, and predicts the ion diffusivity and activation energy. Furthermore, the dynamics of bond lengths, bond angles, dihedral angles and relative orientation can be studied.

Bond valence sum calculations

The bond valence sum (BVS) calculations are based on the empirical softBV parameters, R_0 and b.[12,13] Calculating the softBV force field involves a Morse-type term as well as a

Coulomb term, describing the attractive cation-anion and repulsive cation-cation/anion-anion interactions. For solid electrolytes, calculation of a BVS-based bond-valence site energy (BVSE)[12] or bond-valence energy landscape (BVEL)[14] enables analyzing the potential energy landsape for a probed cation. Usually, the unit cell is divided into an integer number of voxels with a distance of around 0.05 to 0.1 Å, producing a 3D grid. At each grid point the BSVE for the probed ion is calculated, resulting in an energy surface across the unit cell. The energy surface can be studied similar to the nudged-elastic band (NEB) approach in DFT calculations, where a start and end point for a migrating ion is defined, giving the activation barrier as a function of the pathway length. The BVS-based activation barriers positively correlates with the activation energies calculated by from experiment and DFT-NEB, as shown for many different ion conducting solids.[12,15] The BVS approach is not only advantageous to study ion migration pathways and their dimensionality, but can also be used to identify possible low-energy sites for the mobile ion. Especially for lithium-compounds, where the crystallographic position of lithium is often difficult to identify, BVSE maps hint for lithium occupied sites. Details on the used programs to compute BVS and BVEL are presented in the appendices A, B, and C of this thesis.

Discrete element method and finite volume analysis

While DFT, AIMD and BVS-based calculations focus on the atomic length-scale (nm) to study intrinsic material properties, the discrete element method (DEM) and finite volume analysis (FVA) are applied for particle simulations on a microscopic (µm) length-scale. DEM simulations are based on numerically computing the physical interaction of an ensemble of particles, and is historically related to molecular dynamics simulations. The particles can be assigned different attributes, like size and initial position, and obey classic physical lows describing effects like friction, gravitation, or repulsion of particles. The force acting on each individual particle is then iteratively computed, leading a new particle position and velocity. With DEM, the microstructure of a solid electrolyte compact can be simulated.
For analyzing the simulated microstructure, finite volume analysis (FVA) can be applied. There, the microstructure is divided into small voxels to create a discrete microstructure, on which partial differential equations are numerically solved. For solid electrolytes, calculation of the effective current density is of interest, as it defines the effective conductivity of the sample. More details on DEM and FVA are presented in Appendix E.

References

(1) Warren, B. E. *Phys. Rev.* **1941**, *59*, 693–698.

(2) Terban, M. W.; Billinge, S. J. L. *Chem. Rev.* **2022**, *122*, 1208–1272.

(3) Smith, E.; Dent, G., *Modern Raman Spectroscopy: A Practical Approach*; Wiley: 2013.

(4) Mehrer, H., *Diffusion in solids: fundamentals, methods, materials, diffusion-controlled processes*; Springer Science & Business Media: 2007; Vol. 155.

(5) Egerton, R.; Li, P.; Malac, M. *Micron* **2004**, *35*, 399–409.

(6) Orazem, M.; Tribollet, B., *Electrochemical Impedance Spectroscopy*; Wiley: 2011.

(7) Huggins, R. A. *Ionics* **2002**, *8*, 300–313.

(8) Barsoukov, E.; Macdonald, J. R., *Fundamentals of Impedance Spectroscopy*; Wiley: 2005.

(9) Brug, G. J.; van den Eeden, A. L. G.; Sluyters-Rehbach, M.; Sluyters, J. H. *J. Electroanal. Chem. Interfacial Electrochem.* **1984**, *176*, 275–295.

(10) Irvine, J. T. S.; Sinclair, D. C.; West, A. R. *Adv. Mat.* **1990**, *2*, 132–138.

(11) Marx, D.; Hutter, J., *Ab Initio Molecular Dynamics: Basic Theory and Advanced Methods*; Cambridge University Press: 2009.

(12) Chen, H.; Wong, L. L.; Adams, S. *Acta Cryst. B* **2019**, *75*, 18–33.

(13) Chen, H.; Adams, S. *IUCrJ* **2017**, *4*, 614–625.

(14) Sale, M.; Avdeev, M. *J. Appl. Cryst.* **2012**, *45*, 1054–1056.

(15) Wong, L. L.; Phuah, K. C.; Dai, R.; Chen, H.; Chew, W. S.; Adams, S. *Chem. Mater.* **2021**, *33*, 625–641.

CHAPTER 3

Research Objective

Solid electrolytes can advance lithium and sodium-ion battery technology by enabling higher energy density, safety and cycle life. One of the most important core objectives for solid electrolytes is high ionic conductivity. To this end, sulfide- and especially thiophosphate-based lithium and sodium ionic conductors have been identified that exceed the application-relevant ionic conductivity of more than $>1 \cdot 10^{-3}\,\mathrm{S\,cm^{-1}}$. In crystalline solid electrolytes, high ionic conductivity is the result of the interwoven interactions between the cation and anion sublattices leading to favorable ion migration pathways through the solid. To facilitate the search for new, high-performance solid electrolytes, a comprehensive understanding of the relationship between structure and transport properties is of paramount importance. The overall aim of this work is to investigate how crystal structure, material preparation and modification, as well as microstructure influence the transport properties of sulfide and thiophosphate-based compounds.

A large number of publications addressing this relationship have focused on the effects of tuning the crystal structure by iso- and aliovalent substitution to improve ionic conductivity, particularly in solid electrolytes containing the simple, tetrahedral building block PS_4^{3-}. Studies on compounds containing more complex thiophosphate anions such as $P_2S_6^{4-}$ are less frequently reported. Filling this knowledge gap is essential to explore possible correlations between the nature of the thiophosphate anion and the cation transport property. Therefore, ternary and quaternary model compounds containing the $P_2S_6^{4-}$ anion are synthesized and characterized with respect to their structure, stability and conductivity. The lithium and sodium ion conducting model compounds, $Li_4P_2S_6$ and $Na_4P_2S_6$, are well suited for this purpose.

In $Li_4P_2S_6$, the conductivity is sensitive to the aliovalent substitution of Li^+ by divalent Mg^{2+}.[1] Besides divalent metals, trivalent metals such as lanthanides can also form $ALnP_2S_6$ compounds (A = alkali metal, Ln = lanthanide).[2] To further extend the phase space, stability and ionic conductivity of quaternary $LiM^{III}P_2S_6$ compounds, Sc is a promising candidate for substitution as it already forms $ALnP_2S_6$-like compounds with A = Ag, Cu, Na.

For the higher homolouge of $Li_4P_2S_6$, $Na_4P_2S_6$, Rush *et. al* reported a lower migration barrier for $Na_4P_2S_6$ compared to $Li_4P_2S_6$.[3,4] Although different structures have been com-

putationally investigated in the study of Rush *et al.*, it remains unclear which structure is stable and how high the ionic conductivity of $Na_4P_2S_6$ actually is. $Na_4P_2S_6$ is particularly interesting because it can be synthesized *via* different routes. Thoroughly investigating the cation and anion sublattices and thus the transport properties of two differently synthesized samples should enable evaluation of the role of the synthesis pathway on material properties. Based on these findings, the phase stability of $Na_4P_2S_6$ needs to be reassessed.

While substitution and modified synthetic routes are well-established tools in solid-state chemistry to increase ionic conductivity, other measures such as topotactic/topochemical reactions or confinement effects, especially in two-dimensional materials, are less considered. Since the discovery of layered lithium compounds, many new materials with two-dimensional lithium ion transport and intercalation have been identified. Although most of these materials are considered as cathode materials, there are some exceptions such as the ion conductor $Li_2Sn_2S_5$.[5] Previous studies on this compound showed excellent exfoliation behavior in water, which was attributed to the hydration of lithium ions.[6] This suggests that exfoliation is the result of a topochemical reaction of water with the layered structure. Water molecules are expected to form a hydration sphere around the lithium ions in the interlayer, eventually separating the layers. Determination the correlation of the water content, interlayer spacing and transport properties could elucidate the role of lithium ion hydration in shielding Coulomb interactions.

Although the ionic conductivity in crystalline materials is mainly determined by the crystal structure, in polycrystalline samples other, more extrinsic properties can additionally influence the effective ionic conductivity. An important extrinsic parameter that is often discussed in all solid-state batteries is pressure, as the application of pressure is inevitable for the construction and operation of such a battery. From an application perspective, it is of great importance to determine the effects of pressure, as under pressure not only chemical aspects, such as bond lengths, can change, but also the microstructure of a granular sample. Therefore, investigating macroscopic and microscopic effects of applied pressure could clarify the role of microstructure and unit cell compression on the effective ionic conductivity of granular samples. Bearing in mind particle physics and mechanics, the particle size distribution may play an additional role for polycrystalline, granular solid electrolytes. The fast ion conductor, tetragonal Li_7SiPS_8, is a suitable model compound for such a multi-parameter investigation, as its application relevant ionic conductivity promises knowledge transfer to other high-performance glassy ceramic solid electrolytes.

The objectives of this thesis reveal a cornucopia of possible factors influencing the ionic conductivity in sulfide and thiophosphate solid electrolytes. This thesis will investigate not only the structure and composition, but also how sample preparation and post-synthetic modification, as well as how microstructure affect the ionic conductivity. By gaining a more comprehensive understanding of these diverse factors, this research will help to improve our ability to optimize sulfide and thiophosphate solid electrolytes by in part unconventional means.

References

(1) Takada, K. *Solid State Ion.* **2002**, *147*, 23–27.

(2) Schoop, L. M.; Eger, R.; Kremer, R. K.; Kuhn, A.; Nuss, J.; Lotsch, B. V. *Inorg. Chem.* **2017**, *56*, 1121–1131.

(3) Rush, L. E.; Holzwarth, N. A. W. *Solid State Ion.* **2016**, *286*, 45–50.

(4) Rush, L. E. J. First-Principles Investigation of Electronic Properties in Sodium-Ion Electrolytes for Solid-State Battery Materials, Thesis, 2017.

(5) Holzmann, T.; Schoop, L. M.; Ali, M. N.; Moudrakovski, I.; Gregori, G.; Maier, J.; Cava, R. J.; Lotsch, B. V. *Energy Environ. Sci* **2016**, *9*, 2578–2585.

(6) Kuhn, A.; Holzmann, T.; Nuss, J.; Lotsch, B. V. *J. Mater. Chem. A* **2014**, *2*, 6100–6106.

CHAPTER 4

Synthesis and characterization of: $Li_{4-3x}Sc_xP_2S_6$ ($x = 0.358$), *m*-$LiScP_2S_6$, and *t*-$LiScP_2S_6$

Leslie Mareike Schoop, Roland Eger, Florian Pielnhofer, Christian Schneider, Jürgen Nuss, Bettina Valeska Lotsch

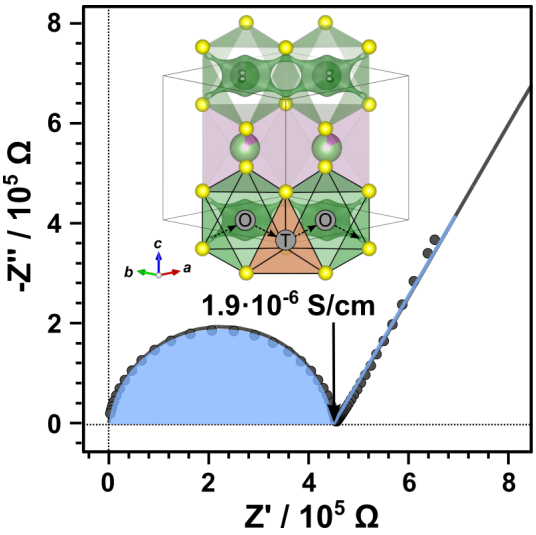

This work was published in and adopted from:
Zeitschrift für Anorganische und Allgemeine Chemie **2018**, *644*, 1854-1862.

Supporting information can be found in Appendix A.
Author contributions can be found in Appendix F.

Contents of Chapter 4

4.1 Abstract

We report the first examples of lithium rare earth metal hexathiohypodiphosphates(IV). Three new lithium-scandium hexathiohypodiphosphates(IV) were synthesized and characterized. The compounds crystallize in three different structure types, featuring isolated ethane-like $P_2S_6^{4-}$ hexathiohypodiphosphate(IV) units. $Li_{2.926}Sc_{0.358}P_2S_6$ or $Li_{4-3x}Sc_xP_2S_6$ ($x = 0.358$) crystallizes in the space group $P\bar{3}1m$ (no. 162) with $a = b = 6.0966(5)$ Å, $c = 6.5866(6)$ Å, V = 212.02(4) Å^3, and $Z = 1$. The compound is isostructural to $Li_2FeP_2S_6$ as well as the Li ion conductor $Li_{4-2x}Mg_xP_2S_6$ ($x = \frac{1}{3}, \frac{2}{3}$). Monoclinic $LiScP_2S_6$ was found to be a layered compound with van der Waals gaps. The layers consist of edge sharing octahedra that are occupied by Li, Sc, and P2 in an alternating fashion. It is isostructural to $LiAlP_2S_6$ and crystallizes in the space group $C2/c$ (no. 15) with $a = 6.933(1)$ Å, $b = 10.754(2)$ Å, $c = 11.694(2)$ Å, $\beta = 94.41(3)°$, V = 869.3(3) Å^3, and $Z = 4$. Trigonal $LiScP_2S_6$ crystallizes in the space group $P31c$ (no. 163) with a $= b = 6.363(1)$ Å, $c = 12.386(3)$ Å, V = 434.3(2) Å^3, and $Z = 2$, and is isostructural to $AgInP_2S_6$ and $AgScP_2S_6$. Its structure is closely related to the monoclinic version, except that trigonal $LiScP_2S_6$ features disordered $[P_{2/2}P_{6/6}S_6]^{4-}$ units. The new phases were investigated by Raman spectroscopy, thermal analysis, and DFT calculations. We further demonstrate that $Li_{4-3x}Sc_xP_2S_6$ shows significantly enhanced Li ion conductivity compared to the parent compound $Li_4P_2S_6$.

4.2 Introduction

Solid state lithium ion conductors continue to attract great interest due to their promise to enable high-performance all solid state lithium batteries.[1] A fundamental characterization of the structure and Li dynamics of these materials is crucial in order to understand and further develop the next generation of solid electrolytes.[2–6] Lithium thiophosphates are potential candidates for high lithium ion conductivities, but the number of known thiophosphate compounds that are lithium superionic conductors is relatively small. Inspired by the lack of lithium compounds in our systematic studies on quaternary rare earthmetal thiophosphates,[7] we extensively investigated the Li–Sc–P–S system and found three new lithium-scandium hexathiohypodiphosphates(IV). The compounds exist in three different structure types with either two or three dimensional topologies. They complete the structural stability diagram of $ALnP_2S_6$ compounds (A = Na, K, Rb, Cs; Ln = lanthanide) that we published recently.[7]

To this date, five distinct thiophosphate anions are reported, which are shown in Figure 4.1.[8,9] Most common are the tetrahedral tetrathioorthophosphate(V) ($[PS_4]^{3-}$) anion and the ethane-shaped hexathiohypodiphosphate(IV) ($P_2S_6^{4-}$) anion, in which the six sulfur atoms form an octahedron, just like in staggered ethane. Less commonly found thiophosphate anions are the pyrothiophosphate(V) ($[P_2S_7]^{4-}$) anion, where two $[PS_4]$ tetrahedra share a corner, and the hexathiometadiphosphate(V) ($[P_2S_6]^{2-}$) anion, where two $[PS_4]$ tetrahedra share an edge. Very recently, we reported on a disordered version of the hexathiohypodiphosphate(IV) ($P_2S_6^{4-}$), which shows a Raman spectrum that is distinct from its ordered cousin.[8] In accordance with the abundance of the different anions, all reported quaternary scandium thiophosphates contain the hexathio-

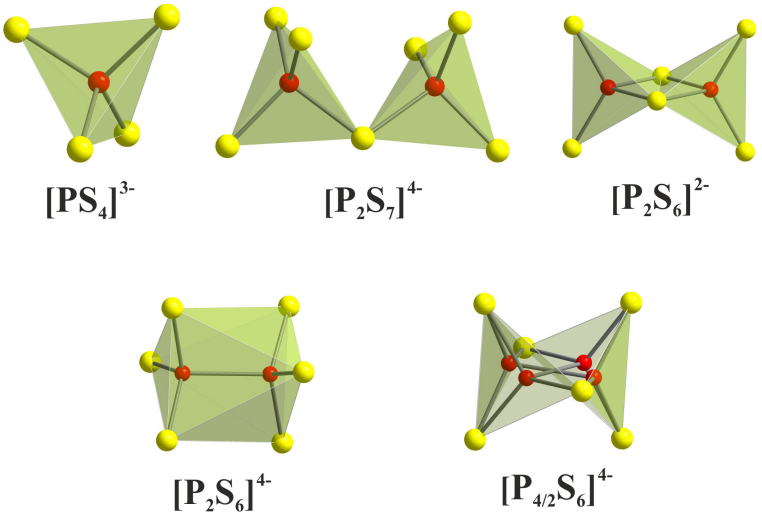

Figure 4.1: Previously known thiophosphate anions: tetrathioorthophosphate(V) ($[PS_4]^{3-}$), pyrothiophosphate(V) ($[P_2S_7]^{4-}$), hexathiometadiphosphate(V) ($[P_2S_6]^{2-}$), hexathiohypodiphosphate(IV) ($P_2S_6^{4-}$), and disordered hexathiohypodiphosphate(IV) ($[P_{4/2}S_6]^{4-}$) (P drawn in red,S shown yellow, polyhedra drawn in green).

hypodiphosphate(IV) anion ($AgScP_2S_6$,[10] $CuScP_2S_6$,[11] $NaScP_2S_6$[7]) with the exception of $TlScP_2S_7$.[11] The three Li–Sc hexathiohypodiphosphates(IV), which are reported herein, are the first lithium containing scandium thiophosphates. All remaining lithium rare earth metal thiophosphates known to date are tetrathioorthophospates(V) such as $LiEuPS_4$,[12] $Li_9Ln_2(PS_4)_5$,[13,14] (Ln = Gd, Nd) and $Li_6Ln_3(PS_4)_5$[15] (Ln = Y, Gd, Dy, Yb, Lu). No lithium ion conductivities of these compounds have been reported.

In contrast to the known lithium rare earth metal thiophosphates, some lithium rare earth metal phosphates show decent lithium ion conductivities, e.g.: $LiLn(PO_3)_4$ (Ln = La, Gd),[25,30] $Li_3Sc_2(PO_4)_3$,[26,27] $Li_{3-2x}(Sc_{1-x}M_x)_2(PO_4)_3$ (M = Ti, Mg, $0 \leq x \leq 0.30$),[28] as well as $LiScP_2O_7$[29] (see Table 4.1). The most prominent lithium thiophosphates in terms of their Li^+ ion conductivities are glasses, glass ceramics, and crystalline phases within the quasi-binary Li_2S-P_2S_5 system, or within quasi-ternary systems containing, for example, SiS_2, GeS_2, Li_3PO_4, or halides.[31–34] Lithium phosphidosilicates[35] can also exhibit ionic conductivities. Other examples (see Table4.1) include the ternary compounds Li_3PS_4,[16] $Li_2P_2S_6$,[17] $Li_4P_2S_6$,[18,36] argyrodite Li_7PS_6[19] and $Li_7P_3S_{11}$,[20,37] or the quaternary compound Li_4PS_4I.[21] Further interesting thiophosphate based ion conductors are $Li_{4-2x}Mg_xP_2S_6$ ($x = \frac{1}{3}, \frac{2}{3}$),[38] the argyrodite-type phases Li_6PS_5X (X = Cl, Br, I),[19,39] and tetragonal $Li_{10}GeP_2S_{12}$ (LGPS)[22,40] along with its derivatives, including $Li_{11}Si_2PS_{12}$, $Li_{10}SnP_2S_{12}$,[23] and $Li_{9.54}Si_{1.74}P_{1.44}S_{11.7}Cl_{0.3}$, which are closely related to the thio-LISICON (*LI*thium *S*uper*I*onic *CON*ductor) family of compounds. LGPS-type materials are currently the record holders in terms of Li^+ ion conductivity in the solid state with up to $1.6 \cdot 10^{-2}\,S\,cm^{-1}$.[24,41]

Table 4.1: Lithium ionic conductivities of prominent thiophosphates and rare earth metal phosphates at 298 K.

Compound	E_A / eV	σ / S cm^{-1}	Ref.
β-Li_3PS_4 (bulk)	0.47	$3 \cdot 10^{-7}$	[16]
$Li_2P_2S_6$	0.48	$7.8 \cdot 10^{-11}$	[17]
$Li_4P_2S_6$	0.48	$1.6 \cdot 10^{-10}$	[18]
Li_6PS_5Cl	0.38	$1.3 \cdot 10^{-6}$	[19][a]
$Li_7P_3S_{11}$	0.12	$3 \cdot 10^{-3}$	[20]
$Li_{4-2x}Mg_xP_2S_6$ (x=$\frac{2}{3}$)	0.47	$1 \cdot 10^{-6}$	[21]
$Li_{10}GeP_2S_{12}$	0.22	$1.2 \cdot 10^{-2}$	[22]
$Li_{10}SnP_2S_{12}$	0.25	$4 \cdot 10^{-3}$	[23]
$Li_{9.54}SI_{1.74}P_{1.44}S_{11.7}Cl_{0.3}$	0.25	$1.6 \cdot 10^{-2}$	[24]
$LiGd(PO_3)_4$	0.47	$2 \cdot 10^{-4}$	[25][b]
$Li_3Sc_2(PO_4)_3$	0.38–0.62	$10^{-5} - 10^{-2}$	[26][c]
$Li_3Sc_2(PO_4)_3$	—	$3 \cdot 10^{-6}$	[27]
$Li_{2.6}(Sc_{0.8}Ti_{0.2})_2(PO_4)_3$	—	10^{-5}	[28]
$LiScP_2O_7$	1.06	$4 \cdot 10^{-7}$	[29][d]

a) T = 313 K. b) T ≤ 873 K. c) T = 600 K, different orientations. d) T = 573 K.

4.3 Results and discussion

4.3.1 Synthesis of trigonal $Li_{4-3x}Sc_xP_2S_6$

The soft and very fragile, transparent trigonal compound $Li_{4-3x}Sc_xP_2S_6$ was first obtained with side phases, by following the reaction 4.1:

$$Sc + 0.5\,Li_2S + P_2S_5 + 0.5\,S \longrightarrow LiScP_2S_6 \tag{4.1}$$

Pure samples were synthesized from the pure elements using the following reaction Equation 4.2:

$$Sc + (4 - 3\,x)Li + 2P + 6S \longrightarrow Li_{4-3x}Sc_xP_2S_6 \tag{4.2}$$

We varied the value of x from 0.6 to 1.0 within different batches. The stoichiometric mixture was sealed in an evacuated quartz tube, heated (100 K h^{-1}) up to 973 K and kept at that temperature for 4 d. Afterwards the ampoule was cooled down slowly (25 K h^{-1}) and annealed at 773 K for 2 d. The furnace was switched off and the ampoule was removed from the furnace at room temperature.

4.3.2 Synthesis of monoclinic $LiScP_2S_6$

Brittle and transparent monoclinic $LiScP_2S_6$ was obtained according to reaction Equation 4.3:

$$Sc + Li + 2\,P + 6\,S \longrightarrow LiScP_2S_6 \tag{4.3}$$

The stoichiometric mixture was sealed in an evacuated quartz tube, heated ($100\,\mathrm{K\,h^{-1}}$) up to 1073 K and kept at that temperature for 4 d. Afterwards the ampoule was cooled down slowly ($25\,\mathrm{K\,h^{-1}}$) and annealed at 873 K for 2 d. The furnace was switched off and the ampoule was removed from the furnace at room temperature.

4.3.3 Synthesis of trigonal $LiScP_2S_6$

Fragile and colorless trigonal $LiScP_2S_6$ is possible to synthesize according to reaction Equation 4.1 and 4.3. The stoichiometric mixture was sealed in an evacuated quartz tube, heated ($100\,\mathrm{K\,h^{-1}}$) up to 1073 K and kept at that temperature for 6 d. Afterwards the ampoule was quenched to room temperature in cool water. Phase pure trigonal $LiScP_2S_6$ was found at the top of the quartz tube.

4.3.4 Structure of $Li_{4-3x}Sc_xP_2S_6$ ($x = 0.358$)

The crystal structure of $Li_{2.926}Sc_{0.358}P_2S_6$ (see Figure 4.2 and Table 4.2) was solved in the space group $P\bar{3}1m$ (no. 162) with $a = b = 6.0966(5)$ Å, $c = 6.5866(6)$ Å, $V = 212.02(4)$ Å^3, and $Z = 1$. It is the first representative of a solid solution $Li_{4-3x}Sc_xP_2S_6$ with $x = 0.358$. The refined structure is very similar to the structure of $Li_4P_2S_6$,[18] but Sc prefers to occupy a single site (Li1), thus leading to an ordered variant of $Li_4P_2S_6$ with lower symmetry. The compound is isostructural to $Li_2FeP_2S_6$[42] and to the Li ion conductor $Li_{4-2x}Mg_xP_2S_6$.[38] It is composed of sulfur atoms that are arranged in a *hcp* packing, where Li, Sc, and P_2 dumbbells occupy the octahedral holes. The P_2 dumbbells in a $[S_6]$ octahedron form the $P_2S_6^{4-}$ anion. The structure is a quasi-layered structure, since Sc prefers to substitute the Li1 site, which causes the octahedra to be occupied in an alternating fashion along the c axis (see Figure 4.2). The P_2 dumbbells approximately occupy $\frac{1}{3}$ of the octahedral voids within each second layer, so that the Li^+/Sc^{3+} cations are arranged in a honeycomb-like network. In this sense the structure is related to that of Li_2SnO_3[43] or Na_2IrO_3.[44] Within the *ab* plane all octahedra are edge sharing, whereas they share faces in the c direction. Note that the P occupation in each layer is vastly different. The P atoms reside mostly in the layer containing Sc, while the layer containing lithium mostly contains vacancies on the respective P position. This distribution of the P_2 dumbbells is reflected by the site occupation factors of SOF(P1) = 0.925 and SOF(P2) = 1−SOF(P1), which agrees well with the site distribution found in $Li_{4-2x}Mg_xP_2S_6$ ($x = \frac{2}{3}$).[38]

The bond lengths within the $P_2S_6^{4-}$ anions are similar to the ones commonly found (P–P: 2.22 Å; P–S: 2.03 Å). The Sc/Li(1)–S bond length is 2.63 Å and the Li(2)–S bond length is 2.66 Å. These bond lengths are in good agreement with the isostructural $Li_2FeP_2S_6$[42] and other related $AScP_2S_6$ compounds (A = Ag, Na).[7,10] The Li-ion conductivity of $Li_4P_2S_6$[18,36] was previously measured to be very low (see Table 4.1) but it increases with increasing magnesium content x in the range of $x \leq \frac{2}{3}$ (see Table 4.1); beyond that value it decreases again.[38] Therefore, we suspected that $Li_{4-3x}Sc_xP_2S_6$ could show enhanced Li ion conductivity, compared to the parent compound $Li_4P_2S_6$. This expectation was indeed confirmed, as we show below. SEM-EDX analyses of several $Li_{4-3x}Sc_xP_2S_6$ crystals from the same batch (starting composition $x = 0.6$) showed different Sc concentrations, which all lie within the stoichiometry range of $x = 0.362$ - 0.458 (lithium was not detected). In total, we investigated more than 50 crystals from different batches and found compositional

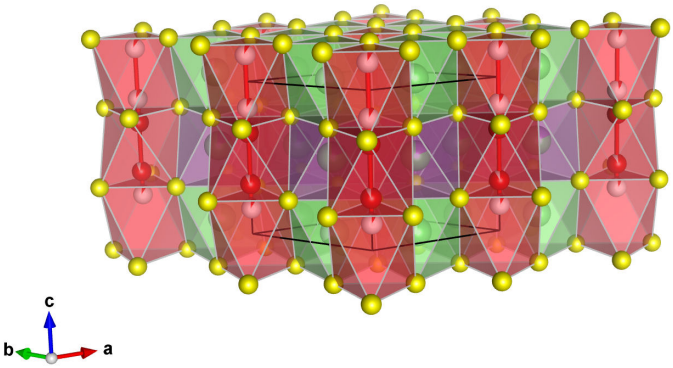

Figure 4.2: Crystal structure of $Li_{4-3x}Sc_xP_2S_6$ ($x = 0.358$), (Sc shown in purple, Li in green, P drawn in red, S in yellow, isolated $P_2S_6^{4-}$ units drawn as light red polyhedra.

ranges between $x = 0.353$ and 0.615. DTA measurements indicate that $Li_{4-3x}Sc_xP_2S_6$ is stable up to approximately 760 °C.

Table 4.2: Crystallographic data of $Li_{2.926}Sc_{0.358}P_2S_6$ ($Li_{4-3x}Sc_xP_2S_6$ with $x = 0.358$) and of trigonal *t*-$LiScP_2S_6$ as obtained from single-crystal X-ray diffraction at 298 K. For atomic coordinates and equivalent isotropic displacement factors please refer to Tables A.1 and A.3.

	$Li_{2.926}Sc_{0.358}P_2S_6$	*t*-$LiScP_2S_6$
Crystal shape	platelet	platelet
Crystal color	colorless transparent	colorless transparent
Diffraction method	single-crystal	single-crystal
Radiation	Mo-K_α	Mo-K_α
Crystal symmetry	trigonal	trigonal
Space group	$P\bar{3}1m$ (no. 162)	$P\bar{3}1c$ (no. 163)
Lattice parameters	$a = b = 6.0966(5)$ Å	$a = b = 6.363(1)$ Å
	$c = 6.5866(6)$ Å	$c = 12.386(3)$ Å
	$\gamma = 120°$	$\gamma = 120°$
Cell volume	212.02(4) Å^3	434.3(2) Å^3
Cell content	$Z = 1$	$Z = 2$
2θ range	$6.19° \leq 2\theta \leq 72.71°$	$6.58° \leq 2\theta \leq 47.36°$
Index range	$-10 \leq h \leq 10$	$-7 \leq h \leq 7$
	$-10 \leq k \leq 10$	$-7 \leq k \leq 7$
	$-10 \leq l \leq 10$	$-13 \leq l \leq 13$
Total reflections	4023	2110
Unique reflections	391	224
Parameters	21	26
Residual electron density (min/max)/e Å^{-3}	0.910 / -0.285	0.243 / -0.242
R_{int}	0.0222	0.0810
R_1 ($> 4\sigma$)	0.0228	0.0385
wR_2 ($> 4\sigma$)	0.0605	0.1021
GooF	1.254	1.114
Deposition no.	CSD-1864274	CSD-1864273

4.3.5 Structure of *m*-$LiScP_2S_6$

Monoclinic $LiScP_2S_6$ is a layered compound (see Figure 4.3, Table 4.3) and isostructural to $LiAlP_2S_6$.[45] It crystallizes in space group $C2/c$ (no. 15) with $a = 6.933(1)$ Å, $b = 10.754(2)$ Å, $c = 11.694(2)$ Å, $\beta = 94.41(3)°$, $V = 869.3(3)$ Å^3, and $Z = 4$ (see Table 4.3). The layers are separated by van der Waals gaps, and each layer is composed of $P_2S_6^{4-}$ hexathiohypodiphosphate(IV) units as well as $[ScS_6]$ and $[LiS_6]$ octahedra; the octahedra share edges. All three types of octahedra make $\frac{1}{3}$ of the layers, and the different cations alternate. In the ethane-like $P_2S_6^{4-}$ anion, the P–P bond length is 2.21 Å and the P–S bond lengths are 2.02–2.04 Å. The orientation of the P_2 dumbbells in the octahedral voids (and thus of the $P_2S_6^{4-}$ ions in the layer) is different from that in most other layered hexathiohypodiphosphates(IV).[45,46] While in most layered hexathiohypodiphosphates(IV), the P–P bond is usually oriented perpendicular to the sulfur layers, it is

almost oriented horizontally within the layers here, thus connecting each phosphorus atom with three sulfur atoms from two different planes. The Sc–S bond lengths are 2.60 Å and the Li–S bond lengths are 2.64–2.74 Å. These bond lengths agree well with the bond lengths in the isostructural compound $LiAlP_2S_6$.[45] Differential scanning calorimetry (DSC) measurements (Figures A.1 and A.2, Appendix A) indicate that *m*-$LiScP_2S_6$ transforms endothermally to *t*-$LiScP_2S_6$ upon heating to roughly 560 °C. Temperature dependent X-ray diffraction measurements (Figure A.3, Appendix A) show the transformation as well.

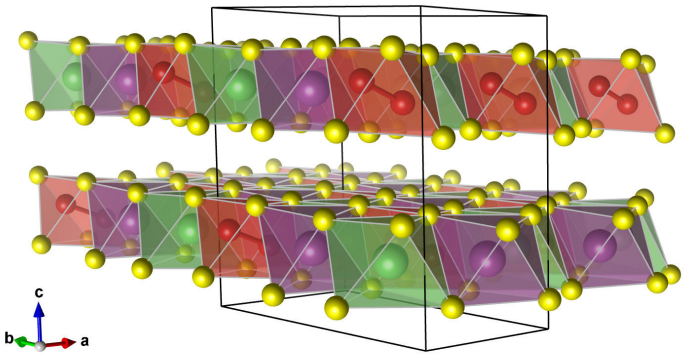

Figure 4.3: Crystal structure of monoclinic $LiScP_2S_6$ (Sc shown in purple, Li in green, P drawn in red, S in yellow, isolated $P_2S_6^{4-}$ units drawn as light red polyhedra.

4.3.6 Structure of *t*-$LiScP_2S_6$

Trigonal $LiScP_2S_6$ crystallizes in space group $P\bar{3}1c$ (no.163) with $a = b = 6.363(1)$ Å, $c = 12.386(3)$ Å, $V = 434.3(2)$ Å^3, and $Z = 2$ and is the high temperature phase of the system, since it was obtained *via* quenching from 1073 K, whereas slow cooling leads to the *m*-phase. The structure (see Figure 4.4, Table 4.3) is a variant of the $Fe_2P_2S_6$[47] structure type and isostructural to $AgInP_2S_6$[48] and $AgScP_2S_6$,[10] as well as the selenodiphosphates(IV) $M^{I}M^{III}P_2Se_6$ (M^{I} = Cu, Ag; M^{III} = Cr, Al, Ga, In)[49] and $AgLnP_2Se_6$ (*Ln* = Sc, Er, Tm).[11] $CuScP_2Se_6$ was additionally proposed to crystallize in this structure type.[11] The structure is also layered and very closely related to the one of *m*-$LiScP_2S_6$. The two phases exhibit the same stacking sequence and the cation distribution within the layers is similar, with one exception: trigonal $LiScP_2S_6$ contains disordered $P_2S_6^{4-}$anions. We refer to these disordered anions as isolated $[P_{2/2}P_{6/6}S_6]^{4-}$ units (see Figure 4.5), because there are 8 P sites, two are occupied by $\frac{1}{2}$ and 6 are occupied by $\frac{1}{6}$. The half occupied P position forms the P_2 dumbbell that is aligned parallel to the *c* axis, making it the preferred orientation. This orientation of the staggered $P_2S_6^{4-}$ anions is exclusively present in ordered [SOF(P) = 1] $AgScP_2S_6$ and $AgInP_2S_6$. The remaining disordered P position in *t*-$LiScP_2S_6$ (SOF(P2) = $\frac{1}{6}$) represents three further orientations of the P_2 dumbbell in the $[S_6]$ octahedron with the same atomic arrangement as in the

Table 4.3: Crystallographic data of monoclinic $LiScP_2S_6$ as obtained from single-crystal X-ray diffraction at 298 K. For atomic coordinates and equivalent isotropic displacement factors please refer to Table A.2

	m-$LiScP_2S_6$
Crystal shape	platelet
Crystal color	colorless transparent
Diffraction method	single-crystal
Radiation	Mo-K_α
Crystal symmetry	monoclinic
Space group	$C2/c$ (no. 15)
Lattice parameters	a = 9.933(1) Å b= 10.754(2) Å c= 11.694(2) Å β = 94.41(3)°
Cell volume	869.3(3) Å^3
Cell content	$Z = 4$
2θ range	6.98° ≤ 2θ ≤ 47.46°
Index range	-7 ≤ h ≤ 7 -12 ≤ k ≤ 12 -13 ≤ l ≤ 13
Total reflections	2257
Unique reflections	646
Parameters	47
Residual electron density (min/max)/e Å^{-3}	1.177 / -0.521
R_{int}	0.0555
R_1 ($> 4\sigma$)	0.0402
wR_2 ($> 4\sigma$)	0.0952
GooF	0.929
Deposition no.	CSD-1864272

staggered C_2H_6 molecule. In total, the disorder of the two P sites describes all four possible orientations of the P_2 unit in an octahedral environment with P atoms pointing towards opposite triangular faces.

To the best of our knowledge trigonal $LiScP_2S_6$ is the first example containing the described disordered $[P_{2/2}P_{6/6}S_6]^{4-}$ unit. As mentioned above, we recently reported a different disordered thiophosphate anion, $[P_{4/2}S_6]^{4-}$, in $Cs_{10}Y_4Cl_{10}(P_2S_6)_3$.[8] The version described here exhibits an even higher degree of disorder. In the $[P_{2/2}P_{6/6}S_6]^{4-}$ anion the P(1)–P(1) and P(2)–P(2) bond lengths are 2.17 − 2.18 Å, and the P(1)–S and P(2)–S bond lengths are 2.08 Å and 2.07-2.18 Å, respectively. The Sc–S bond length is 2.60 Å and the Li–S bond length is 2.71 Å. These bond lengths are in good agreement with related $AScP_2S_6$ compounds (A = Na, Ag)[7,10] and with $Cs_{10}Y_4Cl_{10}(P_2S_6)_3$.[8] SEM-EDX analyses show no differences in the composition (excluding Li) of monoclinic and trigonal $LiScP_2S_6$.

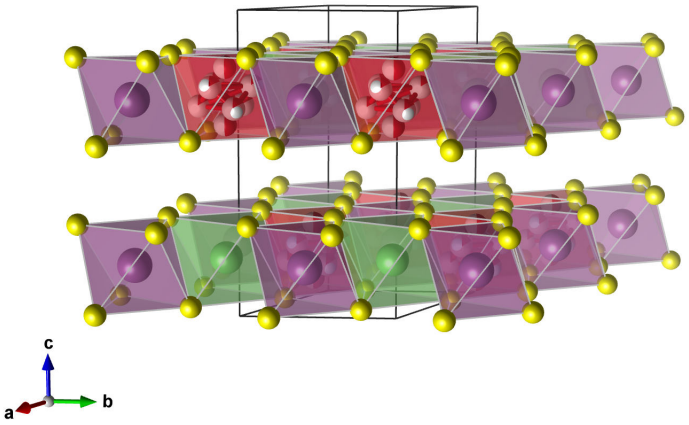

Figure 4.4: Crystal structure of trigonal $LiScP_2S_6$ (Sc shown in purple, Li in green, P drawn in red, S in yellow, isolated $[P_{2/2}P_{6/6}S_6]^{4-}$ units drawn as light red polyhedra).

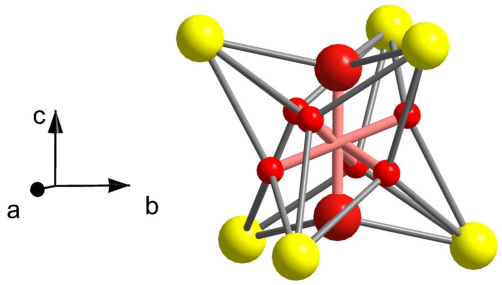

Figure 4.5: Disordered $[P_{2/2}P_{6/6}S_6]^{4-}$ anion (P drawn in red, S shown in yellow). Note: Only two opposite P positions are simultaneously occupied and the preferred orientation parallel to the c axis is highlighted by larger P atoms.

Differential thermal analysis DTA and DSC measurements indicate that both m- and t-$LiScP_2S_6$ decompose at similar temperatures, between 800 and 840 °C. Note that m-$LiScP_2S_6$ transforms to the t-phase before decomposition. High temperature X-ray diffraction shows that the decomposition product is mostly Sc_2S_3, mixed with small amounts of $Li_{4-3x}Sc_xP_2S_6$.

4.3.7 DFT modeling

Since t-$LiScP_2S_6$ features disorder on the P positions, it structure as determined from XRD cannot simply be used as input for density functional theory (DFT) calculations, making an energetically comparison of m- and t-$LiScP_2S_6$ impossible. That is why we derived fully ordered models from the real structure. As mentioned above, the same

stacking sequence of the colored Li–Sc honeycomb like layers is found in *m*- and *t*-$LiScP_2S_6$. The significant difference in the structures is the orientation of the P_2 entities in the voids of the honeycomb. Interestingly, all possible orientations of the P_2 dumbbells are realized in *t*-$LiScP_2S_6$ by disorder with a preferred orientation along the *c* axis. This means that the P2 orientation as found in *m*-$LiScP_2S_6$ is also present in the *t*-modification. The most simple model for *t*-$LiScP_2S_6$ with an ordered P_2 dumbbell that preserves the space group symmetry is by fully occupying the SOF(P1) = 0.5 positions, making it isotypic to $AgScP_2S_6$ and $AgInP_2S_6$, subsequently called *t**-$LiScP_2S_6$. A full occupation of one SOF(P2) = $\frac{1}{6}$ position results in space group $C2/c$, making *m*-$LiScP_2S_6$ a borderline case of *t*-$LiScP_2S_6$. However, calculating the equations of state for both idealized *t**-$LiScP_2S_6$ and *m*-$LiScP_2S_6$ reveals that the *t**-model is preferred over the *m*-modification by 26 kJ mol^{-1} (see Figure 4.6). Moreover, the modeling of the further dumbbell orientations in *t*-$LiScP_2S_6$ by full structural relaxations indeed results in almost the same arrangement and energy as for *m*-$LiScP_2S_6$ (see Table A.5, Appendix A). Since *t*-$LiScP_2S_6$ contains lower symmetric monoclinic structural features which are higher in energy, the ordered *t**-model is energetically preferred (note that configurational entropy contributions are neglected). We thus infer that *m*- and disordered *t*-$LiScP_2S_6$ are both metastable compared to a fully ordered *t**-$LiScP_2S_6$, which has not been synthesized yet.

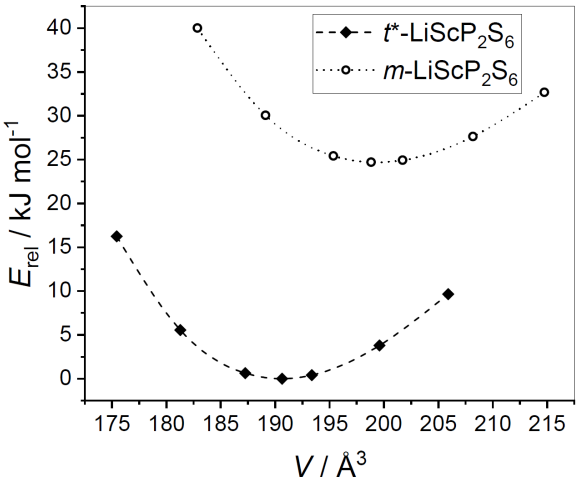

Figure 4.6: Calculated E vs.V curves for idealized *t**-$LiScP_2S_6$ and *m*-$LiScP_2S_6$.

4.3.8 Raman spectroscopy

For Raman spectroscopy, single crystals were selected under a microscope in dried petroleum, mounted into glass capillaries, and sealed under inert atmosphere. The Raman spectra of the three phases (see Figure 4.7) are very similar to the reported ones of $KLaP_2S_6$,[50] i.e. the compounds have the same type of Raman bands at very similar wavenumbers. In order to interpret the observed spectra for *m*- and *t*-$LiScP_2S_6$, the Raman modes were also calculated theoretically employing DFT (see Figure 4.7 and Appendix A for all calculated Raman active modes). The different types of P–S stretching vibrations are found at ca. 580 cm^{-1} (calculated 576–544 cm^{-1}). At 570 cm^{-1}, the first P–P stretching occurs [calculated 515 cm^{-1} (*t**) and 507 cm^{-1} (*m*)]. The small peak at 450 cm^{-1} that is present for both $LiScP_2S_6$ modifications is absent in the simulation for the fully ordered trigonal model but can be explained with the monoclinic structure. It is a further symmetric P–S stretching with the P–P dumbbell inclined horizontally within the layer. The most characteristic signal at 390 cm^{-1} has been previously assigned to the A_{1g} symmetric stretch of the ethane-like $P_2S_6^{4-}$ anion,[8,50–52] and is confirmed by the simulations. The disordered $[P_{2/2}P_{6/6}S_6]^{4-}$ anion does not show a distinct Raman spectrum, in contrast to the previously reported disordered $[P_{4/2}S_6]^{4-}$ anion.[8] However,the peaks in the spectrum of the trigonal phase are broadened compared to the sharp maxima of the monoclinic modification, caused by the disorder of the $P_2S_6^{4-}$ anion that can be regarded as a superposition of different similar spectra. From 320 cm^{-1} and below, the modes consist of P–S bending and Li–S and Sc–S stretching vibrations.

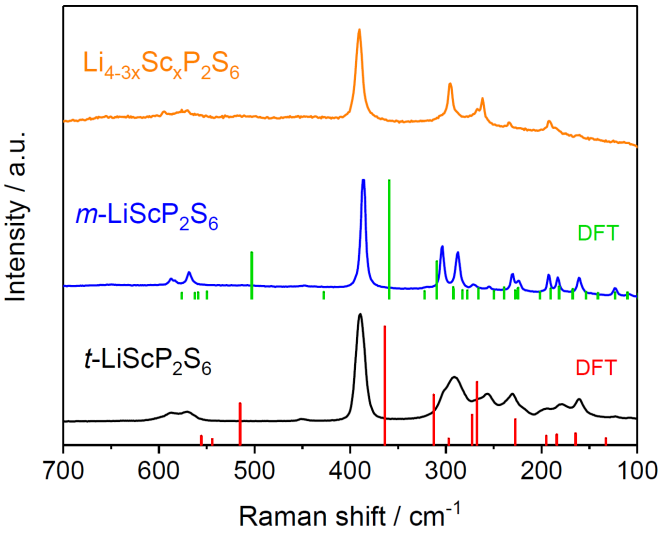

Figure 4.7: Raman spectra of the three new lithium-scandium hexathiohypodiphosphate phases with simulated Raman modes from DFT (green and red sticks). Not that the ordered *t**-model was taken for comparison with *t*-$LiScP_2S_6$.

4.3.9 Electrochemical impedance spectroscopy

Electrochemical impedance spectroscopy (EIS) measurements were performed in an argon-filled glovebox at room temperature. The Nyquist plots of cold pressed pristine and Ru sputtered pellets of $Li_{4-3x}Sc_xP_2S_6$ are shown in Figure 4.8a. The ionic conductivity of pressed pellets is on the order of $1.2 \cdot 10^{-6}\,S\,cm^{-1}$, and the corresponding chemical capacitance amounts to about $5 \cdot 10^{-11}\,Fcm^{-2}$, thus indicating a bulk process. The lithium ion motion in the parent crystalline compound $Li_4P_2S_6$[18] was reported to be four orders of magnitude lower ($1.6 \cdot 10^{-10}\,S\,cm^{-1}$). Partial substitution of Li^+ ions by Mg^{2+} ions in $Li_{4-2x}Mg_xP_2S_6$, increases the ionic conductivity by several orders of magnitude ($1 \cdot 10^{-6}\,S\,cm^{-1}$),[38] similarly to the conductivity of $Li_{4-3x}Sc_xP_2S_6$. Probing electronic conductivity by *dc* polarization experiments was not possible due to high signal-to-noise ratios at low excitation voltages. Higher applied potentials resulted in decomposition of the electrolyte or reaction with the electrode. Therefore, modeling a resistor parallel to the (R CPE)-(CPE) circuit was used to qualitatively probe the partial electronic conductivity (σ_{eon}) compared to a model representing a sole ionic conductor. An electronic conductivity of ca. $10^{-9}\,S\,cm^{-1}$ was calculated by the fit of the extended equivalent circuit. Since the fit quality did not improve by adding electronic conductivity to the model, it was therefore simplified to acknowledge the negligible electronic contribution to the total conductivity.

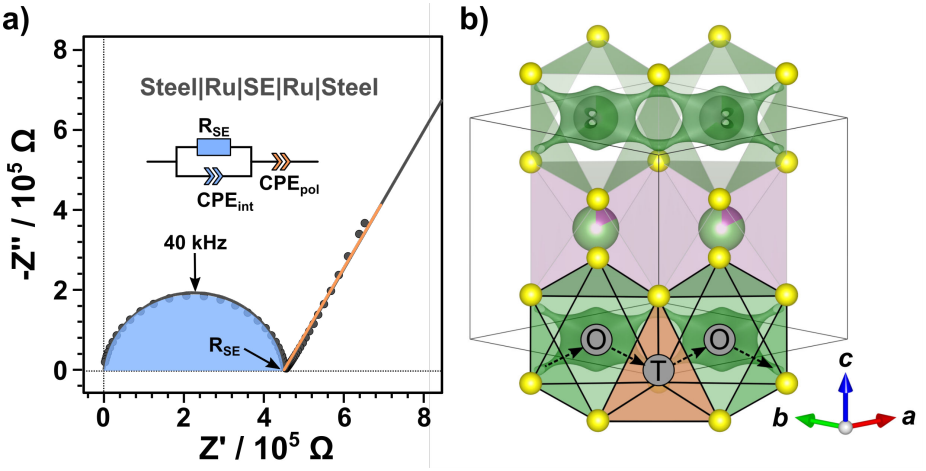

Figure 4.8: (a) Nyquist-plot obtained by EIS measurement of $Li_{4-3x}Sc_xP_2S_6$ with equivalent circuit fit. Ru metal was sputtered on adjacent faces of the pellet to reduce contact resistance. Fitted values for R_{SE}, CPE_{int} and CPE_{pol} are tabulated in Table A.8 (Appendix A). (b) Bond valence energy landscape of $Li_{2.926}Sc_{0.358}P_2S_6$ (single crystal data) at isoenergy value of $-4.5\,eV$ ($E_{min} = -6.6\,eV$). Li drawn in green, Sc drawn in purple, S drawn in yellow.

The lithium trajectory within the structure was modeled by exploring the bond valence energy landscape (BVEL) of $Li_{2.926}Sc_{0.358}P_2S_6$ (Figure 4.8b) using the program 3DBVSMAPPER (see Experimental Section). The calculation suggests that an octahedral-

tetrahedral-octahedral (O–T–O) trajectory of lithium ion movement within the *ab* plane *via* face-sharing (occupied) octahedra and (unoccupied) tetrahedra (see Figure 4.8b) is possible. Lithium conduction through the layers (in *c* direction) is prohibited by partial occupation of Li sites by Sc^{3+} due to electrostatic repulsion during Li^+ movement, rendering this material a 2D ion conductor. Electrochemical impedance spectra of monoclinic *m*- and trigonal *t*-$LiScP_2S_6$ are given in Figure A.5 (Appendix A). The conductivity of both phases is measured to be less than $10^{-9}\,S\,cm^{-1}$. This can be explained by the full occupation of Li sites within the layered structure, prohibiting more facile Li ion hopping between otherwise partially occupied sites as in $Li_{2.926}Sc_{0.358}P_2S_6$. The calculated lithium ion pathways in the *m*- and *t*-phase can be best described with an octahedral-octahedral-tetrahedral-octahedral-octahedral (O_l–O_i–T_i–O_i–O_l) trajectory, as shown in Figure A.4 (Appendix A). At low energies (see Figure A.4, e and f) Li ions can diffuse from (intra-)layer octahedral sites (O_l) to interlayer octahedral (O_i) vacancies through a shared-face. Higher energies (Figure A.4, i and j) open up a pathway between two edge-sharing O_i sites, which share faces with an interlayer tetrahedral site (T_i). The network of Li ion motion is per se three-dimensional; however we expect high activation energies for O_i–T_i–O_i hopping to inhibit a significant long-range dc conductivity in both structures, as confirmed by our measurements.

4.4 Conclusions

Three new lithium-scandium hexathiohypodiphosphates(IV) were synthesized and characterized. The crystal structures, ionic conductivity and Raman scattering was investigated and the stability of the $LiScP_2S_6$ modifications was probed by DFT modeling. The compounds exist in three different structure types (see Table A.4, Appendix A). They complete the structural stability diagram of $ALnP_2S_6$ compounds (A = Na, K, Rb, Cs; Ln = lanthanide).[7] All three contain isolated ethane-like $P_2S_6^{4-}$ hexathiohypodiphosphate(IV) building blocks. In contrast, the high temperature phase *t*-$LiScP_2S_6$ contains a previously unidentified disordered version of the $P_2S_6^{4-}$anion. We thus refer to this anion as $[P_{2/2}P_{6/6}S_6]^{4-}$. From DFT modeling both *m*- and the disordered *t*-$LiScP_2S_6$ are predicted to be less stable than a yet unknown ordered version of the trigonal modification, which would be isotypic to $AgScP_2S_6$. The Raman spectra of the three lithium-scandium hexathiohypodiphosphates show the most characteristic signal at $390\,cm^{-1}$, which can be assigned to the A_{1g} symmetric stretch of the ethane-like $P_2S_6^{4-}$anion. HT-XRD measurements show that *m*-$LiScP_2S_6$ transforms between 500 °C and 700 °C into *t*-$LiScP_2S_6$. DTA and DSC-measurements indicate that the three compounds decompose between 800 and 840 °C. *t*-$LiScP_2S_6$ and *m*-$LiScP_2S_6$ are bad ionic conductors at room temperature (less than $10^{-9}\,S\,cm^{-1}$), whereas $Li_{4-3x}Sc_xP_2S_6$ shows a significant increase in Li^+ conductivity compared to the parent compound $Li_4P_2S_6$. Simple structure-property relationships reveal that cationic disorder in $Li_{2.926}Sc_{0.358}P_2S_6$ is responsible for the improved ionic conductivity in comparison to both $LiScP_2S_6$ modifications, which comprise fully occupied Li and Sc positions only.

4.5 Experimental section

4.5.1 Synthesis

All preparations and manipulations were carried out in an argon atmosphere. For the solid state reactions, Li_2S (Alfa Aesar,99.9%), P_2S_5 (Acros, 98+%), S (Alfa Aesar, 99.5%), and Sc (Johnson Matthey, pieces, distilled dendritic, 99.99%) were vacuum-sealed in uncoated quartz tubes (length: 200 mm, inside diameter: 10 mm). It is also possible to synthesize $LiScP_2S_6$ from the elements [Li granules (Alfa Aesar, 99%), red P (Alfa Aesar, 98.9%), S (Alfa Aesar, 99.5%), and Sc (Johnson Matthey, pieces, distilled dendritic, 99.99%)]. The three $LiScP_2S_6$ phases are extremely moisture sensitive and must be stored and handled under inert conditions. To prevent damaging of the sealed quartz tube due the initial strongly exothermic reaction the intimately mixed starting material was additionally placed inside a small quartz container (length: 80 mm, out-side diameter: 8 mm). All products were characterized with single-crystal X-ray diffraction (SXRD) and powder X-ray diffraction(PXRD), and the composition (without lithium) was confirmed by scanning electron microscopy coupled with energy-dispersive X-ray analysis (SEM-EDX) spectroscopy.

4.5.2 X-ray diffraction

Powder X-ray diffraction patterns were measured in sealed glass capillaries with a STOE StadiP diffractometer working with Ge-monochromatic Mo-K_α radiation in Debye-Scherrer setup. Single crystals suitable for single-crystal X-ray diffraction were picked under a microscope in dried petroleum and mounted into sealed glass capillaries for single-crystal X-ray diffraction measurements. Single crystal X-ray diffraction of $Li_{2.927}Sc_{0.358}P_2S_6$ was carried out with a SMART-APEX CCD X-ray diffractometer (Bruker AXS) working with graphite-monochromated Mo-K_α radiation. For the integration of the reflections, the SAINT software (Bruker AXS) was used. The data collection of *m*-$LiScP_2S_6$ and *t*-$LiScP_2S_6$ was performed with a STOE IPDS II working with graphite-monochromatic Mo-K_α radiation. Integration of the reflection intensities and calculation of the reciprocal lattice planes was performed using the STOE X-Area 1.56 software. The structure was solved with Direct Methods and refined by least-squares fitting using the SHELXTL program.[53] Crystallographic data (excluding structure factors) for the structures in this paper have been deposited with the Cambridge Crystallographic Data Centre, CCDC, 12 Union Road, Cambridge CB21EZ, UK. Copies of the data can be obtained free of charge on quoting the depository numbers CCDC-1864274 ($Li_{2.926}Sc_{0.358}P_2S_6$) CCDC-1864273 (*t*-$LiScP_2S_6$), and CCDC-1864272 (*m*-$LiScP_2S_6$) (Fax: +44-1223-336-033; E-Mail: deposit@ccdc.cam.ac.uk, http://www.ccdc.cam.ac.uk).

4.5.3 Raman spectroscopy

The Raman spectra were recorded with a JobinYvon Typ V 010 Labram single grating spectrometer, equipped with a double super razor edge filter and a peltier cooled CCD camera. The resolution of the spectrometer (grating 1800 Lines/mm) was 1 cm^{-1}.

4.5.4 Electrochemical impedance spectroscopy Measurements

Electrochemical impedance spectroscopy (EIS) measurements were performed to determine the ionic and electronic conductivity of the Li^+ containing phases. An impedance-analyzer Alpha-A (Novocontrol Technologies), interfaced with a computer was used to measure impedance of the $LiScP_2S_6$ phases in the frequency range of 0.1 Hz to 1 MHz and a root-mean-square AC amplitude of 100 mV. Approximately 30–60 mg of the phase-pure compound were thoroughly ground, pressed into 5 mm diameter pellets (> 90% geometrical density) and sandwiched between two lithium ion blocking polished steel electrodes employing a TSC Battery cell (RHD Instruments). The spring-loaded cell was maintained at 3.5 bar to ensure good contact between the sample and the electrodes. Impedance data was analyzed using the RelaxIS 3.0 software (RHD Instruments). Proportional weighting method was used to fit the equivalent circuits shown in Table A.8 (Appendix A). Kramers-Kronig tests were performed to test data reliability before fitting.

4.5.5 DTA/DSC measurements

DTA and DSC measurements have been used to determine the thermal behavior and the decomposition of the $LiScP_2S_6$ phases. For this purpose we worked under inert atmospheres in sealed quartz containers with home-built equipment (DTA)[23] and a 404 F1 Pegasus DSC from NETZSCH. DSC measurements were performed in flowing argon with the following temperature profile: heat 10 K min^{-1} to 600 °C, dwell 2 h at 600 °C, heat 2 K min^{-1} to 900 °C.

4.5.6 HT-XRD measurements

HT-XRD diffraction patterns were recorded in sealed quartz capillaries with a D8-Advance (Bruker) diffractometer working with Ge(220) monochromated Mo-$K_{\alpha 1}$ radiation ($\lambda = 70.930$ pm), equipped with a Lynx-Eye 1 mm detector.

4.5.7 EDX analyses

Several single crystals were mounted on carbon tape and measured with a Tescan SEM (Vega TS 5130 MM) equipped with a SDD (silicon drift detector, Oxford).

4.5.8 DFT calculations

Quantum chemical calculations were performed in the framework of density functional theory (DFT) using a linear combination of Gaussian-type functions (LCGTF) Scheme as implemented in CRYSTAL17.[54,55] Due to the layered nature of the investigated compounds Grimmes D3 dispersion correction was included in the modeling.[56] The total energy calculations including full structural optimizations were performed with the GGA (PBE)[57] *xc*-functional. The convergence criterion considering the energy was set to $1 \cdot 10^{-8}$ a.u. with a *k*-mesh sampling of $12 \times 12 \times 12$. All-electron basis sets for Li, P, and S were taken from references[58–60] and a pseudo potential Hay-Wadt basis set was used for Sc.[61] The vibrational frequencies including Raman intensities were computed

on the basis of the relaxed structures using the coupled-perturbed Kohn-Sham(CPKS) mode.[62,63] Vibrational modes were visualized with the *J-ICE* application.[64]

4.5.9 BVEL calculations

Bond valence energy landscape (BVEL) calculations were performed using the free-ware program 3DBVSMAPPER, that is based on soft-bond-valence parameters and additional (penalty)terms to convert bond valence sum (BVS) mismatch into an energy scaled map.[65] The cutoff distance used for the BVS calculations was fixed to a maximum value of 8 Å. The BVEL method in the 3DBVSMAPPER program is operating as follows: (i) Removal of all low occupancy atoms (SOF < 0.05). (ii) Removal of the mobile ion(here Li). (iii) Generation of a 3D grid (here 0.05 Å for $Li_{2.926}Sc_{0.358}P_2S_6$ and 0.2 Å for *m*-, *t*-$LiScP_2S_6$) covering the unit cell. (iv) Calculation of BVEL term at each grid point. (v) Analysis of the calculated result (volume and surface area of connected isosurface). (vi) Generation of volumetric data file (grd). As a consequence of this operation the following constraints of this method are: (i) Relaxation of the anionic sublattice during ion movement is not considered. The activation energies for conduction are therefore overestimated. (ii) Ions of same charge as the tested ion exhibit a strong repulsion towards the test ion. Mixed occupied sites of the test ion and other ions strongly inhibit conduction pathways. (iii) Removal of all examined ions (here Li) entail missing repulsion of mobile ions during conduction. Despite these constrains both BVS and BVEL have proven to be a valid empirical tool to describe diffusion paths in ionic solids.[66]

References

(1) Janek, J.; Zeier, W. G. *Nat. Energy* **2016**, *1*, 16141.

(2) Lotsch, B. V.; Maier, J. *J. Electroceramics* **2017**, *38*, 128–141.

(3) Knauth, P. *Solid State Ion.* **2009**, *180*, 911–916.

(4) Yao, X.; Huang, B.; Yin, J.; Peng, G.; Huang, Z.; Gao, C.; Liu, D.; Xu, X. *Chin. Phys. B* **2016**, *25*, 018802.

(5) Takada, K. *Acta Mater.* **2013**, *61*, 759–770.

(6) Wang, Y.; Richards, W. D.; Ong, S. P.; Miara, L. J.; Kim, J. C.; Mo, Y.; Ceder, G. *Nat. Mater.* **2015**, *14*, 1026–1031.

(7) Schoop, L. M.; Eger, R.; Kremer, R. K.; Kuhn, A.; Nuss, J.; Lotsch, B. V. *Inorg. Chem.* **2017**, *56*, 1121–1131.

(8) Schoop, L. M.; Eger, R.; Nuss, J.; Pielnhofer, F.; Lotsch, B. V. *Z. Anorg. Allg. Chem.* **2017**, *643*, 1818–1823.

(9) Wu, Y.; Bensch, W. *Cryst. Eng. Comm.* **2010**, *12*, 1003–1015.

(10) Lee, S.; Colombet, P.; Ouvrard, G.; Brec, R. *Inorg. Chem.* **1988**, *27*, 1291–1294.

(11) Seidlmayer, S. Strukturchemische Untersuchungen an Hexachalkogenohypodiphosphaten und verwandten Verbindungen, Dissertation, 2010.

(12) Jörgens, S.; Alili, L.; Mewis, A. *Z. Naturforsch. B* **2005**, *60*, 705–708.

(13) Komm, T.; Schleid, T. *J. Alloys Compd.* **2006**, *418*, 106–110.

(14) T. Komm, T. S. *Z. Kristallogr. Suppl.* **2005**.

(15) Müller, C.; Jörgens, S.; Mewis, A. *Z. Anorg. Allg. Chem.* **2007**, *633*, 1633–1638.

(16) Tachez, M.; Malugani, J.-P.; Mercier, R.; Robert, G. *Solid State Ion.* **1984**, *14*, 181–185.

(17) Dietrich, C.; Weber, D. A.; Culver, S.; Senyshyn, A.; Sedlmaier, S. J.; Indris, S.; Janek, J.; Zeier, W. G. *Inorg. Chem.* **2017**, *56*, 6681–6687.

(18) Dietrich, C.; Sadowski, M.; Sicolo, S.; Weber, D. A.; Sedlmaier, S. J.; Weldert, K. S.; Indris, S.; Albe, K.; Janek, J.; Zeier, W. G. *Chem. Mater.* **2016**, *28*, 8764–8773.

(19) Deiseroth, H.-J.; Maier, J.; Weichert, K.; Nickel, V.; Kong, S.-T.; Reiner, C. *Z. Anorg. Allg. Chem.* **2011**, *637*, 1287–1294.

(20) Yamane, H.; Shibata, M.; Shimane, Y.; Junke, T.; Seino, Y.; Adams, S.; Minami, K.; Hayashi, A.; Tatsumisago, M. *Solid State Ion.* **2007**, *178*, 1163–1167.

(21) Sedlmaier, S. J.; Indris, S.; Dietrich, C.; Yavuz, M.; Dräger, C.; Von Seggern, F.; Sommer, H.; Janek, J. *Chem. Mater.* **2017**, *29*, 1830–1835.

(22) Kamaya, N.; Homma, K.; Yamakawa, Y.; Hirayama, M.; Kanno, R.; Yonemura, M.; Kamiyama, T.; Kato, Y.; Hama, S.; Kawamoto, K.; Mitsui, A. *Nat. Mater.* **2011**, *10*, 682–686.

(23) Kuhn, A.; Gerbig, O.; Zhu, C.; Falkenberg, F.; Maier, J.; Lotsch, B. V. *Phys. Chem. Chem. Phys.* **2014**, *16*, 14669–14674.

(24) Xu, R.; Wu, Z.; Zhang, S.; Wang, X.; Xia, Y.; Xia, X.; Huang, X.; Tu, J. *Eur. J. Chem.* **2017**, *23*, 13950–13956.

(25) Ettis, H.; Naïli, H.; Mhiri, T. *J. Solid State Chem.* **2006**, *179*, 3107–3113.

(26) Bykov, A. B.; Chirkin, A. P.; Demyanets, L. N.; Doronin, S. N.; Genkina, E. A.; Ivanov-shits, A. K.; Kondratyuk, I. P.; Maksimov, B. A.; Mel'nikov, O. K.; Muradyan, L. N.; Simonov, V. I.; Timofeeva, V. A. *Solid State Ion.* **1990**, *38*, 31–52.

(27) Amatucci, G. G.; Safari, A.; Shokoohi, F. K.; Wilkens, B. J. *Solid State Ion.* **1993**, *60*, 357–365.

(28) Suzuki, T.; Yoshida, K.; Uematsu, K.; Kodama, T.; Toda, K.; Ye, Z.-G.; Ohashi, M.; Sato, M. *Solid State Ion.* **1998**, *113-115*, 89–96.

(29) Vītiņš, Ģ.; Kaņepe, Z.; Vītiņš, A.; Ronis, J.; Dindūne, A.; Lūsis, A. *J. Solid State Electrochem.* **2000**, *4*, 146–152.

(30) Mounir, F.; Karima, H.-N.; Khaled, B. S.; Mokhtar, F. *Phys. B: Condens. Matter* **2012**, *407*, 2593–2600.

(31) Pradel, A.; Ribes, M. *Solid State Ion.* **1986**, *18-19*, 351–355.

(32) Aotani, N.; Iwamoto, K.; Takada, K.; Kondo, S. *Solid State Ion.* **1994**, *68*, 35–39.

(33) Souquet, J. L.; Robinel, E.; Barrau, B.; Ribes, M. *Solid State Ion.* **1981**, *3-4*, 317–321.

(34) Kennedy, J. H.; Zhang, Z. *J. Electrochem. Soc.* **1988**, *135*, 859–862.

(35) Toffoletti, L.; Kirchhain, H.; Landesfeind, J.; Klein, W.; van Wüllen, L.; Gasteiger, H. A.; Fässler, T. F. *Chem. Eur. J.* **2016**, *22*, 17635–17645.

(36) Hood, Z. D.; Kates, C.; Kirkham, M.; Adhikari, S.; Liang, C.; Holzwarth, N. *Solid State Ion.* **2016**, *284*, 61–70.

(37) Mizuno, F.; Hayashi, A.; Tadanaga, K.; Tatsumisago, M. *Solid State Ion.* **2006**, *177*, 2721–2725.

(38) Takada, K. *Solid State Ion.* **2002**, *147*, 23–27.

(39) Deiseroth, H.-J.; Kong, S.-T.; Eckert, H.; Vannahme, J.; Reiner, C.; Zaiß, T.; Schlosser, M. *Angew. Chem. Int. Ed.* **2008**, *47*, 755–758.

(40) Kuhn, A.; Köhler, J.; Lotsch, B. V. *Phys. Chem. Chem. Phys.* **2013**, *15*, 11620.

(41) Kato, Y.; Hori, S.; Saito, T.; Suzuki, K.; Hirayama, M.; Mitsui, A.; Yonemura, M.; Iba, H.; Kanno, R. *Nat. Energy* **2016**, *1*, 16030.

(42) Takada, K. *Solid State Ion.* **2003**, *159*, 257–263.

(43) Lang, G. *Z. Anorg. Allg. Chem.* **1954**, *276*, 77–94.

(44) McDaniel, C. L. *J. Solid State Chem.* **1974**, *9*, 139–146.

(45) Kuhn, A.; Eger, R.; Nuss, J.; Lotsch, B. V. *Z. Anorg. Allg. Chem.* **2013**, *639*, 1087–1089.

(46) Klingen, W.; Ott, R.; Hahn, H. *Z. Anorg. Allg. Chem.* **1973**, *396*, 271–278.

(47) Klingen, W.; Eulenberger, G.; Hahn, H. *Z. Anorg. Allg. Chem.* **1973**, *401*, 97–112.

(48) Ouili, Z.; Leblanc, A.; Colombet, P. *J. Solid State Chem.* **1987**, *66*, 86–94.

(49) Pfeiff, R.; Kniep, R. *J. Alloys Compd.* **1992**, *186*, 111–133.

(50) Evenson; Dorhout, P. K. *Inorg. Chem.* **2001**, *40*, 2884–2891.

(51) Pätzmann, U.; Brockner, W. *Z. Naturforsch. A* **1987**, *42*, 593–596.

(52) Wu, Y.; Bensch, W. *J. Solid State Chem.* **2009**, *182*, 471–478.

(53) Sheldrick, G. M. *Acta Crystallogr.* **2008**, *A64*, 112–122.

(54) Dovesi, R.; Erba, A.; Orlando, R.; Zicovich-Wilson, C. M.; Civalleri, B.; Maschio, L.; Rérat, M.; Casassa, S.; Baima, J.; Salustro, S.; Kirtman, B. *Wiley Interdiscip. Rev. Comput. Mol. Sci.* **2018**, *8*, e1360.

(55) Dovesi, R. et al. CRYSTAL17 User's Manual, Manuscript, 2017.

(56) Grimme, S.; Antony, J.; Ehrlich, S.; Krieg, H. *J. Chem. Phys.* **2010**, *132*, 154104.

(57) Perdew, J. P.; Burke, K.; Ernzerhof, M. *Phys. Rev. Lett.* **1996**, *77*, 3865–3868.

(58) Sophia, G.; Baranek, P.; Sarrazin, C.; Rerat, M.; Dovesi, R. Li_5–11(1d)G_baranek_ 2013_LiNbO3, `http://www.crystal.unito.it/Basis_Sets/lithium.html`, Web Page, 2013.

(59) Zicovich-Wilson, C. M.; Bert, A.; Roetti, C.; Dovesi, R.; Saunders, V. R. *J. Chem. Phys.* **2002**, *116*, 1120–1127.

(60) Lichanot, A.; Aprà, E.; Dovesi, R. *Phys. Status Solidi B* **1993**, *177*, 157–163.

(61) Bredow, T.; Jug, K.; Evarestov, R. A. *Phys. Status Solidi B* **2006**, *243*, R10–R12.

(62) Ferrero, M.; Rérat, M.; Orlando, R.; Dovesi, R. *J. Comput. Chem.* **2008**, *29*, 1450–1459.

(63) Ferrero, M.; Rérat, M.; Kirtman, B.; Dovesi, R. *J. Chem. Phys.* **2008**, *129*, 244110.

(64) Canepa, P.; Hanson, R. M.; Ugliengo, P.; Alfredsson, M. *J. Appl. Crystallogr.* **2011**, *44*, 225–229.

(65) Sale, M.; Avdeev, M. *J. Appl. Cryst.* **2012**, *45*, 1054–1056.

(66) Avdeev, M.; Sale, M.; Adams, S.; Rao, R. P. *Solid State Ion.* **2012**, *225*, 43–46.

CHAPTER 5

Phase formation through synthetic control: polymorphism in the sodium-ion solid electrolyte $Na_4P_2S_6$

Tanja Scholz, Christian Schneider*, Roland Eger, Viola Duppel, Igor Moudrakovski, Armin Schulz, Jürgen Nuss and Bettina Valeska Lotsch*
*Equal contribution to this work

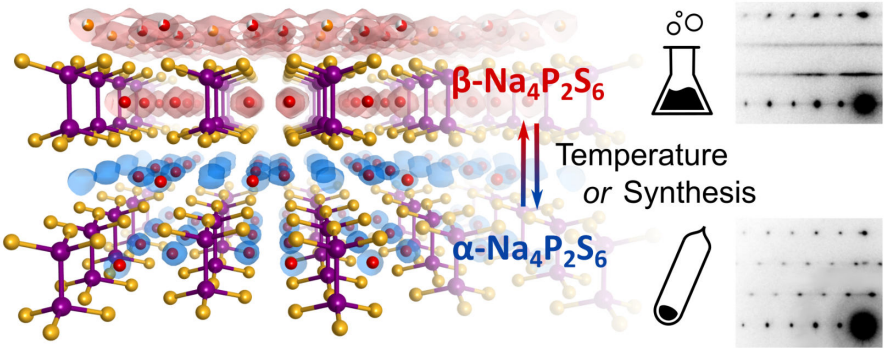

This work was published in and adopted from:
Journal of Materials Chemistry A **2021**, *9*, 8692-8703.

Supporting information can be found in Appendix B.
Author contributions can be found in Appendix F.

Contents of Chapter 5

5.1 Abstract

The development of all-solid-state sodium batteries for scalable energy storage solutions requires fast sodium conducting solid electrolytes. To fast-track their discovery, candidate materials need to be identified that are synthesized from abundant resources *via* cheap and green synthesis routes. Their ion conducting mechanism has to be understood and adapted to meet the stringent requirements for long-term operation in all-solid-state batteries. Here, structure and properties of the sodium hexathiohypodiphosphate $Na_4P_2S_6$ obtained by two different synthesis methods are compared: a solid-state reaction and a precipitation route from aqueous solution. Combined investigations using powder X-ray diffraction (PXRD), precession electron diffraction (PED), differential scanning calorimetry (DSC), solid-state nuclear magnetic resonance spectroscopy (ssNMR), and Raman spectroscopy reveal that the solid-state synthesized material is characterized by a Na^+ and vacancy disorder-driven enantiotropic phase transition at 160 °C (α- to β-$Na_4P_2S_6$), which is accompanied by a symmetry change of the $P_2S_6^{4-}$ anion. Precipitated $Na_4P_2S_6$ already crystallizes in a β-like polymorph at room temperature, likely assisted by inter- and intralayer defects. Bond-valence and nudged elastic band (NEB) calculations were employed to identify a low energy, 2D conduction network in β-$Na_4P_2S_6$, suggesting facile 2D long-range Na^+ diffusion. Electrochemical impedance spectroscopy reveals a higher ionic conductivity at room temperature in precipitated β-like $Na_4P_2S_6$ ($2 \cdot 10^{-6}\,S\,cm^{-1}$) compared to the solid-state α polymorph ($7 \cdot 10^{-7}\,S\,cm^{-1}$). The activation energy is around 0.4 eV for both materials. The findings highlight that even subtle structural changes can significantly impact the sodium-ion diffusion in solid electrolytes and at the same time reveal an intricate interplay between phase formation and synthetic control.

5.2 Introduction

All-solid-state batteries based on solid electrolytes as core components have emerged as potential alternatives to state-of-the-art lithium ion batteries that have become indispensable in powering our modern-day society. Especially in the critical areas of electromobility and renewable energy storage where conventional concepts cannot keep up with the ever-growing energy requirements, solid-state batteries promise improved power and energy density as well as safety and versatile cell geometries. For some applications such as stationary, large-scale energy storage where the critical geo-political abundance and cost of lithium are the most pressing issues, rechargeable sodium-ion batteries promise to be a viable alternative. This has revitalized intense research on sodium-ion conducting materials for solid electrolytes.[1–3] However, in order to increase the number of competitive Na^+ solid electrolytes, candidate materials need to be identified that are synthesized from abundant resources (*e.g.* sulfur and phosphorus) *via* cheap and green synthesis routes, and their ion conduction mechanisms need to be understood and adapted to meet the stringent requirements for long-term operation in all-solid-state batteries.

Historically, well-known Na^+ solid electrolytes are Na-β-Al_2O_3[4] and the NaSICON family[5,6] that both typically use operating temperatures of about 300 °C to provide sufficiently high ion mobilities.[3] In the last years, superionic polyborates of closo-borate anions $B_nH_n^{2-}$ such as $Na_2(B_{12}H_{12})_{0.5}(B_{10}H_{10})_{0.5}$ have attracted much attention as they

offer promising room temperature conductivities as high as $0.9\,\mathrm{mS\,cm^{-1}}$.[7,8]

A new direction in Na^+ solid electrolyte research opened up in 2012 when Hayashi *et al.* described the stabilization of the cubic β-sodium ortho-thiophosphate Na_3PS_4 phase in a "glass-ceramic" state at ambient temperature with an ionic conductivity of $0.2\,\mathrm{mS\,cm^{-1}}$ to $0.46\,\mathrm{mS\,cm^{-1}}$.[9–11] That is an improvement by two orders of magnitude compared to the thermodynamically stable tetragonal α-Na_3PS_4 phase.[12] Only recently, this compound hit yet another milestone when a second high temperature polymorph (γ) was described as a plastic crystal.[13] The potential of thiophosphates as a material class for solid electrolytes is reflected in numerous studies that were able to further improve the ionic conductivity by substitution of phosphorus or sulfur in tetrahedral PS_4^{3-}.[14–18] Structural expansion, changing the polarizability, and creating Na^+ interstitials and vacancies through iso- or aliovalent doping are common concepts to enhance ion mobility. $Na_{2.9}P_{0.9}W_{0.1}S_4$ and $Na_{2.9}Sb_{0.9}W_{0.1}S_4$ are the fastest ion conductors derived from the parent compound Na_3PS_4 known today with conductivities of $13\,\mathrm{mS\,cm^{-1}}$ and $41\,\mathrm{mS\,cm^{-1}}$, respectively.[19,20]

As portrayed by these works, the sodium thiophosphate family is a powerful material class for fast ion conduction and, more importantly, already proved functional in all-solid state batteries.[9,10] Recently, Fritsch *et al.* studied the ionic conductivity and local structure of the sodium hexathiometadiphosphate $Na_2P_2S_6$[21] with a conductivity of $10^{-8}\,\mathrm{S\,cm^{-1}}$ in the amorphous material obtained by a ball milling synthesis compared to $10^{-11}\,\mathrm{S\,cm^{-1}}$ in the crystalline compound.[22] The enhanced conductivity in the amorphous materials arises from sodium disorder and single PS_4^{3-} tetrahedra incorporated in addition to $P_2S_6^{2-}$. Another superionic sulfide-based electrolyte with thiophosphate and thiostannate anions is $Na_{11}Sn_2PS_{12}$.[23,24] Its high conductivity of $4\,\mathrm{mS\,cm^{-1}}$ originates from significant intrinsic Na^+ vacancies and a large variety of alternative three-dimensional pathways with similar migration barriers along different directions.

Sodium hexathiohypodiphosphate $Na_4P_2S_6$, the compound discussed in this publication, was first mentioned in a study on precipitated $Na_4P_2S_6 \cdot 6\,H_2O$ as its dehydration product.[25] The crystal structure was reported later by our group where $Na_4P_2S_6$ was obtained *via* a solid-state synthesis.[21] The main characteristic of the monoclinic structure is a layered arrangement of $P_2S_6^{4-}$ anions in planes with an [ABC] stacking (*cf.* Figure 5.1a and Appendix B). In these planes and between them are two crystallographically different sodium ions, coordinated octahedrally by sulfur atoms. The molecular axes of the $P_2S_6^{4-}$ anions are tilted by 4° from the layer normal while they are parallel in related compounds like $FePS_3$. The $P_2S_6^{4-}$ layer is reminiscent of a hexagonal pattern. This structure is unique among the alkali hexathiohypodiphosphates $A_4P_2S_6$: $Li_4P_2S_6$ is also a layered structure but with an [AA] stacking resulting in a different distribution of alkali ions between the layers, whereas $K_4P_2S_6$ and $Rb_4P_2S_6$ exhibit three-dimensional structures.[21,26] Rush *et al.* modeled the Na^+ ion dynamics of $Na_4P_2S_6$ with DFT calculations and estimated a low activation energy of $E_a \approx 0.4\,\mathrm{eV}$.[27] A more recent comprehensive DFT study of the same group emphasizes the potential of $Na_4P_2S_6$ as Na^+ ionic conductor, stresses the low activation energy of the material, and reveals considerable Na^+ ion motion in two dimensions in MD simulations.[28] Indeed, for precipitated $Na_4P_2S_6$ (*via* the hydrate) Hood showed a room temperature conductivity of $3.4 \cdot 10^{-6}\,\mathrm{S\,cm^{-1}}$ with $E_a = 0.35\,\mathrm{eV}$ and pointed out that rehydration and subsequent dehydration does not impact the electrochemical performance, making this compound more compliant with battery applications.[29] Based on our study, we assume that $Na_4P_2S_6$ prepared by Hood is

similar to our precipitated β-like samples.

In this paper, we compare the structure and properties of $Na_4P_2S_6$ obtained by different synthesis routes and describe a new high-temperature polymorph (β) that has significant intrinsic Na^+ vacancies and forms above 160 °C when synthesized *via* a solid-state route according to Ref. [21] . Combined investigations using powder X-ray diffraction (PXRD), differential scanning calorimetry (DSC), precession electron diffraction (PED), solid-state nuclear magnetic resonance spectroscopy (ssNMR), and Raman spectroscopy reveal that precipitated $Na_4P_2S_6$ *via* solution synthesis (*cf.* Ref. [25]), however, already crystallizes in a β-like polymorph at room temperature which is stabilized by subtle structural defects, *e.g.* stacking faults. A comprehensive mechanistic study based on bond valence energy landscape (BVEL) and nudged elastic band (NEB) calculations pinpoint how the ionic conductivity is influenced by structural changes upon the phase transition and the presence of Na^+ vacancies. Electrochemical impedance spectroscopy measurements portray precipitated β-like $Na_4P_2S_6$ as an ion conductor with a room-temperature conductivity of $2 \cdot 10^{-6}\,S\,cm^{-1}$ and an activation energy of 0.4 eV while solid-state α-$Na_4P_2S_6$ has a lower conductivity of $7 \cdot 10^{-7}\,S\,cm^{-1}$ with a similar activation energy.

5.3 Results and discussion

5.3.1 Polymorphism in $Na_4P_2S_6$

As a starting point to elucidate the phase formation and polymorphism of $Na_4P_2S_6$, we synthesized $Na_4P_2S_6$ *via* two alternative synthesis routes—a solid-state route[21] and by precipitation from aqueous solution.[25] The high-temperature behavior of the as-obtained materials was investigated by PXRD (Figure 5.1b, c). For the solid-state thiophosphate a phase transition appears at around 200 °C with a splitting of the reflection at 7° 2θ (Mo $K\alpha_1$, indices (0 2 0) and (1 1 0)). The structure of this new high-temperature polymorph, dubbed β-$Na_4P_2S_6$, is closely related to the low-temperature polymorph and crystallizes in the same space group $C2/m$ (Figure 5.1a). The phase transition is primarily characterized by the occupation of a new sodium position (Na3, Wyckoff position $2d$) at the expense of Na2. The $2d$ position is an unoccupied, distorted S_6 octahedral void in the α phase's van der Waals gap. Therefore, the phase transition generates an exceptionally high amount of intrinsic Na^+ vacancies. Further, subtle structural changes such as in the distances and tilting of the $P_2S_6^{4-}$ anions occur, which we discuss in detail below. Recently, Li *et al.* computationally predicted the $2d$ position to be the energetically most favorable interstitial site.[28] Their MD simulations already suggest an involvement of this site in the Na^+ migration path, and we present here experimental proof for the occupation of the Na3 position at elevated temperatures. Empty voids are also present in the structure of $Li_4P_2S_6$, but they are capped by the $P_2S_6^{4-}$ anion and their occupation is energetically much more unfavorable.[26] β-$Na_4P_2S_6$ is still observed at 500 °C and the α–β transition is reversible upon cooling.

The precipitation route also gives a crystalline $Na_4P_2S_6$ solid that is, however, characterized by broad reflections in the PXRD pattern that do not allow for the α–β differentiation. Upon heating no phase transition can be tracked by PXRD until about 500 °C where sharp reflections of the β phase occur. Cooling back to room temperature,

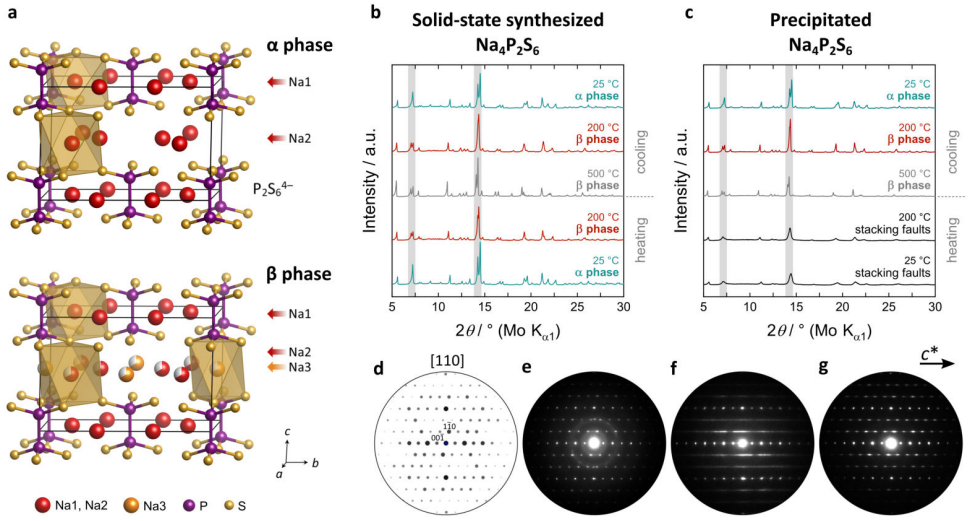

Figure 5.1: (a) Crystal structure of solid-state synthesized $Na_4P_2S_6$ in the monoclinic space group $C2/m$ (no. 12) at room temperature (α) and high temperature (β) with a layered arrangement of $P_2S_6^{4-}$ (P: purple, S: yellow). Sodium atoms (red and orange) are coordinated octahedrally by sulfur atoms. (b), (c) HT-XRD patterns of solid-state and precipitated $Na_4P_2S_6$ with shaded regions to differentiate between the polymorphs. (d) Simulated PED pattern in comparison to measured PED patterns of (e) sublimed (representing the solid-state material), (f) precipitated, and (g) annealed $Na_4P_2S_6$.

however, the α phase develops into the annealed material. To unravel the differences of solid-state, precipitated, and annealed $Na_4P_2S_6$, we recorded PED patterns that are presented in Figure 5.1d-g. Note that the PED pattern of the solid-state $Na_4P_2S_6$ was obtained from a sample that was additionally sublimed at 750 °C, since the recording of the desired direction was not feasible in the raw solid-state reaction product. This sample shows sharp reflections that are in agreement with those of a simulated pattern along the [110] zone axis. Contrary, diffuse scattering occurs as streaks in precipitated $Na_4P_2S_6$. This indicates the presence of planar defects, which are located in the c direction, the stacking direction of the crystal structure. These defects modulate the layer distance and can stem from *e.g.* stacking faults, residual crystal water, and/or thiophosphate disorder. The remaining sharp reflections agree with the simulated pattern. The defects are largely healed in the annealed sample where the diffuse scattering is reduced in intensity and reflections become visible and are comparable to the solid-state product.

With the structural differences of the two synthesized samples roughly understood, DSC measurements, ssNMR experiments, and Raman spectroscopy were carried out to follow the α–β phase transition and elucidate the subtle structural differences.

Differential scanning calorimetry

DSC curves were recorded between 80 and 300 °C in three consecutive runs and are illustrated in Figure 5.2a-c. Upon heating, solid-state α-$Na_4P_2S_6$ shows an endothermic signal composed of two convoluted peaks, a small one followed by a larger peak. The latter has an onset temperature of 160 °C. The combined exchanged heat of both peaks is 10 ± 1 J g^{-1}. Cooling down the sample, the corresponding β to α transition occurs as a sharp exothermic peak with an onset of 160 °C. Again two peaks are convoluted. However, upon cooling the larger peak appears first. The measured thermogram is completely reversible upon cycling, suggesting an enantiotropic phase transition. Since thermal effects could stem from rearrangements of anions or reshuffling of site occupancies to allow the structure to relax into a lower energy polymorph, we attribute the signals in the solid-state material to be of such a structural transition.

Precipitated $Na_4P_2S_6$ shows a very different DSC thermogram, in fact, no sharp exothermic nor endothermic signal can be measured, suggesting that the phase transition is suppressed and that a β-like structure is stabilized already at room temperature. This observation holds for multiple cycles around the expected transition temperature.

In the above diffraction experiments annealed $Na_4P_2S_6$ appears "healed" from stacking faults, however, its DSC signal shows no sharp peak around the temperature where we observe a signal for solid-state $Na_4P_2S_6$, but rather a sharp kink of the DSC signal around 150 °C, compared to the precipitated sample shown in Figure 5.2b. Cooling the sample, a smeared out thermal event appears at around 140 °C, indicated by a black arrow in Figure 5.2c. Since this broad peak is absent in the precipitated sample, we assume it to originate from a sluggish phase transition with a low exchanged heat. This suggests a material with structural properties midway between those of the solid-state and precipitated samples.

Solid-state nuclear magnetic resonance spectroscopy

ssNMR experiments were conducted at room temperature to elucidate the local environment of sodium by ^{23}Na magic angle spinning (MAS) NMR; the anionic thiophosphate sublattice as well as (thio-)phosphate impurities are revealed by ^{31}P MAS NMR. The spectra of the solid-state α, precipitated β-like, and annealed $Na_4P_2S_6$ are depicted in Figure 5.2d-i. The fits of the ^{23}Na MAS NMR spectra yield two signals for both the solid-state and the precipitated sample, and three signals for the annealed $Na_4P_2S_6$. Two different sodium positions of equal occupation are expected from the crystal structure of solid-state synthesized α-$Na_4P_2S_6$.[21] The fitted integral ratio of 50% (Na1) to 50% (Na2) for the solid-state material, therefore, reflects the previously reported structure.[21] The two resonance peaks at $\delta_{iso} = 18.2$ ppm and $\delta_{iso} = 5.6$ ppm were fitted with a model accounting for second order quadrupolar line broadening ($I = \frac{2}{3}$ ^{23}Na nucleus), observed especially for the signal at $\delta_{iso} = 5.6$ ppm. We assign these two resonances to the crystallographic positions Na1, residing in a symmetrical environment in the $P_2S_6^{4-}$ layer, and the less symmetrically coordinated Na2 site, indicated by the larger quadrupolar coupling constant, in the interlayer space, respectively (*cf.* Figure 5.1a). For the discussion of the ^{31}P spectra we make use of the short range order (SRO) notation for phosphate compounds as described by Kmiec *et al.*[30] Besides the main resonance at $\delta_{iso} = 112.9$ ppm ($P_2S_6^{4-}$, P^{1P}), the ^{31}P MAS spectrum of solid-state $Na_4P_2S_6$ reveals one small additional

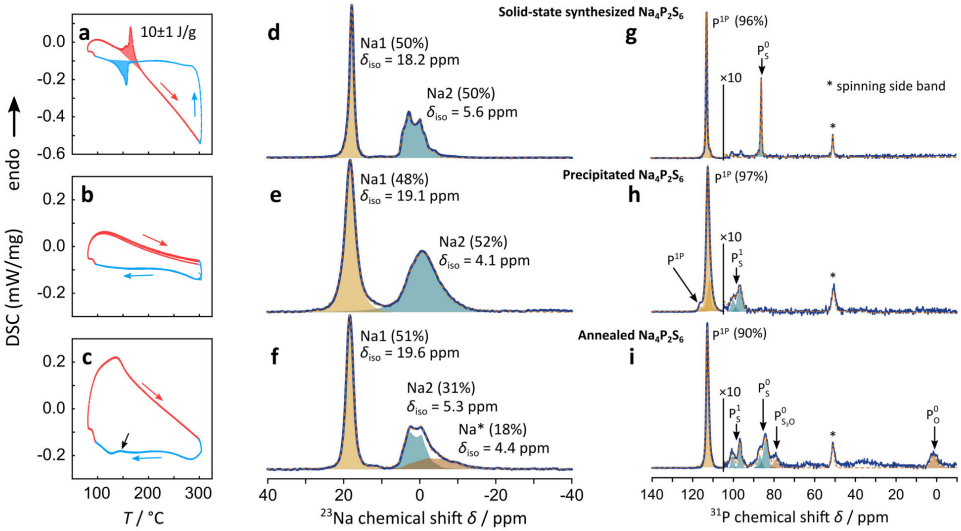

Figure 5.2: DSC curves of (a) solid-state α/β, (b) precipitated β-like, and (c) annealed $Na_4P_2S_6$. The three-times consecutively measured heating and cooling scans are depicted in red and blue, respectively. The initial heating scan was discarded. ^{23}Na (d-f) and ^{31}P (g -i) MAS ssNMR spectra of $Na_4P_2S_6$ at room temperature. The measured and calculated spectra are depicted as blue and orange lines, respectively. Fitted peaks are displayed as half-transparent peak areas of different color. The integral ratio is displayed as numbers in parentheses. For the ^{31}P-NMR spectra high field peaks next to the peak for $P_2S_6^{4-}$ are 10-fold magnified.

signal at $\delta_{iso} = 86.7$ ppm. We attribute this to Na_3PS_4 impurities as this chemical shift is characteristic for the ortho-thiophosphate anion PS_4^{3-} (P_S^0).

Comparing the ^{23}Na MAS spectrum of precipitated β-like with solid-state α-$Na_4P_2S_6$ there is one notable difference: The resonance peaks for Na1 and Na2 are clearly broader for the precipitated sample, indicating a more disordered material on the local or long-range scale (*e.g.* differences in the local Na environment, stacking faults, *etc.*). This observation is in line with the TEM study that was performed on sublimed and crude precipitated $Na_4P_2S_6$. The integral ratio of 48% Na1 to 52% Na2 is close to the expected half/half distribution of interlayer and intralayer sodium. The ^{31}P spectrum of precipitated $Na_4P_2S_6$ shows the resonance peak of P^{1P} in addition to two smaller signals with a similar chemical shift. We conclude that the higher disorder produced by the precipitation route leads to slightly different chemical environments not only for the Na^+, but also for the $P_2S_6^{4-}$ anion, which is displayed in the three different P^{1P} resonances. The precipitation route also leads to a small impurity, which is different from the one observed for the solid-state synthesis in the studied batch of material. The chemical shift of around δ_{iso} = 90-100 ppm portends a side phase containing P_S^1 SRO units like in $Na_4P_2S_7$.

Annealing the precipitated $Na_4P_2S_6$ at 500 °C introduces a new ^{23}Na signal as a high-field shifted tail to Na2, in addition to low-field shifting the chemical shifts compared

to the pristine sample. The integral ratio of 51% for the Na1 signal remains close to the expected 50% for this position, whereas the other resonance intensity is shared by Na2 (31%) and the new Na*(18%) signal. The latter signal broadens significantly and is high-field shifted compared to Na2, while the Na1 and Na2 signals show a smaller FWHM, comparable to the values found for the solid-state synthesized sample, indicating a gain in (long range) order upon annealing. The fact that for the annealed sample a third signal with a chemical shift close to the Na2 resonance is present, speaks yet again for a material in between the solid-state and precipitated $Na_4P_2S_6$. Note that also additional resonances arise in the ^{31}P MAS spectrum upon annealing the material. We assign these signals to a variety of thio-, thio/oxo- and oxo-phosphate impurities[30] (about 10% compared to 3% side phase in the precipitated sample). The main ^{31}P signal ($\delta_{iso} = 112.8$ ppm) shows a smaller FWHM and no visible distribution of chemical shifts after annealing the sample.

To summarize, the solid-state synthesis yields the purest material, although a Na_3PS_4 side phase is present and difficult to avoid. Preparing $Na_4P_2S_6$ from solution holds the advantage of an easier synthesis but comes at the cost of higher disorder in addition to a side phase. Assisted by these defects, the precipitated material crystallizes in a β-like polymorph below the α–β phase transition temperature. The subsequent annealing "healed" some degree of disorder, however, at the same time leads to the formation of additional side phases by presumably hydrolytic decomposition. Rapid cooling of the solid-state synthesized and annealed $Na_4P_2S_6$ from a temperature well above the transition point yields solely the α phase.

Raman spectroscopy

Raman spectra give access to the symmetry of the $P_2S_6^{4-}$ anion that is known to either exist in the low symmetric C_{2h} or the highly symmetric, ethane-like D_{3d} configuration (*cf.* Appendix B for details). Selected Raman spectra at different temperatures are shown in Figure 5.3 for an α-$Na_4P_2S_6$ single crystal obtained by the solid-state synthesis and precipitated β-like $Na_4P_2S_6$ powder. For a detailed summary of Raman band positions and their assignments to individual modes refer to Appendix B. At room temperature the Raman spectrum of solid-state $Na_4P_2S_6$ shows at least eleven peaks, of which six can be assigned to bending and stretching modes of the $P_2S_6^{4-}$ anion (marked as shaded regions). Here, the anion resembles its molecular anion with C_{2h} point symmetry. The remaining bands in the fingerprint region are assigned to lattice vibrations. Going above the α–β phase transition (200 °C) the Raman spectra suggest a change in symmetry to the highly symmetrical D_{3d} configuration. The modes at 257 and 274 cm^{-1} and at 574 cm^{-1} (two convoluted modes at lower temperature) degenerate to two modes of the type E_g. The strongest band centered at 379 cm^{-1}, representing the characteristic P–P stretching mode, is persistent over the entire measured temperature range. Only a minor signal at around 420 cm^{-1} is observed at 500 °C, hinting at a possible appearance of ortho-thiophosphates at elevated temperatures.

Contrary to the solid-state sample, precipitated $Na_4P_2S_6$ reveals a $P_2S_6^{4-}$ anion with D_{3d} symmetry already at room temperature, further supporting the proposition it is a β-like polymorph. Here, the PS_3 deformation mode is observed around 200 cm^{-1} with significant intensity that is less pronounced in the single crystal solid-state $Na_4P_2S_6$. Additional Raman measurements on ground solid-state $Na_4P_2S_6$ show, however, similar

intensities compared to the precipitated product, suggesting the orientation of the single crystal to be the reason for the low intensity of the deformation mode. We only measured up to 200 °C, a temperature well above the α–β phase transition temperature in the solid-state material, but lower than the annealing temperature for precipitated $Na_4P_2S_6$ (observed at approx. 500 °C according to XRD results, *cf.* Figure 5.1c) to avoid the formation of side phases and to stay within the β-like polymorph. However, upon cooling the material already show a splitting of the modes as for the α polymorph, suggesting the beginning of annealing and "healing" from (stacking) faults of the precipitated sample already at temperatures below 500 °C.

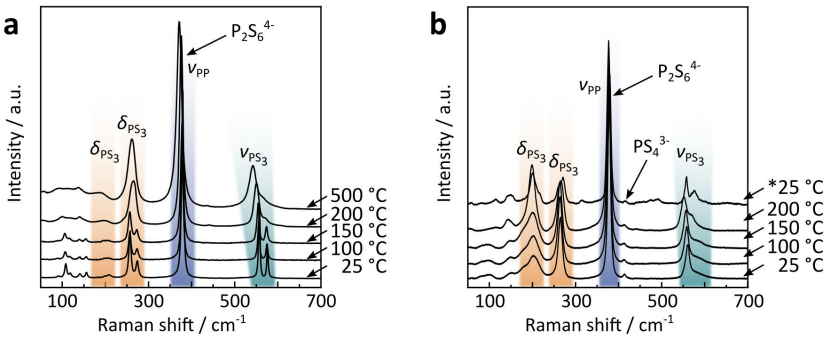

Figure 5.3: Temperature dependent Raman spectra of (a) solid-state α/β and (b) precipitated β-like $Na_4P_2S_6$. The asterisk indicates that the spectrum was recorded after cooling down the sample from 200 °C. A full assignment of Raman modes for $Na_4P_2S_6$ can be found in Table B.9 in Appendix B.

Structural changes of the phase transition

To gain deeper insight into the structural changes of the α–β transition, Rietveld refinements of a series of HT-XRDs (between 20 °C and 300 °C) were evaluated. The manuscript refers to the solid-state $Na_4P_2S_6$, but the same analysis for the annealed $Na_4P_2S_6$ (with some amorphous side phase as informed from NMR) is included in Appendix B. As already mentioned above, the main feature of the β polymorph is the new sodium position Na3 that populates during the phase transition. As Figure 5.4a illustrates, this occurs at the expense of Na2 until both sites are equally occupied by $\frac{2}{3}$ (remember the different multiplicities of $4h$ and $2d$). This is an exceptionally high amount of intrinsic Na^+ vacancies (33%) in an ion conducting material. The refined occupation of Na3 at room temperature varies from 0% to 11±4%. Furthermore, we found a correlation of the quality of the prepared batch and the refined Na3 occupation, where samples with less side phase can be refined to a lower Na3 occupation. The Rietveld refinements further confirm the reversibility of the phase transition with only a slight shift for the very first heating process, consistent with the DSC measurements. To analyze the subtleties of the occupation of Na2 and Na3, the phase transition was additionally examined in a single crystal with single crystal X-ray diffraction at room temperature, subsequently at 227 °C,

and again at room temperature. Here, the occupation of Na3 is completely reversible from zero (due to the absence of a side phase) to $\frac{2}{3}$ and again to zero (*cf.* Appendix B for single crystal data).

Figure 5.4b displays the volume of the unit cell that changes discontinuously (+0.6%) as expected for a first order phase transition. Please refer to Appendix B for temperature dependency of a, b, c, and β. The thermal expansion of β-$Na_4P_2S_6$ is higher than for the α polymorph with expansion coefficients of $6.2 \cdot 10^{-6}\,K^{-1}$ and $4.5 \cdot 10^{-6}\,K^{-1}$, respectively. Given these values, both belong in the group of intermediate expanding materials.[31] Considering the structural changes during the phase transition, an interesting question is whether for β-$Na_4P_2S_6$ the $P_2S_6^{4-}$ layers now resemble a hexagonal pattern more closely. To this end, we evaluated the two relevant distances of the $P_2S_6^{4-}$ units (defined as the middle of the P–P dumbbell) as shown in Figure 5.4c. The distances indeed approach each other after the phase transition (6.61/6.66 Å at 200 °C) as compared to the α phase (6.54/6.72 Å at 20 °C). Nevertheless, they are still unequal in the β-$Na_4P_2S_6$ polymorph and the symmetry thus is not hexagonal. Furthermore, we were interested in the unique tilting of $P_2S_6^{4-}$ along the stacking direction, measured by the P–P–P angle of two neighboring anions in a direction. This angle changes from 86° in α to 91° in β-$Na_4P_2S_6$ (Figure 5.4d). At the phase transition it was even refined to more extreme values of up to 95°, presumably reflecting the Na^+ rearrangement and changes in unit cell dimensions.

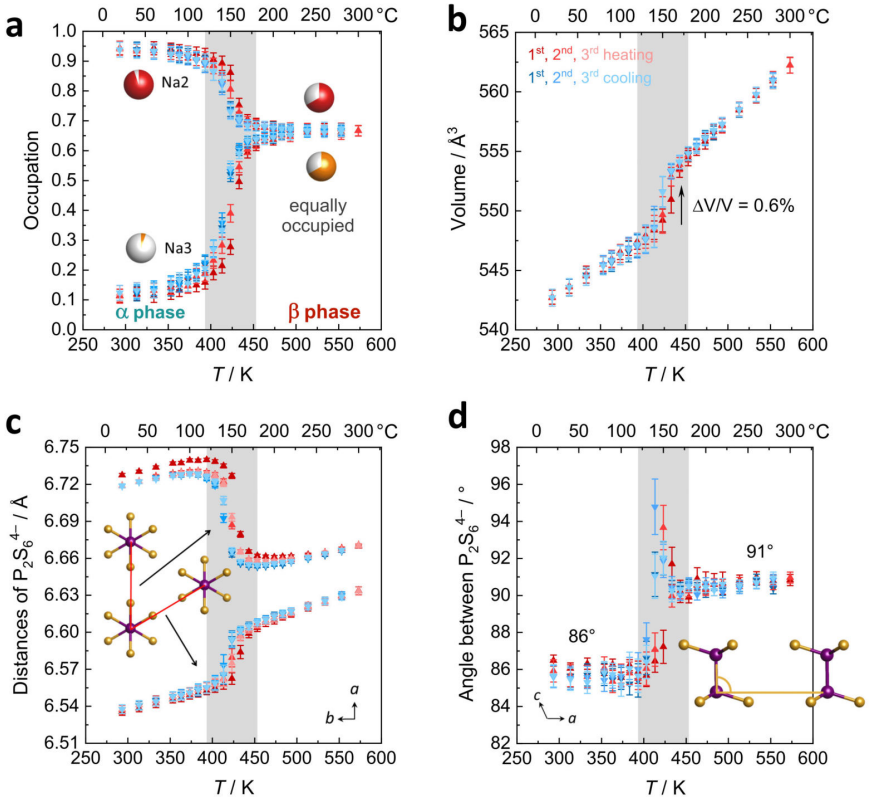

Figure 5.4: Results of the Rietveld refinements for the α–β phase transition upon heating (red data points) and cooling (blue data points) for the first three cycles (color code from dark to light with increasing cycle number). (a) Occupation of the sodium positions Na2 and Na3 between the $P_2S_6^{4-}$ layers. (b) Volume change with temperature. (c) Distances of the $P_2S_6^{4-}$ anions as a measure for the hexagonality of the layer. (d) Tilting of neighboring $P_2S_6^{4-}$ anions in a direction expressed as the P–P–$P_{neighbor}$ angle.

5.3.2 Sodium-ion conductivity

Pathways of Na^+ conductivity

To investigate possible Na^+ migration pathways and the effect of the α–β phase transition on the Na^+ trajectory, the bond valence energy landscape (BVEL) was calculated for both $Na_4P_2S_6$ polymorphs. Figure 5.5a illustrates the iso-energy surface in the Na2/Na3 layer of α-$Na_4P_2S_6$ with increasing energy from left to right. At low potential energy, the BVEL reveals two possible sites that are indeed the Wyckoff positions $4h$ (Na2) and $2d$ (Na3). The Na2 position is 0.2 eV lower in potential energy than the Na3 position. This finding is in line with sodium solely occupying the Na2 position in the ground state and populating Na3 at higher temperature, hence higher energy. Increasing the energy further, an interstitial site of tetrahedral symmetry appears as a local minimum that connects both low energy octahedrally coordinated sodium sites through two transition states. Note that this pathway covers only three sodium sites and is not forming a long-range conduction pathway across the unit cells (*cf.* 2.1 eV). We introduce the word 'triple' for this Na2–Na3–Na2 island for later discussion. However, since an extended pathway is crucial for long-range ion diffusion, an additional energy of 0.9 eV is necessary to interconnect the triples (*cf.* Figure 5.5b, Figure B.11). Overall, the migration energy for Na^+ in this two-dimensional network in the *ab* plane is calculated to be about 3.0 eV, a very high value for an ion conducting material. Note, however, that calculations based on the bond valence (BV) approach are known to overestimate migration barriers, as the BV method is based on calculating potential energies at fixed grid points of a "stiff" lattice. Relaxation of the anionic sublattice during ion migration is not part of this method, hence barriers are higher than one would measure in a real sample. Sodium ions Na1 occupying the octahedral sites within the $P_2S_6^{4-}$ layers are not part of this Na^+ network, since they experience a much stronger interaction with the close-by $P_2S_6^{4-}$ dumbbells, narrowing possible channels for ion migration (*cf.* Figure 5.5c). We thus expect these Na1 sites to be rather immobile, rendering ion transport in this material essentially 2D. For comparison, the BVEL of β-$Na_4P_2S_6$ is also drawn in Figure 5.5c. The structural changes of the phase transition only have a minimal impact on the intra-triple Na2–Na3–Na2 diffusion ('), but significantly reduce the energy barrier for the important long-ranged inter-triple sodium diffusion (") from 3.0 eV to about 2.3 eV. On this account, we expect the phase transition to significantly affect the Na^+ diffusion. The BVEL method, however, does not consider local atomic orderings and does not account for the important influence of the vacancies in this material.

A more local approach, namely, nudged elastic band (NEB) calculations on the basis of DFT were carried out to obtain a complimentary view on the Na^+ migration. In the calculations, we neither attempted a full treatment of disorder nor accounted for correlated ion motion. The reader is referred to the experimental section for simplifications we made and reasons for it. Therefore, the following considerations provide a qualitative rather than a quantitative understanding. Both α- and β-$Na_4P_2S_6$ were studied for comparison. Further, we anticipated the importance of the local environment and re-used the classification for migration scenarios from the bond valence study: Na2' $\rightleftharpoons$ Na3' intra-triple diffusion (') and inter-triple diffusion ("), whereby the latter was divided in Na2' $\rightleftharpoons$ Na3" and Na2' $\rightleftharpoons$ Na2" diffusion. For all three classes we picked exemplary sodium ion–vacancy orderings and migration scenarios along the established tetrahedral

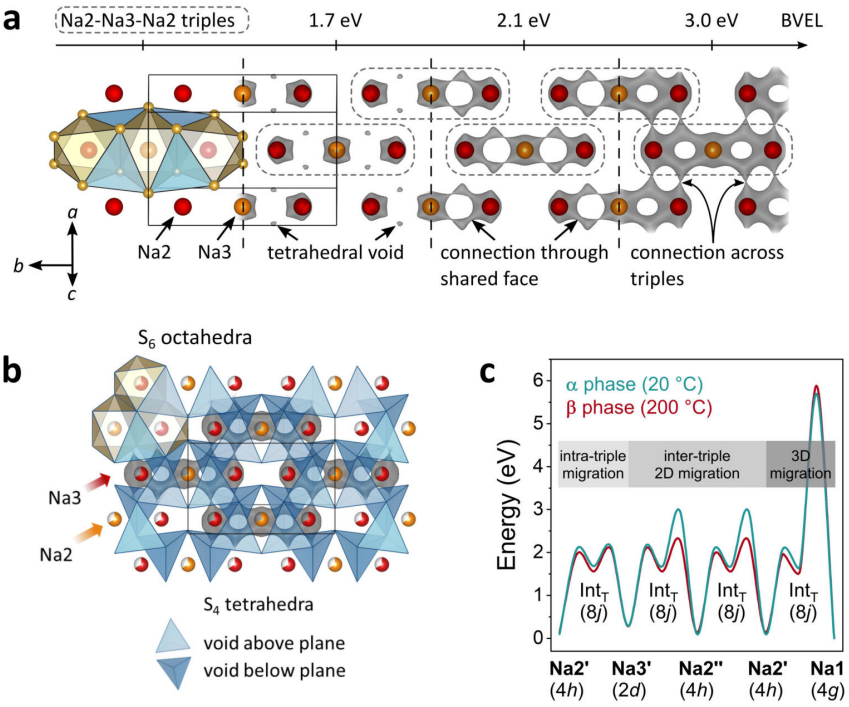

Figure 5.5: (a) Evolution of bond valence energy landscapes in the $(0\,0\,\frac{1}{2})$ plane with increasing energy for the Na2–Na3–Na2 triple. (b) Overlay of BVEL and section of the crystal structure with tetrahedral interstitials (blue tetrahedra). (c) Energy diagram for intra-triple (') and inter-triple (") Na2 and Na3 migration and migration to a Na1 site illustrated for α- and β-$Na_4P_2S_6$ at 20 °C and 200 °C, respectively.

voids and tried to keep the ordering of Na^+ ions that are not involved in the jump as comparable as possible for the different scenarios. Li *et al.*[28] considered in their recent study only the Na2' $\rightleftharpoons$ Na2" diffusion in α-$Na_4P_2S_6$ along the direct connection of the sites and not the tetrahedral interstitials. Figure 5.6 displays the chosen scenarios and results of the NEB calculations.

Scenario 1 is the Na^+ migration from a Na2 site to an unoccupied Na3 site within a triple (Na2' $\rightarrow$ Na3') along the BVEL pathway and, therefore, stands for the first step in the α to β phase transition. Contrary to the BVEL, the tetrahedral interstitial is a maximum in the energy curve with $E_{\mathrm{mig}} = 1.1\,\mathrm{eV}$ for both α- and β-$Na_4P_2S_6$. This barrier is overestimated as a consequence of our DFT simplifications; this assumption is consistent with the fact that the phase transition already happens at considerably low thermal energy (160 °C). After the migration, the energy of the system has significantly increased and this flattens the energy landscape for the ensuing ion motion. Scenario 2, which is a consecutive Na2' $\rightarrow$ Na3' migration but in a neighboring triple, exhibits only $E_{\mathrm{mig}} = 0.5\,\mathrm{eV}$. For long-range diffusion to the next triple higher energy barriers have to

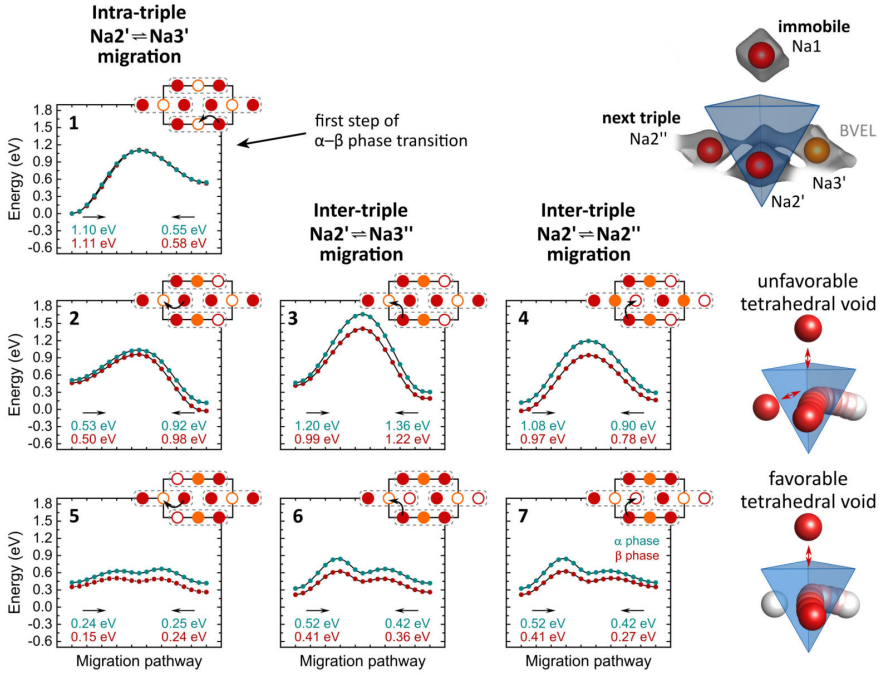

Figure 5.6: Energy curves for Na^+ migration of Scenarios 1–7 from NEB calculations. Corresponding migration energies are displayed under each curve. The Na^+ pathways in the Na2/Na3 layer are sketched with Na2 in red, Na3 in orange and the triples indicated with dashed gray lines. Un-/occupied positions are displayed with empty/filled circles. Unfavorable and favorable tetrahedral voids are illustrated on the right side. The arrangement of tetrahedral voids within the unit cell can be found in Figure 5.5b.

be overcome as shown in Scenarios 3 and 4 (α: $E_{\mathrm{mig}} > 0.9\,\mathrm{eV}$, β: $E_{\mathrm{mig}} > 0.8\,\mathrm{eV}$). The structural changes from α- to β-$Na_4P_2S_6$ reduce the energy barriers for the scenarios by about 0.1 eV but still differentiate between intra- and inter-triple migration. This said, the local method provides a different view than the BVEL calculations where the energy pathways almost align for intra- and inter-triple migration in the β polymorph.

All NEB scenarios so far have in common that the pathway is through a tetrahedral interstitial that experiences electrostatic repulsion from one (immobile) Na1 and one Na2 or Na3 ion that do not partake in the ion migration (*cf.* Figure 5.6). This is a rather unfavorable tetrahedral void, and hence unfavorable diffusion pathway. Recalculating the Scenarios 2–4 with favorable tetrahedral voids having a free site next to the pathway results in a local energy minimum for the tetrahedral site (Scenarios 5–7). The barriers for ion motion are reduced by about $\frac{1}{2}$ and can be expected to be even smaller in the real material because of the energy overestimation due to our DFT simplifications. The favorable Scenarios 5–7 interconnect the entire Na2/Na3 layer and enable long-range Na^+ migration in the *ab* plane.

In the crystal structure exists only one tetrahedral site (Wyckoff position $8j$). In α-$Na_4P_2S_6$ this site is unfavorable due to the Na^+ ordering. However, in β-$Na_4P_2S_6$ the local environment changes, and under the condition that Na2 and Na3 are equally occupied as refined from the PXRD pattern, there are, in purely statistical terms, 44% unfavorable and 22% favorable tetrahedral voids (besides 33% impossible voids with four or only one Na^+, namely Na1, around). Every Na2 or Na3 site is surrounded by four of these tetrahedral voids (38% probability that at least one of them is favorable), and the high number of five or six target sites can be reached from a Na2 or Na3 position, respectively (*cf.* Figure 5.5b). Thus, the probability for low-energy ion migration pathways is high. In essence, the vacant sites are the key difference for the ionic conductivity in α- and β-$Na_4P_2S_6$.

Generally, vacancies are cumbersome to introduce by chemical substitutions to enhance the ionic conductivity. High amounts of sodium vacancies in thiophosphates are to our knowledge only known for $Na_{11}Sn_2PS_{12}$, where they lead to superionic conductivity,[24] but they have not been observed in more highly condensed thiophosphates yet.

Electrochemical impedance spectroscopy

After revealing the structural differences in $Na_4P_2S_6$ prepared *via* different synthetic routes, the ionic conductivity was tested with impedance spectroscopy on cold pressed pellets. The measurements were performed on solid-state synthesized powder (batches ss1 and ss2) resembling the α phase at room temperature, on precipitated material (p1 and p2) with a more β-like structure and inter- and intralayer disorder, and on annealed powder (a1) characterized by an intermediate structure with significant impurities as discussed above.

First, we present results on the Arrhenius behavior of all samples well below the phase transition temperature ($\leq 100\,°C$). Representative complex impedance spectra in the Nyquist-representation are shown in Figure 5.7a for all three $Na_4P_2S_6$ types. Please refer to Appendix B for a more detailed discussion of the impedance spectra interpretation and fitting. All spectra recorded at room temperature consist of only one (depressed) semicircle with an associated (averaged) capacitance of $7 \cdot 10^{-11}\,F/cm^2$ and $8 \cdot 10^{-11}\,F/cm^2$ for ss1 and ss2, $1 \cdot 10^{-10}\,F/cm^2$ and $4 \cdot 10^{-11}\,F/cm^2$ for p1 and p2, and $6 \cdot 10^{-11}\,F/cm^2$ for a1. A capacitance on the order of 10 pF is usually expected for bulk processes, whereas a capacitance of nF is commonly attributed to grain boundaries.[32,33] We checked all spectra for a possible second (grain boundary) semicircle that could overlap with the first high frequency arc by adding an additional (R)(CPE) circuit in series. The resulting fits were unsatisfactory, both visually and as seen from calculated errors of the individual circuit units. Therefore, we conclude that only one process at ambient temperature, based on the associated capacitances presumably a bulk process, is observable for this material, similar to the findings of Krauskopf *et al.* for Na_3PS_4.[11] The room temperature ionic conductivity for solid-state $Na_4P_2S_6$ is about $7 \cdot 10^{-7}\,S\,cm^{-1}$, whereas the precipitated material has a higher mean conductivity of $2 \cdot 10^{-6}\,S\,cm^{-1}$. The difference may be directly attributed to the different polymorphs of $Na_4P_2S_6$ as we expect a higher conductivity for the β-like phase with Na^+ and vacancy disorder as well as structural defects. Considering the batch-to-batch variations, a smaller spread in conductivities is observed for the solid-state than for the precipitated material. This speaks for a more homogeneous solid-state product, in

line with the high crystallinity of the α polymorph. For precipitated $Na_4P_2S_6$ the greater spread in conductivities is rationalized with the different sample histories due to slow or fast precipitation, re-crystallization, and dehydration, and also the varying amount of disorder in the material. With this in mind, we trace back the difference to the reported bulk conductivity for precipitated $Na_4P_2S_6$ ($\sigma_{bulk} = 3.4 \cdot 10^{-6}\,S\,cm^{-1}$)[29] to the higher dehydration temperature, namely 175 °C instead of 100 °C in this study. Hood[29] found that at a dehydration temperature of 175 °C the ionic conductivity was highest, whereas at 100 °C $Na_4P_2S_6$ has a conductivity of around $5 \cdot 10^{-7}\,S\,cm^{-1}$. Annealed $Na_4P_2S_6$ has a room temperature ionic conductivity of $2.3 \cdot 10^{-7}\,S\,cm^{-1}$, which is considerably lower than for both solid-state and precipitated $Na_4P_2S_6$. We attribute this decrease to the variety of low Na^+ conducting thio-, thio/oxo- and oxo-phosphate impurities in this sample.

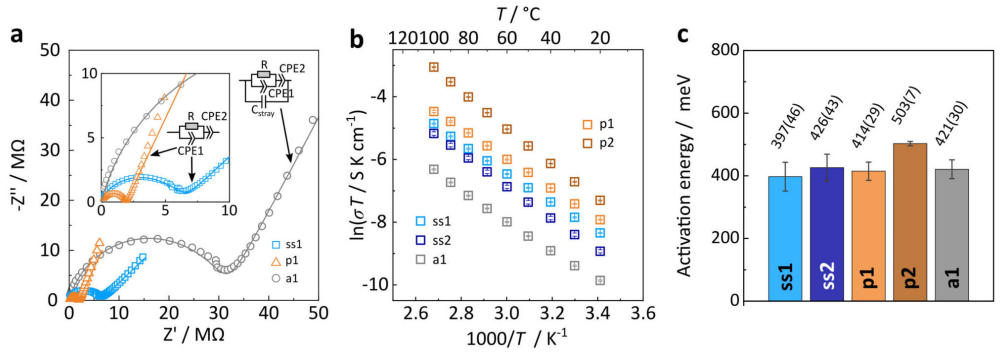

Figure 5.7: (a) Exemplary Nyquist plots of solid-state α, precipitated β-like, and annealed $Na_4P_2S_6$ measured at 20 °C. (b) Arrhenius plots and (c) corresponding activation energies (averages of three different pellets, error bars indicated). ss1, ss2 - solid-state; p1, p2 - precipitated; a1 - annealed batches.

Next, activation energies of solid-state, precipitated, and annealed $Na_4P_2S_6$ were deduced from individual Arrhenius plots $ln(\sigma T)$ as a function of inverse temperature (Figure 5.7b,c). They are on the order of 0.40 eV to 0.50 eV, with on average higher barriers for precipitated $Na_4P_2S_6$ compared to the solid-state material. The activation energy remains the same when annealing the precipitated p1 $Na_4P_2S_6$ sample. Based on our theoretical considerations and calculations we expect a lower activation energy for the β polymorph. However, we observe that α and β-like $Na_4P_2S_6$ have a comparable mean activation energy. Real structure effects (and side phases), especially present in the precipitated sample, could be accountable for this unexpected result.

As reported before, first principles investigation of the electrochemical properties of α-$Na_4P_2S_6$ performed by Rush *et al.* and Li *et al.* yielded an activation energy of $E_a \approx 0.4\,eV$[27,34] and 0.34 eV,[28] respectively. MD simulations suggest an activation energy of 0.41 eV along with an experimentally confirmed activation energy of 0.39 eV.[28] All activation energies published so far are in good agreement with the values presented in this study. Although this level of agreement is encouraging and reinforces the notion that $Na_4P_2S_6$ has an activation energy of around 0.4 eV, one should be careful in comparing

ionic conductivities and activation barriers reported by different groups, as reinforced by a recent benchmarking study.[35] Not only sample history and preparation can have an impact on measured ionic conductivity, but also factors such as applied pressure and sample-electrode contacts. The study of Ohno *et al.*[35] found that the spread of reported activation values can be as big as 0.13 eV, depending on the setup and cell preparation used for measuring impedance on a one-batch-material distributed within different research groups.

Finally, the electronic conductivity of α (ss2) and β-like (p1) $Na_4P_2S_6$ was deduced from DC galvanostatic polarization measurements, establishing the material as a nearly pure sodium ion conductor with an electronic conductivity on the order of nS/cm (*cf.* Appendix B). This is at least two orders of magnitude lower than the ionic conductivity, hence the transference number for sodium ions is calculated to be ≥ 0.99.

Overall, the measured transport data are in line with the other structure sensitive methods and confirm substantial differences between the $Na_4P_2S_6$ samples due to changes at the structural level, induced by different sample histories.

5.4 Conclusion

The development of all-solid-state sodium-ion batteries for scalable energy storage solutions requires fast sodium conducting solid electrolytes. Abundant resources and a cheap and green synthesis are seen as highly beneficial for large-scale application. Here, we have prepared $Na_4P_2S_6$ following two different routes, a solid-state and a precipitation method, and traced the resulting differences back to the following changes at the structural level.

First, a Na^+ and vacancy disorder-driven first order phase transition (α to β) is observed for the solid-state synthesized material at temperatures around 160 °C, which is associated with a symmetry change of the $P_2S_6^{4-}$ anion and changes in the population of the sodium sublattice. Second, the β-like polymorph is stabilized already at room temperature for precipitated $Na_4P_2S_6$, presumably through the assistance of inter- and intralayer defects. Electrochemical impedance measurements and theoretical calculations reveal that the sodium-ion conduction is substantially affected by these structural differences. The key findings are as follows: Using bond-valence calculations, low-energy unoccupied sodium positions in both α- and β-$Na_4P_2S_6$ and possible short- and long-range 2D Na^+ migration pathways especially in the β polymorph were identified. Since the BVEL method does not capture local environments such as Na^+ vacancies which are present in high amounts in $Na_4P_2S_6$, NEB calculations were used as a more local approach to demonstrate that the Na^+ disorder leads to many possible migration paths with a wide spread of E_{mig}. Additional disorder, *e.g.* stacking faults, residual crystal water, or thiophosphate disorder in precipitated $Na_4P_2S_6$, even multiplies these possibilities. Finally, the ion transport for both polymorphs with different types of disorder were studied by impedance spectroscopy. The measurements suggest that the Na^+ conductivity in the precipitated sample is slightly higher than that of the solid-state sample ($2 \cdot 10^{-6}\,S\,cm^{-1}$ *versus* $7 \cdot 10^{-7}\,S\,cm^{-1}$ with $E_a \approx 0.4$ eV for both materials at room temperature), which is consistent with the stabilization of the more conductive β phase at room temperature in the precipitated sample. In summary, the results point out that synthetic and post-synthetic treatment of solid electrolytes can substantially impact a material's properties. In fact, differences

in sample preparation cannot only change the speciation and, hence, product outcome, but also change more subtle structural properties such as phase formation and stability range. Without critical investigation, important changes such as phase transitions with small structural changes and low heat tinting can be easily overlooked. The findings thus point to a rich and potentially unexplored phase space in thiophosphate solid electrolytes, and at the same time motivate a somewhat underappreciated approach for the design of improved solid electrolytes: Phase formation through synthetic control.

References

(1) Zhang, Z.; Shao, Y.; Lotsch, B.; Hu, Y.-S.; Li, H.; Janek, J.; Nazar, L. F.; Nan, C.-W.; Maier, J.; Armand, M.; Chen, L. *Energy Environ. Sci.* **2018**, *11*, 1945–1976.

(2) Famprikis, T.; Canepa, P.; Dawson, J. A.; Islam, M. S.; Masquelier, C. *Nat. Mater.* **2019**, *18*, 1278–1291.

(3) Hueso, K. B.; Armand, M.; Rojo, T. *Energy Environ. Sci.* **2013**, *6*, 734–749.

(4) Lu, X.; Xia, G.; Lemmon, J. P.; Yang, Z. *J. Power Sources* **2010**, *195*, 2431–2442.

(5) Guin, M.; Tietz, F. *J. Power Sources* **2015**, *273*, 1056–1064.

(6) Goodenough, J. B.; Hong, H. Y. P.; Kafalas, J. A. *Mater. Res. Bull.* **1976**, *11*, 203–220.

(7) Udovic, T. J.; Matsuo, M.; Unemoto, A.; Verdal, N.; Stavila, V.; Skripov, A. V.; Rush, J. J.; Takamura, H.; Orimo, S.-i. *Chem. Commun.* **2014**, *50*, 3750–3752.

(8) Duchêne, L.; Kühnel, R. S.; Rentsch, D.; Remhof, A.; Hagemann, H.; Battaglia, C. *Chem. Commun.* **2017**, *53*, 4195–4198.

(9) Hayashi, A.; Noi, K.; Sakuda, A.; Tatsumisago, M. *Nat. Commun.* **2012**, *3*, 856.

(10) Hayashi, A.; Noi, K.; Tanibata, N.; Nagao, M.; Tatsumisago, M. *J. Power Sources* **2014**, *258*, 420–423.

(11) Krauskopf, T.; Culver, S. P.; Zeier, W. G. *Inorg. Chem.* **2018**, *57*, 4739–4744.

(12) Jansen, M.; Henseler, U. *J. Solid State Chem.* **1992**, *99*, 110–119.

(13) Famprikis, T.; Dawson, J. A.; Fauth, F.; Clemens, O.; Suard, E.; Fleutot, B.; Courty, M.; Chotard, J.-N.; Islam, M. S.; Masquelier, C. *ACS Mater. Lett.* **2019**, *1*, 641–646.

(14) Zhang, L.; Zhang, D.; Yang, K.; Yan, X.; Wang, L.; Mi, J.; Xu, B.; Li, Y. *Adv. Sci.* **2016**, *3*, 1600089.

(15) Bo, S.-H.; Wang, Y.; Ceder, G. *J. Mater. Chem. A* **2016**, *4*, 9044–9053.

(16) Krauskopf, T.; Pompe, C.; Kraft, M. A.; Zeier, W. G. *Chem. Mater.* **2017**, *29*, 8859–8869.

(17) Chu, I.-H.; Kompella, C. S.; Nguyen, H.; Zhu, Z.; Hy, S.; Deng, Z.; Meng, Y. S.; Ong, S. P. *Sci. Rep.* **2016**, *6*, 33733.

(18) De Klerk, N. J. J.; Wagemaker, M. *Chem. Mater.* **2016**, *28*, 3122–3130.

(19) Hayashi, A.; Masuzawa, N.; Yubuchi, S.; Tsuji, F.; Hotehama, C.; Sakuda, A.; Tatsumisago, M. *Nat. Commun.* **2019**, *10*, 5266.

(20) Fuchs, T.; Culver, S. P.; Till, P.; Zeier, W. G. *ACS Energy Lett.* **2020**, *5*, 146–151.

(21) Kuhn, A.; Eger, R.; Nuss, J.; Lotsch, B. V. *Z. Anorg. Allg. Chem.* **2014**, *640*, 689–692.

(22) Fritsch, C.; Hansen, A.-L.; Indris, S.; Knapp, M.; Ehrenberg, H. *Dalton Trans.* **2020**, *49*, 1668–1673.

(23) Zhang, Z.; Ramos, E.; Lalère, F.; Assoud, A.; Kaup, K.; Hartman, P.; Nazar, L. F. *Energy Environ. Sci.* **2018**, *11*, 87–93.

(24) Duchardt, M.; Ruschewitz, U.; Adams, S.; Dehnen, S.; Roling, B. *Angew. Chem., Int. Ed.* **2018**, *57*, 1351–1355.

(25) Fincher, T.; LeBret, G.; Cleary, D. A. *J. Solid State Chem.* **1998**, *141*, 274–281.

(26) Neuberger, S.; Culver, S. P.; Eckert, H.; Zeier, W. G.; Schmedt auf der Günne, J. *Dalton Trans.* **2018**, *47*, 11691–11695.

(27) Rush, L. E.; Holzwarth, N. A. W. *Solid State Ion.* **2016**, *286*, 45–50.

(28) Li, Y.; Hood, Z. D.; Holzwarth, N. A. W. *Phys. Rev. Mater.* **2020**, *4*, 045406.

(29) Hood, Z. D. Lithium and sodium solid electrolytes for next-generation batteries: Bridging mechanistic understanding and their performance, Ph.D. Thesis, Georgia Institute of Technology, 2018.

(30) Kmiec, S.; Joyce, A.; Martin, S. W. *J. Non-Cryst. Solids* **2018**, *498*, 177–189.

(31) Roy, R.; Agrawal, D. K.; McKinstry, H. A. *Annu. Rev. Mater. Sci.* **1989**, *19*, 59–81.

(32) Kuhn, A.; Gerbig, O.; Zhu, C.; Falkenberg, F.; Maier, J.; Lotsch, B. V. *Phys. Chem. Chem. Phys.* **2014**, *16*, 14669–14674.

(33) Fleig, J.; Maier, J. *J. Am. Ceram. Soc.* **1999**, *82*, 3485–3493.

(34) Rush, L. E. J. First-Principles Investigation of Electronic Properties in Sodium-Ion Electrolytes for Solid-State Battery Materials, Thesis, 2017.

(35) Ohno, S. et al. *ACS Energy Lett.* **2020**, *5*, 910–915.

CHAPTER 6

Superionic conduction in the plastic crystal polymorph of $Na_4P_2S_6$

Tanja Scholz, Christian Schneider*, Maxwell W. Terban, Zeyu Deng, Roland Eger, Martin Etter, Robert E. Dinnebier, Pieremanuele Canepa, and Bettina Valeska Lotsch*
*Equal contribution to this work

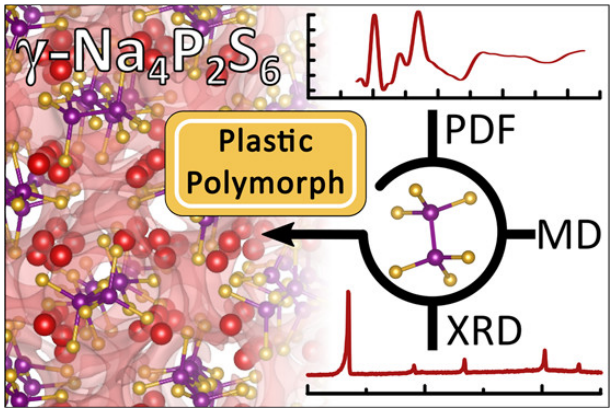

This work was published in and adopted from:
ACS Energy Letters **2022**, *7*, *4*, 1403–1411.

Supporting information can be found in Appendix C.
Author contributions can be found in Appendix F.

Contents of Chapter 6

6.1 Abstract

Sodium thiophophates are promising materials for large-scale energy storage applications benefiting from high ionic conductivities and the geopolitical abundance of the elements. A representative of this class is $Na_4P_2S_6$, which currently shows two known polymorphs – α and β. This work describes a third polymorph of $Na_4P_2S_6$, γ, that forms above 580 °C, exhibits fast-ion conduction with low activation energy, and is mechanically soft. Based on high-temperature diffraction, pair distribution function analysis, thermal analysis, impedance spectroscopy, and *ab initio* molecular dynamic calculations, the γ-$Na_4P_2S_6$ phase is identified to be a plastic crystal characterized by dynamic orientational disorder of the $P_2S_6^{4-}$ anions translationally fixed on a body-centered cubic lattice. The prospect of stabilizing plastic crystals at operating temperatures of solid-state batteries, with benefits from their high ionic conductivities and mechanical properties, could have a strong impact in the field of solid-state battery research.

6.2 Introduction

The rich chemistry of thiophosphates is an excellent platform for exploring compounds with interesting and functional properties. The plethora of possible thiophosphate anions ranges from the tetrahedral ortho-thiophospate PS_4^{3-} to larger units, such as corner-sharing $P_2S_7^{4-}$ or $P_2S_6^{4-}$ having a P–P central bond. The ability of sulfur to form disulfur –S–S– bridges and the broad range of oxidation states of phosphorus allow for even larger, ring-like or square-shaped anions.[1,2]

Many thiophosphate compounds containing alkaline metals are ion conductors. However, the number of highly conducting phases is still limited to a few well-known representatives (*e.g.* Na_3PS_4). The as-prepared tetragonal (low temperature) structure of Na_3PS_4 shows a low ionic conductivity of around $4.2 \cdot 10^{-6}\,S\,cm^{-1}$ (50 °C), but it can be improved up to $\sim 4.6 \cdot 10^{-4}\,S\,cm^{-1}$ (room temperature) by stabilizing the high temperature cubic phase as a glass–ceramic.[3–5] This was achieved by ball-milling the starting materials and subsequently annealing the glass at a low temperature of 270 °C to precipitate the cubic phase. Recently, Krauskopf *et al.* have suggested that the room-temperature stabilized cubic phase comprises tetragonal-like local-structure motifs.[6]

Another example of the phase-space flexibility of thiophosphates is $Na_4P_2S_6$.[7,8] This material can be synthesized *via* a precipitation route, as well as by high-temperature solid-state synthesis.[9,10] Depending on the preparation method, $Na_4P_2S_6$ crystallizes in the monoclinic polymorphs α- and β-$Na_4P_2S_6$.[10,11] These polymorphs can be transformed into each other by heating or annealing the sample. In this study, we identify a new high-temperature polymorph of $Na_4P_2S_6$, γ, which displays plastic crystal characteristics.

Plastic crystals are characterized by a high degree of reorientational freedom, often found for spherical molecules, or conformational freedom, often found for polymers, of a cationic, anionic, or neutral sub-lattice of a solid.[12–14] The disordered species are translationally fixed, therefore maintaining the lattice. This renders the material a solid with weak interactions in the partly "molten" anion sub-lattice. A number of inorganic ion conductors show these characteristics, including ABH_4 (A = Li, Na, K, Rb, Cs),[15–17] Li_2SO_4,[18,19] $LiAgSO_4$,[20] $LiNaSO_4$,[21] $Li_4Zn(SO_4)_3$[21] Na_3PO_4,[22,23] Na_2AC_{60} (A = K, Rb, Cs),[24–26]

$Na_2B_{12}H_{12}$,[27–29] $Na_2B_{10}H_{10}$,[30] $ACB_{11}H_{12}$ (A = Li, Na),[31] $Li_2B_{12}H_{12}$,[29] $Rb_2B_{10}H_{10}$,[32] Na_3PS_4,[33] and $Na_4Zn(PO_4)_2$[34] (sorted by publication year). All these examples contain rather globular-shaped anions with high point-group symmetries, such as I_h (*e.g.* $B_{12}H_{12}^{2-}$ and C_{60}^{3-}), D_{4d} (*e.g.* $B_{10}H_{10}^{2-}$), or T_d (*e.g.* SO_4^{2-}). High intrinsic symmetry of the anion species lowers the sterical hindrance for fast reorientational motion..[35]

The implementation of fast sodium ion conductors in solid-state batteries is vital for large-scale applications like power-grid regulation and short-term wind or solar energy storage. Cost and resource analyses have shown that using cheaper current collectors and cathode materials can reduce the price and weight of Na-ion (solid-state) batteries compared to their Li analogs, especially if relevant resources such as copper and cobalt continue to increase to price up..[36] The more homogeneous distribution of Na deposits and the higher natural abundance (2.36% Na *versus* 0.002% Li)[37] clearly points to a sodium-driven future in grid (solid-state) battery technology. Solid-state batteries require amongst other properties high intrinsic ion conductivity and a robust mechanical interface between the ion conductor and the electrodes to provide high performance and long cycle life. Plastic ion conductor materials can beneficially provide weaker cation–anion interactions and increased volumes that allow for easier ion transport. Furthermore, the ductility of the plastic phase can help to maintain better contact with the electrode and reduce physical degradation of the interface during cycling. A major caveat is that plastic phase transitions in ion conductors are often observed at high temperatures, which impedes their application in real devices. Thus, it is vital to better understand the nature and formation behavior of plastic crystals to inform strategies for rationally lowering the transition temperature toward ambient conditions.

Here, we discover the new γ polymorph of $Na_4P_2S_6$ which exhibits fast Na^+ conduction with a low activation energy, a cubic crystal structure, and plastic crystal characteristics. The plastic phase transition is driven by the reorientational freedom of the elongated thiophosphate anion $P_2S_6^{4-}$, rendering $Na_4P_2S_6$ the first example of a salt, based on a prolate, complex anion, showing plastic crystal behavior.

6.3 Results and discussion

Variable-temperature powder X-ray diffraction (PXRD) experiments were performed on $Na_4P_2S_6$ well above the α–β phase transition at 160 °C.[11] A new set of Bragg peaks is observed to emerge at 580 °C, as shown in Figure 6.1. The diffraction peaks of β-$Na_4P_2S_6$ and the new crystalline phase coexist up to 585 °C (measured every 5 K), at which point the β phase disappears. This suggests the existence of a third polymorph of $Na_4P_2S_6$, which we refer to as γ-$Na_4P_2S_6$. Upon cooling, the transition is reversible with the reformation of β- and α-$Na_4P_2S_6$.

Several remarkable features of the PXRD patterns of γ-$Na_4P_2S_6$ are discussed in the following (labelled (i)–(iv)). These points lead us to conclude that γ is a newly observed member of the plastic crystal family.

(i) The Bragg peaks of γ-$Na_4P_2S_6$ can be indexed to the cubic space group $Im\bar{3}m$ (no. 229) with a lattice parameter of 8.4509(3) Å at 580 °C. However, this high symmetry is not compatible with the ethane-like D_{3d} configuration of the $P_2S_6^{4-}$ anions, suggesting that the anions cannot be crystallographically oriented in the structure.

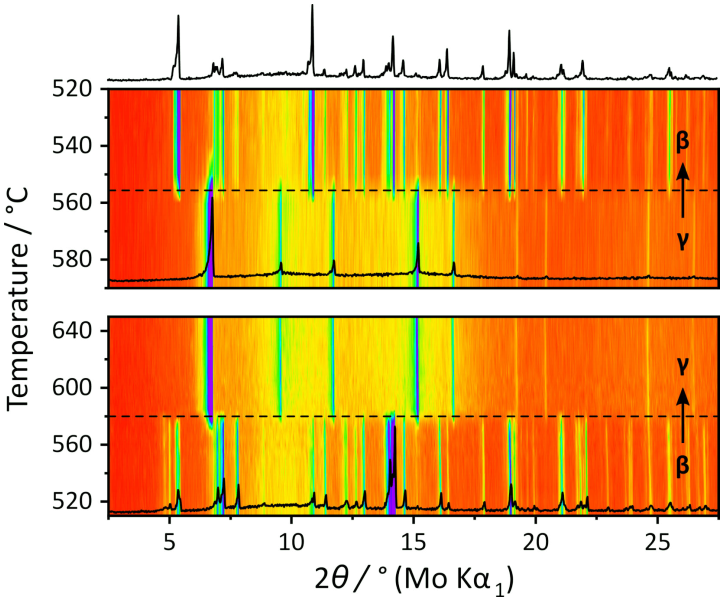

Figure 6.1: Variable temperature PXRD of $Na_4P_2S_6$ upon heating (bottom) and cooling (top) across the β–γ phase transition: contour plot of diffractograms (the color code, red to purple/blue, indicates the ranges from low to high diffraction intensities, respectively) and exemplary diffractograms (black) at 520 °C (β), 620 °C (γ), and 520 °C (β after heating above the phase transition). The selected diffractograms are additionally depicted in Figure C.1.

This observation suggests that some kind of static or dynamic disorder is present in the anion orientations.

(ii) The β–γ phase transition is accompanied by a large increase in diffuse scattering intensities, and the observed Bragg peak intensities rapidly decrease and disappear at higher angles. The diffuse scattering can be due to significant disorder, which could result for instance from different anion orientations, and lead to the destructive interference of higher order diffraction components. These are common features observable in the plastic crystal materials mentioned above.

(iii) The β to γ phase transition is accompanied by an unusually high increase in the volume of the unit cell, from 575.4 $Å^3$ to 603.8 $Å^3$/f.u. (assuming $Z = 2$ for γ). This gives an increase of ∼4.9% (see Figure 6.2a), which compares well to *e.g.* ∼3.2% for the monoclinic to cubic transition in Li_2SO_4 and ∼10% for the cubic to orthorhombic transition in Na_3PS_4.[18,33,38]

(iv) A considerable hysteresis of ∼30 K in the β–γ transformation is observed from the diffraction data between heating and cooling, comparable to 40 K in Na_3PS_4.[33]

It is worth noting that after cooling γ-$Na_4P_2S_6$, changes in relative peak intensities are sometimes observed for the subsequent β and α phases (see Figure 6.1 and Appendix C).

Similar behavior reported for γ-Na_3PS_4 was attributed to the development of preferred orientation.[39] However, as no clear preferential orientations could be identified, and the effect was not observed in other experiments where the sample spent less time at elevated temperature (e.g. Figure C.2), possible effects due to reaction or degradation of the sample cannot be excluded.

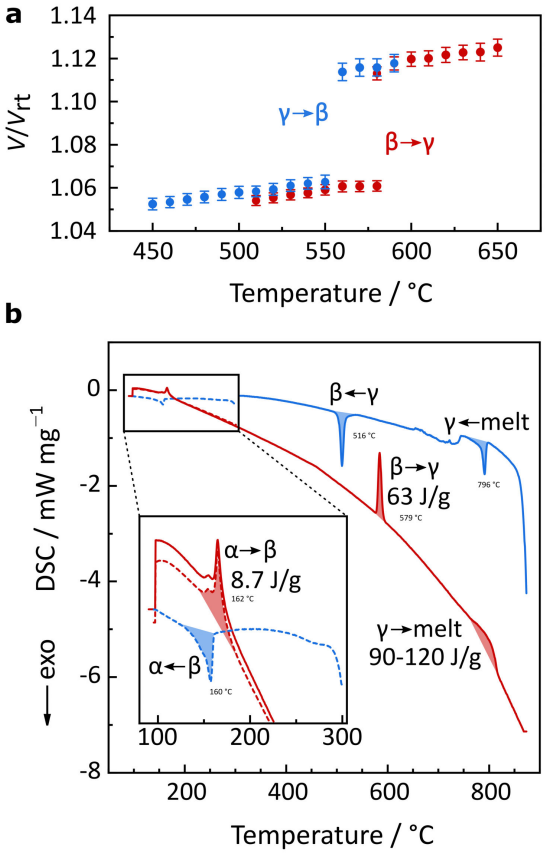

Figure 6.2: (a) Temperature-dependent volume expansion and contraction across the $\beta \rightarrow \gamma$ phase transition relative to the room temperature unit cell volume V_{rt} of $Na_4P_2S_6$. (b) Differential scanning calorimetry (DSC) curve.

The phase transitions in $Na_4P_2S_6$ were additionally studied with differential scanning calorimetry (DSC) as shown in Figure 6.2b, using a much faster heating rate ($20\,K\,min^{-1}$) than in the diffraction experiments. Overall, the DSC data confirm all three transitions $\alpha \rightarrow \beta$ (160 °C), $\beta \rightarrow \gamma$ (580 °C), and γ to the melt (~800 °C), and back. Additional PXRD patterns of α-, β-, γ- and molten $Na_4P_2S_6$ are displayed in Figure C.2. The $\alpha \rightarrow \beta$ phase transition involves very small atomic rearrangements and shows a correspondingly small latent heat of ~8.7 J/g.[11] In contrast, the $\beta \rightarrow \gamma$ transition has a latent heat corresponding to about half that of the melting transition (~60 J/g vs. ~90–120 J/g). This implies that

substantial structural rearrangements are now required to form the γ phase. Other known plastic phase transitions also exhibit latent heats of this magnitude, for example, 214 J/g in Li_2SO_4 or 150 J/g in Na_3PS_4.[18,39] While the $\beta \rightarrow \gamma$ phase transition is observed at the same temperature as in the diffraction experiments (580 °C), the hysteresis on cooling appears much larger, ∼60 K. This could suggest kinetic limitations for the transformation back to the β phase.

To check if the $P_2S_6^{4-}$ anion undergoes any structural change during the $\beta \rightarrow \gamma$ transition, we measured high-temperature Raman spectra. The spectra of Figure C.3 display no change in the local D_{3h} anion symmetry from $\beta \rightarrow \gamma$-$Na_4P_2S_6$, supporting the assumption of an intact $P_2S_6^{4-}$ unit at high temperature.

A direct structural solution of the γ-phase from the PXRD pattern is complicated by the incompatibility between the observed space group symmetry and the lower symmetry of the $P_2S_6^{4-}$ anions. Therefore, we turned to the pair distribution function (PDF) analysis[40,41] of synchrotron diffraction data to determine possible configurations to describe the local structure. Figure 6.3a shows the experimental PDF of γ-$Na_4P_2S_6$ at ∼650 °C. Sharp peaks observed at 2.048 and 3.392 Å can be assigned to P–P/P–S and S–S (i–iii) atom-pair distances within the $P_2S_6^{4-}$ anion. Another sharp peak at 2.801 Å can be assigned to the nearest-neighbor Na–S atom pairs. The peaks expected to correspond to pairs of S atoms located at opposite ends of the anion are not distinctly observed, which may suggest disorder of the anion dihedral angle.

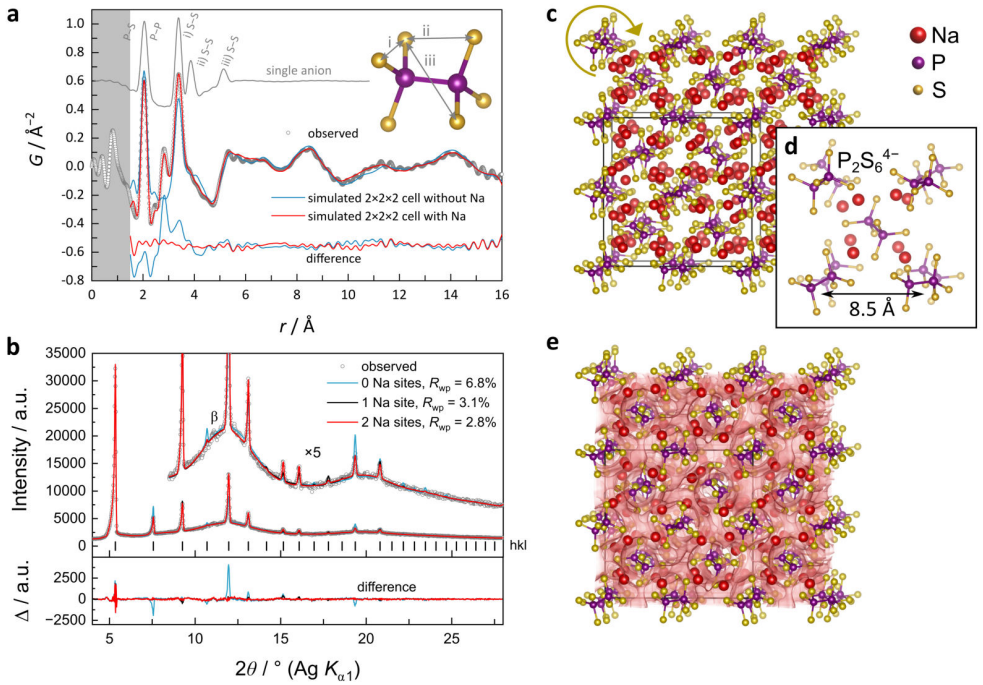

Figure 6.3: (a) Experimental synchrotron PDF with PDFs simulated from the fitted structure model and $P_2S_6^{4-}$ anion only and (b) Rietveld fit of the PXRD pattern for γ-$Na_4P_2S_6$ at 650 °C. (c) Illustration of the PDF-refined γ-structure with a static approximation of the $P_2S_6^{4-}$ anions in a 2×2×2 cell, and (d) in a single unit cell. (e) Overlay of bond valence energy landscape (red surface) and the crystal structure visualizing the 3-dimensional Na^+ conducting pathways.

Above 6 Å, the features in the PDF are broad and low-intensity, in contrast to the PDFs measured for the α and β phases (see Appendix C Figure C.4). In line with the body-centered cubic (bcc) space group from indexing, a pseudo-cubic model was constructed, with $P1$ space group symmetry, in which the $P_2S_6^{4-}$ anion barycenters are translationally fixed on the lattice points. The rotational orientations about the lattice points were allowed to refine freely against the experimental PDF data. A single cell model ($Z' = 2$) gives good agreement to short-range distances and indicates that neighboring anions prefer not to align in the same orientation. However, the model fails when r is greater than the lattice parameter due to the fixed geometry of the second nearest neighbor anions. A $2 \times 2 \times 2$ supercell ($Z' = 16$) was further constructed to test against the data at longer distances. This model allows for a much larger distribution of relative anion orientations sampled at any given distance and also showed good agreement to the data up to approximately 16 Å. Overall, the data at higher distances prefer models with more orientational disorder. This suggests weak or no correlation between relative anion orientations at long distances (see Appendix C Figure C.5).

In order to generate a complete model that is compatible with the data, 8 Na sites were introduced to the single cell model (64 Na sites to the supercell model), and allowed to refine with restraints set for the distances of closest approach: 2.5 Å (Na–S), 3.4 Å (Na–P), and 3.5 Å (Na–Na). A unique set of positions could not be determined, but the refinements preferred the Na atoms to distribute throughout the "interstitial" space around the structure-forming anions, optimizing to give the best agreement to the preferred Na–S neighbor distance. The good agreement between simulated and experimental PDFs and resulting structure are shown in Figures 6.3a, c, d.

Inspired by the real-space model, Rietveld refinements were performed using the space group $Im\bar{3}m$ with a single anion fixed at the origin, giving 48 anions each at the corner and body-center position (mirroring free rotation of the anions averaged over all unit cells). Crystallographic data and refinement details, as well as atomic positions and displacement parameters are compiled in table C.1 and C.2 in Appendix C. The occupancy was fixed to $\frac{1}{48}$. Then Na atom sites were sequentially added and refined until the Bragg peaks could be reproduced. This resulted in two symmetry independent sites giving 96 positions each, with the occupancies constrained to give the expected stoichiometry (details in the Experimental Section). Similar to the model from PDF refinement, the Na atoms again distribute to fill the "interstitial" space around the structure-forming anions. The Rietveld fit is shown in Figure 6.3b. By comparison of the $Im\bar{3}m$ model to higher distances in real-space (see Appendix C Figure C.5), it is found to accurately reproduce the on-average pair-density fluctuations beyond ∼8 Å. For the real-space refinements, it was necessary to set up the models with separate intra- and intermolecular atomic displacement parameters to properly describe the correlated motion.[42] To test for disorder within the anions, separate parameters were defined to describe the peak widths of different atom-pair types.[43] We found that correlations between opposing S–S pairs were broader than other atom-pair contributions by a factor of more than 2, which further supports the hypothesis of torsional distortions (along the P–P bond) of the anions.

In a complementary approach to locate and count low-energy sites and possible migration pathways for Na^+, softBV (bond valence) analysis[44,45] was conducted for the PDF-derived static approximation in a $2 \times 2 \times 2$ cell. Figure 6.3e illustrates the BV landscape and reveals many of the possible interstitials that exceed the number of Na^+

by far. Therefore, the crystal structure offers a high number of vacancies, which are beneficial for fast ion conduction. A large number of alternative pathways can be found in this structure with energy barriers of comparable barrier heights of ∼230 meV.

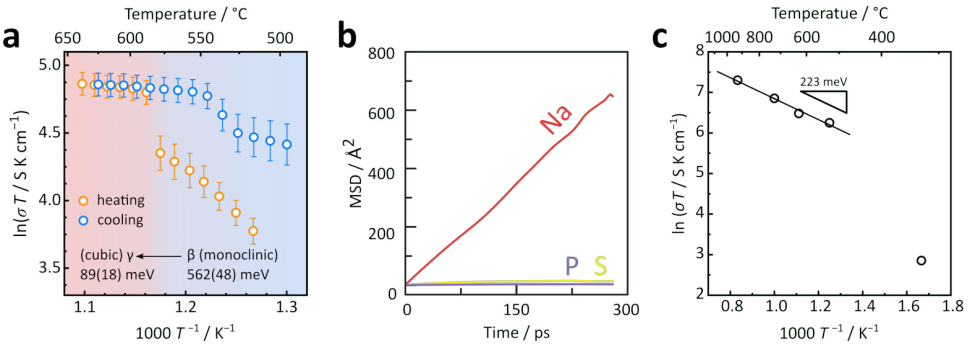

Figure 6.4: (a) Arrhenius plot of ionic conductivity and activation energies derived from impedance spectroscopy. The heating and cooling segments are indicated by orange and blue circles. The activation energy was extracted from the orange (heating) data points, since the cooling data points possibly describe a mixed ionic-electronic conducting (MIEC) phase. The error bars arise from the standard deviation of ionic conductivity measured on three distinct pellets. (b) Mean-squared displacements (MSD) of Na, P, and S at 1000 K from AIMD simulations. (c) Arrhenius plot of the ionic conductivity and activation energy from AIMD simulations.

After obtaining insights into the ion transport pathways of γ-$Na_4P_2S_6$ *via* BV modelling, an experimental characterization was attempted. High-temperature electrochemical impedance spectroscopy (EIS) measurements were performed on pellets of $Na_4P_2S_6$. The malleability of γ-$Na_4P_2S_6$ resulted in pellets being deformed under the slightest contact pressure, changing their thickness as a result, and even leaking out of the set-up. Additionally, the chemically aggressive nature of $Na_4P_2S_6$ had major implications on the corrosion of electrodes and contacts within a short amount of time. Contrary to good EIS measuring practice, the data shown here were obtained with low contact pressures on the pellets, short equilibration time and low temperature-step density, but, nevertheless, highlight the characteristics of the phase transition. The results of the measurement are presented in the Arrhenius plot of Figure 6.4a (see Appendix C Figure C.8 for exemplary spectra). For β-$Na_4P_2S_6$ (520 °C to 578 °C), an activation energy of 562(48) meV was found, which is slightly higher than the previously reported value obtained in measurements at lower temperature.[11] The β→γ transition at around 580 °C causes an abrupt increase in the ionic conductivity from 92(11) mS cm^{-1} to 140(12) mS cm^{-1}. The order of magnitude in ionic conductivities for β- and γ-$Na_4P_2S_6$ is comparable to Na_3PS_4, where the β→γ transition at 500 °C is accompanied with a jump from ∼40 mS cm^{-1} to ∼400 mS cm^{-1}.[39] γ-$Na_4P_2S_6$ exhibits a lower activation energy of about 89(18) meV, much lower than the BV calculated value on a rigid model, but comparable to γ-Na_3PS_4 (110(10) meV).[39] The behavior of ionic conduction is reversible on cooling, with a similar hysteresis of ∼40 K as found in the diffraction experiments. The extracted ionic conductivities upon cooling the

pellet are higher than for heating. This unusual behavior can be explained by accelerated decomposition of $Na_4P_2S_6$ at elevated temperatures. The visual appearance of the pellet changed from initially white to dark gray after cooling down. The aggressive nature of $Na_4P_2S_6$ at elevated temperatures is reflected in the corrosion of the platinum electrodes after the EIS measurement (see Images C.7). Presumably, $Na_4P_2S_6$ reacts with the Pt electrodes and forms some electronically conducting phases that increase the conductivity, leading to apparent lower activation energies compared to the heating cycle. Hence, the extraction of a true activation energy for ionic motion is vitiated for the cooling cycle. We suspect the loss of sulfur and the reaction of sodium ions with ceramic or quartz glass parts of our setups to be the origin of the accelerated decomposition of γ-$Na_4P_2S_6$ that we observed in some experiments. We refer to Appendix C for more details. Extrapolating the linear Arrhenius behavior of γ-$Na_4P_2S_6$ to 25 °C results in a room-temperature ionic conductivity of 50(24) mS cm^{-1}, similar to the findings of Famprikis *et. al.* for Na_3PS_4.[39] Despite our efforts to rapidly quench $Na_4P_2S_6$ from high temperature by submerging an ampule in ice water, we were not successful in stabilizing the cubic γ phase at room temperature.

So far, the experimental results strongly suggest plastic behavior of γ-$Na_4P_2S_6$, but do not yet distinguish a dynamic versus static nature of the rotational disorder of the $P_2S_6^{4-}$ anions. Therefore, the atomic motions of Na^+ and $P_2S_6^{4-}$ were tested using *ab initio* molecular dynamics (AIMD) simulations, with the PDF-derived 2×2×2 model as a starting point for optimization and subsequent MD calculations at different sampling temperatures (600–1200 K). The average mean-squared displacement of the atoms of Figure 6.4b supports the significant mobility of all Na^+, while P and S atoms do not undergo long-range motion. The calculated activation energy for Na^+ migration above 800 K (the MD calculation temperature) is 223 meV, though is again much higher than the experimentally obtained activation barrier (89(18) meV). For the 600 K calculation, the Na^+ diffusivity is many orders of magnitude smaller.

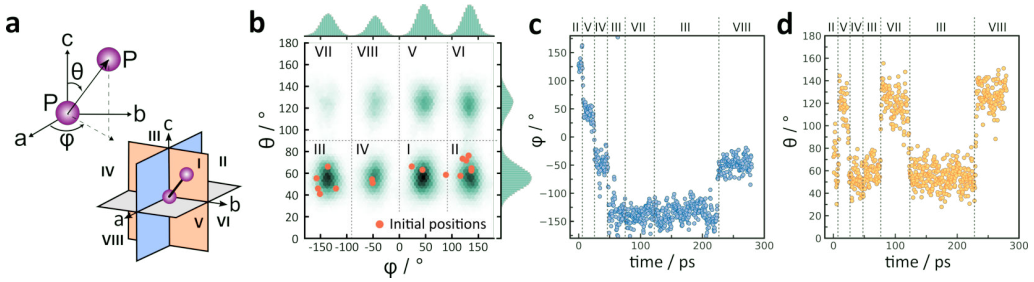

Figure 6.5: (a) Scheme of the definition of the azimuthal angle (ϕ) and polar angle (θ) with respect to the P–P handle, and scheme of the P–P orientation in Cartesian octants. (b) Orientation heatmap of all $P_2S_6^{4-}$ in a 2 × 2 × 2 cell at 1000 K in a 300 ps simulation. (c) Azimuthal angle (ϕ) and (d) polar angle (θ) as a function of time of an exemplary $P_2S_6^{4-}$ at 1000 K.

To determine the possibility for dynamic rotational motion of $P_2S_6^{4-}$ anions, the P–P bond orientations were tracked during the AIMD simulations. A detailed discussion about the analysis of the AIMD simulation can be found in Appendix C. The orientation of

individual P–P bonds within the cubic cell can be expressed in terms of azimuthal (ϕ) and polar (θ) angles as depicted in Figure 6.5a. Starting from P–P orientations marked as orange dots, the orientation of all 16 $P_2S_6^{4-}$ anions were tracked throughout the AIMD simulation and shown as a 2D histogram in Figure 6.5b. The polar coordinate system allows for the division of the observed eight clusters into eight octants as depicted at the bottom right in Figure 6.5a. Because the anions rotate about their center of mass, rather than the P atom fixed at the origin, octants related by inversion (*e.g.* octants II and VIII) signify the same orientation of the P–P handle with respect to the crystal lattice (but with inverted P atoms). Thus, the ensuing population of these initially empty octants indicates that significant reorientation of individual anions occurs. The four orientational groupings point approximately along the body diagonals of the cell. Notably, the population density of the 2D histogram at 1000 K is not uniform after the simulation time of 300 ps. With higher simulation temperature the population density approaches a more uniform distribution of orientations, as depicted in Figure C.9. Longer simulation runs would result in a similar picture, *i.e.* a more equal distribution of orientations.

Figure 6.5c and d illustrate the ϕ and θ angles of an exemplary anion from the AIMD simulations at 1000 K and enable the derivation of reorientation times of 20–100 ps. The time evolution of the azimuthal and polar angles of four other anions are illustrated in Figure C.10. Here, a direct comparison to plastic phases of sodium *closo*-borane $Na_2B_{12}H_{12}$ can be made: Just above the first-order transition from the low-T monoclinic to the high-T cubic phase near 520 K, the reorientational jump rate τ^{-1}, derived from NMR experiments, is 10^{11} Hz (equal to 10 ps),[27] a comparable value to the time between $P_2S_6^{4-}$ reorientations, although the different shape and size of the anions should be taken into account. Meanwhile, the Na^+ short-ranged hopping time was calculated to be ∼0.6 ps at 1000 K (see Appendix C, Figure C.13), two orders of magnitude faster than the anion motion.

Another degree of freedom for the anion is conformational freedom or rotation around the PS_3–PS_3 bond similar to ethane and its derivatives. This is measured as the dihedral angle spanned by S–P–P–S. The AIMD simulations suggest that the P–P bond rotation happens on a similar timescale as the directional reorientation of the entire anion. We refer to Appendix C for a more detailed analysis, including figures depicting the time and population evolution of the dihedral angle.

To summarize, while showing dynamic disorder, the orientation distribution after 300 ps suggests that the anions prefer to point roughly along the four body diagonals of their respective unit cells. This is in agreement with the on-average ($Im\bar{3}m$) structure obtained from Rietveld refinement, where the P–P bonds of all orientations on the lattice point overlap to form a roughly cubic distribution that is co-oriented with the crystallographic cell (see Appendix C). The results suggest that dynamic reorientation of the $P_2S_6^{4-}$ units occurs, consisting primarily of hops between the four body diagonal orientations of the cubic lattice. The frequency of the $P_2S_6^{4-}$ reorientation increases with the simulation temperature. Further analysis of this behavior suggests that reorientation of one anion does not necessarily induce a change in its neighbors' orientations.

6.4 Conclusion

In this work we have identified a new high-temperature phase transition at 580 °C in the thiophosphate Na^+ conductor $Na_4P_2S_6$. The phase transition is accompanied by a large latent heat, a change in crystal structure (from monoclinic $C2/m$ to cubic $Im\bar{3}m$), as well as a jump in sodium ion transport properties. A structure model with $P_2S_6^{4-}$ anions occupying the bcc lattice points was derived from pair distribution function analysis. The PDF structure model was used to simulate cation and anion dynamics with *ab initio* molecular dynamics. We demonstrate that while sodium shows a high diffusion coefficient in the AIMD simulation, the $P_2S_6^{4-}$ anions form a translationally fixed sublattice characterized by orientational disorder and the ability to dynamically reorient, primarily between the four body diagonal directions. $Na_4P_2S_6$ is malleable at high temperature and mechanically deforms under even slight compressive stress: a property in solid ion conductors that is unique to plastic phases. Altogether, the evidence suggests that γ-$Na_4P_2S_6$ is a new member of the plastic ionic conductors.

Despite the advantageous mechanical and conduction properties of plastic ion conductors, the temperatures needed to stabilize these phases are still far too high for operation in solid-state batteries. A key goal in solid-state battery chemistry is thus to stabilize such plastic phases at close to ambient temperature. Thus, further search and a detailed understanding of the underlying structure–property relationships of such phases will be necessary to identify plastic phases with lower transition temperatures.

6.5 Experimental methods

6.5.1 Preparation of $Na_4P_2S_6$

$Na_4P_2S_6$ can be prepared using two different synthesis routes. A solid-state reaction as described in Ref. [10] yields a very crystalline powder from which also single crystals can be extracted. Further, the solution synthesis *via* the hydrated compound $Na_4P_2S_6 \cdot 6\,H_2O$ as in Ref. [9] gives a powder product with stacking faults. The latter anneales above 500 °C to a product very similar to the solid-state material. The structural differences are discussed in detail in Ref. [11]. The $\beta \rightarrow \gamma$ phase transition is not affected by the $Na_4P_2S_6$ synthesis.

6.5.2 Variable-temperature powder X-Ray diffraction

Variable temperature powder X-Ray diffraction (PXRD) patterns were measured using a STOE StadiP diffractometer (Mo-$K_{\alpha 1}$ radiation ($\lambda = 0.7093$ Å), curved germanium (111) monochromator, DECTRIS Mythen2R 1K detector) with a STOE capillary furnace in Debye-Scherrer geometry. Fine powdered samples were filled in quartz glass capillaries of 0.5 mm diameter by Hilgenberg and sealed under argon. Data collection was done in the range from 2° to 62° 2θ with a step size of 0.015° in the temperature range of 510, 650, and 440 °C in steps of 5 K around the immediate $\beta \rightarrow \gamma$ phase transition and 10 K for more distant temperatures. The indexing of the powder patterns was performed with Jana2006[46] in space groups $C/2m$ and $Im\bar{3}m$ for β- and γ-$Na_4P_2S_6$, respectively. Errors of the results of the Rietveld refinements are specified as 3σ.

6.5.3 Total scattering measurements

Total scattering measurements were carried out using beamline P02.1 at PETRA III of the Deutsches Elektronen-Synchrotron (DESY). Data were collected in rapid acquisition mode[47] with a large-area 2D PerkinElmer detector (2048×2048 pixels, 200×200 μm^2 each) and sample-to-detector distance of 311.36 mm. The incident energy of the X-rays was 59.772 keV ($\lambda = 0.20743$ Å). Samples were loaded into 0.7 mm diameter quartz glass capillaries and measured at roughly 30 and 100–650 °C in increments of 50 °C. An empty capillary was measured to account for the background, and a LaB_6 standard was measured at room temperature for calibration of the setup. Sample temperature was controlled using a custom ceramic heater operated using a Eurotherm 2408 temperature controller. Calibration, polarization correction, and azimuthal integration to 1D diffraction patterns were performed using the software pyFAI.[48] Further correction, background subtraction, and normalization of the 1D diffraction intensities were carried out to obtain the total scattering structure function, $F(Q)$, which was Fourier transformed to the PDF, $G(r)$, using PDFgetX3 within xPDFsuite.[49,50] The maximum value of the momentum transfer Q used in the Fourier transform was 19.5 $Å^{-1}$. Additional total scattering measurements were performed using a Stoe Stadi-P diffractometer with Ag-$K\alpha 1$ radiation ($\lambda = 0.55941$ Å), a Ge(111) Johann monochromator, and an array of three DECTRIS Mythen 1K detectors measured at two different positions in Debye-Scherrer geometry. The temperature was controlled using a hot air blower from FMB Oxford. Data were directly corrected for the 2θ offset of the instrument, polarization, and background scattering.

6.5.4 Pair distribution function and Rietveld refinements

Pair distribution function (PDF) refinements were carried out using TOPAS Academic v6.[51,52] In all refinements, the $P_2S_6^{4-}$ anions were set up as rigid bodies defined by the P–P and P–S bond lengths and P–P–S bond angle. Anion positions were fixed at the lattice points but allowed to rotate freely about their center of mass. When added, Na atom positions were allowed to be refined with anti-bump constraints set to prevent unrealistic distances. PDF refinements were performed in $P1$ symmetry with either two separate anions (single cell model) refined over 1.5–7 Å, or sixteen separate anions (supercell model) refined over 1.5–16 Å. The damping of the experimental signal due to instrumental resolution and effects of data truncation were accounted for and fixed, and the lattice parameter and scale factor were refined. B_{iso} was fixed to 2.0 Å^2 for S and P atoms, and separate intramolecular pair linewidths were described with five parameters corresponding to P–P, bonding P–S, adjacent S–S, non-bonding P–S, and opposing S–S, to account for intra-anion disorder.[43] Since Na atoms only show correlation at short distances, the partial pair widths were described using an empirical function ($x_1 + x_2 r + x_3 r^2$) that allows for high correlation with neighbor atoms at short distances and progression to low structural correlation at higher distances.

Rietveld refinements[53,54] were performed with the $Im\bar{3}m$ model refined over a range of 4–28° 2θ. The background was described using Chebychev polynomials of 19th order. The Lorentz-Polarization factor was set to 9.825. A zero-error correction was refined to correct for detector offset, and a simple axial model was used to describe the instrumental peak shape along with Gaussian and Lorentzian components for crystallite size and strain broadening. The lattice parameter, global scaling factor, and two separate isotropic displacement parameters for Na and S/P were additionally refined. Convergence of the reciprocal- and real-space refinements was achieved using the global optimization method of simulated annealing in real space.[55]

6.5.5 Differential scanning calorimetry

For Differential Scanning Calorimetry (DSC) measurements 50 mg of fine powdered sample were sealed in quartz ampules (6 mm diameter, 10 to 15 mm in height) under vacuum. For improved heat flow ampules with a flat bottom were used. DSC measurements were performed on a NETZSCH STA 449 F5 Jupiter in a temperature range of 30–850 °C. The heating rate for all segments was set to 20 K min^{-1}. This rate is a good tradeoff between measurement stability (rate linearity) and sensitivity. Data evaluation was performed using the NETZSCH software package Proteus.

6.5.6 Electrochemical impedance spectroscopy

Electrochemical impedance spectroscopy (EIS) measurements were performed using a NOVOCONTROL TECHNOLOGIES Alpha-A analyzer. For sample preparation fine powder of $Na_4P_2S_6$ (ca. 70 mg) was pressed uniaxially at 1 GPa into pellets of 6 mm diameter. Both sides of the pellets were sputtered with platinum to ensure electrical contact during the the high-temperature impedance measurement. Pellets were placed between two lithium ion blocking platinum electrodes and loaded onto an in-house built cell. To prevent the deformation of the pellet due to mechanical softening in the γ phase, the pellet was placed in a hole in a ceramic spacer of 1 mm height. This has proven to give reproducible results that are only affected by sample decomposition and corrosion of the electrode by sulfur at high temperature. The equilibration time prior to each impedance measurement at the programmed temperature steps was set to 15 min. A short equilibration time translates into a shorter time the sample is exposed to high temperatures. This was necessary as the sample decomposes within in day at 600 °C or above. On the other hand, short equilibration times bear the difficulty of measuring in a non-equilibrium state, that can result in visible drifts in long impedance measurements. Hence, the spectra were recorded in a frequency range of 1 MHz to 10 Hz and with an applied voltage of $V_{\mathrm{RMS}} = 100$ mV. The spectra were recorded between 500–640 °C. Data treatment and evaluation was performed using the RHD INSTRUMENTS software package RelaxIS 3. To check data reliability Kramers-Kronig relation tests were performed prior to fitting. Fitting the impedance spectra to equivalent circuits was done by weighting the data points proportionally. Given error bars stem from error propagation of uncertainties in pellet geometric area, pellet thickness, and applied temperature as well as errors in resistance obtained by equivalent circuit fitting.

6.5.7 Raman spectroscopy

Temperature dependent Raman spectra were recorded using a Jobin Yvon Type 010 labram single grating spectrometer equipped with a double super razor edge filter. Data collection was performed with a peltier cooled CCD camera (spectral resolution: 1 cm^{-1}).

6.5.8 Computational methods

DFT simulations were performed using the Vienna *ab initio* Simulation Package.[56,57] The unknown exchange correlation energy in DFT was approximated by the generalized gradient approximation,[58] and van der Waals forces were captured using the Grimme scheme.[59] Valence electrons were expanded as plane-waves with a maximum kinetic energy of 520 eV, and DFT total energies integrated at the Γ-point. Core electrons were described with projected augmented wave potentials,[60,61] treating the following electrons explicitly: Na ($2s^1$), S ($3s^2 3p^4$) and P ($3s^2 3p^3$).

Starting from the PDF-derived crystal structures of γ-$Na_4P_2S_6$ ($2 \times 2 \times 2$ cell), all $P_2S_6^{4-}$ units were oriented along the $\langle 111 \rangle$ directions and being perpendicular with each other in the (100) and (010) planes. Then a structure optimization was performed until the interatomic forces are less than 0.01 eV/Å while keeping the cell volume fixed to that derived from the temperature dependent diffraction experiments.

Using the DFT-optimized γ-$Na_4P_2S_6$ model, canonical (NVT) ensemble *ab initio* molecular dynamics (AIMD) simulations were performed at selected temperatures of 600, 800, 900, 1000 and 1200 K, respectively. The NVT ensemble was achived via a Nosé–Hoover thermostat[62,63] with a 2 fs time step. The simulations were initialized at 100 K, and temperatures were ramped to target values within 2 ps. MD runs were performed with a production time of 600 ps (for 600 and 800 K) and 300 ps (for 1000 and 1200 K). Trajectories were collected for the data analysis excluding the initial period of 20 ps for equilibration.

References

(1) Wiberg, N., *Lehrbuch der Anorganischen Chemie*; De Gruyter: 2008.

(2) Yang, Y.; Song, M.; Wu, X.; Wu, K. *J. Phys. D* **2021**, *54*, 463002.

(3) Jansen, M.; Henseler, U. *J. Solid State Chem.* **1992**, *99*, 110–119.

(4) Hayashi, A.; Noi, K.; Sakuda, A.; Tatsumisago, M. *Nat. Commun.* **2012**, *3*, 856.

(5) Hayashi, A.; Noi, K.; Tanibata, N.; Nagao, M.; Tatsumisago, M. *J. Power Sources* **2014**, *258*, 420–423.

(6) Krauskopf, T.; Culver, S. P.; Zeier, W. G. *Inorg. Chem.* **2018**, *57*, 4739–4744.

(7) Rush, L. E.; Holzwarth, N. A. W. *Solid State Ion.* **2016**, *286*, 45–50.

(8) Rush, L. E. J. First-Principles Investigation of Electronic Properties in Sodium-Ion Electrolytes for Solid-State Battery Materials, Thesis, 2017.

(9) Fincher, T.; LeBret, G.; Cleary, D. A. *J. Solid State Chem.* **1998**, *141*, 274–281.

(10) Kuhn, A.; Eger, R.; Nuss, J.; Lotsch, B. V. *Z. Anorg. Allg. Chem.* **2014**, *640*, 689–692.

(11) Scholz, T.; Schneider, C.; Eger, R.; Duppel, V.; Moudrakovski, I.; Schulz, A.; Nuss, J.; Lotsch, B. V. *J. Mater. Chem. A* **2021**, *9*, 8692–8703.

(12) Timmermans, J. *J. Phys. Chem. Solids* **1961**, *18*, 1–8.

(13) Lunkenheimer, P.; Michl, M.; Loidl, A. In *J. Adv. Dielectr.* Springer International Publishing: 2018, pp 277–300.

(14) MacFarlane, D. R.; Forsyth, M. **2001**, *13*, 957–966.

(15) Tsang, T.; Farrar, T. C. *J. Chem. Phys.* **1969**, *50*, 3498–3502.

(16) Matsuo, M.; Nakamori, Y.; Orimo, S.-I.; Maekawa, H.; Takamura, H. *Appl. Phys. Lett.* **2007**, *91*, 224103.

(17) Hagemann, H.; Gomes, S.; Renaudin, G.; Yvon, K. *J. Alloys Compd.* **2004**, *363*, 129–132.

(18) Nilsson, L.; Thomas, J. O.; Tofield, B. C. *J. Phys., C, Solid state Phys.* **1980**, *13*, 6441–6451.

(19) Aronsson, R.; Jansson, B.; Knape, H. E. G.; Lundén, A.; Nilsson, L.; Sjöblom, C.-A.; Torell, L. M. *J. Phys. Colloq.* **1980**, *41*, C6-35-C6–37.

(20) Boerjesson, L.; Torell, L. M. *Phys. Rev. B* **1985**, *32*, 2471–2477.

(21) Lundén, A. *Solid State Ion.* **1988**, *28-30*, 163–167.

(22) Jansen, M. *Angew. Chem. Int. Ed.* **1991**, *30*, 1547–1558.

(23) Witschas, M.; Eckert, H.; Wilmer, D.; Banhatti, R.; Funke, H.; Fitter, J.; Lechner, R. E.; Korus, G.; Jansen, M. *Z. Phys. Chem.* **2000**, *214*, 643–673.

(24) Kniaź, K.; Fischer, J. E.; Zhu, Q.; Rosseinsky, M. J.; Zhou, O.; Murphy, D. W. *Solid State Commun.* **1993**, *88*, 47–50.

(25) Tanigaki, K.; Hirosawa, I.; Manako, T.; Tsai, J. S.; Mizuki, J.; Ebbesen, T. W. *Phys. Rev. B* **1994**, *49*, 12307–12310.

(26) Saito, T.; Maniwa, Y.; Oda, H.; Kume, K.; Kosaka, M.; Hirosawa, I.; Tanigaki, K. *J. Phys. Soc. Japan* **1995**, *64*, 4513–4517.

(27) Skripov, A. V.; Babanova, O. A.; Soloninin, A. V.; Stavila, V.; Verdal, N.; Udovic, T. J.; Rush, J. J. *J. Phys. Chem. C.* **2013**, *117*, 25961–25968.

(28) Udovic, T. J.; Matsuo, M.; Unemoto, A.; Verdal, N.; Stavila, V.; Skripov, A. V.; Rush, J. J.; Takamura, H.; Orimo, S.-i. *Chem. Commun.* **2014**, *50*, 3750–3752.

(29) Kweon, K. E.; Varley, J. B.; Shea, P.; Adelstein, N.; Mehta, P.; Heo, T. W.; Udovic, T. J.; Stavila, V.; Wood, B. C. *Chem. Mater.* **2017**, *29*, 9142–9153.

(30) Udovic, T. J.; Matsuo, M.; Tang, W. S.; Wu, H.; Stavila, V.; Soloninin, A. V.; Skoryunov, R. V.; Babanova, O. A.; Skripov, A. V.; Rush, J. J.; Unemoto, A.; Takamura, H.; Orimo, S.-I. *Adv. Mater.* **2014**, *26*, 7622–7626.

(31) Tang, W. S.; Unemoto, A.; Zhou, W.; Stavila, V.; Matsuo, M.; Wu, H.; Orimo, S.-i.; Udovic, T. J. *Energy Environ. Sci.* **2015**, *8*, 3637–3645.

(32) Dimitrievska, M.; Stavila, V.; Soloninin, A. V.; Skoryunov, R. V.; Babanova, O. A.; Wu, H.; Zhou, W.; Tang, W. S.; Faraone, A.; Tarver, J. D.; Trump, B. A.; Skripov, A. V.; Udovic, T. J. *J. Phys. Chem* **2018**, *122*, 15198–15207.

(33) Famprikis, T.; Dawson, J. A.; Fauth, F.; Clemens, O.; Suard, E.; Fleutot, B.; Courty, M.; Chotard, J.-N.; Islam, M. S.; Masquelier, C. *ACS Mater. Lett.* **2019**, *1*, 641–646.

(34) Saha, S.; Rousse, G.; Courty, M.; Shakhova, Y.; Kirsanova, M.; Fauth, F.; Pomjakushin, V.; Abakumov, A. M.; Tarascon, J. M. *Inorg. Chem.* **2020**, *59*, 6528–6540.

(35) Geirhos, K.; Lunkenheimer, P.; Michl, M.; Reuter, D.; Loidl, A. *J. Chem. Phys.* **2015**, *143*, 081101.

(36) Vaalma, C.; Buchholz, D.; Weil, M.; Passerini, S. *Nat. Rev. Mater.* **2018**, *3*, 18013.

(37) Haynes, W., *CRC Handbook of Chemistry and Physics*; CRC Press: 2016, pp 14–17.

(38) Meilander, B. E.; Nilsson, L. *Z. Naturforsch. A* **1983**, *38*, 1396–1399.

(39) Famprikis, T.; Dawson, J. A.; Fauth, F.; Clemens, O.; Suard, E.; Fleutot, B.; Courty, M.; Chotard, J.-N.; Islam, M. S.; Masquelier, C. *ACS Mater. Lett.* **2019**, *1*, 641–646.

(40) Egami, T.; Billinge, S. J. L., *Underneath the Bragg peaks: structural analysis of complex materials*, 2nd; Elsevier: Amsterdam, 2012.

(41) Terban, M. W.; Billinge, S. J. L. *Chem. Rev.* **2022**, *122*, 1208–1272.

(42) Prill, D.; Juhás, P.; Schmidt, M. U.; Billinge, S. J. L. *J. Appl. Cryst.* **2015**, *48*, 171–178.

(43) Terban, M. W.; Russo, L.; Pham, T. N.; Barich, D. H.; Sun, Y. T.; Burke, M. D.; Brum, J.; Billinge, S. J. L. *Mol. Pharmaceutics* **2020**, *17*, 2370–2389.

(44) Adams, S.; Rao, R. P. *Phys. Status Solidi A* **2011**, *208*, 1746–1753.

(45) Chen, H.; Wong, L. L.; Adams, S. *Acta Cryst. B* **2019**, *75*, 18–33.

(46) Petříček, V.; Dušek, M.; Palatinus, L. *Z. Kristallogr.* **2014**, *229*, 345–352.

(47) Chupas, P. J.; Qiu, X.; Hanson, J. C.; Lee, P. L.; Grey, C. P.; Billinge, S. J. L. *J. Appl. Crys.* **2003**, *36*, 1342–1347.

(48) Kieffer, J.; Ashiotis, G.; Deschildre, A.; Nawaz, Z.; Wright, J. P.; Karkoulis, D.; Picca, F. E. *J. Appl. Crys.* **2015**, *48*, 510–519.

(49) Juhás, P.; Davis, T.; Farrow, C. L.; Billinge, S. J. L. *J. Appl. Crys.* **2013**, *46*, 560–566.

(50) Yang, X.; Juhás, P.; Farrow, C.; Billinge, S. J. L. **2015**, *arXiv:1402.3163*.

(51) Coelho, A. A.; Chater, P. A.; Kern, A. *J. Appl. Crys.* **2015**, *48*, 869–875.

(52) Coelho, A. A. *J. Appl. Cryst.* **2018**, *51*, 210–218.

(53) Rietveld, H. M. *J. Appl. Cryst.* **1969**, *2*, 65–71.

(54) Dinnebier, R. E.; Leineweber, A.; Evans, J. S. O., *Rietveld Refinement: Practical Powder Diffraction Pattern Analysis Using TOPAS*, 1st; De Gruyter STEM: Berlin, 2019.

(55) Coelho, A. A. *J. Appl. Cryst.* **2000**, *33*, 899–908.

(56) Kresse, G.; Furthmüller, J. *Phys. Rev. B* **1996**, *54*, 11169–11186.

(57) Kresse, G.; Furthmüller, J. *Comput. Mater. Sci.* **1996**, *6*, 15–50.

(58) Perdew, J. P.; Burke, K.; Ernzerhof, M. *Phys. Rev. Lett.* **1996**, *77*, 3865–3868.

(59) Grimme, S.; Antony, J.; Ehrlich, S.; Krieg, H. *J. Chem. Phys.* **2010**, *132*, 154104.

(60) Blöchl, P. E. *Phys. Rev. B* **1994**, *50*, 17953–17979.

(61) Kresse, G.; Joubert, D. *Phys. Rev. B* **1999**, *59*, 1758–1775.

(62) Nosé, S. *J. Chem. Phys.* **1984**, *81*, 511–519.

(63) Hoover, W. G. *Phys. Rev. A* **1985**, *31*, 1695–1697.

CHAPTER 7

Impact of hydration on ion transport in $Li_2Sn_2S_5 \cdot xH_2O$

Markus Joos, Christian Schneider, Andreas Münchinger, Igor Moudrakovski, Robert Usiskin, Joachim Maier and Bettina Valeska Lotsch

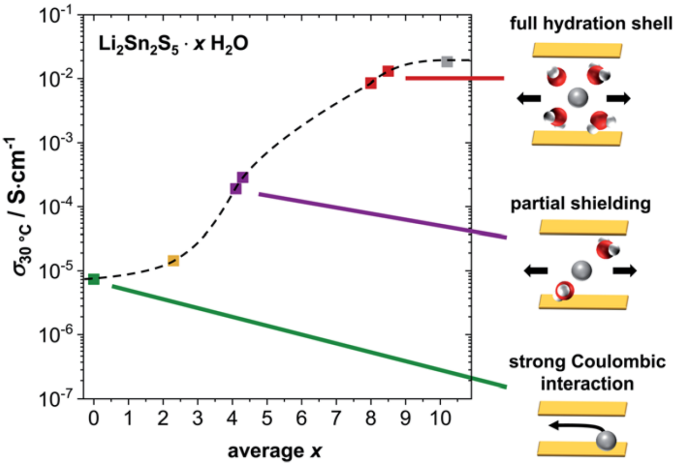

This work was published in and adopted from:
Journal of Materials Chemistry A **2021**, *9*, 16532-16544.

Supporting information can be found in Appendix D.
Author contributions can be found in Appendix F.

Contents of Chapter 7

7.1 Abstract

This work investigates the structure and transport properties of the layered material $Li_2Sn_2S_5 \cdot xH_2O$. The anhydrous phase shows a room-temperature Li^+ diffusivity below $10^{-9}\,cm\,s^{-2}$ and conductivity below $10^{-5}\,S\,cm^{-1}$. Upon exposure to humidity, water intercalates between the layers and increases the interlayer distance, inducing first-order transitions to a hydrated phase ($x \approx 2$–4) and then to a second hydrated phase ($x \approx 8$–10). The latter is soft and sticky but remains solid. Diffusion of both Li^+ ions and H_2O remains predominantly two-dimensional under all conditions. The Li^+ diffusivity and conductivity both increase by three orders of magnitude upon hydration, reaching values of $5 \cdot 10^{-7}\,cm\,s^{-2}$ and $10^{-2}\,S\,cm^{-1}$ in the second hydrate. These transport rates are extraordinary for a solid electrolyte and approach what is typically seen in aqueous solutions. The material $Li_2Sn_2S_5 \cdot xH_2O$ thus bridges the gap between a hydrated solid electrolyte and a confined liquid electrolyte, which is scientifically interesting and potentially useful in battery applications. In the light of these findings, a previous work on $Li_2Sn_2S_5$ from our groups is revisited.

7.2 Introduction

Hydration is relevant for both fundamental science and technological applications because it can strongly modify the charge transport properties of materials. In general, the reversible incorporation of water can proceed by a dissociative or a molecular mechanism. Dissociative incorporation is frequently encountered in oxides, hydroxides, and apatites,[1] and it leads to the formation of OH species, which are often accommodated on oxygen sites. Molecular incorporation of H_2O can arise in a broad range of structures, including oxides with roomy structures.[2,3] Criteria as to whether water is incorporated in a dissociative or non-dissociative way are based on site and bond properties.[4] Both mechanisms frequently lead to a substantial increase in H^+ conductivity, as seen in a variety of materials including minerals[5–13] and polymers.[14,15] Some of these materials (Nafion, Y-doped $BaZrO_3$) play a crucial role in state-of-the-art electrochemical devices. Hydration can also promote the transport of other cations besides protons. For example, perfluorinated ionomer membranes can be converted by ion exchange into single-ion conductors for various cations.[16,17] Similarly, layered silicate compounds can be converted into Li^+, Na^+, Mg^{2+} or Ca^{2+} conductors. Water uptake can influence the cation mobility by solvation or by modifying the crystallographic geometry, usually by incorporating water into the SiO_2–Al_2O_3 sheets and consequent coordination to the present cation, which increases the interlayer distance.[5–13] The ability to undergo cation exchange is a general feature of layered structures and is observed in various chemical compositions.[18–20] The two-dimensional (2D) arrangement must remain intact after hydration for the cations in the interlayer galleries to remain highly mobile.[21] Another example is Li-exchanged Nafion, which shows high Li^+ conductivity when hydrated.[22] In the case of solid Li^+ and Na^+ conductors, hydration studies are rather scarce[23–29] and tend to suggest that water uptake promotes Li^+ and Na^+ conduction;[30] one recent paper reported a material in which the opposite is true.[29] The compound $Li_2Sn_2S_5$ is a good candidate for hydration studies. In an initial report, $Li_2Sn_2S_5$ was shown to be a layered material consisting of

covalently-bonded (and partially Li-substituted) tin sulfide sheets which are held together by ionic bonds to interlayer Li^+ ions.[31] Upon immersion in water, the ionic bonds are disrupted, and the material exfoliates into a suspension of monolayer sheets. A follow-up work explored reassembling the exfoliated sheets as part of a Bragg stack.[32] The water content, interlayer spacing, and optical properties of the restacked sheets were shown to be sensitive to the surrounding water partial pressure, a property that can be used for humidity sensing. Another work characterizing the structure and ion transport properties of the restacked material is forthcoming.[33] A fourth work confirmed by XRD refinement that 75% of the Li^+ ions are on interlayer sites ($Li^+_{\parallel}$), while the remaining 25% substitute onto Sn^{4+} sites within the sheets ($Li^+_{\perp}$), such that the available interlayer Li^+ sites are only 38% occupied.[34] Accordingly, the general formula of this solid solution system can be written $(Li_{\parallel})_{3z}[(Li_{\perp})_z Sn_{1-z}S_2]$. That work also reported that $Li_2Sn_2S_5$ shows fast Li^+ diffusion,[34] which raises questions about the mechanism and about whether the transport properties can be further improved by hydration. One can be optimistic that the material will not decompose, since other lithium tin sulfides are reportedly stable under air and moisture[35–41] (unlike the thiophosphates),[39–55] while Li_4SnS_4 and other alkali tin sulfides can form stable hydrates.[35,56] Here we show that the water content in $Li_2Sn_2S_5 \cdot xH_2O$ can be varied from $x = 0$ to 10 by adjusting the humidity. The material undergoes first-order phase transitions to two hydrated phases, but the layered structure remains largely intact. Pulsed-field gradient nuclear magnetic resonance (PFG NMR) reveals that the Li^+ transport remains predominantly 2D at all water contents. The transport in the anhydrous material is far slower than previously reported. NMR and impedance spectroscopy measurements reveal strong increases in the Li^+ mobility, Li^+ conductivity, and H_2O mobility with increasing water content. The fully hydrated compound remains solid, but exhibits liquid-like Li^+ conductivity and Li^+ diffusivity values of $10^{-2}\,S\,cm^{-1}$ and $10^{-7}\,cm\,s^{-2}$ at room temperature. These transport rates are extraordinary in a solid and approach what is seen in concentrated aqueous electrolytes.[57] The amount of water incorporated is sufficient to provide the interlayer Li^+ ions with a full hydration shell. Connections between the behavior of hydrated layered solids and confined concentrated liquids are discussed, and the final two sections re-evaluate our previous work on $Li_2Sn_2S_5$ and offer an outlook for applications.

7.3 Results

7.3.1 TGA and XRD: hydration study

A typical measurement of the water content x in $Li_2Sn_2S_5 \cdot xH_2O$ is shown in Figure 7.1a. The thermogravimetric analyzer (TGA) can resolve changes in x of about 0.01 or larger. After an increase in the water partial pressure p_{H_2O}, x stabilizes at a higher value on a typical timescale of several hours. Dehydration steps show far longer stabilization times, on the order of tens of hours. Due to the sluggish kinetics, for practical reasons the humidity was usually switched at the onset of a plateau in the mass–time trace, before the mass had truly stabilized. Follow-up experiments with longer dwell times suggest that the error in x introduced by this approach is below 0.1 (Figure D.4a). A substantial contribution from surface adsorption is unlikely in light of the slow kinetics and the large particle size ($\sim 50\,\mu m$). The variation of water content with humidity and temperature is summarized in Figure 7.1b. Values of x in the range 0.4 to 1.6 do not appear, which suggests the presence of a miscibility gap, *i.e.*, a first-order phase transition. The position of the phase boundary can be estimated by averaging the steepest and shallowest lines that fall between the brown and blue points in Figure 7.1b. If the water content changes across the transition by y molecules of H_2O per formula unit, the law of mass action can be written:

$$K_h = \left(\frac{p_{H_2O}}{1\,bar}\right)^{-y} = \exp\left(-\frac{(\Delta_h H^\circ - T\Delta_h S^\circ)}{k_B T}\right) \tag{7.1}$$

where K_h is the equilibrium constant, $\Delta_h H^\circ$ and $\Delta_h S^\circ$ are the standard enthalpy and entropy of the transition, and k_B and T are the Boltzmann constant and temperature. Fitting the boundary line by this equation yields (-0.52 ± 0.03) eV and (-1.20 ± 0.09) meV K^{-1} for the standard enthalpy and entropy, normalized per mole of water. The intervals give the range of possible values that are consistent with the data in Figure 7.1b. Similar values are reported for dissociative hydration of perovskite oxides (about -0.65 eV and -1.4 meV K^{-1}).[58] The phase with $x \leq 0.4$ is hereafter denoted 'anhydrous', with the understanding that this term is not strictly correct under all conditions.

Samples that are cycled between the anhydrous and hydrated ($x \approx 2$–3) states show a small but reproducible hysteresis. Specifically, the dehydration steps require a higher temperature by 20-30 °C than the rehydration steps (Figure D.1 and D.2). Similar hysteresis is observed in isothermal measurements (Figure D.3). Hydrolysis can be ruled out, as discussed in Appendix D.

Figure 7.2a shows XRD patterns measured from ten powder samples with different average water contents. The pattern obtained for $x = 0$ shows good agreement to that reported previously for anhydrous $Li_2Sn_2S_5$.[34] A few small additional reflections are visible, which likely arise from stacking faults.[59,60] This attribution is supported by XRD patterns acquired from a single anhydrous particle, which show multiple diffraction spots in close proximity, consistent with some degree of stacking faults, twinning, and/or mosaicism (Figure D.16a). From the published structural determination, the reflection at 6.5° can be attributed to (001) planes. Using that reflection, the interlayer distance d is found from Bragg's law to be 6.24 Å, similar to the value of 6.17 Å obtained previously (Figure 7.2b). The samples with an average water content of 1.0, 1.6, and 1.9 show similar patterns as

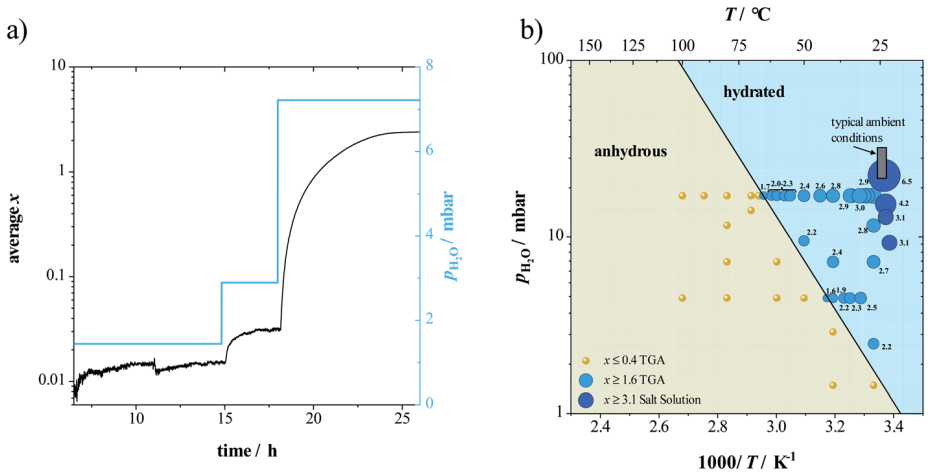

Figure 7.1: Average water content x in $Li_2Sn_2S_5 \cdot xH_2O$. (a) Typical gravimetric data (after buoyancy correction) measured under isothermal conditions (here 39 °C) while varying the absolute humidity p_{H_2O}. (b) Dependence of x on p_{H_2O} and temperature, as measured using a TGA (brown and light blue circles) or a balance and salt solutions (dark blue circles). Black line shows the estimated boundary between the anhydrous and hydrated phases. Typical ambient conditions are also shown, assuming a relative humidity of 50–70%.

the anhydrous sample, except a new reflection appears at 4.9°, and the intensity of the reflection at 6.5° is somewhat smeared to lower angles. With increasing x, the reflection intensity increases at 4.9° and decreases at 6.5°, until at $x = 2.7$ the reflection at 6.5° is entirely absent. This behavior is consistent with a first-order phase transition to a hydrated phase with an interlayer distance of 8.4 Å.

The patterns at $x = 2.7$–3.4 show no additional reflections, suggesting that in this range a single phase is present into which water is miscible. New reflections appear and increase in intensity when the average water content is increased to $x = 5.9$ or 7.4, and they are the only reflections visible at $x = 10.5$, consistent with a first-order transition to a second hydrated phase. Assuming the reflection at 3.7° corresponds to (001) planes, an interlayer distance of 11.1 Å is obtained. Thus, upon hydration, the interlayer distance jumps by 2.0 Å when transitioning to the first hydrate, and it jumps by another 2.7 Å when transitioning to the second hydrate. The latter jump matches the diameter of an oxygen ion in a water molecule (about 2.7 Å).[61] The interlayer distance remains essentially constant within the single-phase ranges ($x \approx$ 2-4 for the hydrated phase, $x \approx$ 8–10 for the swollen phase), suggesting that in these ranges, incorporation is accommodated by denser packing of the water molecules rather than swelling of the material. Pattern refinements and a more detailed structural discussion will be given in a future work.

In terms of mechanical properties, the material remains solid up to $x = 10.5$ but becomes noticeably softer and stickier with increasing water content. At high water contents ($x \geq 7.4$), it seemed possible to squeeze some water out of the material by the

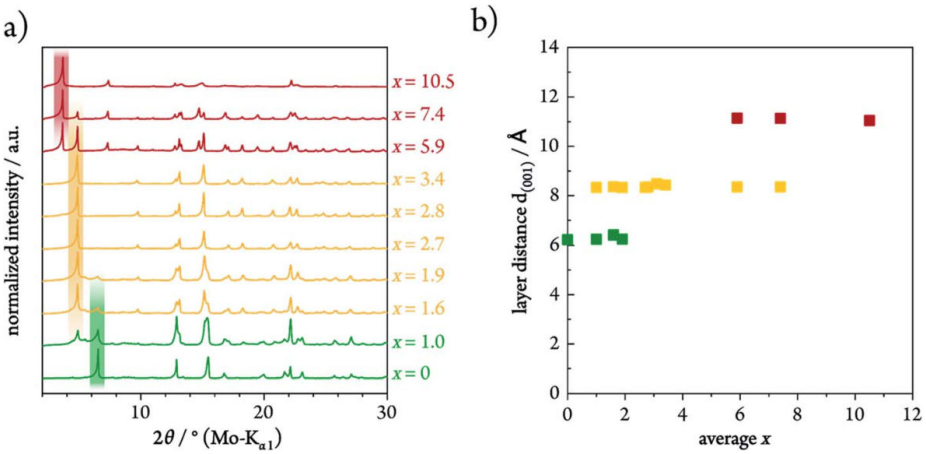

Figure 7.2: (a) Powder X-ray diffraction patterns of $Li_2Sn_2S_5 \cdot xH_2O$ samples with increasing degree of hydration. The patterns are vertically offset to facilitate comparisons. (b) Distance between (001) planes inferred from the patterns in (a).

application of pressure. At $x > 11$ the material was deliquescent and became a solid-liquid composite; this situation was observed at the saturation pressure of water (40-120 mbar) at 30-50 °C.

7.3.2 NMR: Li^+ and H^+ diffusion

$Li_2Sn_2S_5 \cdot xH_2O$ has a layered structure, so anisotropic properties are expected. Electron density analysis of anhydrous $Li_2Sn_2S_5$ predicted a far higher Li^+ diffusivity in-plane than out-of-plane.[34] To test this suggestion, the normalized echo signal attenuation data obtained by PFG NMR can be fit by a standard isotropic 3D model with a single diffusivity,[62] as well as an anisotropic 2D model with different in-plane and out-of-plane diffusivities.[63] For all water contents, the 2D model yields visually satisfactory fits (Figure 7.3), acceptable values of the goodness of fit, and reasonable confidence intervals for the fit parameters. In contrast, the 3D model leads to substantially worse fits (Figure D.6). Additional models were also attempted and discarded. By averaging over all possible crystal orientations, the effective Li^+ diffusivity $D^*_{\text{eff}}(Li^+)$ of a polycrystalline sample is obtained. More details are given in Appendix D.

The dependence of $D^*_{\text{eff}}(Li^+)$ on temperature and average water content is shown in Figure 7.4. The overall trend is clear: the Li^+ diffusivity increases monotonically with increasing x. For $x \approx 8.0$, the diffusivity reaches $5 \cdot 10^{-7}\,\text{cm}\,\text{s}^{-2}$ at room temperature, which is three orders of magnitude higher than the corresponding (extrapolated) value for the anhydrous material. Similar results are obtained when the diffusion time in the PFG measurement is increased from 10 to 100 ms (see also Figure D.5). The activation energy determined from the linear fits in Figure 7.4a is 0.28, 0.29, 0.28, and 0.31 eV for the $x \approx 0$, 2.3, 4.0, and 8.0 samples. The fact that the activation energy is nearly constant suggests that the faster diffusivity is due to an increased exponential pre-factor, and specifically an increased attempt frequency, since the entropy of migration is expected to be small.

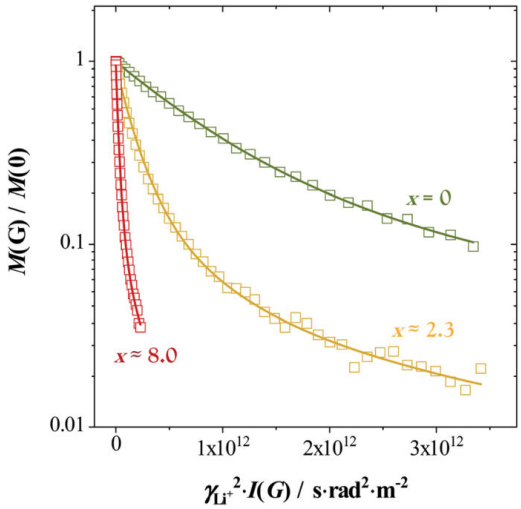

Figure 7.3: Normalized echo signal versus the squared gyromagnetic ratio times the integral I(G), as measured by ^{7}Li PFG NMR at 180 °C (green), 140 °C (orange) and 60 °C (red) from $Li_2Sn_2S_5 \cdot xH_2O$ samples with the indicated water contents. Points are raw data; curves are fits by the 2D model. See Appendix D for details.

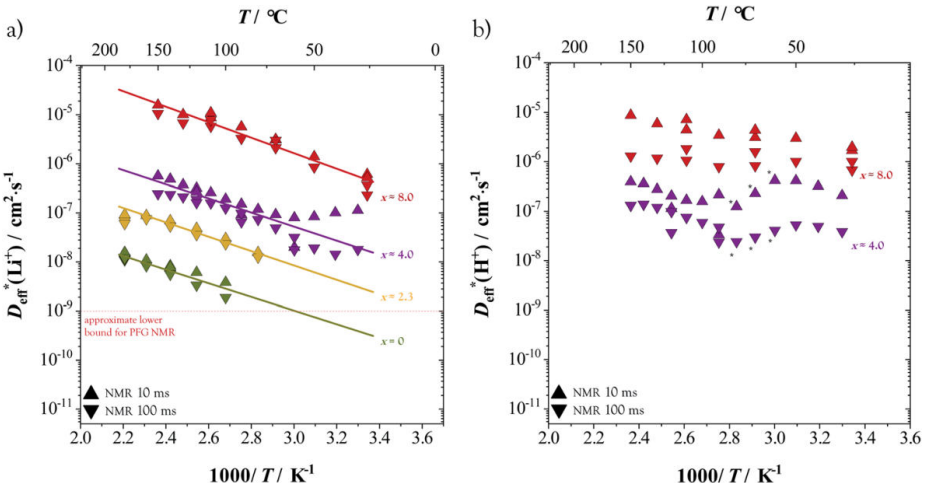

Figure 7.4: Effective diffusivity of (a) Li^+ and (b) H^+ in $Li_2Sn_2S_5 \cdot xH_2O$ samples, as determined from ^{7}Li and ^{1}H PFG NMR measurements using a diffusion time of 10 or 100 ms. In (a), solid lines are linear fits to all points at a given water content, except the data for x ≈ 4.0 below 80 °C show significant scatter and were excluded. For a few points in (b), the goodness of fit in the PFG data was noticeably worse; these are marked with an asterisk.

At lower water contents and lower temperatures, the degree of attenuation was below

the PFG NMR detection limit, so diffusivity values could not be reliably extracted. The ^{7}Li data for $x \approx 4.0$ show somewhat anomalous behavior near room temperature, which is tentatively attributed to small variations in water content due to condensation in the NMR capillary. The condensation issue was mitigated before acquiring the $x \approx 8.0$ data, as described in the Experimental details.

Figure 7.4b shows the results from ^{1}H PFG NMR measurements. The effective proton diffusivity $D^{*}_{\mathrm{eff}}(\mathrm{H}^{+})$ is comparable to the effective Li^{+} diffusivity in samples with $x \approx 4$ and 8. This proton motion is attributed to the diffusion of water molecules, since there is no evidence for the presence of protonic defects, as discussed below. Assuming this attribution is correct, the data indicate that Li^{+} ions and water molecules in the interlayer galleries have a comparable mobility. The diffusivity of water decreases by a somewhat larger factor (3-10×) than the Li^{+} diffusivity when the diffusion time is increased from 10 to 100 ms, which hints that grain boundaries are more blocking for water molecules than for Li^{+} ions. The data show more scatter compared to Li^{+}; the underlying reason may again be small variations in water content due to a tiny amount of condensation inside the sealed NMR capillary. Measurements by ^{1}H PFG NMR for $x \approx 2.3$ were also attempted, however, the T_2 relaxation time was too short to apply feasible gradient durations.

Magic angle spinning (MAS) ^{6}Li NMR spectra acquired at various water contents and temperatures are shown in Figure 7.5a. To facilitate comparisons, the spectra are normalized to have the same maximum intensity. The ^{6}Li spectrum for $x = 0$ at room temperature can be fit by 5 signals. The strong signals at 2.2 and 1.2 ppm exhibit an intensity ratio of 0.8 and are nearly identical to those seen in previous work.[34] The weak signals at 1.7 and −0.1 ppm can be attributed to the presence of ∼4% crystalline Li_2SnS_3.[34] The signal at 0.8 ppm comprises ∼30% of the Li present and was not observed in the previous work. These observations are corroborated by a $^{1}_{1}$Sn MAS spectrum (Figure D.8b), which shows three strong signals consistent with those previously observed for $Li_2Sn_2S_5$; a weak (∼4%) signal consistent with Li_2SnS_3; and two broader signals which were not observed in the previous work and which comprise ∼40% of the Sn present.[34] We assign these signals to a disordered Li-Sn-S side phase, reflecting the possible phase width and stacking disorder in this system. The presence of side phases adds some uncertainty to the interpretation of changes in overall water content; in principle, it is possible that the apparent phase widths at $x = 2$–4 and 8–10 are due to hydration of the side phases rather than $Li_2Sn_2S_5 \cdot xH_2O$. Otherwise the side phases are unlikely to affect the conclusions about $Li_2Sn_2S_5 \cdot xH_2O$ in this work. One reason is that the PFG NMR data show the fast-conducting phase is a layered material; if the disordered side phase is not layered, then it is unlikely to be the fast conductor. As a note, the spectra acquired for $x = 0$ below room temperature required long measurements times and are less reliable due to possible drift.

The spectra at $x \approx 2$, $x \approx 3$ (not shown), and $x \approx 4$ are nearly identical, and they are clearly distinct from the spectra at $x = 0$ and $x \approx 8$, consistent with the phase transitions seen by XRD between $x = 0$, 2–4, and 8. For simplicity, we fit all the ^{6}Li spectra from the hydrated samples by two signals. The signals are labeled 1 and 2 in Figure 7.5; example fits are shown in Figure D.8a; and the full width at half maximum (FWHM) and chemical shift data are plotted in Figure D.9. The FWHM of signal 1 remains approximately constant throughout, while signal 2 narrows as the temperature increases from −90 to 23 °C. The latter is a signature of motional narrowing.[64] A likely explanation is that the

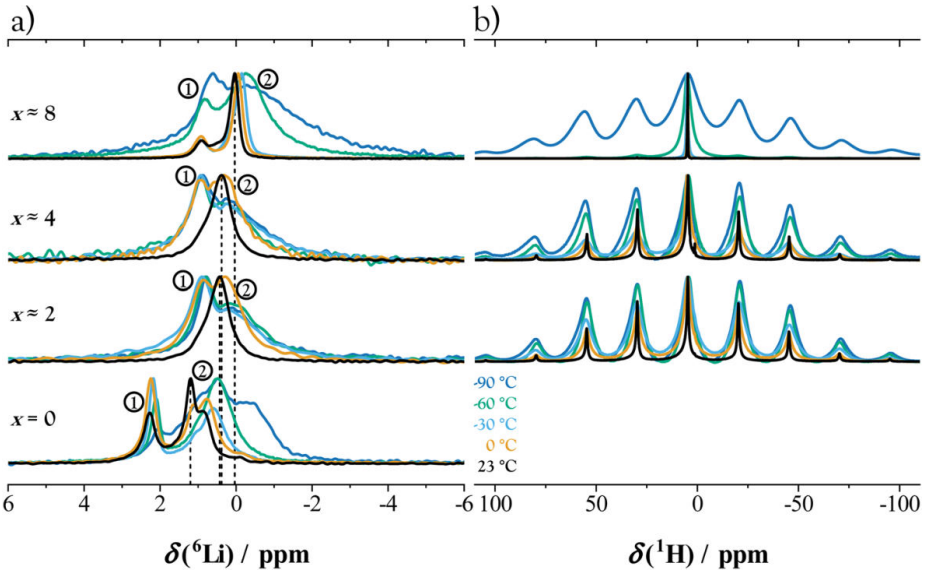

Figure 7.5: (a) ^{6}Li and (b) ^{1}H NMR measurements of $Li_2Sn_2S_5 \cdot xH_2O$ for various water contents and temperatures.

Li^+ ions on tin sites ($Li^+_\perp$) correspond to signal 1 and remain immobile, while the Li^+ ions in the interlayer galleries ($Li^+_\parallel$) give rise to signal 2 and are increasingly mobile with increasing temperature or water content. Upon hydration from $x \approx 4$ to 8, the chemical shift of signal 1 remains unchanged, while signal 2 shifts to ~ 0 ppm, consistent with interlayer Li^+ ions becoming solvated by the incorporated water. For comparison, fully solvated Li^+ in liquid water shows a similar chemical shift, slightly below 0 ppm.[65,66] Although we cannot exclude that the two signals are a convolution of multiple signals, the simple fitting approach used here leads to a reasonable physical interpretation.

The signals in the ^{1}H spectra also narrow with increasing temperature, consistent with the presence of mobile protons (Figure 7.5 b). Indeed, the concurrent broadening of the ^{6}Li and ^{1}H signals suggests coupled short-range motion of Li^+ and H_2O under all hydrated conditions. Also, the ^{1}H spectra at $x \approx 2$ and 4 show spinning sidebands, consistent with a low diffusivity of water, while the sidebands disappear above -60 °C for $x \approx 8$, suggesting a higher (more liquid-like) diffusivity of water.

To review, the MAS NMR results suggest:

- (i) for all x values there are $Li^+_\perp$ and $Li^+_\parallel$ present, but only the latter are mobile;
- (ii) the behavior in the range $x \approx 2$,- 4 is similar;
- (iii) Li^+ and H_2O exhibit coupled short-range motion, with higher mobilities at $x \approx 8$ than at $x \approx 4$.

7.3.3 EIS: ion transport

The conductivity and dielectric properties of $Li_2Sn_2S_5 \cdot xH_2O$ were characterized by impedance spectroscopy.[67] Figure 7.6 shows representative spectra for three degrees of hydration. At all x, a depressed high frequency semicircle and a low-frequency blocking arc were observed. The latter is typical for blocking of ions at a metal electrode. For samples with $x \lesssim 4.0$, cooling below 25 °C was required to observe the semicircle. The semicircle was fit by the simple equivalent circuit shown in Figure 7.6. The resistance scales linearly with sample thickness (Figure D.10), as expected for bulk conduction. The dielectric constant ϵ_r and conductivity σ were extracted using standard relations (see Experimental details). The ϵ_r values are unusually high, falling in the range 80-300 depending on temperature and humidity (Figure D.15). The reason is unclear. For comparison, the dielectric constant of pure water in the kHz range is 80 at room temperature.[68]

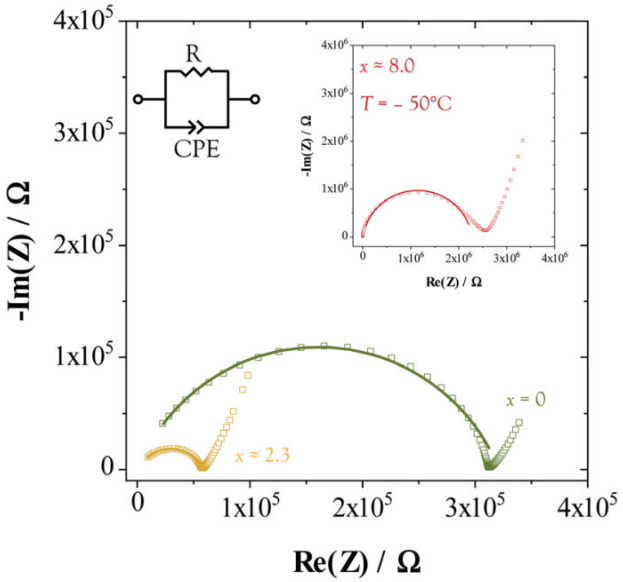

Figure 7.6: Typical impedance spectra measured from $Li_2Sn_2S_5 \cdot xH_2O$ compacts at 30 °C (x = 0 and $x \approx 2.3$) and −80 °C ($x \approx 8.0$, inset).

An apparent high dielectric constant seems to be a common feature in hydrates (*cf.* $Li_3InCl_6 \cdot 1.5H_2O$),[29] which suggests that the presence of H_2O molecules induces polarization effects. It can be ruled out that the capacitance is due to blocking grain boundaries; strong blocking behavior would show two distinct (non-overlapping) semicircles, but here only one is observed, even after cooling as low as −130 °C. The red-orange color of the material hardly changes upon hydration, which suggests that the bandgaps of the hydrated phases are near that measured previously[31] for the anhydrous phase (1.9 eV).

Figure 7.7 shows that the conductivity increases strongly and monotonically with increasing water content. At room temperature the increase is by more than three orders of magnitude, from $7 \cdot 10^{-6}$ to $2 \cdot 10^{-2}$ S cm^{-1} as x increases from 0 to 10.0. The activation energy (determined from the slope of σT) is 0.40, 0.57, 0.39, 0.34, and 0.24 eV for $x \approx 0$,

2.3, 4.0, 8.0, and 10.0. The influence of porosity is judged to be minor due to adequate densification and the soft nature of the hydrated materials. Additional conductivity data showing reproducibility as well as heating and cooling steps are given in Figure D.11.

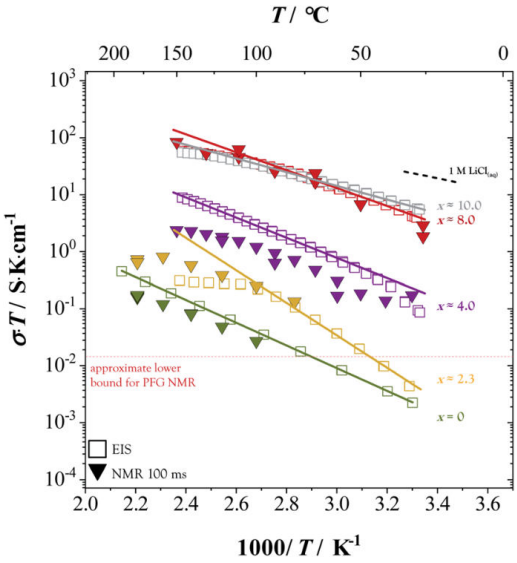

Figure 7.7: Conductivity values measured from $Li_2Sn_2S_5 \cdot xH_2O$ by electrochemical impedance spectroscopy (EIS, open squares). Solid lines are linear fits. Also shown are conductivity values estimated from the ^{7}Li PFG NMR results in Fig. 7.4 using the Nernst–Einstein equation (triangles), as well as values measured previously for a 1 M aqueous solution of LiCl (dashed line).[57]

For comparison, one can estimate the conductivity from the effective diffusivity obtained by PFG NMR using the Nernst–Einstein equation:

$$\sigma_{Li^+} T = \frac{e^2 [Li^+] D^*_{\mathrm{eff}}(Li^+)}{k_B} \tag{7.2}$$

where e is the charge of an electron. For this calculation, it was assumed that only the $Li^+_{\parallel}$ ions in the interlayer galleries are mobile, and to account for $\sim$10% porosity, the conductivity was multiplied by a factor of 0.9 (the precise equation used to calculate $[Li^+]$ is given in Appendix D). The resulting Li^+ conductivity values show reasonable agreement in both magnitude and activation energy to the values measured by impedance spectroscopy (Figure 7.7). This agreement provides confidence in both the PFG NMR and impedance results; it supports the assumption that all the interlayer Li^+ ions are mobile; and it strongly suggests that the conductivity is due predominantly to Li^+ ions.

A few final experiments are noteworthy. Below room temperature, the conductivity of $Li_2Sn_2S_5 \cdot 8\,H_2O$ was found to drop far more quickly than that of $Li_2Sn_2S_5$, such that the conductivity trends for those phases cross at −60 °C (Figure D.12). Thus, below −60 °C the presence of H_2O is detrimental to ion transport. In addition, conductivity and electromotive force (EMF) experiments performed using Li and LiAl electrodes indicate

that $Li_2Sn_2S_5$ reacts in contact with Li to yield a composite material with a high overall electronic conductivity (Figure D.13). Simultaneously, the apparent dielectric constant ϵ_r increases by a factor of ~ 50 (Figure D.14), suggesting that the electronic conductivity is dominated by pathways within the grain boundary network.

7.4 Discussion

7.4.1 (a) Overall interpretation

Reasonable quantitative agreement between the Li^+ diffusivity and the total conductivity is obtained if all Li^+ ions in the interlayer galleries are assumed to be mobile. The agreement suggests that the improved conductivity upon hydration is due almost entirely to increased Li^+ mobility, while the concentration of mobile Li^+ carriers remains roughly constant (decreasing slightly with increasing x due to volume expansion). Such behavior is reasonable, given the ability of water to promote ion motion. It is also chemically intuitive that the Li^+ ions in the interlayer galleries would be hydrated by adjacent water molecules. The coupling offers a natural explanation for why Li^+ and H^+ exhibit comparable diffusivities in this system.

Because the water diffusivity in $Li_2Sn_2S_5 \cdot xH_2O$ strongly increases with increasing water content, water incorporation effectively accelerates during hydration and decelerates during dehydration. This phenomenon explains why dehydration is far more sluggish than hydration, and it suggests that the hydration process is diffusion-limited, at least for the 50 µm particle size used in this work.

The protonic conductivity is probably quite low, due to a lack of protonic charge carriers. Significant dissociation of the incorporated water is not observed in the MAS NMR data. An internal ion exchange process (whereby H^+ ions exchange positions with Li^+ in the layers, leaving behind excess OH^- carriers in the interlayer galleries) is also unsupported by the data. By comparison, pure liquid H_2O also shows a high water diffusivity and a low proton conductivity.[57,69–71]

In unconfined aqueous solutions, Li^+ ions are hydrated by 4–5 H_2O molecules.[72] To provide the same coordination for the 1.5 interlayer Li^+ ions per formula unit of $Li_2Sn_2S_5 \cdot xH_2O$, approximately 6–8 water molecules per formula unit are required. One might therefore predict that the Li^+ transport rates in $Li_2Sn_2S_5 \cdot xH_2O$ will approach "liquid-like" values when $x > 6$. The data are broadly consistent with this simple picture. For example, a 1 M aqueous solution of LiCl shows a total conductivity of $2.3 \cdot 10^{-2}\,S\,cm^{-1}$ at room temperature (Figure D.7),[57] which—since the cation transference number in liquids is usually around $\frac{1}{3}$—implies a Li^+ conductivity of $8 \cdot 10^{-3}\,S\,cm^{-1}$. The second hydrate, $Li_2Sn_2S_5 \cdot 8\,H_2O$, exhibits a virtually identical value of $9 \cdot 10^{-3}\,S\,cm^{-1}$ at 25 °C. However, since the negatively-charged tin sulfide layers are immobile, the Li^+ transference number in $Li_2Sn_2S_5 \cdot xH_2O$ is probably unity. Thus, $Li_2Sn_2S_5 \cdot 8\,H_2O$ achieves a liquid-like conductivity with a solid-like Li^+ transference number. Both of these features are beneficial for electrolyte applications.

Further hydration up to $x \approx 10$ provides almost no additional conductivity benefit, which is consistent with the idea that the electrostatic influence of the tin sulfide sheets on the interlayer Li^+ ions is already fully screened out at $x \approx 8$. This point suggests more broadly that the transport rates in concentrated aqueous solutions represent an upper bound to what is achievable in hydrated layered solids such as $Li_2Sn_2S_5 \cdot xH_2O$. In this work the highest measured conductivity at 27 °C was $2 \cdot 10^{-2}\,S\,cm^{-1}$ in $Li_2Sn_2S_5 \cdot 10.2H_2O$, surpassing prominent oxide Li^+ electrolytes such as $Li_7La_3Zr_2O_{12}$ ($3 \cdot 10^{-4}\,S\,cm^{-1}$)[73] and on par with state-of-the-art sulfide electrolytes such as $Li_{9.54}Si_{1.74}P_{1.44}S_{11.7}Cl_{0.3}$ ($2.5 \cdot 10^{-2}\,S\,cm^{-1}$).[74]

To recapitulate, the simple model discussed so far involves a nearly constant mobile Li^+ concentration, a Li^+ mobility which is promoted by increasing water content up to $x \approx 8$, and H_2O molecules which coordinate to the Li^+ ions and show similar mobility. Further hydration above $x \approx 8$ yields little or no additional benefit in conductivity. The Li^+ migration enthalpy remains in the range 0.3–0.6 eV. Figure 7.8 summarizes the basic picture: At $x = 0$ conductivity is poor because of electrostatic interactions (trapping as extreme case) with the tin sulfide layers (A). The interaction is weakened by increasing temperature or introducing water. A moderate water content ($x \approx 4$) leads to efficient screening (B), while a high water content ($x \approx 8$) enables liquid-like nano-ionic transport (C).

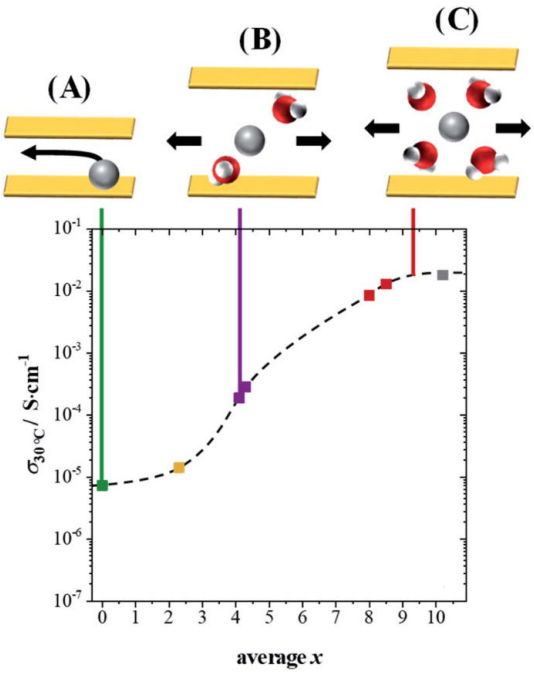

Figure 7.8: Conductivity at 30 °C as a function of the average water content in $Li_2Sn_2S_5 \cdot xH_2O$. Dashed line is a guide for the eye. Schematics show the interlayer water (red/white) and $Li^+_{\|}$ ions (gray).

This model explains the major trends at 25 °C and above. Below room temperature, some refinement may be needed. Aqueous solutions freeze slightly below 0 °C, and the formation of a rigid ice lattice causes the conductivity of dissolved ions to drop sharply by several orders of magnitude.[75] In contrast, $Li_2Sn_2S_5 \cdot 8\,H_2O$ is solid at room temperature, and the ionic conductivity shows no first-order transition during cooling to −70 °C (Figure D.12). Evidently the formation of an ice lattice is hindered by the water molecules being confined between the tin sulfide layers.[76,77] Instead, during cooling the activation energy increases steadily for $x \approx 8$. It is unclear if this change is due to a concentration or a mobility effect. One can speculate that "ice-like" clusters of water

molecules gradually form upon cooling and associate with Li^+ ions (reducing the mobile Li^+ concentration) and/or change the potential landscape (causing the Li^+ mobility to decrease more rapidly with decreasing temperature).

7.4.2 (b) Previous work revisited

The previous work from our groups[34] on anhydrous $Li_2Sn_2S_5$ must be reinterpreted in two respects:

First, in the current work we consistently find that anhydrous $Li_2Sn_2S_5$ exhibits a Li^+ diffusivity below $10^{-9}\,cm\,s^{-2}$ at 25 °C. The higher value of $10^{-7}\,cm\,s^{-2}$ reported previously is obtained here only at hydration levels of $x \geq 8$. The simplest and most likely explanation is that the PFG NMR measurements published previously were inadvertently conducted on hydrated samples. An alternative possibility is that the different synthesis protocols in the previous work led to structural differences which facilitate ion transport, such as fewer stacking faults or reduced amorphous content. Our numerous attempts to confirm this alternative were unsuccessful, but it cannot be entirely ruled out.

Second, anhydrous $Li_2Sn_2S_5$ exhibits an ionic conductivity slightly below $10^{-5}\,S\,cm^{-1}$ at 25 °C. The value of $10^{-4}\,S\,cm^{-1}$ reported previously using LiAl electrodes appears to correspond not to ion conduction, but rather to electron conduction that arises when $Li_2Sn_2S_5$ is reduced by LiAl and electronic pathways form in the microstructure (Figure D.13 and D.14).

7.4.3 (c) Outlook

An interesting avenue for future work is to incorporate other solvents besides water into $Li_2Sn_2S_5$, to promote Li^+ conductivity while making the material compatible with non-aqueous conditions. Another promising direction is to investigate hydrated layered compounds based on higher-valent cations such as Mg^{2+} or Zn^{2+}. The anhydrous forms of such materials will likely show quite poor cation conductivity due to strong coulombic interactions with the immobile lattice. However, the hydrated forms may achieve a liquid-like ionic conductivity while remaining solid, as in the present work, due to the ability of water to promote ion motion. A few examples of this approach have already been demonstrated.[9,47,78]

Although not attempted in this work, it should be possible to use $Li_2Sn_2S_5 \cdot xH_2O$ as a battery electrolyte. At $x \approx 8$ the Li^+ conductivity is competitive with that of liquid electrolytes, and the material is soft enough that simple pressing may be sufficient to assemble composite electrodes with good interfacial contact at the electrode-electrolyte interfaces. As with any solid-state battery, the key challenge is to maintain good interfacial contact during cycling despite interfacial reactivity and volume changes. The softness of $Li_2Sn_2S_5 \cdot xH_2O$ at high water contents could plausibly help in this regard. The practical voltage window for battery cycling may extend beyond the limits associated with splitting of liquid water, since $Li_2Sn_2S_5 \cdot 8\,H_2O$ is conceptually similar to water-in-salt electrolytes,[79] and the geometric confinement of H_2O might even widen the window further. The fact that the Li^+ transference number is probably near unity is also beneficial for avoiding concentration polarization effects at high current densities. However, some concerns are worth noting. Despite the possible suppression of water

splitting, the electrochemical stability window of $Li_2Sn_2S_5 \cdot xH_2O$ is narrow, as seen for other sulfides.[80] In particular, contact with low-voltage anodes may be impractical due to Sn^{4+} reduction and the formation of a mixed-conducting passivation layer, similar to the impact of Ti^{4+} reduction in well-known electrolyte materials such as $LiLaTiO_3$ or $Li_{1+x}Al_xTi_{2-x}(PO_4)_3$.[81,82] The addition of water could mitigate this issue, because the typical hydrolysis products of lithium (LiOH, Li_2O, LiH) are electronically blocking,[83] but it seems risky to rely on this point.[84,85] Another concern is that the application of pressure—a standard method for restoring interfacial contact in solid-state batteries—may squeeze water out of $Li_2Sn_2S_5 \cdot 8\,H_2O$ and thereby reduce the Li^+ conductivity. The surrounding water partial pressure may also need to be controlled to avoid deliquescence. Finally, high current densities may deplete water on one side of the electrolyte due to the coupled motion of Li^+ and H_2O; it seems reasonable to expect that this phenomenon is a general feature of hydrated layered materials.

7.5 Conclusion

Upon exposure to humidity, water intercalation into the layered structure of $Li_2Sn_2S_5$ is facile. The resulting material $Li_2Sn_2S_5 \cdot xH_2O$ shows a water content x that varies from 0 to about 10 depending on the humidity and temperature. Both Li^+ and H_2O are transported within the material predominantly by 2D diffusion in the interlayer galleries. The transport rates increase strongly with increasing water content up to about $x \approx 8$, which corresponds approximately to a full hydration shell of 4–5 water molecules for each interlayer Li^+ ion. At $x \approx 8$ the material remains a soft solid, but the Li^+ diffusivity and conductivity reach liquid-like values of $5 \cdot 10^{-7}\,cm\,s^{-2}$ and $10^{-2}\,S\,cm^{-1}$. Anhydrous $Li_2Sn_2S_5$ consistently showed far lower transport rates than those reported in a previous work by our groups. The discrepancy is most likely due to inadvertent hydration of the material in the previous work, but an alternative explanation based on structural differences cannot be ruled out. In any case, $Li_2Sn_2S_5 \cdot xH_2O$ offers a case study of the transition between a hydrated solid electrolyte and a confined liquid electrolyte, which is both scientifically interesting and potentially useful in applications.

7.6 Experimental

7.6.1 General

Anhydrous samples were prepared, handled, and measured under dry inert gas (Ar or N_2 with < 1 ppm H_2O) or vacuum. Hydrated samples were sealed in containers with small dead volumes to minimize water loss. The water content, x, was assessed gravimetrically; for a two-phase mixture, the reported value of x is an average over both phases. Some transfer steps required exposing hydrated samples to dry inert gas for a short time, on the order of minutes. The water loss during these transfer steps was estimated by weighing representative samples before and after exposure. The cumulative decrease in x from these transfers was estimated to be 0.5 or less and was neglected. Although $Li_2Sn_2S_5 \cdot xH_2O$ appears to be stable in ambient air, the water content is sensitive to water partial pressure (p_{H_2O}), so air exposure was avoided except where indicated. See Appendix D for more details.

7.6.2 Sample preparation

Anhydrous $Li_2Sn_2S_5$ was synthesized by solid state reaction of Li_2S (99.9%, Alfa Aesar) and SnS_2 at 650 °C. Hydrated $Li_2Sn_2S_5 \cdot xH_2O$ was prepared using either a TGA or saturated salt solutions. Both materials were compacted by uniaxial pressing for impedance measurements; anhydrous $Li_2Sn_2S_5$ with 5–10 kbar and various pressure values for $Li_2Sn_2S_5 \cdot xH_2O$ depending on x. Various heat treatments were attempted to increase the density of anhydrous $Li_2Sn_2S_5$ further. See Appendix D for more details.

7.6.3 Thermogravimetric analysis

The equilibrium water content in $Li_2Sn_2S_5 \cdot xH_2O$ was measured by installing anhydrous powder samples (70-600 mg) inside a quartz crucible in a TGA system. The sample was exposed to ambient air for approx. 30 s during transfers. The TGA was a Netzsch STA 449 instrument with a protective N_2 gas flow (< 10 ppm H_2O including trace leaks, 60 mL min^{-1}). To remove water absorbed during sample installation, a pre-anneal was typically conducted under flowing N_2. The sample mass was measured after a typical dwell time of 1–2 h under humid N_2 at various temperatures in the range 27-100 °C and p_{H_2O} in the range 1.4–17.1 mbar (0.4–48.2% relative humidity). The humidity was set by mixing dry and humidified N_2 in different ratios (0-60 mL min^{-1} dry or wet N_2). The N_2 gas was humidified by bubbling dry N_2 gas through deionized water in a double-walled glass container, which was temperature controlled using a thermostat in the range 5–18 °C. The flow rates were sufficiently low that saturation could be assumed, such that the humidity is given by the saturation pressure of water at the thermostat set point. The exhaust gas of the TGA was analyzed by a Balzers Prisma quadrupole mass spectrometer. A buoyancy correction was performed by subtraction of mass changes at measurement temperatures from data obtained of an empty crucible in a separate measurement. The recorded mass changes of the empty crucible were fit with a polynomial and the extrapolation line was used for the buoyancy correction.

7.6.4 X-ray diffraction

Powder XRD measurements were acquired using a STOE StadiP diffractometer (curved Ge (111) monochromator, DECTRIS Mythen2R 1K detector, Debye–Scherrer geometry, Mo-$K_{\alpha 1}$, wavelength 0.7093 Å). Powder samples with lower x values (0-4.0) were packed in borosilicate capillaries (Hilgenberg, 0.3 mm diameter) and flame sealed under argon. Due to their soft and sticky consistency, samples at higher x values (4.0-10.0) were prepared in Kapton tubes of 0.8 mm diameter. These data were analyzed using WinXPow (STOE). Phase analysis checks were performed on a second setup, as described in Appendix D.

7.6.5 Pulsed-field-gradient nuclear magnetic resonance

$Li_2Sn_2S_5 \cdot xH_2O$ powder was packed at one end of an NMR glass capillary (Deutero, D400) with ground joints, and a solid glass rod that matched the capillary inner radius was inserted to reduce the dead volume. The capillary was then sealed under slightly reduced pressure ($\sim$0.5 bar) of inert gas. Water loss during the sealing was negligible. Capillaries prepared in this way were installed in the NMR instrument (Bruker Avance III 400) equipped with either a diff60 gradient probe (max. 2900 G/cm, specialized RF inserts for ^{1}H and ^{7}Li) or a double resonance broad band probe (max. 1750 G/cm, BBO 400 MHz W1/S2 5 mm with Z-gradient) with tuneable frequency for different nuclei. The sample end of the capillary was heated stepwise between 25-180 °C. After a $\sim$0.5 h effective dwell time at each temperature to allow for equilibration, NMR measurements were acquired. At all temperatures the intent was to keep the water content in the powder constant. However, some amount of condensation was visible at the protruding cold (non-sample) end of the capillary, suggesting the samples underwent a small (and reversible) amount of water loss during heating. For the $x \approx 8.0$ sample, the capillary sealing was modified to essentially eliminate the dead volume of gas, and no condensation was observed. Data were acquired using a stimulated echo sequence with spoiler gradients. Various diffusion times in the range 10-100 ms were used, with effective gradient durations of 1–3 ms. Remagnetization times were chosen to be 4 to 5 times higher than the spin–lattice relaxation time, T_1. The measured echo-signal attenuation peaks were phase corrected, and the integrated areas were used to extract the diffusivities. The main analysis approach assumed anisotropic diffusion with negligible out-of-plane diffusivity, so the procedure given in Ref. [63] was used to calculate the diffusivity.

7.6.6 Solid state nuclear magnetic resonance

Powder samples were filled in a Pyrex magic angle spinning (MAS) rotor insert (Rototec) under argon. The insert was custom fitted with a ground glass joint for transfers. The sample bottom part of the insert was immersed in liquid nitrogen, and under slight static vacuum ($\sim$0.5 bar) the sample was flame sealed. Spectra were acquired on a Bruker Avance III 400 MHz instrument (magnetic field of 9.4 T) at Larmor frequencies of 400 MHz (^{1}H), 155.5 MHz (^{7}Li), 149.15 MHz (^{119}Sn) and 58.8 MHz (^{6}Li), using a Bruker BL4 double resonance MAS probe and 4 mm OD ZrO_2 spinners (10 kHz if not stated otherwise). The MAS spectra for all nuclei were acquired with a simple Bloch

Decay experiment (*i.e.*, pulse-acquisition), and acquisition delays sufficiently long for a complete magnetization recovery. The ^{7}Li experiments were performed using central transition selective 90° pulses (the non-selective liquid 90° pulses were scaled by a factor of $(I + 0.5) - 1 = 0.5$).[86,87] ^{7}Li and ^{6}Li variable temperature spin–lattice T_1 relaxation times measurements were performed both on spinning and non-spinning samples using saturation-recovery method. Experiments with static samples were performed in a Bruker static double resonance PE400 probe with a horizontal 5 mm coil. Between 8 and 64 scans were commonly averaged for a good signal-to-noise ratio. The temperature in the probes was regulated with a Bruker BVT3000 temperature controller. Actual temperature of the sample was calibrated on ^{207}Pb signal of powdered $Pb(NO_3)_2$.[88] Chemical shifts were referenced externally relative to tetramethylsilane (^{1}H, $\delta_{iso} = 0.0$ ppm), to tetramethyltin (^{119}Sn, $\delta_{iso} = 0.0$ ppm), using SnO_2 as a secondary standard (−603 ppm), and to 1 M LiCl ($^{6.7}$Li, $\delta_{iso} = 0.0$ ppm).[89]

7.6.7 Electrochemical impedance spectroscopy

Depending on x, samples were contacted either by sputtering ruthenium electrodes or with stainless steel rods. For $x = 0$, measurements were conducted under inert gas flow, and for $x > 0$, a closed set-up was used. In either case the impedance was measured with a Novocontrol Alpha-A analyzer (2-wire measurement, 106 to 10^{-1} Hz, 0.1 V amplitude). When necessary, the stray impedance of the measurement setup was measured separately (by short-circuiting the electrodes at the respective temperatures) and pointwise subtracted out. Impedance spectra were fit using either Zview (Scribner, Version 3.5.c) or RelaxIS 3 (rhd instruments) in the high-frequency range by an equivalent circuit consisting of a resistor and constant phase element (CPE) in parallel. The obtained values for resistance and capacitance when including the low-frequency blocking feature by an additional CPE and having the dielectric capacitance in parallel were comparable. The conductivity σ and dielectric constant ϵ_r were extracted using the standard relations:

$$\sigma = \frac{L}{RA} \ , \tag{7.3}$$

$$\epsilon_r = \frac{C_{eff} L}{\epsilon_0 A} \ , \tag{7.4}$$

where R is resistance, L is sample thickness, A is cross-sectional area, ϵ_0 is the electrical permittivity of free space, and C_{eff} is the effective capacitance calculated from:

$$C_{eff} = Q^{n^{-1}} R^{n^{-1}-1} \ , \tag{7.5}$$

where Q and n are the magnitude and exponent of the CPE.[67] See Appendix D for more details.

References

(1) Kreuer, K. *Annu. Rev. Mater. Res.* **2003**, *33*, 333–359.

(2) Gopalakrishnan, J.; Bhat, V. *Inorg. Chem.* **1987**, *26*, 4299–4301.

(3) Øygarden, V.; Fjellvåg, H.; Sørby, M. H.; Sjåstad, A. O. *Inorg. Chem.* **2016**, *55*, 7630–7636.

(4) Spaeth, M.; Kreuer, K. D.; Maier, J.; Cramer, C. *J. Solid State Chem.* **1999**, *148*, 169–177.

(5) Hougardy, J.; Stone, W. E. E.; Fripiat, J. J. *J. Chem. Phys.* **1976**, *64*, 3840–3851.

(6) Suzuki, M.; Wada, N.; Hines, D.; Whittingham, M. S. *Phys. Rev. B* **1987**, *36*, 2844–2851.

(7) Stanley Whittingham, M. *Solid State Ion.* **1989**, *32-33*, 344–349.

(8) Maraqah, H.; Li, J.; Whittingham, M. S. *J. Mater. Chem. A* **1991**, *138*, L61–L63.

(9) Whittingham, M. S. *Solid State Ion.* **2004**, *168*, 255–263.

(10) Sheffield, S. H.; Howe, A. T. *Mater. Res. Bull.* **1979**, *14*, 929–935.

(11) Slade, R. C. T.; Barker, J.; Hirst, P. R.; Halstead, T. K.; Reid, P. I. *Solid State Ion.* **1987**, *24*, 289–295.

(12) Kawada, T.; Yokokawa, H.; Dokiya, M. *Solid State Ion.* **1988**, *28-30*, 210–213.

(13) Whittingham, M. S. *Solid State Ion.* **1987**, *25*, 295–300.

(14) Kreuer, K.-D.; Paddison, S. J.; Spohr, E.; Schuster, M. *Chem. Rev.* **2004**, *104*, 4637–4678.

(15) Kusoglu, A.; Weber, A. Z. *Chem. Rev.* **2017**, *117*, 987–1104.

(16) Heitner-Wirguin, C. *J. Membr. Sci.* **1996**, *120*, 1–33.

(17) Kreuer, K.-D.; Wohlfarth, A.; De Araujo, C. C.; Fuchs, A.; Maier, J. *ChemPhysChem* **2011**, *12*, 2558–2560.

(18) Zhao, J.; Islam, S. M.; Kontsevoi, O. Y.; Tan, G.; Stoumpos, C. C.; Chen, H.; Li, R. K.; Kanatzidis, M. G. *J. Am. Chem. Soc.* **2017**, *139*, 6978–6987.

(19) Wang, R.; Chen, H.; Xiao, Y.; Hadar, I.; Bu, K.; Zhang, X.; Pan, J.; Gu, Y.; Guo, Z.; Huang, F.; Kanatzidis, M. G. *J. Am. Chem. Soc.* **2019**, *141*, 16903–16914.

(20) Sotiles, A. R.; Baika, L. M.; Grassi, M. T.; Wypych, F. *J. Am. Chem. Soc.* **2019**, *141*, 531–540.

(21) Li, N.; Zhang, L.; Chen, Y.; Fang, M.; Zhang, J.; Wang, H. *Adv. Funct. Mater.* **2012**, *22*, 835–841.

(22) Doyle, M.; Wang, L.; Yang, Z.; Choi, S. K. *J. Electrochem. Soc.* **2003**, *150*, D185.

(23) Hartwig, P.; Weppner, W. *Solid State Ion.* **1981**, *3-4*, 249–254.

(24) Poulsen, F. W. *Solid State Ion.* **1981**, *2*, 53–57.

(25) Poulsen, F. W. *Acta Chem. Scand., Ser. A* **1985**, *39*, 290–292.

(26) Schwering, G.; Hönnerscheid, A.; Van Wüllen, L.; Jansen, M. *ChemPhysChem* **2003**, *4*, 343–348.

(27) Sagua, A.; Rivera, A.; León, C.; Santamaría, J.; Sanz, J.; Morán, E. *Solid State Ion.* **2006**, *177*, 1099–1104.

(28) Takano, A.; Oikawa, I.; Kamegawa, A.; Takamura, H. *Solid State Ion.* **2016**, *285*, 47–50.

(29) Sacci, R. L.; Bennett, T. H.; Drews, A. R.; Anandan, V.; Kirkham, M. J.; Daemen, L. L.; Nanda, J. *J. Mater. Chem. A* **2021**, *9*, 990–996.

(30) Adhikary, A.; Yaghoobnejad Asl, H.; Sandineni, P.; Balijapelly, S.; Mohapatra, S.; Khatua, S.; Konar, S.; Gerasimchuk, N.; Chernatynskiy, A. V.; Choudhury, A. *Chem. Mater.* **2020**, *32*, 5589–5603.

(31) Kuhn, A.; Holzmann, T.; Nuss, J.; Lotsch, B. V. *J. Mater. Chem. A* **2014**, *2*, 6100–6106.

(32) Szendrei-Temesi, K.; Sanchez-Sobrado, O.; Betzler, S. B.; Durner, K. M.; Holzmann, T.; Lotsch, B. V. *Adv. Funct. Mater.* **2018**, *28*, 1705740.

(33) Hatz, A.-K.; Moudrakovski, I.; Bette, S.; Terban, M. W.; Etter, M.; Joos, M.; Vargas-Barbosa, N. M.; Dinnebier, R. E.; Lotsch, B. V. *Chem. Mater.* **2021**, *33*, 7337–7349.

(34) Holzmann, T.; Schoop, L. M.; Ali, M. N.; Moudrakovski, I.; Gregori, G.; Maier, J.; Cava, R. J.; Lotsch, B. V. *Energy Environ. Sci* **2016**, *9*, 2578–2585.

(35) Kaib, T.; Haddadpour, S.; Kapitein, M.; Bron, P.; Schröder, C.; Eckert, H.; Roling, B.; Dehnen, S. *Chem. Mater.* **2012**, *24*, 2211–2219.

(36) Brant, J. A.; Massi, D. M.; Holzwarth, N. A. W.; Macneil, J. H.; Douvalis, A. P.; Bakas, T.; Martin, S. W.; Gross, M. D.; Aitken, J. A. *Chem. Mater.* **2015**, *27*, 189–196.

(37) Park, K. H.; Oh, D. Y.; Choi, Y. E.; Nam, Y. J.; Han, L.; Kim, J.-Y.; Xin, H.; Lin, F.; Oh, S. M.; Jung, Y. S. *Adv. Mater* **2016**, *28*, 1874–1883.

(38) Kwak, H.; Park, K. H.; Han, D.; Nam, K.-W.; Kim, H.; Jung, Y. S. *J. Power Sources* **2020**, *446*, 227338.

(39) MacNeil, J. H.; Massi, D. M.; Zhang, J.-H.; Rosmus, K. A.; Brunetta, C. D.; Gentile, T. A.; Aitken, J. A. *J. Alloys Compd.* **2014**, *586*, 736–744.

(40) Sahu, G.; Lin, Z.; Li, J.; Liu, Z.; Dudney, N.; Liang, C. *Energy Environ. Sci.* **2014**, *7*, 1053–1058.

(41) Choi, Y. E.; Park, K. H.; Kim, D. H.; Oh, D. Y.; Kwak, H. R.; Lee, Y.-G.; Jung, Y. S. *ChemSusChem* **2017**, *10*, 2605–2611.

(42) Radhakrishnan, B.; Ong, S. P. *Front. Energy Res.* **2016**, *4*, DOI: 10.3389/fenrg.2016.00016.

(43) Wenzel, S.; Randau, S.; Leichtweiß, T.; Weber, D. A.; Sann, J.; Zeier, W. G.; Janek, J. *Chem. Mater.* **2016**, *28*, 2400–2407.

(44) Hood, Z. D.; Kates, C.; Kirkham, M.; Adhikari, S.; Liang, C.; Holzwarth, N. *Solid State Ion.* **2016**, *284*, 61–70.

(45) Lau, J.; Deblock, R. H.; Butts, D. M.; Ashby, D. S.; Choi, C. S.; Dunn, B. S. *Adv. Energy Mater.* **2018**, *8*, 1800933.

(46) Park, K. H.; Bai, Q.; Kim, D. H.; Oh, D. Y.; Zhu, Y.; Mo, Y.; Jung, Y. S. *Adv. Energy Mater.* **2018**, *8*, 1800035.

(47) Kundu, D.; Adams, B. D.; Duffort, V.; Vajargah, S. H.; Nazar, L. F. *Nat. Energy* **2016**, *1*, 16119.

(48) Banerjee, S.; Zhang, X.; Wang, L.-W. *Chem. Mater.* **2019**, *31*, 7265–7276.

(49) Muramatsu, H.; Hayashi, A.; Ohtomo, T.; Hama, S.; Tatsumisago, M. *Solid State Ion.* **2011**, *182*, 116–119.

(50) Ong, S. P.; Mo, Y.; Richards, W. D.; Miara, L.; Lee, H. S.; Ceder, G. *Energy Environ. Sci.* **2013**, *6*, 148–156.

(51) Ohtomo, T.; Hayashi, A.; Tatsumisago, M.; Kawamoto, K. *J. Mater. Sci.* **2013**, *48*, 4137–4142.

(52) Ohtomo, T.; Hayashi, A.; Tatsumisago, M.; Kawamoto, K. *J. Non-Cryst. Solids* **2013**, *364*, 57–61.

(53) Oh, D. Y.; Nam, Y. J.; Park, K. H.; Jung, S. H.; Cho, S.-J.; Kim, Y. K.; Lee, Y.-G.; Lee, S.-Y.; Jung, Y. S. *Adv. Energy Mater.* **2015**, *5*, 1500865.

(54) Chen, H. M.; Maohua, C.; Adams, S. *Phys. Chem. Chem. Phys.* **2015**, *17*, 16494–16506.

(55) Jung, Y. S.; Oh, D. Y.; Nam, Y. J.; Park, K. H. *Isr. J. Chem.* **2015**, *55*, 472–485.

(56) Jiang, T.; Ozin, G. A. *J. Mater. Chem.* **1998**, *8*, 1099–1108.

(57) Tanaka, K.; Tamamushi, R. *Z. Naturforsch. A* **1991**, *46*, 141–147.

(58) Zohourian, R.; Merkle, R.; Raimondi, G.; Maier, J. *Adv. Funct. Mater.* **2018**, *28*, 1801241.

(59) Bette, S.; Dinnebier, R. E.; Freyer, D. *J. Appl. Crystallogr.* **2015**, *48*, 1706–1718.

(60) Diehl, L.; Bette, S.; Pielnhofer, F.; Betzler, S.; Moudrakovski, I.; Ozin, G. A.; Dinnebier, R.; Lotsch, B. V. *Chem. Mater.* **2018**, *30*, 8932–8938.

(61) Zhang, Y.; Xu, Z. *Am. Min.* **1995**, *80*, 670–675.

(62) Price, W. S. *Concepts Magn. Reson.* **1997**, *9*, 299–336.

(63) Kimmerle, F.; Majer, G.; Kaess, U.; Maeland, A. J.; Conradi, M. S.; McDowell, A. F. *J. Alloys Compd.* **1998**, *264*, 63–70.

(64) Abragam, A., *The Principles of Nuclear Magnetism*; Clarendon Press: 1961.

(65) Hall, C.; Haller, G.; Richards, R. *Mol. Phys.* **1969**, *16*, 377–394.

(66) Umecky, T.; Takamuku, T.; Matsumoto, T.; Kawai, E.; Takagi, M.; Funazukuri, T. *J. Phys. Chem. B.* **2013**, *117*, 16219–16226.

(67) Orazem, M.; Tribollet, B., *Electrochemical Impedance Spectroscopy*; Wiley: 2011.

(68) Francis Weston Sears Mark Waldo Zemansky, H. D. Y., *University physics*, 6th ed.; Reading, Mass. : Addison-Wesley Pub. Co.: 1982.

(69) Mills, R. *J. Phys. Chem.* **1973**, *77*, 685–688.

(70) PHoenix Co., V. L. Education Series - Conductivity Guide, `http://www.vl-pc.com/default/index.cfm/technical-info/conductivity-guide/`, Web Page.

(71) Tanaka, K.; Nomura, M. *J. Chem. Soc., Faraday Trans. 1* **1987**, *83*, 1779.

(72) Mason, P. E.; Ansell, S.; Neilson, G. W.; Rempe, S. B. *J. Phys. Chem. B.* **2015**, *119*, 2003–2009.

(73) Murugan, R.; Thangadurai, V.; Weppner, W. *Angew. Chem. Int. Ed.* **2007**, *46*, 7778–7781.

(74) Kato, Y.; Hori, S.; Saito, T.; Suzuki, K.; Hirayama, M.; Mitsui, A.; Yonemura, M.; Iba, H.; Kanno, R. *Nat. Energy* **2016**, *1*, 16030.

(75) Horne, R. A.; Courant, R. A. *J. Phys. Chem.* **1964**, *68*, 1258–1260.

(76) Eyraud, C.; Quinson, J. F.; Brun, M. In *Studies in Surface Science and Catalysis*, Unger, K. K., Rouquerol, J., Sing, K. S. W., Kral, H., Eds.; Elsevier: 1988, pp 295–305.

(77) Alba-Simionesco, C.; Coasne, B.; Dosseh, G.; Dudziak, G.; Gubbins, K. E.; Radhakrishnan, R.; Sliwinska-Bartkowiak, M. *J. Condens. Matter Phys.* **2006**, *18*, R15–R68.

(78) Novák, P.; Scheifele, W.; Joho, F.; Haas, O. *J. Mater. Chem. A* **1995**, *142*, 2544–2550.

(79) Demir-Cakan, R.; Palacin, M. R.; Croguennec, L. *J. Mater. Chem. A* **2019**, *7*, 20519–20539.

(80) Richards, W. D.; Miara, L. J.; Wang, Y.; Kim, J. C.; Ceder, G. *Chem. Mater.* **2016**, *28*, 266–273.

(81) Inaguma, Y.; Liquan, C.; Itoh, M.; Nakamura, T.; Uchida, T.; Ikuta, H.; Wakihara, M. *Solid State Commun.* **1993**, *86*, 689–693.

(82) Knauth, P. *Solid State Ion.* **2009**, *180*, 911–916.

(83) Tian, Y.; Sun, Y.; Hannah, D. C.; Xiao, Y.; Liu, H.; Chapman, K. W.; Bo, S.-H.; Ceder, G. *Joule* **2019**, *3*, 1037–1050.

(84) Armstrong, R. D.; Landles, K. *J. Appl. Electrochem.* **1981**, *11*, 247–251.

(85) Armstrong, R. D.; Landles, K. *J. Appl. Electrochem.* **1982**, *12*, 533–535.

(86) MacKenzie, K. J. D.; Smith, M. E. In *Pergamon Materials Series*, MacKenzie, K. J. D., Smith, M. E., Eds.; Pergamon: 2002.

(87) Apperley, D.; Harris, R.; Hodgkinson, P., *Solid-State NMR: Basic Principles and Practice*; Momentum Press: 2012.

(88) Bielecki, A.; Burum, D. P. *J. Magn. Reson., Ser. A* **1995**, *116*, 215–220.

(89) Harris, R. K.; Becker, E. D.; Cabral de Menezes, S. M.; Goodfellow, R.; Granger, P. *Solid State Nucl. Magn. Reson.* **2002**, *22*, 458–483.

CHAPTER 8

Effect of particle size and pressure on the transport properties of the fast ion conductor t-Li_7SiPS_8

Christian Schneider, Christoph P. Schmidt, Anton Neumann, Moritz Clausnitzer, Marcel Sadowski, Sascha Harm, Christoph Meier, Timo Danner, Karsten Albe, Anrulf Latz, Wolfgang A. Wall, and Bettina V. Lotsch

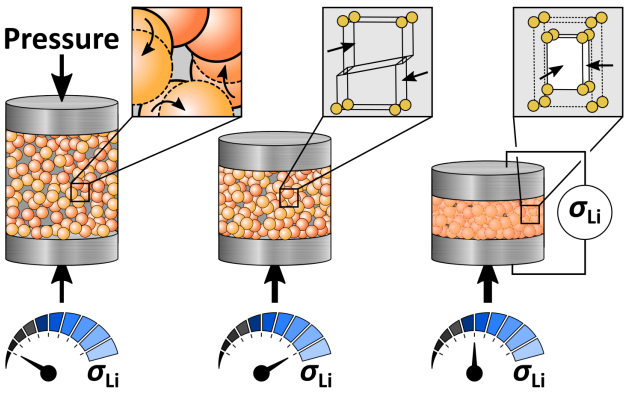

Supporting information can be found in Appendix E.
Author contributions can be found in Appendix F.

Contents of Chapter 8

8.1 Abstract

All-solid-state batteries promise higher energy and power densities as well as increased safety compared to lithium ion batteries, by using non-flammable solid electrolytes and metallic lithium as the anode. As the liquid electrolyte is replaced by a solid electrolyte, ensuring permanent and close contact between the various components as well as between the individual particles is key for the long-term operation of a solid-state cell. Currently, there are few studies on how a solid-state electrolyte behaves when compressed by external pressure. Here we present a study in which the compression mechanics and ionic conductivity evolution of the fast solid-state conductor Li_7SiPS_8 were investigated under pressure on two samples with different particle sizes. *In operando* electrochemical impedance spectroscopy under pressure allows the determination of the activation volume of Li_7SiPS_8. In addition to the experiments under pressure, we show that the determined ionic conductivity additionally depends on the contact pressure. Furthermore, we simulate pelletizing using the discrete element method followed by finite volume analysis, where the effect of the pressure dependent microstructure can be distinguished from the atomistic effect of the activation volume. We conclude not only that the pelletizing pressure is an important parameter for describing the ionic conductivity of a solid, but also the particle size and morphology as well as the contact pressure during the measurement affect the impedance of a solid tablet. Furthermore, the relative density of a tablet is a weaker descriptor for the sample's impedance, compared to the particle size distribution.

8.2 Introduction

The global market for lithium-ion batteries (LIB) is expected to grow rapidly due to the need for high-energy storage media for consumer electronics and automotive applications. For battery electric vehicles (BEVs), high capacity is critical to compete with the high mileage of conventional internal combustion engine vehicles. The all-solid-state (lithium-ion) battery (ASSB), which is based on a solid rather than liquid electrolyte, promises to meet the growing energy needs of modern BEVs. The ASSB design not only enables bipolar stacking, but could also enable the use of high-capacity lithium metal- or silicon-based anodes as an alternative to low-capacity carbon-based anodes in LIBs.[1] These advantages in cell design promise to increase energy density by about 70% compared to conventional LIBs.[2] In a fully solid system, close contact between particles is required to generate homogeneous electric fields and minimize internal resistance. In industry, the consolidation of powdered starting materials by calendering, *i.e.*, pressing between two rotating steel cylinders, is the established standard, while isostatic or uniaxial pressing is used for laboratory-scale pellet and solid-state battery production. Besides the consolidation effect caused by pressing, large external and internal forces can lead to undesirable effects, such as the pressing of lithium metal into separator pores.[3–5] A recent interlaboratory study by Ohno *et al.* pointed out that in solid electrolyte research, no uniform protocol for fabricating and measuring ion conductors exists. The study found that both the pelletizing pressure and stack pressure (pressure during measurement) influence the reported ionic conductivities, especially for mechanically soft thiophosphates.[6] We refer to stack pressure as the pressure constantly applied during operation by the cell housing or an external

system. Although the influence of (stack) pressure on the ionic conductivity of materials like silver halides,[7–10] lithium borohydrides,[11,12] lithium metal oxides (e.g. lithium lanthanum titanate (LLTO)[13] and Li-β-alumina[13]), as well as sodium ion conductors (e.g. Na_3SbS_4[14] and Na_3PS_4[15]) have been studied, data for lithium thiophosphates is still sparse. To classify the existing literature, two effects need to be distinguished. First, pressure can impact the state of sample densification. If the (crystalline) sample under study is not a single crystal, the relative density ρ_{rel}, *i.e.*, the ratio of the geometric density ρ_{geo} and the crystallographic density ρ_{cryst} normally is $0 < \rho_{rel} < 1$. While low ionic conductivity is commonly expected at low relative density, higher relative densities promise higher ionic conductivity, because the amount of non-contributing voids between solid electrolyte particles is lower and particle contacts are increased. Kodama *et al.* imaged the compression of Li_6PS_5Br particles using X-ray computed tomography (CT) and used the three-dimensional information to simulate the evolution of ion transport in the sample at different pressure levels.[16] They concluded for increasing pressure that the particles are crushed and fill empty cavities, which is similar to a sintering process at room temperature. Following this work, Kodama *et al.* used morphological descriptors such as sphericity and contact ratio measured on individual particles *via* X-ray CT. They showed that the increased ionic conductivity was due to the collapse of the cavities and the increase in contact area with increasing pressure.[17] While these studies focused on the compression of a powdered sample - a microstructural phenomenon[14,16–19] - other research groups focused on the atomistic effect of pressure on ionic conductivity.[8–13,15,20,21] Although often neglected, solids can be elastically compressed by shrinkage of the unit cell, resulting in smaller bond lengths and different bond angles. All these effects alter the dynamics of ion migration by changing the volume required for migration between different sites. This fundamental thermodynamic effect is described by the activation volume which we will discuss in more detail further below.

Figure 8.1 compiles literature data on some lithium, sodium and silver ion conductors. The hollow data points represent measurements where the pressure on the powder sample was increased, thus compressing the sample into a pellet. The filled data points represent conductivity measurements made on preformed pellets (circle) or, in the case of Li-β alumina, on a single crystal (diamond). While the conductivity data measured on pre-pressed pellets mostly show a linear behavior of $\ln(\sigma)$ with pressure, the measurements starting with unpressed powder show a different trend. With increasing pressure, the ionic conductivity increases rapidly at first, eventually approaching a maximum. For Na_3PS_4, the pressure behavior after reaching the maximum in conductivity is similar to the behavior of pre-compressed samples.[15] Famprikis *et al.* explained this behavior with two regimes, an extrinsic compaction regime at low and an intrinsic activation volume regime at high pressure.[15] However, the extrinsic regime for the second and third compression cycle exhibits the low pressure characteristics of the first cycle, indicating detrimental electrode-sample contacts at low pressure. In the extrinsic, low pressure region, the compaction of the powder dominates,[15] while at higher pressure the effect of unit cell compressibility, as observed in β-AgI,[8] $LiBH_4$,[12] Li-β-alumina,[13] and LLTO,[22] dominates.

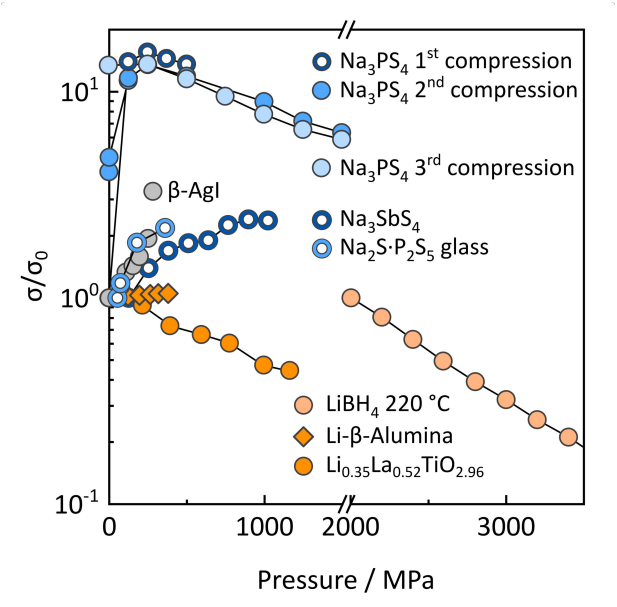

Figure 8.1: Pressure behaviour of Na_3PS_4,[15] Na_3SbS_4,[14] $Na_2S \cdot P_2S_5$ glass,[18] β-AgI,[8] $LiBH_4$,[12] Li-β-alumina,[13] and $Li_{0.35}La_{0.52}TiO_{2.96}$[22] (LLTO) ion conductors extracted from literature. The conductivities σ were normalized to the conductivity σ_0 measured at the lowest available pressure to better compare literature data that is otherwise several orders of magnitude apart.

In this study, we investigate the effect of pelletizing and stack pressure on the powder compression of the $Li_{10}GeP_2S_{12}$-like ion conductor t-Li_7SiSP_8, and show how (stack) pressure affects pellet density and sample impedance. An analysis of the mechanical response of the powder under uniaxial loading shows that the t-Li_7SiSP_8-thiophosphate sample follows the empirical Heckel equation for powder compression, enabling the distinction of different compaction regimes. Furthermore, we show that particle size influences the measured compression mechanics and ionic conductivity, but not the derived activation volume. The transport properties and positive activation volume of t-Li_7SiSP_8 are supported by *ab initio* molecular dynamics (AIMD) calculations. Finally, we demonstrate how image-based analysis of particle size and morphology, in conjunction with simulation using the discrete element method and subsequent finite volume analysis of the microstructure, helps to gain insight into the pellet formation process by only using geometric information as an input.

8.3 Results and discussion

8.3.1 Mechanical stages of powder consolidation

First we investigate the macroscopic mechanical response of t-Li_7SiSP_8 powder to the applied pressure as a function of particle size. To this end, we have prepared two particle size fractions by sieving with a 50 µm mesh-size sieve. We refer to Appendix E for more details on domain and particle size. The fraction passing the sieve is denoted as the <50 µm fraction, while the powder remaining in the sieve is denoted the >50 µm fraction. We determined the (secondary) particle size distribution (PSD) of the two fractions by analyzing scanning electron microscopy (SEM) images with ImageJ[23] plugins[24,25] (see Figure 8.2a). The procedure is included in Appendix E file along with a flowchart (Figure E.2), example images (Figure E.3), and SEM images (Figure E.4 and E.5). Additionally, information about particle morphology is included in Appendix E (Figure E.7 and E.8). Figure 8.2b shows the relative number fraction of binned (1 µm) particle sizes for both samples. The <50 µm sample follows a monomodal particle size distribution (PSD), while the >50 µm sample shows a bimodal PSD. Despite the fact that small particles dominate the number-based PSD for the >50 µm sample, the bulk of the sample consists of >50 µm particles, as shown in the volume-based PSD (see Figure 8.2c, blue dashed line) and indicated by the $D_{10} = 89$ µm value. The D_{10}, D_{50}, and D_{90} values for the PSDs are summarized in Table E.1 and E.2 in Appendix E.

The evolution of the pellet thickness with (uniaxial) pelletizing pressure of the two t-Li_7SiSP_8 powder samples is shown in Figure 8.2d. A scheme representing the experimental procedure is depicted using an insert in Figure 8.2d. Increasing the pressure leads to a fast initial decrease in pellet thickness that saturates at a thickness where the relative density of the pellet approaches 100%. Upon releasing the pressure, the pellet thickness increases and the pellet density decreases by about 4%, as depicted in Figure 8.2e. The <50 µm sample has a higher initial density and results in a denser pellet after pressing at 1.7 GPa compared to the >50 µm sample. To better understand the compaction mechanism of t-Li_7SiSP_8, the empirical Heckel equation[26] derived from the compaction of metal powders was applied to the "in die" pressure-density data. Despite the large number of published mathematical descriptions of powder compaction, the Heckel equation is still widely used in particle technology and pharmaceutics. Assuming that the functional form of pellet formation is formally analogous to a first-order chemical reaction, the Heckel equation takes the form:

$$\ln\left(\frac{1}{1-\rho_{\mathrm{rel}}}\right) = Kp + A, \tag{8.1}$$

where ρ_{rel} is the relative density of the specimen at pressure p. K and A are the slope and y-intercept of the linear region of the Heckel plot. Additionally, Heckel plots can be classified into "in die" and "out of die" measurement conditions. While "in die" plots represent data measured during compaction under pressure, "out of die" plots are generated from data measured at very low or zero pressure.[27]

Generally, three different states of powder compression regimes can be identified in "in die" Heckel plots, if sufficently high pressures are applied.[27,28] A schematic "in die" Heckel plot is given in Figure E.9a in Appendix E. Notably, the three compression regimes may merge and different consolidation mechanisms may prevail at the local level, depending on

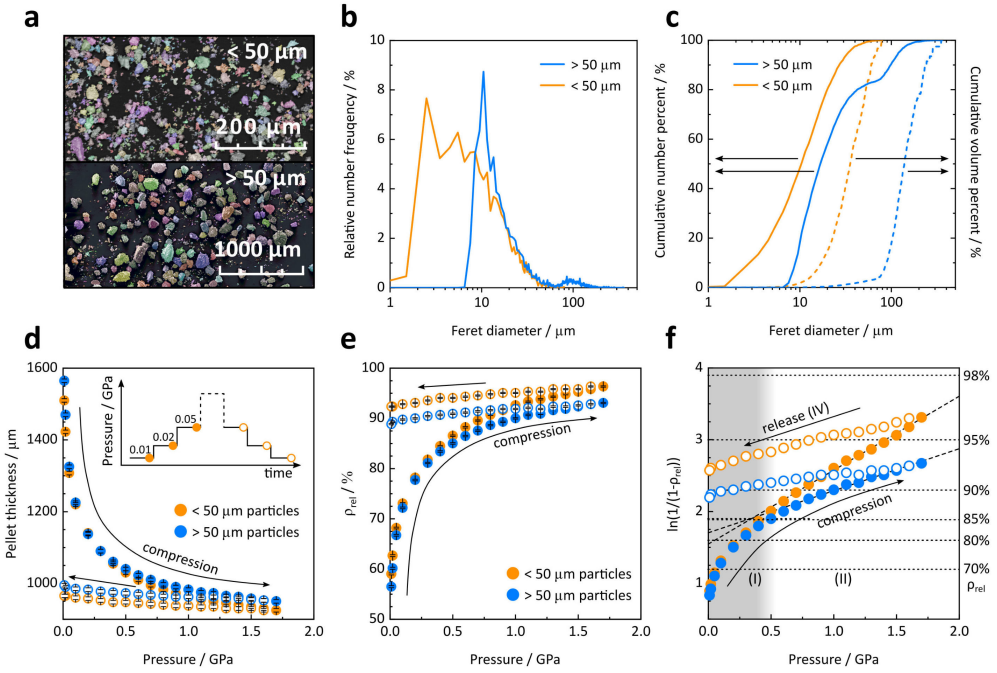

Figure 8.2: (a) False color SEM image of the two *t*-Li_7SiPS_8 sieving fractions. (b) Relative number fraction of *t*-Li_7SiPS_8 particle sizes (expressed as the Feret diameter). (c) Cumulative number- (straight line) and volume-based (dashed line) PSD. The volume-based distribution curves were calculated based on the Feret diameter. Evolution of pellet thickness (d) and pellet relative density (e) of *t*-Li_7SiPS_8 sieving fractions under pelletizing pressure. The insert in (d) schematically depicts the experiment. The filled data points indicate increasing pressure, while the hollow points indicate the release sweep. (f) "in die" Heckel plot analysis for the two sieving fractions. The dashed lines indicate the linear regime, while the dotted lines aid to estimate the relative density of the sample. The gray and white areas correspond to the regions in which particle rearrangement and (agglomerate) fragmentation (I), as well as plastic deformation of the particles (II) dominate the compression sweep.

the local density and the availability of voids. In regime I, individual particles rearrange until they are held in place by interlocking with neighboring particles or the die wall. To some extent, agglomerates may also fragment when the capability for elastic and inelastic deformation of the agglomerate is exhausted. Fragmentation depends on the particle size and critical stress intensity factor that describes the stress needed for crack propagation.[29] This adds to the increase of the relative density as voids are filled and is indicated by the nonlinear regime in the Heckel plot. Figure 8.2f indicates that regime I dominates the compression up to 0.5 GPa and that both sieving fractions behave comparably in this first compression stage.

Once (fragmented) particles are locally fixed, elastic and plastic deformation of a

majority of particles takes place. This phase of the compression is referred to as regime II and dominates for pressures above 0.5 GPa. It can be recognized in Figure 8.2f as a linear region of the Heckel plot, following Equation (8.1). Once local stresses exceed the elastic limit of an individual particle, irreversible mechanical changes, either by plastic deformation or fragmentation, lead to further consolidation.[27,28] Whereas brittle materials tend to break into smaller pieces that can fill voids, softer materials such as thiophosphates may exhibit plastic deformation.[30] While similar in regime I, the two PSD samples exhibit different slopes in regime II. The reciprocal of the slope K can be interpreted as the mean yield pressure P_y of the material, which describes the stress required for plastic flow.[28,30–32] For the <50 µm sample the calculated P_y from the "in die" data is smaller (0.95(3) GPa) than that for the >50 µm sample (1.65(3) GPa), indicating easier plastic deformation for the sample with the smaller particle size. The mean yield pressure calculated from "out of die" data shown in Figure E.9d is higher for both PSDs compared to the "in die" data, but still follows the trend of higher P_y for larger PSD. Lower mean yield strength can indicate lower fracture strength of individual particles, leading to more facile deformation under pressure and thus higher compressibility.[33]

In the final compression stage, regime III starts to dominate when almost all pores are eliminated and the density is close to 90%-95%.[34] At this stage, the individual particles are no longer distinguishable (see Figure E.10 d), and the pellet behaves more like a single body that deforms elastically as the pressure increases.[35] In the Heckel diagram, this condition is usually visible as an upward curvature with increasing pressure, as shown in the schematic Heckel plot in Figure E.9a.[35] For t-Li_7SiSP_8, no distinct deviation from the linear regime is observed at high pressure, indicating that the pressure is not sufficient to enter regime III. However, the comparison of "in die" and "out of die" Heckel plots (see Figure E.9d) clearly depicts elastic contributions in regime II. Since the "out of die" curve is measured at a low stack pressure of 0.01 GPa, where almost no additional elastic recovery is to be expected, the difference between "out of die" and "in die" data is attributed to the elastic deformation of the pellet.[36] Hence, the typical Heckel regimes II and III cannot be visually differentiated for t-Li_7SiSP_8 in the "in die" analysis within the measured pressure range, but pellet elasticity is observed as the difference between "in die" and "out of die" curves.

The release of pressure decreases the density and is commonly described as regime IV of fast elastic recovery/relaxation into the "final" pellet size.[37] The <50 µm sample exhibits a larger elastic recovery compared to the larger sized sample, as indicated by the steeper slope upon pressure release (see Figure 8.2f). This agrees well with the compression sweep that yielded a larger difference between the "in die" and "out of die" P_y for the <50 µm sample compared to the >50 µm sample.

The pellet formation process, which includes elastic and more importantly plastic deformation, leads to microscopic defects in the pellet body. SEM images taken on pellets compressed at 1.7 GPa, depicted in Figure E.10b-c, show signs of cracks on the scale of tens of micrometers after release from the die. While the cracks are caused by the plastic deformation process and can be restrained by elastic deformation at higher pressure, they appear when the pressure is relieved.

8.3.2 Influence of pelletizing pressure on the ionic conductivity of *t*-Li_7SiPS_8

The nontrivial mechanical response of the powder samples, as described in the previous section, clearly affects the ionic conductivity. Figure 8.3 shows the evolution of the ionic conductivity of the two different *t*-Li_7SiPS_8 samples with increasing and decreasing pressure. Exemplary Nyquist plots are shown in Figure E.11. At 0.01 GPa, the untreated and uncompacted powder samples show an ionic conductivity of $0.3 \cdot 10^{-3}\,\mathrm{S\,cm^{-1}}$ for the <50 µm and $0.7 \cdot 10^{-3}\,\mathrm{S\,cm^{-1}}$ for the >50 µm sample. This difference is likely due to contact effects between individual particles: In the <50 µm sample more individual particles are present in the same total sample mass. Consequently, this results in more microscopic grain-to-grain contacts (secondary particles), thus possibly leading to a higher resistance for ionic conduction due to more unfavorable grain-to-grain orientations. Harm *et al.* have shown that in the glass-ceramic *t*-Li_7SiPS_8 intra- and intergrain diffusion processes are mixed, with a higher diffusivity on a shorter (intergrain) length scale.[38] A recent study of Ates *et al.* also points out that grain boundaries impact the ionic conductivity more than particle porosity and tortuosity.[39] As the pressure increases, this trend of lower ionic conductivity for the smaller PSD continues and is observed for all measured pressures.

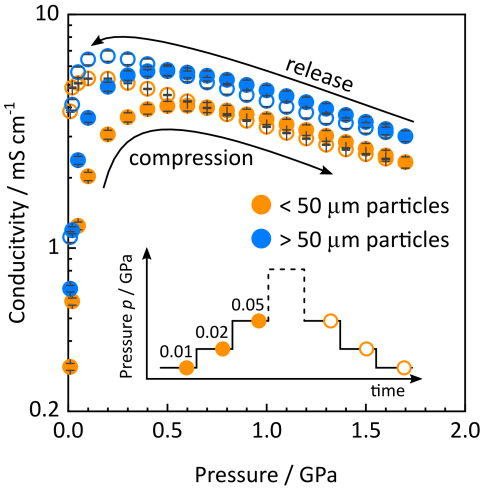

Figure 8.3: Evolution of ionic conductivity with applied uni-axial pressure (first cycle). Orange and blue circles represent < 50 µm and > 50 µm particle size fractions, respectively. Hollow and filled circles denote impedance measurements performed on increasing and decreasing the applied pressure (see inserted scheme).

Both samples show a sharp increase in σ with increasing pressure until a maximum of $4.1 \cdot 10^{-3}\,\mathrm{S\,cm^{-1}}$ is reached for the small and $5.7 \cdot 10^{-3}\,\mathrm{S\,cm^{-1}}$ for the large particle sizes (both at 0.5 GPa). Although the smaller batch is more densely packed (Figure 8.2b), the ionic conductivity is lower, suggesting that detrimental particle-particle contacts dominate the conductivity (*vide supra*). After reaching a maximum ion conductivity, both

samples show a nearly linear decrease in $\ln(\sigma)$ with pressure. Upon pressure release, σ increases until it reaches a maximum of $5.3 \cdot 10^{-3}\,S\,cm^{-1}$ (<50 µm) and $6.6 \cdot 10^{-3}\,S\,cm^{-1}$ (>50 µm) at about 0.1–0.2 GPa. At the lowest applied pressure (0.01 GPa), the pelletized samples exhibit an ionic conductivity of $3.8 \cdot 10^{-3}\,S\,cm^{-1}$ (<50 µm) and $1.1 \cdot 10^{-3}\,S\,cm^{-1}$ (>50 µm). After repeating the compression and release procedure, the ionic conductivity at 0.01 GPa is $4.4 \cdot 10^{-3}\,S\,cm^{-1}$ and $2.1 \cdot 10^{-3}\,S\,cm^{-1}$ (not shown) for the small and large fractions, respectively. While the smaller PSD sample shows only a slight improvement on the second compression cycle, the larger PSD fraction almost doubles in ionic conductivity (at 0.01 GPa). Subsequent compression/release cycles are expected to improve the pellet/electrode interface by plastically deforming the top particles, thus smoothing the surface. A similar behavior for the second and third compression cycle was observed for Na_3PS_4 (see Figure 8.1).[15] We draw two conclusions from the observations so far. First, the ionic conductivity of t-Li_7SiSP_8 powder batches with larger particle fractions is higher than for the smaller particle fraction, regardless of the compression stage during pelletizing. In addition, the >50 µm is more sensitive towards the release of pressure. Relative pellet density has a smaller influence on ionic conductivity than particle size when the pellet is formed. Therefore, higher pellet density, as observed for the <50 µm sample, is not the only influencing factor for higher conductivity, as measured for the >50 µm sample. Our metadata analysis of Ohno's study about the reliability of conductivity measurements on argyrodites also shows that pellet density only weakly correlates with ionic conductivity.[6] For more information, please refer to Appendix E. Second, the ionic conductivity at very low pressure (release sweep) is affected by factors other than pellet compression. As the contact pressure decreases, the contact resistance at the interface between the electrode and the sample has an increasing effect on the measured impedance, and is sensitive towards the particle size distribution. This low pressure effect and possible explanations are presented in a later section.

8.3.3 Influence of activation volume on ionic conductivity

As described before, the non-linear evolution of ionic conductivity of a powder sample under increasing pressure is a result of two effects. The microscopic effect (see above) is governed by powder compression and pellet formation at low pressures, and the atomistic effects of molar volume compression dominates at high pressures. To better understand these atomistic effects, let us first analyze the Li transport properties of t-Li_7SiSP_8 in the absence of pressure.

Harm *et al.*[38] have reported a high total ion conductivity of $2 \cdot 10^{-3}\,S\,cm^{-1}$ and an activation energy of 0.27 eV for t-Li_7SiSP_8. The activation energy is in line with calculated migration barriers of 0.22 eV for 1D ion migration along the c direction and 0.28 eV for 3D migration obtained from bond valence sum simulations,[40–42] as illustrated in Figure 8.4a. This anisotropy is confirmed in *ab initio* molecular dynamics simulations: The diffusion coefficient along the c direction has a lower activation barrier and is found to be approximately four times higher than along the a/b directions (see Figure E.17). For more details on the AIMD simulations, we refer to Appendix E.

At pressures above 0.5–0.7 GPa, the linear decrease of $\ln(\sigma)$ in Figure 8.3 reveals that the effect of molar volume compression dominates the pressure dependence. In other words, the pressure leads to an elastic compression of the formed pellet and thus

the material. To illustrate how this affects the Li migration, AIMD simulations have been performed based on structural models, whose cell parameters have been uniformly rescaled (see Figure 8.4b). Based on the calculated elastic constants (see Appendix E), the estimated pressures of these calculations are 0.8 and 1.7 GPa for the utilized scaling factors f of 0.99 and 0.98, respectively. The resulting Li mean square displacement (MSD) indicate that the diffusion is lowered in compressed cells.

The pressure dependence of the ionic conductivity is connected to the activation volume ΔV. The activation volume can be formally expressed by the following equation:

$$\Delta V = k_\mathrm{B} T \left(\left(\frac{\partial \ln(\sigma_0)}{\partial p} \right)_{T,N_i} - \left(\frac{\partial \ln(\sigma)}{\partial p} \right)_{T,N_i} \right) \tag{8.2}$$

We refer to Appendix E for a more detailed derivation of equation (8.2). The pressure dependence of the pre-exponential factor σ_0 is small (less than 10% of the second term in equation (8.2))[11,15,43–47] as verified with AIMD simulations for $Li_{10}GeP_2S_{12}$.[48] Therefore, we can simplify equation (8.2) to:

$$\Delta V \approx -k_\mathrm{B} T \left(\frac{\partial \ln(\sigma)}{\partial p} \right)_{T,N_i} \tag{8.3}$$

A more accurate approximation of the activation volume, which was derived specifically for cubic crystal systems, is presented in Appendix E. For t-Li_7SiSP_8, we will refer to the simplified definition of the activation volume as given in Equation (8.3).

While activation energy is generally understood as an activation barrier to be overcome, the activation volume has a different physical meaning. In ion-conducting solids, the ions require a certain volume V_m for local migration from one site to another, *i.e.* the space needed at the saddle point, while the (anionic) sublattice provides a free volume V_f. The activation volume ΔV is defined as the difference between V_m and V_f:[13,15,47,49]

$$\Delta V = V_\mathrm{m} - V_\mathrm{f} \tag{8.4}$$

Thus, a non-zero activation volume indicates a mismatch between the free volume of the structure and the volume required for ion migration. If an ion must migrate through a bottleneck too narrow for its size, the lattice locally expands, which is described by a positive activation volume.[13,15,49] In some cases, ΔV is negative and enhanced ion transport with increasing pressure is observed.[13,50]

Based on the data shown in Figure 8.4b we estimate an activation volume of 1.7–2.0 $\mathrm{cm^3 mol^{-1}}$. However, more extensive simulations would be required to accurately verify the computed activation volume. Nevertheless, these results align well with the findings of Fu *et al.* for tetragonal $Li_{10}GeP_2S_{12}$ (LGPS).[48] Through structural relaxation and AIMD simulation, they calculated an activation volume of 2.17 $\mathrm{cm^3 mol^{-1}}$ and found a (positive) linear correlation of lithium ion diffusivity with the volume of the unit cell and the "neck size" of the migration path, similar to the triangle spanned by sulfur ions from tetrahedral units as drawn in Figure 8.4a.[48]

In addition to simulating the effect of cell compression via AIMD calculations, we extracted the activation volume based on experimental data. A small increase in pellet

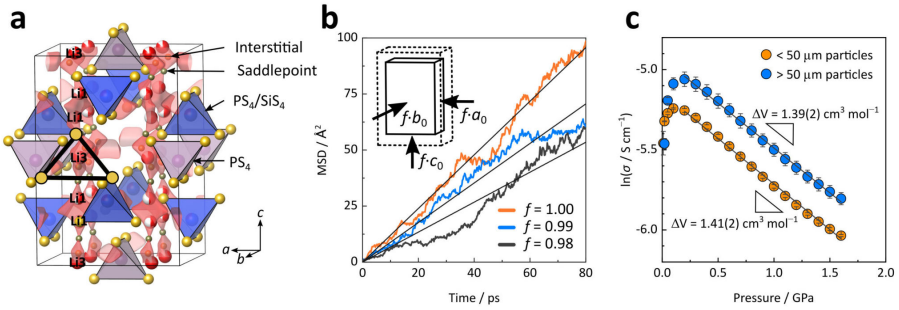

Figure 8.4: (a) Crystal structure of t-Li_7SiPS_8 with the bond valence sum iso-energy landscape in red, indicating favorable 1D conduction channels along the c direction. The black triangle depicts the bottleneck spanned by three sulfur atoms. (b) Li MSD from AIMD simulations at 700 K for different cell volumes of t-Li_7SiPS_8. Linear fits of Li MSD are depicted as straight grey lines. (c) Natural logarithm of ionic conductivity of t-Li_7SiPS_8 from the experiment with pressure. The fitted slope is depicted as a black line. The data points and error bars represent the average and standard deviation of three ($< 50\,\mu m$) and two ($> 50\,\mu m$) consecutive pressure-release sweeps.

density is observed in the second (and third) compression sweep, which affects the calculated ionic conductivity. To exclude further consolidation effects (deviation from linearity), only the release sweeps were considered for evaluating the activation volume. The activation volume resulting from fitting the linear range in Figure 8.4c is approximately $1.4\,cm^3mol^{-1}$ for both size fractions, indicating that the activation volume is independent of particle size and morphology and is an intrinsic material property. The magnitude of the activation volume is in line with our simulations as well as with other lithium and sodium solid electrolytes.[15]

The positive sign of ΔV indicates that the t-Li_7SiSP_8 host structure must expand locally to accommodate a lithium ion at the saddle point of ion migration.

8.3.4 Pressure effect on crystallinity

In addition to the effect of activation volume, phase transitions, as in $LiBH_4$,[11,12] can also lead to changes in the impedance of a sample under pressure. However, phase transitions usually manifest in jumps in one or more properties of a material, like volume expansion, change in crystal structure, or a change in the transport properties. The impedance shows no such jump, hence a pressure induced first-order phase transition can be ruled out. Li_7SiPS_8 is a glass-ceramic[38] in which a side phase limits the ionic conductivity. The side phase was assumed to be amorphous due to the absence of additional Bragg peaks.[38] We measured ^{31}P-solid-state NMR to determine the amount and change of the side phase in the untreated and pressed samples. The ^{31}P MAS NMR spectra are shown in Figure E.12a. The pristine sample has 8.2 to 9.0 wt% side phase, while the sample pressed at a pelletizing pressure of 1.7 GPa has a weight fraction of 9.7 to 10.2% side phase. For samples with larger particles, the weight fraction of the side phase is slightly higher than for the fraction with smaller particles. However, this difference is minute and

unexpected since both particle size fractions were recovered from the same sample. The difference in the side phase is thus probably due to small differences in the homogeneity of the sample or to fitting errors. The increase of around 1–1.5% after pressing could be due to stress from plastic deformations during pellet formation. In particular, where the material flows plastically into voids, the crystalline domains could be subject to greater shear forces, resulting in sliding of lattice planes and thus loss of long-range order. This is reflected in a significant peak broadening (FWHM) for the *t*-Li_7SiSP_8 signals of the pressed samples compared to the unmodified powder (see Figure E.12b). Additionally, the peaks associated with the amorphous side phase exhibit broadening, indicating a wider range of chemical environments for the side phase, likely caused by the stress during compaction.

8.3.5 Influence of stack pressure on the ionic conductivity of *t*-Li_7SiPS_8

As described above, the ionic conductivity of *t*-Li_7SiSP_8 pellets formed at high pressure is lower at low stack pressure. This might be caused by a higher surface roughness, as indicated by the cracks observed in the SEM image in Figure E.10b, leading to lower apparent conductivity of the sample due to current limiting effects. To mitigate this problem, noble metals are usually sputtered onto the pellets to better distribute the current load. Since sputtering is not available for every lab, we systematically investigate how improving the sample-electrode contact can be reached by varying the stack pressure. To this end, we programmed a pressing routine that includes impedance measurements at 0.01 GPa and 0.1 GPa stack pressure in between pelletizing steps at variable pressure. These stack pressures are close to those used in spring-loaded setups such as Swagelok cells or threaded rod press cages, and represent the pressure under which the lowest and highest ionic conductivity was measured previously in the pelletizing pressure experiments. Additionally, any influence of the activation volume on conductivity can be neglected at these pressures.

Figure 8.5 shows the evolution of ionic conductivity of *t*-Li_7SiSP_8 for both particle size fractions at 0.01 and 0.1 GPa stack pressure after being compacted at increasing pelletizing pressures (x-axis in Figure 8.5). It reveals that the trend toward higher ionic conductivities for the >50 µm compared to the <50 µm sample also holds for the stack pressure test. We find that measured ionic conductivity depends not only on the compaction state of the pellet, expressed here by the pelletizing pressure, but also on the pressure applied to the pellet during the impedance measurement. The initial increase in conductivity up to a pelletizing pressure of 0.3–0.5 GPa is observed for both contact pressures and can be explained by the rearrangement and fragmentation of the particles, as previously described in the Heckel plot analysis. However, at low stack pressure, a plateau followed by a further increase in conductivity is observed for both size fractions of *t*-Li_7SiSP_8, while at a higher stack pressure of 0.1 GPa, the measured impedance after the initial regime is almost independent of the pelletizing pressure. Cronau *et al.* observed a similar behavior for glass-ceramic and micro-crystalline Li_6PS_5Br, where a stack pressure of at least 0.05 to 0.1 GPa is needed to achieve low sample impedance.[19]

Here, two effects could explain the observed difference between high and low stack pressure. First, higher stack pressure could result in smoother sample-electrode interfaces,

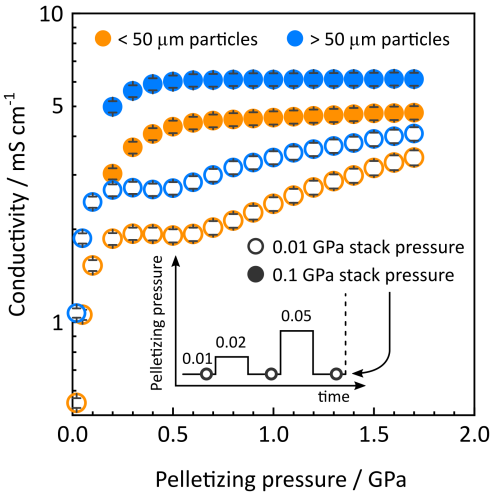

Figure 8.5: Evolution of ionic conductivity with applied uni-axial stack pressure. Hollow and filled circles represent EIS measurements performed at a stack pressure of 0.01 GPa and 0.1 GPa, respectively. The particle size fractions of $< 50\,\mu m$ and $> 50\,\mu m$ are depicted in orange and blue. The inserted scheme describes the measurement procedure of EIS measurements at a fixed stack pressure after pressing at variable pelletizing pressures.

which reduces the interfacial impedance. At very low or zero stack pressure, a pronounced surface roughness is expected. Figure E.10b shows the pellet surface (prepared at 1.7 GPa) imaged by SEM. Although the surface seemed to be smooth when inspected with bare eyes, it exhibits lots of cracks on the scale of tens of micrometers, thus is microscopically rough. A higher stack pressure likely prevents the surface crack opening. As a second effect, the release of pressure down to 0.01 GPa could increase the impedance of the particle-particle contacts. This effect might be larger at low pelletizing pressures where particle binding, *i.e.*, the formation of a solid pellet, is not fully achieved. At higher pelletizing pressures, the impedance between grains should decrease and approach bulk conductivity. As can be seen in Figure 8.5, the conductivity measured at 0.01 GPa stack pressure approaches the conductivity obtained at higher stack pressure, but is still lower even at the highest pelletizing pressure. There, the higher elastic deformation present at higher stack pressure prevents internal crack opening and explains the higher conductivity. This suggests that the mechanical response, as well as the interface contact and the internal crack opening (see Figure E.10) contribute to the unique features of the conductivity evolution at 0.01 GPa stack pressure shown in Figure 8.5. The higher elastic compression at a higher stack pressure can prevent crack opening and ensures a better electrode contact. This agrees well with the finding of Cronau *et al.* who have reported sufficient particle binding in glass-ceramic Li_6PS_5Br at a pelletizing pressure of at least 0.4 GPa.[19] They also suggest to sputter metal electrodes onto the pellet if maintaining a higher stack pressure during the measurement is not possible.

8.3.6 Simulation of powder compression

The influence of t-Li_7SiSP_8 powder compression on the conductivity was further investigated by simulating the pellet compression using a discrete element method (DEM) simulation followed by electrochemical analysis of the obtained pellet microstructures using a finite volume analysis (FVA).

The DEM model, as described in the methods section in detail (see Appendix E), is implemented in the in-house multi-physics research code BACI[51] and used to perform the powder compacting simulations. To parameterize the simulation model, information from the experimental investigations concerning the material, the geometric dimensions of the pelletizing experiments, and the particle size distribution is necessary. Relevant parameters that have been used for the DEM simulations are listed in Table E.5 in Appendix E. A domain with a base of 210×210 µm^2 and a height of 1700 µm was constructed and loaded with 9591 particles for the simulations. Obviously, the lateral dimensions of the pellet in the experiment are significantly larger. However, we chose the lateral dimension in the simulation such that the discrete particle distribution is reasonably close to the experimentally determined one, and such that we can assume that all relevant interaction effects are properly represented. To account for the larger dimensions in reality, periodic boundary conditions where applied in the lateral directions ($x-$ and $y-$direction) to actually extend the area infinitely, whereas the correct pellet thickness in $z-$direction is exactly captured. Furthermore, the required particle size distribution of the synthesized material was measured using SEM image analysis as described before and in more detail in Appendix E.

Figure 8.6a shows the particle distribution of the < 50 µm t-Li_7SiSP_8 sample as a 1 µm bin histogram of the Feret diameter (see definition in Appendix E). The histogram was fitted with a gamma distribution with $a = 1.94431$ and $b = 7.04802$, and the distribution parameters were used as input for the parameterization of the DEM model.

At the end of the particle compacting simulations, we extracted the positions and radii of the particles defining the resulting microstructures, serving as an input to the FVA, for which voxel-based structures were generated. Using the finite volume implementation BEST (Battery and Electrochemistry Simulation Tool)[52,53] effective ionic conductivities of the compressed electrolyte pellets were calculated by simulating the steady state current distribution in the sample for an applied voltage difference. In the first simulation scenario, the bulk conductivity was reduced with the effect of activation volume at constant stack pressure, while in the second scenario the bulk conductivity was reduced with increasing variable pressure. Details concerning the applied FVA method can be found in Appendix E.

The normalized ionic conductivity determined from the experiment under variable pressure and constant stack pressure (0.1 GPa) is shown in Figure 8.6b. In addition, Figure 8.6b includes the results from the DEM/FVA -simulations for both scenarios. Since the conductivity values are normalized, the simulated values do not depend on the assumed bulk conductivity but only on the geometric properties of the input structures. Qualitatively, the simulations show good agreement with the experimental results, capturing the observed effects for both the measurements at constant and variable stack pressure. The applied external pressure results in the compaction of the pellet by rearrangement and deformation of the particles. The larger contact surface between the particles (see

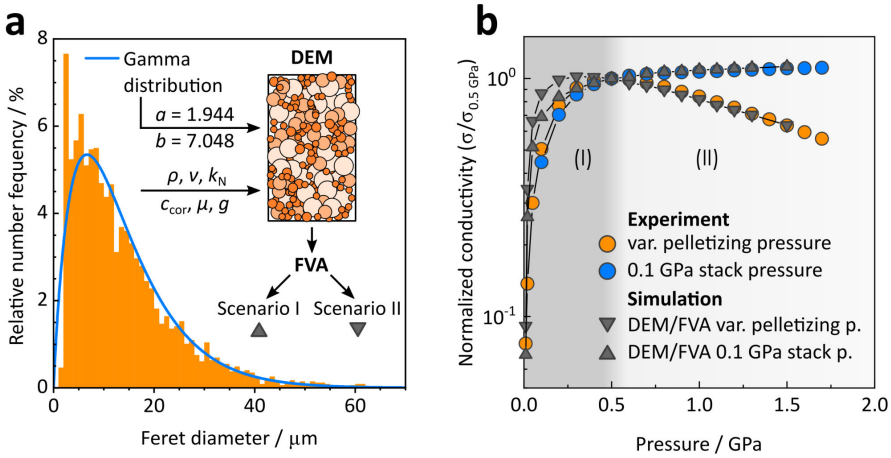

Figure 8.6: (a) Histogram plot of Feret diameter distribution of t-Li_7SiPS_8 ($< 50\,\mu m$) with gamma distribution function fit in blue. A workflow scheme for the DEM/FVA is depicted as an insert. (b) Normalized ionic conductivity from varying pelletizing pressure (orange) and constant stack pressure (0.1 GPa, blue) experiment as a function of variable compression pressure. For the DEM/FVA, the pressure axis relates to the experimental pellet thickness, that was used for parametrization. The activation volume effect was considered in both scenarios, however it is almost negligible in the 0.1 GPa stack pressure scenario (upward triangle) compared to the variable pressure scenario (downward triangle). The experimental conductivity was normalized to the value at 0.5 GPa. At this pressure, the maximum ionic conductivity in the pelletizing pressure experiment was reached.

Figure E.13 in Appendix E), which is modeled by particle overlapping in the DEM, leads to better transport pathways in the electrolyte pellet and a consistently increasing effective conductivity for the first scenario resembling the stack pressure experiment. The good agreement with the experimental measurement shows that the changes of the electrolyte microstructure are captured correctly by the DEM-simulations. For the second case considering the increasing activation volume effect with pressure, the decrease in bulk conductivity with increasing external pressure in the FV-simulations leads to a drop in effective conductivity after reaching a maximum at moderate pressures. The resulting slope corresponds to the experimental values and indicates that the reduction of ionic conductivity described by the activation volume is indeed the prominent effect at variable pelletizing pressure. However, for small pressures in regime (I) the simulated conductivities are consistently higher than the experimental values for both simulation cases. The observed deviation from the experiment can be attributed to the difference between the DEM model consisting of perfect spheres and the powder, which consists of particles that are not perfectly spherical. Consequently, friction and contact resistance effects stemming from the different particle morphology are not fully taken into account in the DEM model. Furthermore, grain boundary resistances, which could be higher for small external pressures, are not included in the FV-simulations. A more detailed discussion on particle morphology is presented in Appendix E.

8.4 Conclusion

In this study, we investigate the macroscopic (*i.e.* microstructural) and microscopic (*i.e.* atomistic) effects of pelletizing and stack pressure on the ionic conductivity of *t*-Li_7SiSP_8, and support our findings by a comprehensive multiscale simulation study of powder compression. Our study reveals a profound influence of particle morphology and particle size distribution (PSD) on the pressure behavior of thiophosphate solid electrolytes. The "in die" (variable pelletizing and stack pressure) and "out of die" (variable pelletizing and constant stack pressure) Heckel analysis suggest that the particle size distribution affects both relative pellet density and the mean yield pressure, and thus the plastic deformation of particles, as well as the elastic recovery. As a consequence, the PSD also has subtle effects on the fraction of amorphous side phases in this thiophosphate glass ceramics, as well as surface and internal crack opening. In all experiments, pellets prepared from larger PSD powders consistently exhibit higher ionic conductivity, despite their lower density compared to pellets consisting of smaller particles. We conclude that a higher number of secondary particle-particle contacts are detrimental for the ionic conductivity of the investigated glass ceramic, which highlights the importance of particle size control to maximize ionic conductivity. This further implies that the PSD should be specified in order to increase the inter-laboratory comparability and reproducibility of conductivity measurements.
In contrast to the microstructural effects, the atomistic effect of elastic unit cell compression is not affected by the PSD of *t*-Li_7SiSP_8. We point out that this intrinsic effect should be considered in high-pressure impedance measurements, as the activation volume influences the conductivity under pressure. The combination of DEM and FVA simulations is able to reproduce the experimental results both at pelletizing and variable stack pressure with high fidelity, confirming the combined effects of microstructure and activation volume on the effective conductivity. Based on our study, we expect samples with an optimized particle size distribution to exhibit an improved mechanical compression response which translates into higher ionic conductivity, thus pinpointing additional handles to improve the performance of solid electrolytes.

To conclude, we summarize the following recommendations for determining ionic conductivities of solid-state ion conductors: To obtain comparable ionic conductivity values, the particle size distribution should be comparable. We suggest using sieves to obtain a fraction with a well defined PSD. Additionally, the influence of pelletizing pressure should be carefully evaluated, as higher pressures can introduce plastic deformation and thus influence phase fractions, like the amount of amorphous side phase in glass ceramics, or lead to a loss in crystallinity. A pelletizing pressure of around 0.5 GPa and a stack pressure of 0.1 GPa are required for glass-ceramic thiophosphates to minimize interfacial resistance and maximize ionic conductivity. These values may well differ for other solid electrolytes with significantly differing elastic moduli. We further note that data measured under high pressure should be interpreted with care, as they can include the atomistic activation volume effect. The same is true for pellet densities, which only present a weak correlation with ionic conductivities. Overall, our study reveals the importance of pressure effects on ionic conductivity and puts forward best practices to ensure a more reproducible reporting of ionic conductivities, thus increasing inter-laboratory comparability of ionic conductivity results.

References

(1) Lee, Y.-G. et al. *Nat. Energy* **2020**, *5*, 299–308.

(2) Janek, J.; Zeier, W. G. *Nat. Energy* **2016**, *1*, 16141.

(3) Doux, J.-M.; Nguyen, H.; Tan, D. H. S.; Banerjee, A.; Wang, X.; Wu, E. A.; Jo, C.; Yang, H.; Meng, Y. S. *Adv. Energy Mater.* **2020**, *10*, 1903253.

(4) Hänsel, C.; Kumar, P. V.; Kundu, D. *Chem. Mater.* **2020**, *32*, 10501–10510.

(5) Hänsel, C.; Kundu, D. *Adv. Mater. Interfaces* **2021**, *8*, 2100206.

(6) Ohno, S. et al. *ACS Energy Lett.* **2020**, *5*, 910–915.

(7) Wagener, K. *Z. Phys. Chem.* **1960**, *23*, 305–312.

(8) Hoshino, H.; Shimoji, M. *J. Phys. Chem. Solids* **1972**, *33*, 2303–2309.

(9) Hoshino, H.; Yanagiya, H.; Shimoji, M. *J. Chem. Soc., Faraday Trans. 1* **1974**, *70*, 281.

(10) Kim, K. S.; Paik, W.-K. *J. Chem. Eng. Data* **1975**, *20*, 356–359.

(11) Takamura, H.; Kuronuma, Y.; Maekawa, H.; Matsuo, M.; Orimo, S. *Solid State Ion* **2011**, *192*, 118–121.

(12) Mezaki, T.; Kuronuma, Y.; Oikawa, I.; Kamegawa, A.; Takamura, H. *Inorg. Chem.* **2016**, *55*, 10484–10489.

(13) Radzilowski, R. H.; Kummer, J. T. *J. Electrochem. Soc.* **1971**, *118*, 714.

(14) Wang, H.; Yu, M.; Wang, Y.; Feng, Z.; Wang, Y.; Lü, X.; Zhu, J.; Ren, Y.; Liang, C. *J. Power Sources* **2018**, *401*, 111–116.

(15) Famprikis, T. et al. *J. Am. Chem. Soc.* **2020**, *142*, 18422–18436.

(16) Kodama, M.; Komiyama, S.; Ohashi, A.; Horikawa, N.; Kawamura, K.; Hirai, S. *J. Power Sources* **2020**, *462*, 228160.

(17) Kodama, M.; Ohashi, A.; Hirai, S. *J. Power Sources Adv.* **2020**, *4*, 100019.

(18) Nose, M.; Kato, A.; Sakuda, A.; Hayashi, A.; Tatsumisago, M. *J. Mater. Chem. A* **2015**, *3*, 22061–22065.

(19) Cronau, M.; Szabo, M.; König, C.; Wassermann, T. B.; Roling, B. *ACS Energy Lett.* **2021**, 3072–3077.

(20) Kurnick, S. W. *J. Chem. Phys.* **1952**, *20*, 218–228.

(21) Mellander, B.-E.; Lazarus, D. *Phys. Rev. B* **1985**, *31*, 6801–6803.

(22) Inaguma, Y.; Yu, J.; Shan, Y.-J.; Itoh, M.; Nakamuraa, T. *J. Electrochem. Soc.* **1995**, *142*, L8–L11.

(23) Schneider, C. A.; Rasband, W. S.; Eliceiri, K. W. *Nat. Methods* **2012**, *9*, 671–675.

(24) Legland, D.; Arganda-Carreras, I.; Andrey, P. *Bioinformatics* **2016**, btw413.

(25) Landini, G. Novel context-based segmentation algorithms for intelligent microscopy, Web Page, accessed: 11.04.2022.

(26) Heckel, R. *Trans Metall Soc AIME* **1961**, *221*, 671–675.

(27) Sun, C.; Grant, D. J. W. *Pharm. Dev. Technol.* **2001**, *6*, 193–200.

(28) Gabaude, C. M.; Guillot, M.; Gautier, J. C.; Saudemon, P.; Chulia, D. *J. Pharm. Sci.* **1999**, *88*, Gabaude, C M Guillot, M Gautier, J C Saudemon, P Chulia, D, 725–30.

(29) Rowe, R. C.; Roberts, R. J. In *Adv. Pharm. Sci.* Ganderton, D., Jones, T., McGinity, J., Eds.; Academic Press: 1995, pp 1–IV.

(30) Hersey, J. A.; Rees, J. E. *Nat. Phys. Sci.* **1971**, *230*, 96–96.

(31) Vreeman, G.; Sun, C. C. *Int. J. Pharm.: X* **2021**, *3*, 100094.

(32) Nordström, J.; Welch, K.; Frenning, G.; Alderborn, G. *J. Pharm. Sci.* **2008**, *97*, 4807–4814.

(33) Khomane, K. S.; Bansal, A. K. *AAPS PharmSciTech* **2013**, *14*, 1169–1177.

(34) Patel, S.; Kaushal, A. M.; Bansal, A. K. *Pharm. Res.* **2007**, *24*, 111–124.

(35) Mahmoodi, F. Compression Mechanics of Powders and Granular Materials Probed by Force Distributions and a Micromechanically Based Compaction Equation, Acta Universitatis Upsaliensis, Thesis, 2012.

(36) Ilić, I.; Govedarica, B.; Šibanc, R.; Dreu, R.; Srčič, S. *Int. J. Pharm.* **2013**, *446*, 6–15.

(37) Paronen, P. *Drug Dev. Ind. Pharm.* **1986**, *12*, 1903–1912.

(38) Harm, S.; Hatz, A.-K.; Moudrakovski, I.; Eger, R.; Kuhn, A.; Hoch, C.; Lotsch, B. V. *Chem. Mater.* **2019**, *31*, 1280–1288.

(39) Ates, T.; Neumann, A.; Danner, T.; Latz, A.; Zarrabeitia, M.; Stepien, D.; Varzi, A.; Passerini, S. *Adv. Sci.* **2022**, *9*, 2105234.

(40) Chen, H.; Adams, S. *IUCrJ* **2017**, *4*, 614–625.

(41) Chen, H.; Wong, L. L.; Adams, S. *Acta Cryst. B* **2019**, *75*, 18–33.

(42) Wong, L. L.; Phuah, K. C.; Dai, R.; Chen, H.; Chew, W. S.; Adams, S. *Chem. Mater.* **2021**, *33*, 625–641.

(43) Jeffery, R. N.; Lazarus, D. *J. Appl. Phys.* **1970**, *41*, 3186–3187.

(44) Allen, P. C.; Lazarus, D. *Phys. Rev. B* **1978**, *17*, 1913–1927.

(45) Bose, D. N.; Parthasarathy, G.; Mazumdar, D.; Gopal, E. S. R. *Phys. Rev. Lett.* **1984**, *53*, 1368–1371.

(46) Daiko, Y.; Takahashi, E.; Hakiri, N.; Muto, H.; Matsuda, A.; Rouxel, T.; Sangleboeuf, J.-C.; Mineshige, A.; Yazawa, T. *Solid State Ion* **2014**, *254*, 6–10.

(47) Fontanella, J. J. *J. Chem. Phys.* **1999**, *111*, 7103–7109.

(48) Fu, Z.-H.; Chen, X.; Zhao, C.-Z.; Yuan, H.; Zhang, R.; Shen, X.; Ma, X.-X.; Lu, Y.; Liu, Q.-B.; Fan, L.-Z.; Zhang, Q. *Energy Fuels* **2021**, *35*, 10210–10218.

(49) Nachtrieb, N. H.; Weil, J. A.; Catalano, E.; Lawson, A. W. *J. Chem. Phys.* **1952**, *20*, 1189–1194.

(50) Fei, H.; Wiedenbeck, M.; Sakamoto, N.; Yurimoto, H.; Yoshino, T.; Yamazaki, D.; Katsura, T. *Phys. Earth Planet. Inter.* **2018**, *275*, 1–8.

(51) BACI A Comprehensive Multi-Physics Simulation Framework, accessed: October 28, 2022. URL `https://baci.pages.gitlab.lrz.de/website/`.

(52) Latz, A.; Zausch, J. *J. Power Sources* **2011**, *196*, 3296–3302.

(53) Danner, T.; Singh, M.; Hein, S.; Kaiser, J.; Hahn, H.; Latz, A. *J. Power Sources* **2016**, *334*, 191–201.

CHAPTER 9

Summary, conclusion and outlook

Solid electrolytes have the potential to pave the way for all solid-state batteries (ASSB). ASSBs, while considered superior to current lithium-ion battery technology, are still in the early stages of academic and industrial research and development. The use of solid electrolytes for ASSBs, either as part of the cathode/anode or as a spatial and electronic separator, is accompanied by solving numerous challenges that have emerged over the past decade. The most pressing goal is to identify materials with high ionic conductivity. Although many classes of materials and compounds with suitable ionic conductivity are currently available, most of them perform poorly in an ASSB. Interfacial problems resulting from ill-fitting electrochemical stability windows or mechanical contact issues due to volume change during cycling often hinder the long-term operation of ASSBs. This work addresses some of the current challenges of sulfide- and thiophosphate-based solid electrolytes by addressing various aspects of enhancing ionic conductivity, including the role of composition, the influence of synthetic routes, anion dynamics, post-synthetic modification, and microstructure engineering.

Summary

An Introduction into battery performance indicators, as well as lithium and sodium ion batteries, including historical developments, material selection and challenges, was given in Chapter 1. Additionally, the concept of the all solid-state battery, fundamental physics of ionic conduction, optimization strategies and an overview of material classes and structures was introduced. Chapter 2 briefly summarized the analytical methods used in this thesis. The research objectives of this work were presented in Chapter 3.

In Chapter 4, three new lithium scandium hypodiphosphates, monoclinic (*m*-)$LiScP_2S_6$, trigonal (*t*-)$LiScP_2S_6$, and $Li_{4-3x}Sc_xP_2S_6$ ($x = 0.\,358$) were presented. Upon heating, *m*-$LiScP_2S_6$ transforms into the trigonal polymorph, which is the first known compound with the disordered version, $[P_{2/2}P_{6/6}S_6]^{4-}$, of the ethane-like $P_2S_6^{4-}$ anion. DFT revealed that both polymorphs are less stable than an ordered trigonal modification. However, this modification, predicted to be isotypic to $AgScP_2S_6$, has not yet been synthesized. Compared to the $LiScP_2S_6$ polymorphs ($\sigma < 10^{-9}\,S\,cm^{-1}$), $Li_{4-3x}Sc_xP_2S_6$ showed an ionic conductivity of $1.2 \cdot 10^{-6}\,S\,cm^{-1}$ that is at least three orders of magnitude higher. This improvement is due to the mixed occupancy of Li and Sc, compared to the ordered, full occupancy of Li and Sc in both monoclinic and trigonal $LiScP_2S_6$ modifications. Chapter 4 illustrated the importance of composition, structure, and cation disorder in improving ionic conductivity and adds to the literature on classical structure-property relationships in solid electrolytes.

Similar to Chapter 4, Chapter 5 and Chapter 6 present the introduction of disorder as a means to improve ionic conductivity of sodium based compounds. In Chapter 5, the influence of two synthesis routes on the structural and transport properties of $Na_4P_2S_6$ is examined in detail, namely a solid-state synthesis and precipitation from a liquid. While the solid-state route yields the highly crystalline, ordered α-$Na_4P_2S_6$ phase, precipitation and subsequent drying of $Na_4P_2S_6 \cdot 6\,H_2O$ leads to the disordered β-phase that exhibits additional defects in its layered structure. Both polymorphs crystallize in the $C2/m$ space group, but the β polymorph differs in the point group symmetry of the $P_2S_6^{4-}$ anion (D_{3d}) and the sodium population in the interlayer. At 160 °C, the α-polymorph transitions to the β-polymorph and *vice versa*. The sodium ion transport pathways calculated with DFT-NEB and BVS are found to be more favorable for the β-polymorph, especially for the 2D long-range migration of Na^+, which is reflected in the slightly higher ionic conductivity for β-$Na_4P_2S_6$. Chapter 5 outlines the often underappreciated importance of synthesis for structure, phase stabilization, and transport properties in solid electrolytes.

High-temperature diffraction and scanning calorimetry experiments on $Na_4P_2S_6$ identified a third polymorph, γ-$Na_4P_2S_6$. In Chapter 6, the cubic structure of γ-$Na_4P_2S_6$ is presented as a consequence of the unique and previously unreported $P_2S_6^{4-}$ anion dynamics. A cubic structure model ($Im\bar{3}m$) obtained from total scattering experiments was used as a starting point to study the cation and anion dynamics by AIMD simulations. It was found that the anions are translationally fixed but dynamically reorient, aligning them mostly along the body diagonal of the cubic cell. The sodium ions, on the other hand, exhibit high translational mobility as reflected by a significant jump in the mean squared displacement obtained from AIMD simulations as well as the in the ionic conductivity during the phase transition from β- to γ-$Na_4P_2S_6$ at 580 °C. The unique properties of

the γ polymorph, i.e., the cubic symmetry, the rotational disorder of the anion on a fixed sublattice, the large heat exchanged during the phase transition, and the soft mechanical nature, strongly suggest that γ-$Na_4P_2S_6$ is a plastic crystal. Indeed, this is the first plastic phase composed of elongated $P_2S_6^{4-}$ anions. Summarizing Chapter 6, the structure of the cubic γ-$Na_4P_2S_6$ was solved and used to computationally simulate the cation and anion dynamics, ultimately demonstrating the potential of utilizing plastic crystal behavior to improve ionic conductivity in solids.

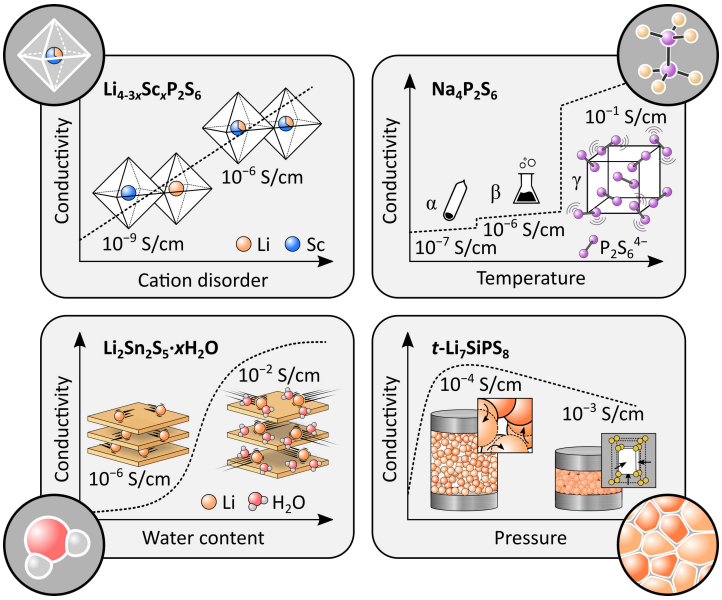

Figure 9.1: Graphical abstract of the projects presented in this thesis. Top left: Chapter 4, top right: Chapter 5 and Chapter 6, bottom left: Chapter 7, bottom right: Chapter 8.

So far, the ionic conductivity of solid electrolytes has been improved by adjusting the composition or by introducing disorder in the cation and anion sublattices. In Chapter 7, a post-synthetic approach was presented using hydration as a tool to effectively screen attractive interactions between the host structure and the migrating ion. For this purpose, water was intercalated into the interlayer space of layered $Li_2Sn_2S_5$ *via* the gas phase. This transforms the anhydrate $Li_2Sn_2S_5$ into two distinctive solid hydrates, $Li_2Sn_2S_5 \cdot xH_2O$, each of which has a broad hydration range in which it exists. A correlation was established between the water content in $Li_2Sn_2S_5 \cdot xH_2O$, ion diffusivity and conductivity, and interlayer spacing. While at zero or low water content ($x < 4$) the ionic conductivity is low ($10^{-6}\,S\,cm^{-1}$–$10^{-5}\,S\,cm^{-1}$), higher water content leads to higher conductivity up to $2 \cdot 10^{-2}\,S\,cm^{-1}$ for $x = 10.2$. This positive correlation between water content and conductivity also applies to the layer distances. The larger the distance between adjacent (negatively charged) layers, the higher the ionic mobility. It is therefore reasonable to assume Coulomb interaction shielding by intercalated water molecules. The hydration shell around the lithium ions facilitates the mobility of lithium

between the layers, in extreme cases ($x > 8$) to almost liquid-like behavior. In addition, the effective proton diffusivity on the order of lithium diffusivity in $Li_2Sn_2S_5 \cdot xH_2O$ ($x \approx 4$ and 8) was observed, indicating a comparable mobility of lithium ions and water molecules. In summary, Chapter 7 demonstrates how the incorporation of water into the two-dimensional structure of $Li_2Sn_2S_5$ improves ionic conductivity by reducing the Coulomb interactions between the lithium cation and the negatively charged layers.

The diffusion of ions in solids can be rationalized by fundamental thermodynamic laws that lead to certain approaches in solid state chemistry to improve ionic conductivity. Some of the commonly known set screws in chemistry and presented in this work are changing the charge carrier concentration, introducing disorder, or shielding trapping forces such as Coulomb interactions. Although these microscopic aspects and properties are the first to be optimized in solid electrolytes, the macroscopic properties of the studied solid should not be ignored. In Chapter 8, a multiscale study of the influence of pressure and particle size on the macroscopic and microscopic behavior of the tetragonal ion conductor Li_7SiPS_8 was presented. Heckel analysis, which describes the evolution of the relative density of a granular sample under compression, was for the first time applied to solid electrolytes and allowed discrimination between at least three mechanical regimes of pellet formation. Particle size distribution (PSD) affects both relative density, mean yield pressure, and elastic recovery. In terms of effective conductivity, samples with a larger PSD exhibit higher overall conductivity than samples with a smaller PSD, suggesting detrimental particle-particle contacts for Li_7SiPS_8. The effect of pressure on conductivity was described by two regimes. While in the first, low pressure regime ($<0.5\,GPa$), powder compression leads to a sharp increase in conductivity, at higher pressure ($>0.5\,GPa$), unit cell compression decreases conductivity, as expected from a material with positive activation volume. The second conductivity regime, governed by the atomistic activation volume effect, is not affected by the PSD. Both regimes were successfully simulated using numerical methods based on laws of continuum mechanics. All in all, in Chapter 8, the importance of controlling PSD and external pressure during sample preparation and measurement was demonstrated by analyzing the mechanical and electrical response of Li_7SiPS_8 *in operando*.

Conclusion and outlook

For compounds with some compositional flexibility, often dictated by structure type, introducing disorder at specific sites on the cation sublattice is a common strategy, especially for materials composed of more than one metal cation. In addition, cation disorder can be achieved by occupying vacant sites with similar potential energy with the mobile cation at the expense of other sites. In this work, cation disorder was used to improve the ion conducting properties of $Li_{4-3x}Sc_xP_2S_6$ by synthetically changing the stoichiometry and—in $Na_4P_2S_6$—by choosing a different synthetic route. This highlights the importance of sample synthesis for a material's properties. Moreover, the results indicate the presence of unexplored polymorphism in thiophosphate-based solid electrolytes due to the structural and dynamic flexibility of molecular thiophosphate anions such as $P_2S_6^{4-}$. A comprehensive study of the influence of synthesis, or even the search for new ways to synthesize a material, holds the potential to identify new, higher-performance compounds or polymorphs.

Compared to cation disorder, which is commonly reported in solid electrolytes and related materials, studies on anion disorder are sparse. Plastic crystals are an excellent example of how anion disorder can be used to enhance ionic motion in solids, as shown in this thesis. In addition, their malleability is an advantageous property for a solid electrolyte. Although some aspects of the plastic crystal behavior of γ-$Na_4P_2S_6$ are beneficial for ASSBs, the high transition temperature stands in the way of its practical application. Stabilization of the plastic phase at lower temperatures should be the main objective for future work. This could be achieved by substituting selenium for sulfur, which should increase the polarizability and covalency of the anion. In addition, the introduction of a cation disorder through the aliovalent substitution of P by Si or Ge could enable the low temperature paddle wheel effect observed in plastic crystals. In the future, high-energy ball milling should be considered as an option to introduce defects, change the crystallite size, or even reach an amorphous state to lower the plastic transition temperature in $Na_4P_2S_6$. As a second goal, an in-depth investigation of the short- and long-range cation-anion interactions and correlations with respect to possible coupled dynamic motion should be performed. For this purpose, advanced characterization techniques such as quasi-elastic neutron scattering, high-temperature solid-state NMR, and AIMD simulations on larger supercells should be employed.

Two-dimensional structures offer the possibility to change the material properties by intercalation of charged or uncharged atoms, ions or molecules. This behavior has been exploited to improve the ionic conductivity of layered $Li_2Sn_2S_5$ by hydration, taking advantage of the hydrophilic nature of lithium ions. At first glance, the combination of water and solid electrolyte is counter-intuitive for sulfide-based systems due to hydrolysis and evolution of H_2S. However, materials with predominantly covalent bonding character, such as $Li_2Sn_2S_5$, are able to largely resist hydrolysis, allowing modification of transport properties due to lower lithium ion trapping interactions. The high ionic conductivities achieved by hydration of $Li_2Sn_2S_5$ are of potential interest for aqueous batteries. In the long term, and in view of the application of ASSB, the goal for further development of this intercalation strategy should be the replacement of water by other types of solvents

that promise improved hydrolysis stability as well as a larger electrochemical window. A reasonable pathway might involve hydration as the first step, followed by gradual displacement of water by protic (alcohols) and finally aprotic (e.g., tetrahydrofuran) solvents. By using larger sized solvents, the layers should have greater spatial separation, leading to better coulombic shielding. A second future project should involve structure determination of hydrated species and investigation of the role of disorder on transport properties, particularly turbostratic disorder introduced during synthesis, hydration, or dehydration.

In addition to synthetic and post-synthetic modifications to optimize the crystal structure for improved ionic conductivity, influencing microstructural aspects such as particle size distribution and residual porosity after compaction is key to achieving high ionic conductivity at the macroscopic level. In particle technology, the influence of PSD on the macroscopic properties of samples prepared from granular powder has long been known, but less attention has been paid to this knowledge in the field of solid electrolytes. The results of this work show the importance of controlling the PSD as well as the pressure used during sample preparation and during measurement. Moreover, the correlation of the regimes of mechanical solid electrolyte powder compaction and the transport properties of the compacted pellet illustrates the validity of applying the Heckel relationship to understand the interplay of microstructure and effective conductivity. This work paves the way for a deeper understanding of macroscopic effects in solid electrolytes and promotes awareness of specifying properties such as pressure and PSD to improve comparability and reproducibility between studies. Several experimental and modeling objectives for the future emerge from the presented study. From an experimental perspective, different classes of materials should be investigated for their pressure and PSD sensitivity to effective ionic conductivity. This can elucidate the influence of mechanical material properties on mechanical behavior under pressure and help to optimize the processing of battery components. In addition, temperature needs to be considered as an important parameter in future mechanical studies of powder compression. Investigating and understanding the sintering behavior of solid electrolytes will allow further optimization of the microstructure by reducing grain boundary effects and achieving higher densities for more homogeneous samples and films. Regarding the microstructure simulations, the following investigations are proposed. First, the simulations should be extended to model grain boundary effects. Possible scenarios could include a core-shell microstructure for single particles or modeling the pellet microstructure with major and minor phase fractions of different conductivities corresponding to the weight fraction in the sample. However, this is more specific to glass-ceramic systems with amorphous side phases, as in Li_7SiPS_8. Second, a future simulations should include testing of different particle size distributions, including monomodal and bimodal distributions, to identify conductivity optimized particle size mixtures. Third, transfer to composite cathodes, testing and simulation of material mixtures with different elastic moduli such as oxides and thiophosphates is of particular interest for the future. The results and simulation models developed in this work could also help to clarify the role of microstructure for heat transport in solid-state batteries, as heat dissipation could be an important aspect in future high C-rate ASSBs.

Closing remarks

Following Aristotle's famous quote "The whole is greater than the sum of its parts", the search for high ionic conductivity in solids is about optimizing many different aspects that can influence each other both positively and negatively. Sulfide- and thiophosphate-based compounds have many desirable properties, such as high structural flexibility, ductility, and single-ion conductivity, making them at the forefront of research on solid electrolytes as separators in ASSBs. Despite their drawbacks, which include interfacial stability issues at very high and very low potentials and a current lack of scalable synthetic routes, this class of materials has been found to be overall suitable as solid-state electrolytes, as well as highly adaptable for unconventional optimization strategies. This work has demonstrated how different synthetic and post-synthetic approaches can be used to improve the ionic conductivity of sulfide- and thiophosphate-based solid electrolytes, given material-specific prerequisites. The results and findings from this research not only contribute to the literature, but also point to new ways to develop and optimize materials or components with high ionic conductivity that have the potential to improve the way we use and store energy.

Appendices

APPENDIX A

Supporting information for "Synthesis and characterization of: $Li_{4-3x}Sc_xP_2S_6$ ($x = 0.358$), *m*-$LiScP_2S_6$, and *t*-$LiScP_2S_6$"

Appendix A contains supporting information for Chapter 4.

Contents of Appendix A

A.1 Crystallographic data

Table A.1: Atomic coordinates and equivalent isotropic displacement factors (Å^2) for trigonal $Li_{4-3x}Sc_xP_2S_6$ ($x = 0.358$) as obtained from single-crystal X-ray diffraction at 298 K.

atom	site	x	y	z	SOF	U_{eq} (Å^2)
Sc1	2d	1/3	2/3	1/2	0.179(1)	0.0166(3)
Li1	2d	1/3	2/3	1/2	1–SOF(SC1)	0.0166(3)
S1	6k	0.32225(5)	0	-0.2538(1)	1	0.0169(1)
P1	2e	0	0	0.3316(1)	0.925(3)	0.0132(2)
P2	2e	0	0	0.1710(14)	1–SOF(P1)	0.018(2)
Li2	2c	1/3	2/3	0	0.642(1)	0.048(3)

Table A.2: Atomic coordinates and equivalent isotropic displacement factors (Å^2) for monoclinic $LiScP_2S_6$ as obtained from single-crystal X-ray diffraction at 298 K.

atom	site	x	y	z	SOF	U_{eq} (Å^2)
Sc1	4e	1/2	1.0082(1)	1/4	1	0.0272(5)
S1	8f	0.1792(2)	0.9854(1)	0.1225(1)	1	0.0291(4)
S2	8f	-0.3325(2)	0.8354(1)	0.1373(1)	1	0.0303(4)
S3	8f	0.1555(2)	0.6739(1)	0.1251(1)	1	0.0298(4)
P1	8f	0.1462(2)	0.8317(1)	0.2189(1)	1	0.0255(4)
Li1	4e	1/2	0.647(1)	1/4	1	0.049(4)

Table A.3: Atomic coordinates and equivalent isotropic displacement factors (Å^2) for trigonal $LiScP_2S_6$ as obtained from single-crystal X-ray diffraction at 298 K.

atom	site	x	y	z	SOF	U_{eq} (Å^2)
Sc1	2a	0	0	1/4	1	0.082(1)
S1	12i	0.6597(2)	0.6804(3)	0.1266(1)	1	0.082(1)
P1	4f	1/3	2/3	0.1622(4)	1/2	0.068(2)
P2	12i	0.168(1)	0.654(1)	0.218(1)	1/6	0.050(2)
Li1	2d	2/3	1/3	1/4	1	0.140(14)

Table A.4: Atomic coordinates and equivalent isotropic displacement factors ($Å^2$) for trigonal $LiScP_2S_6$ as obtained from single-crystal X-ray diffraction at 298 K.

compound	a/Å	b/Å	c/Å	α/°	β/°	γ/°	V/Å^3	space group
$Li_{4-3x}Sc_xP_2S_6$ $x = 0.358$	6.0966(5)	6.0966(5)	6.5866(6)	90	90	120	212.02(4)	$P\bar{3}1m$ (no.162)
m-$LiScP_2S_6$	6.933(1)	10.754(2)	11.694(2)	90	94.41(3)	90	869.3(3)	$C2/c$ (no.15)
t-$LiScP_2S_6$	6.363(1)	6.363(1)	12.386(3)	90	90	120	434.3(2)	$P\bar{3}1c$ (no.163)

A.2 DSC measurements

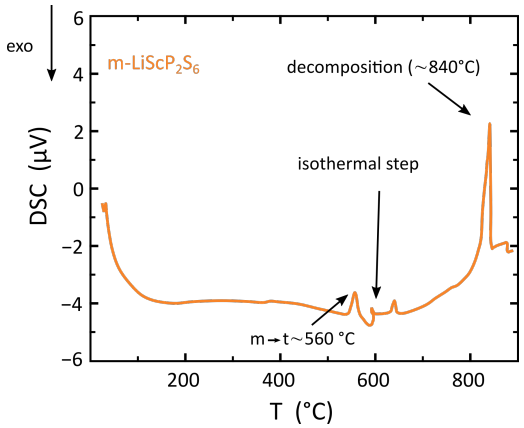

Figure A.1: Temperature dependent DSC measurement for m-$LiScP_2S_6$. The transitions are indicated. m-$LiScP_2S_6$ transforms endothermally to t-$LiScP_2S_6$ at roughly 560 °C. The sample decomposes at roughly 840 °C.

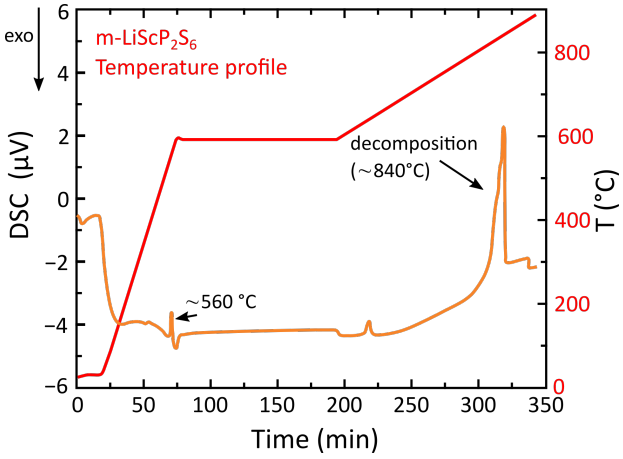

Figure A.2: Time dependent DSC measurements for m- and t-$LiScP_2S_6$. The temperature profile is shown in red. The transitions are indicated.

A.3 Temperature dependent X-ray Diffraction

m-$LiScP_2S_6$ was investigated with temperature dependent X-ray diffraction in a sealed capillary. While there is little change in the powder pattern until 500 °C, the pattern at 700 °C resembles the one of *t*-$LiScP_2S_6$. At 600 °C the pattern shows some intermediate phase. At 850 °C the pattern changes again and most of the peaks can be indexed by Sc_2S_3 with a small amount of additional $Li_{4-3x}Sc_xP_2S_6$. The decomposition is irreversible as shown by the diffraction patterns after cooling. These findings match the results from DSC and suggest that *t*-$LiScP_2S_6$ is the high temperature phase of the system.

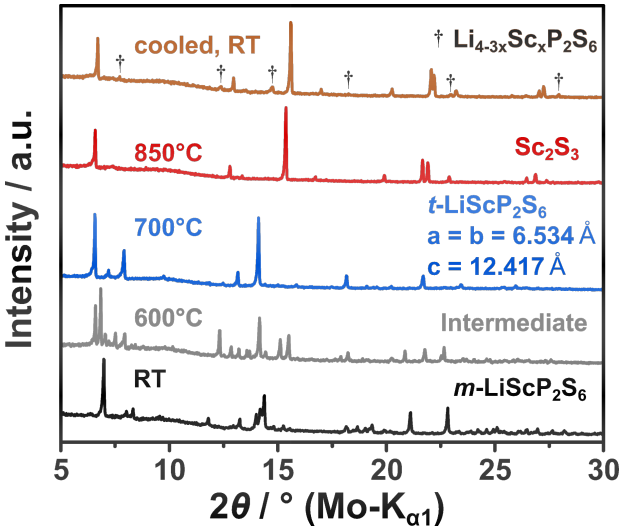

Figure A.3: Temperature dependent power X-ray diffraction patterns of *m*-$LiScP_2S_6$.

A.4 Phase stability calculation

Table A.5: Relative total electronic energies and optimized lattice parameters of $LiScP_2S_6$ structure models, PBE-D3 calculations; monoclinic model served as reference value (*mt*-$LiScP_2S_6$ is the monoclinic model derived from the trigonal structure by full occupation of one of the SOF(P) = 1/6 positions).

model	ΔE/ kJ mol^{-1}	a/Å	b/Å	c/Å	α/°	β /°	γ/°	VZ^{-1}/Å^3	space group
m-$LiScP_2S_6$	0.0	6.876	10.683	10.871	90	94.71	90	198.94	$C2/c$ (no.15)
*t**-$LiScP_2S_6$	-25.8	6.038	6.038	12.038	90	90	120	190.70	$P\bar{3}1c$ (no.163)
mt-$LiScP_2S_6$	0.0	6.876	10.687	10.866	90	85.32	90	198.95	$C2/c$ (no.15)

A.5 Calculation of Raman active modes

Table A.6: Calculated Raman active modes for *t*-$LiScP_2S_6$ (total intensities for polycrystalline samples).

Raman shift/cm^{-1}	irrep.	intensity/a.u.
46	E_g	0
132	E_g	9.89
164	A_{1g}	53.02
184	E_g	43.45
195	E_g	31.05
227	E_g	177.14
267	A_{1g}	509.14
273	E_g	218.16
297	E_g	6.92
313	E_g	395.64
364	A_{1g}	1000
515	A_{1g}	320.02
544	E_g	2.23
556	E_g	30.21

Table A.7: Calculated Raman active modes for m-$LiScP_2S_6$ (total intensities for polycrystalline samples).

Raman shift/cm^{-1}	irrep.	intensity/a.u.
52	A_g	0.28
52	B_g	0
83	B_g	0.06
99	B_g	0.21
110	A_g	7.65
123	B_g	5.43
141	B_g	1.48
154	B_g	12.14
167	A_g	37.16
182	A_g	59.53
191	A_g	41.6
202	B_g	9.55
225	B_g	46.13
228	A_g	24.42
239	A_g	50.41
250	B_g	20.49
266	B_g	42.26
278	A_g	23.48
283	B_g	26.14
292	A_g	35.13
292	B_g	54.1
309	A_g	281.85
322	B_g	16.95
359	A_g	1000
428	B_g	9.85
503	A_g	362.22
550	A_g	13.35
559	B_g	6.4
562	A_g	1.16
576	B_g	2.99

A.6 BVEL calculations and impedance measurements

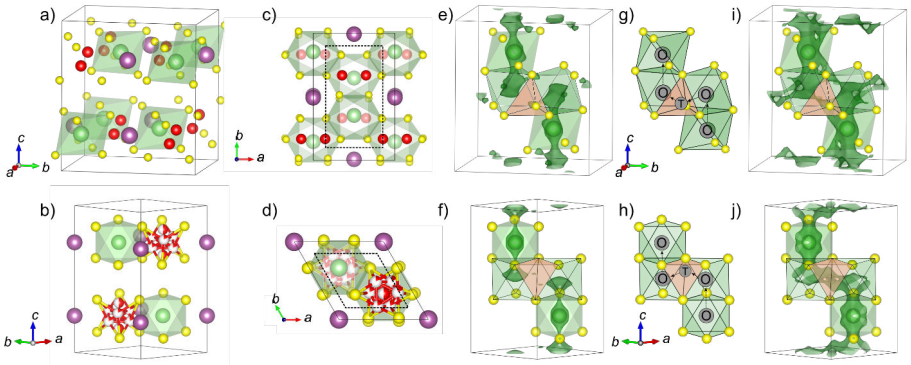

Figure A.4: (a) & (b) Crystal structures of m-$LiScP_2S_6$ and t-$LiScP_2S_6$. (c) & (d) Top view of unit cells of (a) and (b). Dashed lines indicate the cut-off box of bond valence energy landscape isosurfaces shown in (e), (f), (i) and (j). (e) & (f) Isosurface at $E(\mathrm{Li}) = -4.5$ eV and -4.3 eV ($E(\mathrm{Li})_{\mathrm{min}} = -6.1$ eV and -6.2 eV) for m-$LiScP_2S_6$ and t-$LiScP_2S_6$, respectively. (g) & (h) Schematic representation of octahedral-octahedral-tetrahedral-octahedral-octahedral (O_l-O_i-T_i-O_i-O_l) trajectory of Li ion movement through interlayer vacancies. (i) & (j) Isosurface at $E(\mathrm{Li}) = -3.8$ eV and -2.9 eV ($E(\mathrm{Li})_{\mathrm{min}} = -6.1$ eV and -6.2 eV) for m-$LiScP_2S_6$ and t-$LiScP_2S_6$, respectively. Li drawn in green, Sc drawn in purple, P drawn in red and S drawn in yellow.

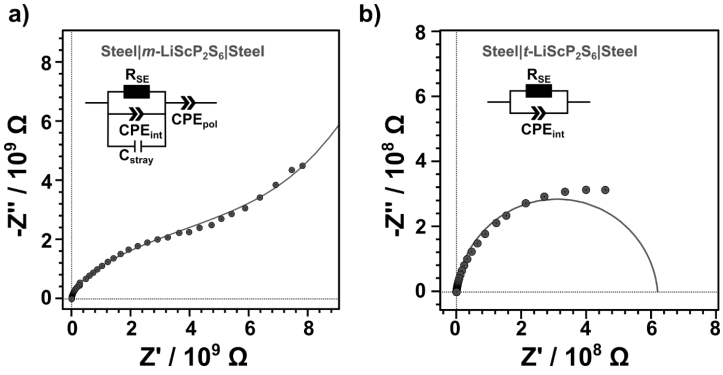

Figure A.5: Nyquist-plots of EIS measurement of m-$LiScP_2S_6$ (a) and t-$LiScP_2S_6$ (b) with equivalent circuit fit (solid line). Fitted values for R_{SE}, CPE_{int} and CPE_{pol} and C_{stray} are tabulated in Table A.8

Table A.8: Fitted equivalent circuit values for $Li_{4-3x}Sc_xP_2S_6$, *m*-$LiScP_2S_6$ and *t*-$LiScP_2S_6$ with calculated conductivities and capacities. Fitting errors are given in brackets.

Circuit element	$Li_{4-3x}Sc_xP_2S_6$	$Li_{4-3x}Sc_xP_2S_6$ (Ru-sputtered)	*m*-$LiScP_2S_6$	*t*-$LiScP_2S_6$
R_{SE}/Ω	$3.0 \cdot 10^5$ (2.8%)	$4.5 \cdot 10^5$ (0.2%)	$1.2 \cdot 10^{10}$ (12%)	$6.2 \cdot 10^8$ (3.1%)
Q_{int}	$3.2 \cdot 10^{-11}$ (14%)	$2.8 \cdot 10^{-11}$ (2.3%)	$7.2 \cdot 10^{-11}$ (7.9%)	$1.2 \cdot 10^{-11}$ (3.1%)
α_{int}	0.93 (1.1%)	0.91 (0.2%)	0.43 (3.3%)	0.95 (0.3%)
Q_{pol}	$1.5 \cdot 10^{-9}$ (1.1%)	$3.2 \cdot 10^{-6}$ (0.9%)	$6.0 \cdot 10^{-10}$ (17%)	
α_{pol}	0.73 (0.3%)	0.67 (0.8%)	0.82 (3.2%)	
C_{stray}/F	$2.3 \cdot 10^{-12}$ (1.8%)			
$\sigma_{SE}/S\,cm^{-1}$	$1.9 \cdot 10^{-6}$	$1.2 \cdot 10^{-6}$	$4.5 \cdot 10^{-11}$	$1.2 \cdot 10^{-9}$
C_{int}/F	$1.3 \cdot 10^{-11}$	$9.2 \cdot 10^{-12}$	$5.9 \cdot 10^{-11}$	$9.3 \cdot 10^{-12}$
C_{pol}/F	$8.7 \cdot 10^{-11}$	$3.8 \cdot 10^{-6}$	$9.3 \cdot 10^{-10}$	

APPENDIX B

Supporting information for "Phase formation through synthetic control: polymorphism in the sodium-ion solid electrolyte $Na_4P_2S_6$"

Appendix B contains supporting information for Chapter 5.

Contents of Appendix B

B.1 Experimental Section

B.1.1 Syntheses

$Na_4P_2S_6$ was prepared using different synthesis routes:

The solid-state reaction was conducted according to Ref. [1] . Stoichiometric amounts of Na (Alfa Aesar, 99.8%), P_4S_{10} (Acros, 98+%), and sulfur (Alfa Aesar, 99.5%, sublimed) were vacuum-sealed in double-walled silica tubes and heated slowly to the reaction temperature of 850 °C with $20\,K\,h^{-1}$. This synthesis yields a highly crystalline white powder from which also colorless single crystals can be extracted.

Further, $Na_4P_2S_6$ was prepared *via* the precipitation of the hydrated compound $Na_4P_2S_6 \cdot 6\,H_2O$ and subsequent dehydration as in Ref. [2] . $Na_2S \cdot 9\,H_2O$ (75 g; Aldrich, ≥99.99%) was dissolved in deionized water (100 mL) under stirring. Next, PCl_3 (6.6 mL; Arcos, 99%) was added slowly over 30 min due to its violent reaction with water. Then, the reaction vessel was placed in an ice bath, and the reaction was stirred for 20 min. During that time, white $Na_4P_2S_6 \cdot 6\,H_2O$ precipitated. The vessel was removed from the ice bath and stirred at room temperature for 1 h. Finally, the reaction mixture was stored at 4 °C over night. After that time, the crude reaction product was separated from the supernatant solution and recrystallized from an 80 °C water : ethanol solution (75:25). The dehydrated phase, $Na_4P_2S_6$, was obtained by heating the colorless crystals of the hexahydrate at 100 °C under dynamic vacuum for 12 h (Büchi furnace). The obtained powder is white and is characterized by inter- and intralayer defects.

On the cost of forming some side phases (e.g. phosphates), the precipitated $Na_4P_2S_6$ can be *annealed* to a product with less defects at 500 °C for 1 h in vacuum-sealed silica tube.

B.1.2 Powder X-Ray diffraction

Powder X-Ray Diffraction (PXRD) patterns were measured using a STOE StadiP diffractometer (Mo $K_{\alpha 1}$ radiation $\lambda = 0.7093$ Å, curved germanium (111) monochromator, DECTRIS Mythen2R 1K detector) in Debye-Scherrer geometry. For room-temperature and high-temperature measurements, finely powdered samples were filled in capillaries of 0.3 mm and 0.5 mm diameter borosilicate and quartz glass (Hilgenberg), respectively. The capillaries were sealed under argon. High-temperature patterns were collected using a STOE capillary furnace. Data collection was done in the range from 2° to 50° 2θ with a step size of 0.015° for temperatures from 20 °C to 300 °C in steps of 10 °C or 20 °C. All data analysis was performed with Jana2006.[3] The structure of β-$Na_4P_2S_6$ was solved starting from the α structure and evaluating the residual electron density at the $2d$ position. For the Rietveld refinements[4] a pseudo-Voigt function with axial divergence was utilized. The sum of occupation of Na2 and Na3 were constrained to one to comply with the chemical formula. Errors of the results of the Rietveld refinements are specified as 3σ taking local correlations into account. To account for the higher sensitivity of the $P_2S_6^{4-}$ tilting, uncertainties were adjusted upwards for internal consistency. Detailed data of the temperature-dependent structural parameters for solid-state and annealed $Na_4P_2S_6$ obtained by Rietveld refinements are available online in an additional supporting information file.

B.1.3 Single crystal X-Ray diffraction

Single crystals suitable for single-crystal X-ray diffraction were collected under a microscope in dried petroleum and mounted into sealed glass capillaries for single-crystal X-ray diffraction measurements. Diffraction data were collected at 25 °C and 227 °C on a Smart APEX-I diffractometer with a Cryostream 700Plus cooling device (Oxford Cryosystems, Oxford, United Kingdom, 80-500 K). The diffractometer (Bruker AXS, Karlsruhe, Germany) uses Mo K_α radiation ($\lambda = 0.710\,73$ Å).

The reflection intensities were integrated with the SAINT subprogram in the Bruker Suite software package.[5] A multi-scan absorption correction was applied using SADABS.[6] The structure was solved by direct methods and refined by full-matrix least-squares fitting with the SHEXTL software package.[7,8]

Crystallographic data for β-$Na_4P_2S_6$ may be obtained from the joint CCDC/FIZ Karlsruhe online deposition service: https://www.ccdc.cam.ac.uk/structures/ by quoting the deposition number CSD-2031308.

B.1.4 Transmission electron microscopy

Powder samples of $Na_4P_2S_6$ were thoroughly ground in an agate mortar in an Argon filled glovebox and subsequently distributed onto a holey carbon/copper grid. A Philips CM 30 ST microscope (300 kV, LaB_6 cathode) was used for taking TEM images (TVIPS TemCam-F216 CMOS camera). Selected area diffraction (SAD) patterns were simulated using the JEMS software package.

B.1.5 Differential scanning calorimetry and thermogravimetric Analysis

For Differential Scanning Calorimetry (DSC) measurements 15-25 mg of fine powdered sample were sealed in quartz ampoules (6 mm diameter, 10 to 15 mm in height) under vacuum. For improved heat flow ampoules with a flat bottom were used. DSC measurements were performed on a NETZSCH STA 449 F3 Jupiter in temperature segments of 30 °C to 300 °C. The heating and cooling rates were set to 10 K min^{-1}. Due to the insulation of the furnace and its inability to actively cool, the actual temperature was cycled between 80 °C to 300 °C. Prior to measuring $Na_4P_2S_6$ samples, a temperature and DSC sensitivity calibration was performed. Thermogravimetry (TG) was measured using the same instrument as for DSC measurements. Some fine powder was filled into an open Al_2O_3-crucible and heated up to 200 °C with a heating rate of 10 K min^{-1}. The data was referenced against an empty crucible to correct for buoyancy. Data evaluation was performed using the NETZSCH software package Proteus.

B.1.6 Solid-state nuclear magnetic resonance Spectroscopy

All ssNMR measurements were performed on a Bruker Avance-III wide bore spectrometer in a magnetic field of 9.4 T. ^{23}Na (Larmor frequency 105.8 MHz) and ^{31}P (Larmor frequency 161.9 MHz) MAS NMR spectra were recorded in 4 mm ZrO_2 rotors using a Bruker BL4 MAS probe at a spinning speed of 10 kHz. Due to the air and moisture sensitivity of the studied materials, they were flame sealed in pyrex MAS inserts for Bruker

4 mm rotors (Wilmad Glass, product # DWGSK2576-1). Measurements on both ^{23}Na and ^{31}P were done using a simple Bloch Decay excitation scheme with a total of 512-4096 accumulations in each experiment. Long enough relaxation delays were used to provide for a complete relaxation of magnetization and ensure quantitative measurements. ^{23}Na spectra were recorded using a very short excitation pulse of $\pi/24$ to ensure homogeneous excitation of the central transitions for sites with very different quadrupolar coupling constants.[9] The spectra were referenced to the external signals of 85% H_3PO_4 (^{31}P) and 0.1 M solution of NaCl (^{23}Na).[10] Spectra fitting and signal integration was performed with the Dmfit software, using a Qmas$\frac{1}{2}$ model for all ^{23}Na spectra and a Gauss lineshape model for all ^{31}P spectra.[11]

B.1.7 Raman spectroscopy

Raman spectra of solid-state synthesized powder and single crystals as well as precipitated powder were recorded using a Jobin Yvon Typ V 010 LabRAM single grating spectrometer, equipped with a double super razor edge filter and a Peltier-cooled charge-coupled device camera. The resolution of the spectrometer (grating, 1800 lines/mm) was 1 cm^{-1}. The spectra were taken in a quasi-backscattering geometry using the linearly polarized 632.817 nm line of a He/Ne gas laser. The power was lower than 1 mW, to protect against local heating. The spot size was 10 µm, focused by a 50× microscope objective on to the surface of the sample. For heating experiments, the set-up is equipped with a heating microscope stage (THMS600, controlled by Linkam TMS 94). The scanning range was from 25 °C to 500 °C at a ramping rate of 5 K min^{-1} under a nitrogen atmosphere. Measurements were taken at temperatures ranging between 25 °C and 500 °C with 0.1 °C accuracy. All spectra were fitted using a Lorentz type profile for all spectral peaks form 50 cm^{-1} to 700 cm^{-1}. The background was modeled to represent a broad central peak with a fixed peak center at 0 cm^{-1}.

B.1.8 Bond valence energy landscape calculations

To identify possible sodium ion diffusion pathways, bond valence energy landscape (BVEL) calculations were performed using the programm 3DBVSMAPPER.[12] The program calculates bond valence (BV) sums based on soft-BV parameters.[13] Additionally, attraction and repulsion terms account for coulombic interactions of different ions with the tested ion and therefore convert bond valence sum maps into an energy-scaled landscape. The cutoff distance for any interaction was set to a maximum value of 8 Å. Images were created with VESTA.[14]

B.1.9 Calculations

All DFT calculations were carried out with the *Vienna Ab initio Simulation Package* (VASP).[15–18] The PBE[19] exchange-correlation functional with the D3[20] dispersion correction and the PAW[21,22] potential were applied. For all electronic structure calculations, a convergence criterion of at least 10^{-5} eV was used. The Monkhorst-Pack[23] k-point mesh used for Brillouin zone integration was energetically converged for all calculations while the energy-cutoff was set to 500 eV.

Nudged elastic band (NEB) calculations[24,25] were used to analyze the Na^+ migration in α- (0 K DFT optimized structure) and β-$Na_4P_2S_6$ (experimental 200 °C structure). In these calculations we neither attempt full treatment of Na^+ disorder nor account for correlated ion motion. Scenarios with different exemplary sodium ion-vacancy orderings (belonging to three classes: Na2' $\rightleftharpoons$ Na3' intra-triple diffusion, Na2' $\rightleftharpoons$ Na3" inter-triple diffusion, and Na2' $\rightleftharpoons$ Na2" inter-triple diffusion) were chosen instead of considering partial Na^+ occupation. The results are considered to provide a qualitative understanding of the ion motion in $Na_4P_2S_6$. The pathways were chosen according to the BVEL results through tetrahedral voids (TV, Wyckoff position $8j$). Therefore, the NEB calculation was divided into two separate parts from start to TV and from TV to the final location. Simplifications were applied in order to reduce calculation time. As a first simplification, NEB calculations were, if not stated otherwise, computed in the unit cell instead of a super cell since a local migration was analyzed. Second, fixed atomic positions were used for defining start, TV, and final structures. Only the migrating Na^+ was allowed to optimize its position prior to the NEB calculation. The benchmarking of different DFT approximations, van der Waals corrections, cell sizes and increasing stages of atomic optimization can be found on page 209 for Scenario 1. All-atom optimization reduces the E_{mig} a lot but also strongly distorts the local environment around the migrating Na^+. Overall, our calculations overestimate E_{mig} so that we only consider qualitative effects for the different examined scenarios.

B.1.10 Electrochemical impedance spectroscopy

Electrochemical impedance spectroscopy (EIS) measurements were performed using a Novocontrol Technologies Alpha-A analyzer (batches ss1, ss2, p1, a1) or a Novocontrol Technologies NEISYS (p2). For sample preparation fine powder of $Na_4P_2S_6$ (30-60 mg) was pressed uniaxially at 1 GPa into pellets of 5 mm diameter. Pellets were placed between two sodium ion blocking polished steel electrodes, In-foils (batches ss1, ss2, p1, a1) or graphite foil (p2) (rhd instruments TSC Battery cell) and loaded onto a Microcell HC cell stand (rhd instruments). A spring-loaded pressure of approximately 10 MPa was applied during the measurement. The spectra were recorded in a frequency range of 3 MHz to 100 mHz and with an applied voltage of V_{RMS} = 100 mV. The spectra were recorded between 20 °C and 100 °C. For each prepared sample, three pellets of different cell constants (variation in pellet thickness) were measured. The average of three extracted conductivities for one sample is presented in this study. Additionally, we measured one heating and subsequent cooling cycle (1 h of equilibration between individual measurements to account for subtle differences between batches and possible hysteresis effects). Data treatment and evaluation was performed using the rhd instruments software package RelaxIS 3. To check data reliability, Kramers-Kronig relation tests were performed prior to fitting. Fitting the impedance spectra to equivalent circuits was done by weighting the data points proportionally. Given error bars stem from error propagation of uncertainties in pellet geometric area, pellet thickness, and applied temperature as well as errors in resistance obtained by equivalent circuit fitting. Galvanostatic polarization measurements were performed with the same two-electrode setup used for EIS measurements. Data collection was performed with a Keithley potentiostat.

B.2 Crystallographic data for α- and β-$Na_4P_2S_6$

B.2.1 Crystal structure of α- and β-$Na_4P_2S_6$

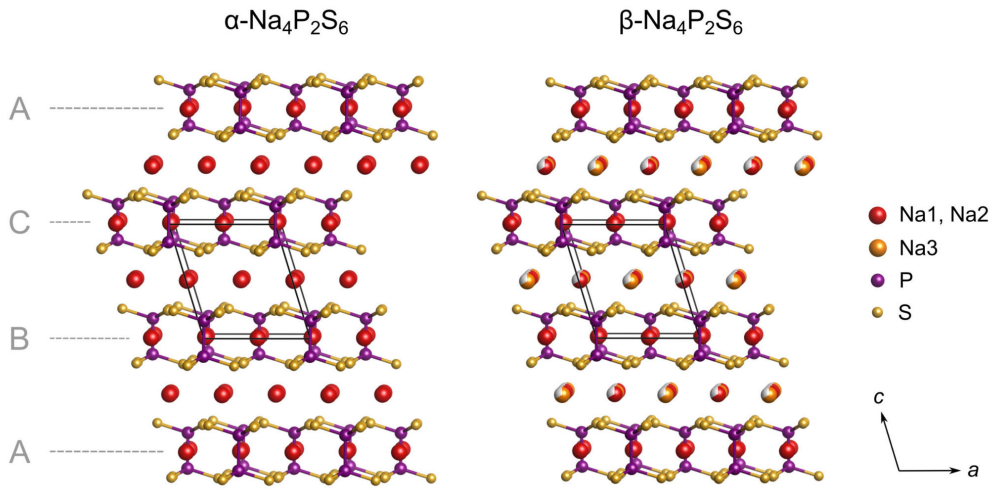

Figure B.1: Layered structure of α-$Na_4P_2S_6$ at room temperature and β-$Na_4P_2S_6$ at 200 °C. The [ABC] stacking order of the $P_2S_6^{4-}$ is indicated by capital Latin letters.

B.2.2 Solid-state synthesis

Table B.1: Crystallographic data and refinement details. Statistical errors as obtained from the Rietveld refinements are given in parentheses.

	α-$Na_4P_2S_6$	β-$Na_4P_2S_6$	β-$Na_4P_2S_6$
Temperature ϑ (°C)	20	200	500
Formula weight M ($g\,mol^{-1}$)	346.3	346.3	346.3
Crystal system	monoclinic	monoclinic	monoclinic
Space group	$C2/m$ (no. 12)	$C2/m$ (no. 12)	$C2/m$ (no. 12)
Lattice parameter a (Å)	6.7358(2)	6.6595(2)	6.7094(3)
Lattice parameter b (Å)	11.1998(3)	11.4256(4)	11.5522(6)
Lattice parameter c (Å)	7.5309(2)	7.6523(3)	7.7786(1)
Monoclinic angle β (°)	107.000(2)	107.093(3)	107.504(3)
Volume V ($Å^3$)	543.31(3)	556.53(3)	575.58(5)
Formula units Z	2	2	2
Crystallographic density ρ ($g\,cm^{-3}$)	2.12	2.07	2.00
X-ray radiation	Mo $K_{\alpha 1}$	Mo $K_{\alpha 1}$	Mo $K_{\alpha 1}$
2θ range (°)	2.000-61.835	2.000-61.835	4.000-35.905
No. of refined parameters	55	55	55
No. of restraints/constraints	0/3	0/3	0/3
R_p, R_{wp} (%)	4.8/6.0	4.1/5.3	5.7/7.1
R_{Bragg}, R_F (%)	7.9/5.0	7.3/5.1	8.7/6.5

Table B.2: Atomic positions and displacement parameters of α-$Na_4P_2S_6$ at 20 °C. Statistical errors as obtained from the Rietveld refinement are given in parentheses.

Atom	Wyckoff position	x	y	z	U_{iso} ($Å^2$)	Occupancy
Na1	4g	0.5	0.1625(6)	0	0.031(1)	1
Na2	4h	0.5	0.3177(4)	0.5	0.031(1)	0.981(4)
Na3	2d	0	0.5	0.5	0.031(1)	2(1−Occ(Na2))
P1	4i	0.5569(5)	0.5	0.1507(4)	0.019(1)	1
S1	4i	0.2916(5)	0.5	0.2423(4)	0.019(1)	1
S2	8j	0.7244(4)	0.3489(2)	0.2325(3)	0.0220(9)	1

Table B.3: Atomic positions and displacement parameters of β-$Na_4P_2S_6$ at 200 °C. Statistical errors as obtained from the Rietveld refinement are given in parentheses.

Atom	Wyckoff position	x	y	z	U_{iso} (Å^2)	Occupancy
Na1	4g	0.5	0.1625(5)	0	0.066(2)	1
Na2	4h	0.5	0.3218(7)	0.5	0.066(2)	0.679(3)
Na3	2d	0	0.5	0.5	0.066(2)	2(1−Occ(Na2))
P1	4i	0.5504(6)	0.5	0.1498(4)	0.026(1)	1
S1	4i	0.2836(7)	0.5	0.2341(4)	0.045(2)	1
S2	8j	0.7251(5)	0.3519(2)	0.2343(3)	0.040(1)	1

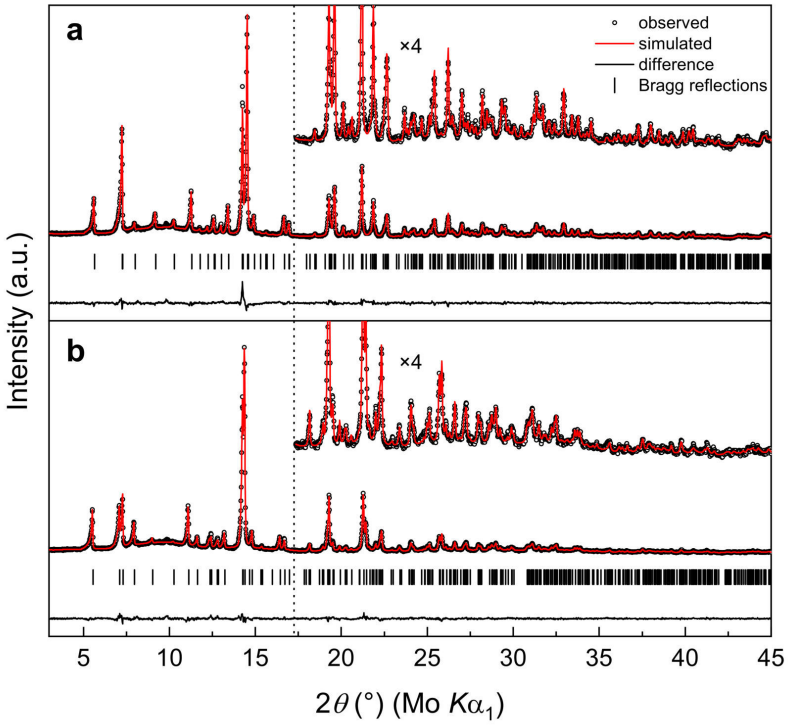

Figure B.2: Rietveld refinement of (a) α-$Na_4P_2S_6$ at 20 °C and (b) β-$Na_4P_2S_6$ at 200 °C.

Table B.4: Atomic positions and displacement parameters of β-$Na_4P_2S_6$ at 500 °C. Statistical errors as obtained from the Rietveld refinement are given in parentheses.

Atom	Wyckoff position	x	y	z	U_{iso} (Å^2)	Occupancy
Na1	4g	0.5	0.1615(5)	0	0.123(3)	1
Na2	4h	0.5	0.3333(7)	0.5	0.123(3)	0.654(5)
Na3	2d	0	0.5	0.5	0.123(3)	2(1−Occ(Na2))
P1	4i	0.5488(8)	0.5	0.1440(6)	0.037(2)	1
S1	4i	0.2883(7)	0.5	0.2364(6)	0.094(3)	1
S2	8j	0.7265(7)	0.3525(5)	0.2369(6)	0.088(2)	1

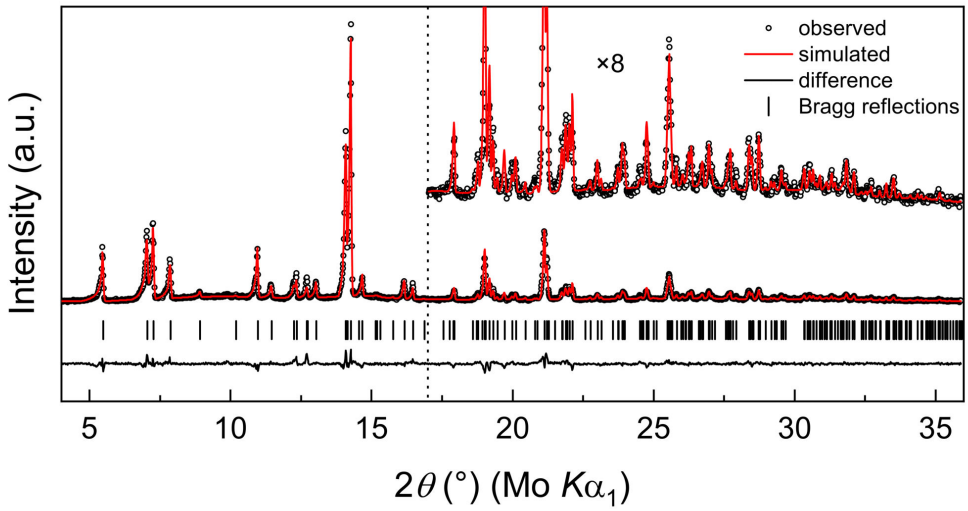

Figure B.3: Rietveld refinement of β-$Na_4P_2S_6$ at 500 °C.

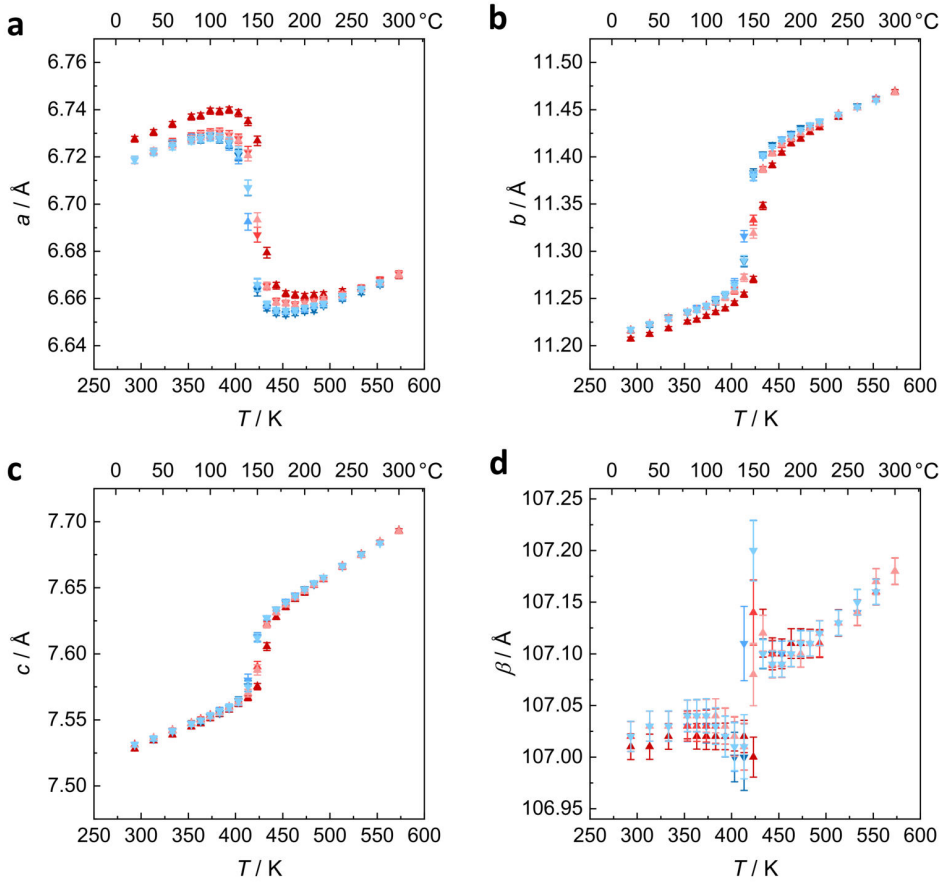

Figure B.4: Results of the Rietveld refinements for the α-β phase transition in solid-state $Na_4P_2S_6$ upon heating and cooling. (a-d) Lattice parameters a, b, c and monoclinic angle β.

B.2.3 Annealed solution-synthesized $Na_4P_2S_6$

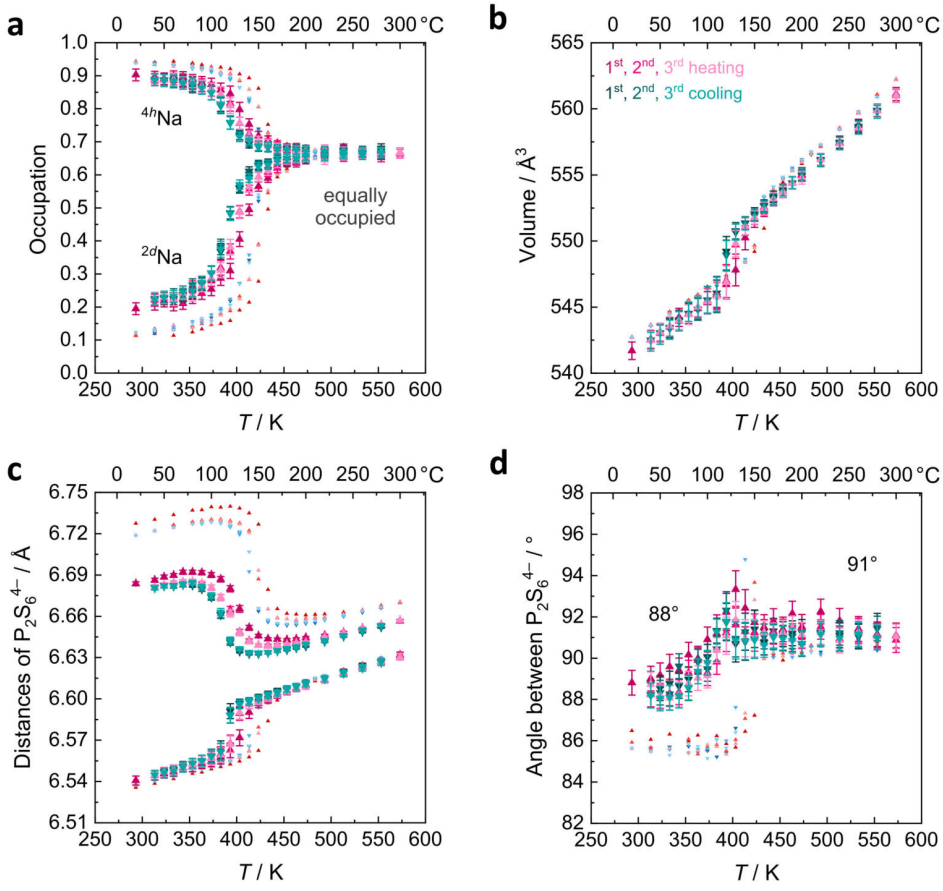

Figure B.5: Results of the Rietveld refinements for the α–β phase transition in annealed $Na_4P_2S_6$ (bold data markers) upon heating (pink data points) and cooling (teal data points) for the first three cycles (color code from dark to light with increasing cycle number). Small data markers are taken from the solid-state synthesized $Na_4P_2S_6$ for comparison. (a) Occupation of the sodium positions Na2 and Na3 between the $P_2S_6^{4-}$ layers. (b) Volume change with temperature. (c) Distances of the $P_2S_6^{4-}$ anions as a measure for the hexagonality of the layer. (d) Tilting of neighboring $P_2S_6^{4-}$ anions in a direction expressed as the P–P–$P_{neighbor}$ angle.

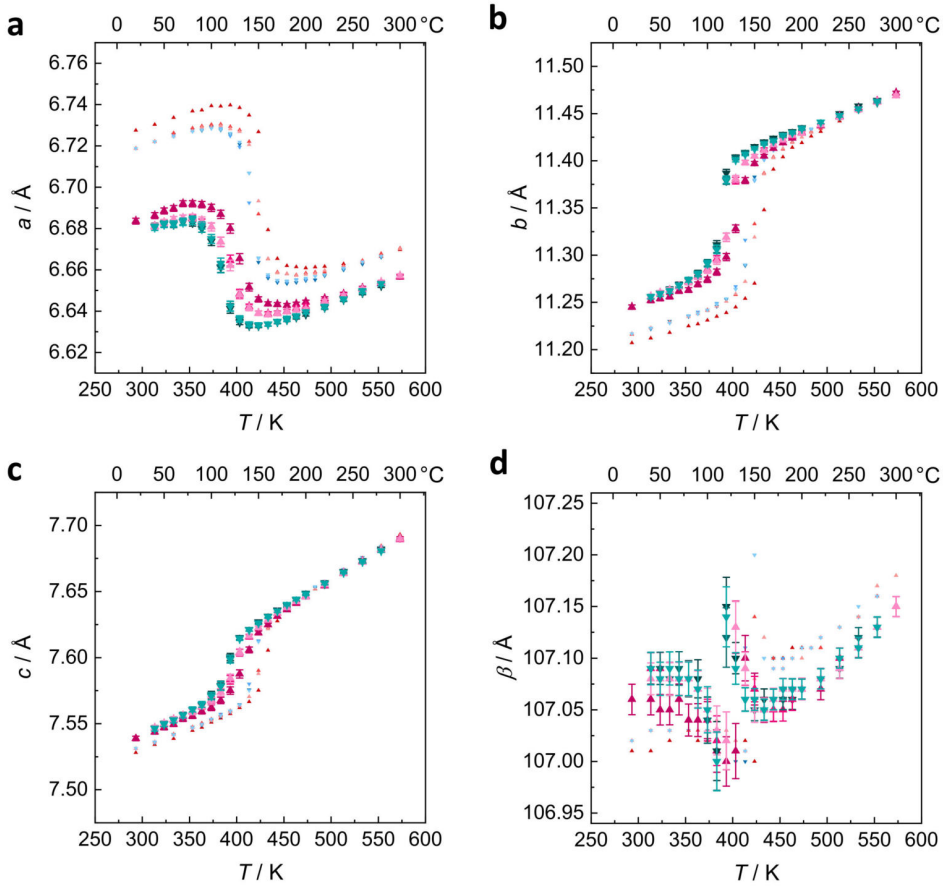

Figure B.6: Results of the Rietveld refinements for the α–β phase transition in annealed $Na_4P_2S_6$ upon heating and cooling (bold data markers). Small data markers are taken from the solid-state synthesized $Na_4P_2S_6$ for comparison. (a-d) Lattice parameters a, b, c and monoclinic angle β.

B.2.4 Single crystal

Table B.5: Crystallographic data as obtained from single-crystal X-ray diffraction (Mo-K_α) measured (a) at 25 °C, (b) subsequently at 227 °C, and (c) again at 25 °C.

	(a) α-$Na_4P_2S_6$	(b) β-$Na_4P_2S_6$	(c) α-$Na_4P_2S_6$
Temperature ϑ (K)	298	500	298
Formula weight M ($g\,mol^{-1}$)	346.3	346.3	346.3
Crystal system	monoclinic	monoclinic	monoclinic
Space group	$C2/m$ (no. 12)	$C2/m$ (no. 12)	$C2/m$ (no. 12)
Lattice parameter a (Å)	6.761(1)	6.671(3)	6.760(1)
Lattice parameter b (Å)	11.233(2)	11.450(5)	11.234(2)
Lattice parameter c (Å)	7.549(2)	7.663(4)	7.550(2)
Monoclinic angle β (°)	107.034(3)	107.107(7)	107.034(3)
Volume V ($Å^3$)	548.2(2)	559.5(4)	548.2(2)
Formula units Z	2	2	2
Crystallographic density ρ ($g\,cm^{-3}$)	2.10	2.06	2.10
2θ range (°)	2.822-35.353	2.781-35.341	2.822-35.353
Index range	$-10 \leq h \leq 10$ $-17 \leq k \leq 17$ $-11 \leq l \leq 12$	$-10 \leq h \leq 10$ $-18 \leq k \leq 18$ $-12 \leq l \leq 12$	$-10 \leq h \leq 10$ $-17 \leq k \leq 17$ $-12 \leq l \leq 11$
Total reflections	4141	3838	4257
Unique reflections	1224	1246	1226
Parameters	32	38	32
$R_1(\geq 2\sigma)$ (%)	2.9	4.6	3.1
wR_2 ($\geq 2\sigma$) (%)	7.7	10.9	8.6
GooF	1.1	1.2	1.1

Table B.6: Atomic coordinates and equivalent isotropic displacement factors of (a) α-$Na_4P_2S_6$ at 298 K.

Atom	Wyckoff position	x	y	z	U_{eq} (Å^2)	Occupancy
Na1	4g	0.5	0.16203(9)	0	0.0267(2)	1
Na2	4h	0.5	0.3149(1)	0.5	0.0305(2)	1
P1	4i	0.55377(8)	0.5	0.15629(7)	0.0146(1)	1
S1	4i	0.29560(8)	0.5	0.24190(7)	0.0197(1)	1
S2	8j	0.72262(6)	0.34949(4)	0.23026(5)	0.0219(1)	1

Table B.7: Atomic coordinates and equivalent isotropic displacement factors of (b) β-$Na_4P_2S_6$ at 500 K.

Atom	Wyckoff position	x	y	z	U_{eq} (Å^2)	Occupancy
Na1	4g	0.5	0.1659(2)	0	0.0495(4)	1
Na2	4h	0.5	0.3199(4)	0.5	0.077(1)	0.656(2)
Na3	2d	0	0.5	0.5	0.109(2)	2(1−Occ(Na2))
P1	4i	0.5502(1)	0.5	0.1539(1)	0.0260(2)	1
S1	4i	0.2860(2)	0.5	0.2311(1)	0.0412(2)	1
S2	8j	0.7229(1)	0.35324(6)	0.2320(1)	0.0397(2)	1

Table B.8: Atomic coordinates and equivalent isotropic displacement factors of (c) α-$Na_4P_2S_6$ at 298 K after heating to 500 K.

Atom	Wyckoff position	x	y	z	U_{eq} (Å^2)	Occupancy
Na1	4g	0.5	0.1620(1)	0	0.0267(2)	1
Na2	4h	0.5	0.3149(1)	0.5	0.0305(3)	1
P1	4i	0.55377(9)	0.5	0.15627(8)	0.0147(1)	1
S1	4i	0.29560(9)	0.5	0.24192(9)	0.0197(1)	1
S2	8j	0.72256(7)	0.34946(4)	0.23024(5)	0.0219(1)	1

B.3 Differential scanning calorimetry

After performing DSC on the three $Na_4P_2S_6$ samples we opened the sealed quartz glass ampoules to record PXRD patterns. A comparison of before and after DSC powder diffraction patterns is given in Figure B.7. Although, the patterns of the DSC treated samples (four-times cycling up to 300 °C) show good agreement to the patterns recorded prior to the DSC, some new reflections mainly around 10° 2θ (Mo K_{α_1}) arise in the precipitated $Na_4P_2S_6$ (see Figure B.7b). We account this to some degree of annealing, since the position of the new reflections is comparable to reflections found in both solid-state and annealed $Na_4P_2S_6$. Cycling the temperature for a few times up to 300 °C over the course of a few hours might have a similar impact on "healing" the β-like precipitated sample as annealing it at 500 °C for a shorter time. Since the ampoules did not show any indication of reaction with the sample, like discoloration or opacification, we exclude degradation of the powder during DSC.

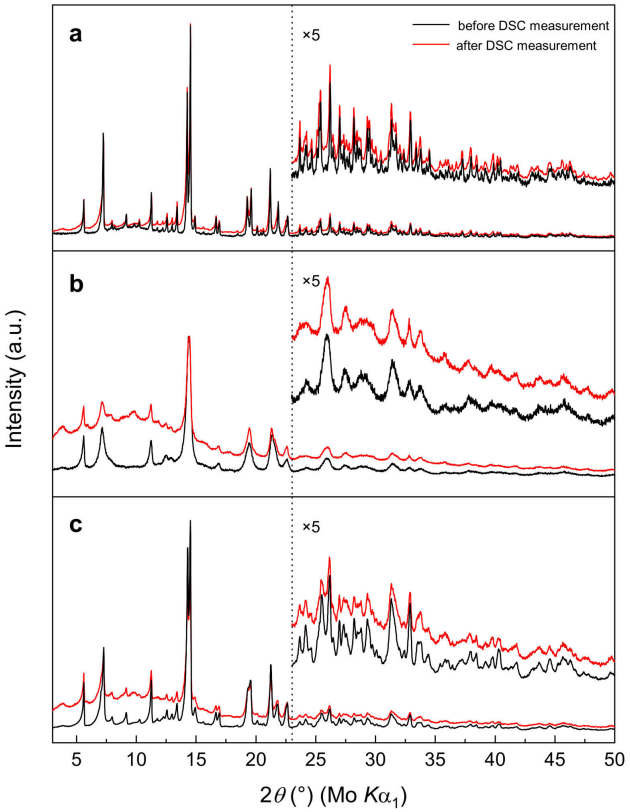

Figure B.7: Room temperature PXRD patterns of (a) solid-state, (b) precipitated, and (c) annealed $Na_4P_2S_6$ before and after DSC measurements up to 300 °C.

B.4 Thermogravimetric analysis

Precipitated $Na_4P_2S_6$ was checked for residual water after drying the hydrate precursor in a Büchi furnace (*cf.* Experimental Section). A thermogravimetric diagram is shown in Figure B.8. The dried compound still holds some residual water, however, the amount is small enough to consider this material as dry. Assuming the observed weight loss to be crystal water, a sum formula is calculated to $Na_4P_2S_6 \cdot 0.004\,H_2O$. Since some degree of re-hydration in air cannot be rules out during the transfer into the instrument, we are confident that the dehydration procedure yields virtually crystal water free $Na_4P_2S_6$.

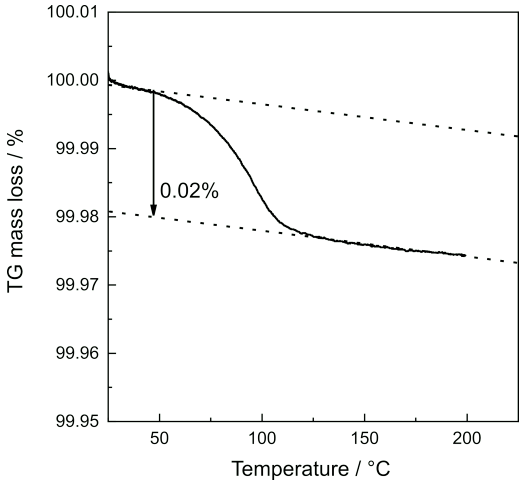

Figure B.8: Thermogram of precipitated $Na_4P_2S_6$.

B.5 Raman spectroscopy

The molecular anion $P_2S_6^{4-}$ can exist in two different point group symmetries, depending on the chemical surrounding. The more symmetrical configuration D_{3d} resembles the symmetry of an ethane molecule, composed of two trigonal pyramids that are connected *via* a central homonuclear bond (C–C or P–P). This symmetry is for example found in $Mg_2P_2S_6$, $(NH_4)_4P_2S_6$, $Na_4P_2S_6 \cdot 6\,H_2O$, and $Li_4P_2S_6$.[26,27] An analysis of the vibrational modes of a molecule of D_{3d} gives:

$$\Gamma_{\mathrm{vib}}(D_{3d}) = 3A_{1g}(\mathrm{R}) + 1A_{1u}(\mathrm{ia}) + 2A_{2u}(\mathrm{IR}) + 3E_g(\mathrm{R}) + 3E_u(\mathrm{IR}),$$

with (R) being Raman active modes, (IR) being infrared active modes, and (ia) being inactive modes. Therefore six Raman active modes should be present for an $P_2S_6^{4-}$ of ethane-like symmetry.

By slightly elongating or shortening one P–S bond and changing the corresponding S–P–S angle the $P_2S_6^{4-}$ anion adapts a less symmetrical C_{2h} point symmetry. Anions of this kind are found in $Ca_2P_2S_6$, $Sr_2P_2S_6$, $Ba_2P_2S_6$, and $Sn_2P_2S_6$.[26,28] According to the

analysis the vibrational modes for a molecule of this symmetry,

$$\Gamma_{\mathrm{vib}}(C_{2h}) = 6A_g(\mathrm{R}) + 4A_u(\mathrm{IR}) + 3B_g(\mathrm{R}) + 5B_u(\mathrm{IR}),$$

nine Raman active modes are expected. A visualization of the $P_2S_6^{4-}$ anion in α- (C_{2h}) and β- (D_{3d}) $Na_4P_2S_6$ is shown in Figure B.9.

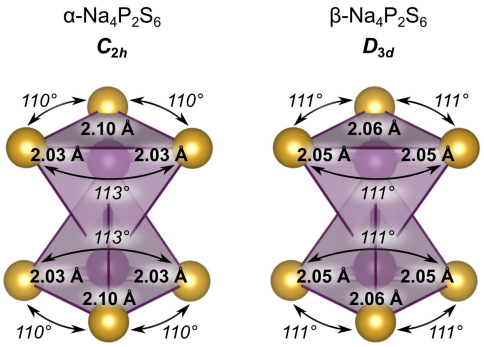

Figure B.9: $P_2S_6^{4-}$ anion in α- and β-$Na_4P_2S_6$ at 20 °C and 200 °C with C_{2h} and D_{3d} symmetry, respectively.

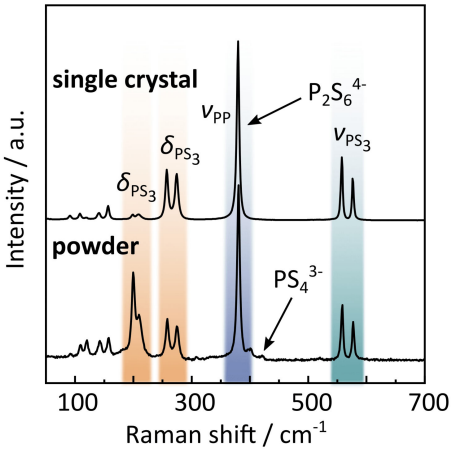

Figure B.10: Room temperature Raman spectra of solid-state synthesized $Na_4P_2S_6$ powder with a more pronounced deformation mode around 200 cm^{-1} compared to the single crystal.

Table B.9: Vibrational frequencies of solid-state synthesized $Na_4P_2S_6$ in cm^{-1}.

Asgmt C_{2h}	Mode	Temperature / °C 25	100	150	200	250	300	400	500	Asgmt D_{3d}	Mode
presumably		91 vw									
lattice		108 w	107 w	106 w	99 vw	102 vw	100 vw	100 vw	97 vw	lattice vib.	
vibrations		119 w	118 vw	117 vw	117 sh						
δ_{PS_3}		141 vw	140 vw	140 vw	142 vw	140 w	137 w	137 w	137 w	δ_{PS_3}	
		156 vw	155 vw	155 vw							
δ_{PS_3}		198 vw	204 vw	202 vw	194 vw	193 vw	192 vw	189 vw	187 vw	δ_{PS_3}	A_{1g} or E_g
δ_{PS_3}		208 vw									
δ_{PS_3}	A_g	257 s	257 s	257 m	264 s	264 s	263 s	262 s	261 s	δ_{PS_3}	E_g
δ_{PS_3}	B_g	274 w	273 w	273 w							
ν_{PP}	A_g	379 vs	378 vs	378 vs	376 vs	375 vs	375 vs	373 vs	371 vs	ν_{PP}	A_{1g}
ν_{PS_3}	A_g	557 s	556 s	554 s	550 s	549 s	548 s	545 s	542 s	ν_{PS_3}	A_{1g}
ν_{PS_3}	A_g	con	con	con	569 sh	567 sh	566 sh	560 sh	554 sh	ν_{PS_3}	E_g
ν_{PS_3}	B_g	576 m	575 m	574 m							

ν: stretching mode, δ: bending mode, w = weak, m = medium, s = strong, v = very, sh = shoulder,
con = convoluted with ν_{PS_3} (A_g) mode at 556 cm^{-1}.

B.6 Cationic and anionic sublattice

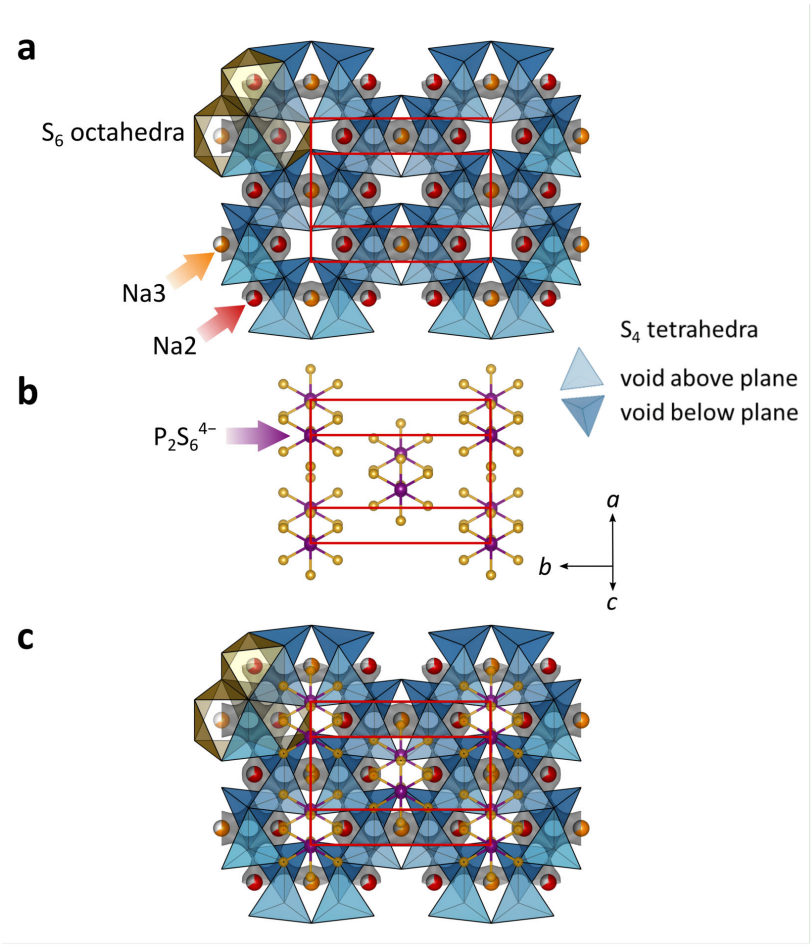

Figure B.11: (a) Na2/Na3 cation and (b) $P_2S_6^{4-}$ anion order in β-$Na_4P_2S_6$. (c) Superimposed images of (c) and (b).

B.7 DFT calculations

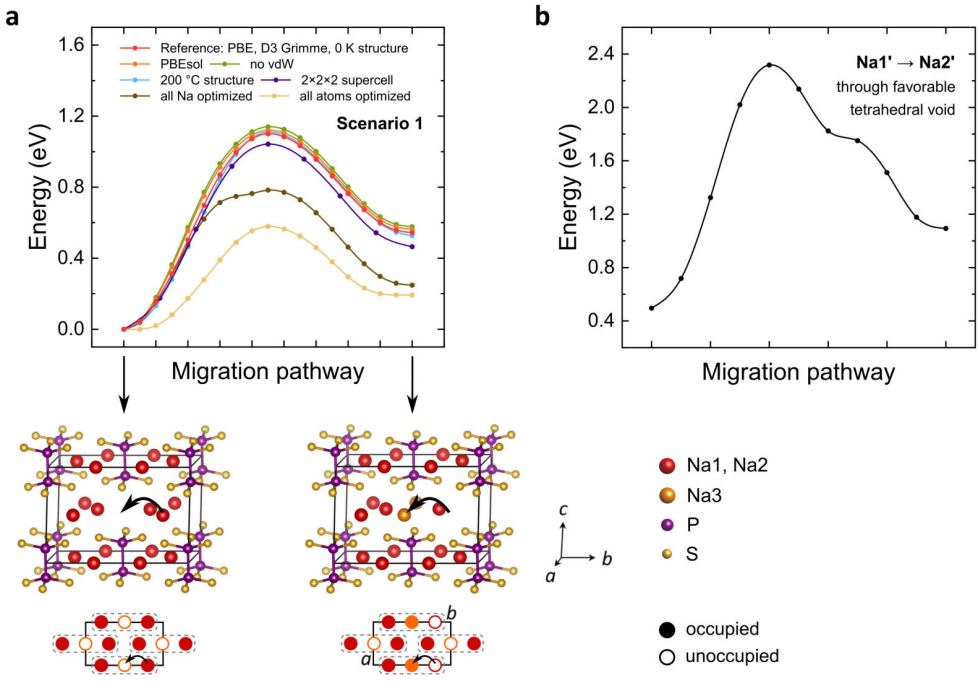

Figure B.12: Energy curves for Na^+ migration in $Na_4P_2S_6$ from NEB calculations. (a) Comparison of different DFT inputs for Scenario 1 to the reference used in Chapter 5 (PBE approximation, D3 Grimme van der Waals correction, DFT-optimized structure (0 K), unit cell, fixed atom positions). PBEsol: PBEsol approximation. no vdW: without D3 correction. 200 °C: experimental 200 °C structure. $2 \times 2 \times 2$ supercell. All Na/all atoms optimized in the NEB calculation. (b) Migration of Na1 through a favorable tetrahedral void to the Na2/Na3 layer with an $E_{mig} = 1.82$ eV.

B.8 Impedance spectroscopy and DC polarization

In this section the fitting process of the measured impedance spectra and the DC polarization measurement is discussed.

B.8.1 Impedance spectroscopy

Typically, impedance spectra of pure ion conductors are composed of a semicircle at high frequencies, described as a parallel arrangement of a resistance R and a constant phase element CPE, followed by a polarization spike at low frequencies, modeled as a second CPE in series of the parallel (R)(CPE1) circuit. For this study, some spectra were fitted using an additional capacitor C parallel to the (R)(CPE1)–CPE2 circuit, to account for parasitic stray capacitance.[29] The stray capacitance was found to be on the order of a few pF for all measured temperatures. Constant phase elements are often used to describe a non ideal behavior entailing a dispersion of relaxation times, often stemming from microscopically imperfect contacts at the sample–electrode contact or a distribution in material properties and thus a non-uniform current through the sample.[30] To extract an effective capacitance (in units of F) from a CPE parallel to a resistance R, the Brug formula $C_{\mathrm{Brug}} = Q^{\frac{1}{\alpha}} R^{(\frac{1}{\alpha}-1)}$ is widely used, with Q being the CPE's numerical value of admittance, α being the element's exponential factor, and R being the resistivity in units of Ω.[31]

Ionic conductivties were calculated by $\sigma_{\mathrm{ion}} = \frac{1}{R}\frac{d}{A}$, with R being the resistivity, d being the sample thickness, and A being the geometrical electrode area.

B.8.2 Electronic conductivity

The electronic conductivity σ_{eon} of a material with an ionic conductivity σ_{eon} and a total conductivity of σ can be determined by measuring the DC galvanostatic polarization in an ion blocking configuration. Cold-pressed pellets of ss2 and p1 $Na_4P_2S_6$ with a thickness of L were sandwiched between two stainless steel electrodes. A constant current I of 1 or 10 nA, depending on the sample, was applied for 2400 s. The polarization curves of ss2 and p1 samples are shown in Figure B.13. The transient time τ^δ (represented as a grey box) was too short to reach a steady state condition (zero slope) but was sufficiently long to reach a region of linear slope (potential U as a function of the square root of time t). The electronic contribution can be estimated by solving the following linear equation[32] for σ_{eon}:

$$U - U_{\mathrm{GB}} = \frac{IL}{\sigma} + \frac{\sigma_{\mathrm{ion}}}{\sigma}\frac{IL}{\sigma_{\mathrm{eon}}}\frac{4}{\pi^{\frac{3}{2}}}\sqrt{\frac{t}{\tau^\delta}}$$

This equation describes the evolution of the potential under an applied current for the characteristic semi-finite chemical diffusion time τ^δ. For practical measurements τ^δ is the time of applied current (here 2400 s). For solving the equation, we made the assumption of $\sigma_{\mathrm{eon}} \ll \sigma_{\mathrm{ion}}$, hence $\sigma \approx \sigma_{\mathrm{ion}}$. Furthermore we expect no significant grain boundary contribution (negligible U_{GB}) since the extracted capacities on the order of 10 pF/cm^2 suggest a bulk rather than a grain boundary limited process. Recently Dawson *et al.* have calculated that for Na_3PS_4 no significant grain-boundary resistance is present in

poly-crystalline samples,[33] which is in good agreement with the experimental findings of Krauskopf *et al.*[34] We therefore suspect a similar behavior for $Na_4P_2S_6$.

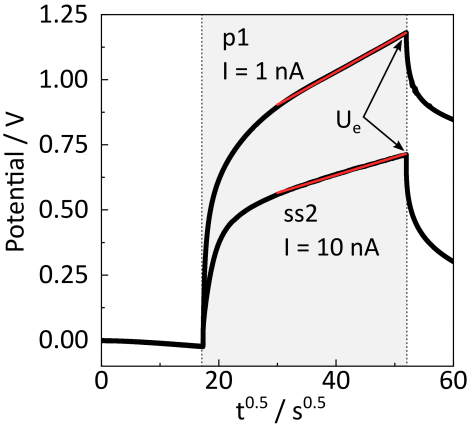

Figure B.13: DC galvanostatic polarization measurements on ss2 and p1 samples of $Na_4P_2S_6$ at room temperature. Pressed pellets were contacted with steel electrodes in an ion blocking configuration.

With these assumptions made we estimate the electronic conductivity of p1 and ss2 $Na_4P_2S_6$ samples to be $1.4 \cdot 10^{-10}\,\mathrm{S\,cm^{-1}}$ and $2.6 \cdot 10^{-9}\,\mathrm{S\,cm^{-1}}$, respectively. The transference number $t(Na^+)$, describing the ratio of sodium ion conductivity to total (ionic and electronic) conductivity, is ≤ 0.99. Hence, $Na_4P_2S_6$ can be described as a nearly pure sodium ion conductor.

References

(1) Kuhn, A.; Eger, R.; Nuss, J.; Lotsch, B. V. *Z. Anorg. Allg. Chem.* **2014**, *640*, 689–692.

(2) Fincher, T.; LeBret, G.; Cleary, D. A. *J. Solid State Chem.* **1998**, *141*, 274–281.

(3) Petříček, V.; Dušek, M.; Palatinus, L. *Z. Kristallogr.* **2014**, *229*, 345–352.

(4) Rietveld, H. M. *J. Appl. Cryst.* **1969**, *2*, 65–71.

(5) Bruker Suite, Version 2019.1. Bruker AXS Inc., Madison, WI, USA, 2019.

(6) Krause, L.; Herbst-Irmer, R.; Sheldrick, G. M.; Stalke, D. *J. Appl. Cryst.* **2015**, *48*, 3–10.

(7) Sheldrick, G. M. *Acta Crystallogr. Sect. A: Found. Crystallogr.* **2008**, *64*, 112–122.

(8) Sheldrick, G. M. *Acta Crystallogr., Sect. C: Struct. Chem.* **2015**, *71*, 3–8.

(9) Freude, D.; Haase, J. Quadrupole Effects in Solid-state NMR, `www.quad-nmr.de`, 2013–2019.

(10) Harris, R. K.; Becker, E. D.; de Menezes, S. M. C.; Goodfellow, R.; Granger, P. *Solid State Nucl. Magn. Reson.* **2002**, *22(4)*, 458–483.

(11) Massiot, D.; Fayon, F.; Capron, M.; King, I.; Le Calvé, S.; Alonso, B.; Durand, J.-O.; Bujoli, B.; Gan, Z.; Hoatson, G. *Magn. Reson. Chem.* **2002**, *40*, 70–76.

(12) Sale, M.; Avdeev, M. *J. Appl. Cryst.* **2012**, *45*, 1054–1056.

(13) Adams, S.; Rao, R. P. *Phys. Status Solidi A* **2011**, *208*, 1746–1753.

(14) Momma, K.; Izumi, F. *J. Appl. Cryst.* **2011**, *44*, 1272–1276.

(15) Kresse, G.; Hafner, J. *Phys. Rev. B* **1993**, *47*, 558–561.

(16) Kresse, G.; Hafner, J. *Phys. Rev. B* **1994**, *49*, 14251–14269.

(17) Kresse, G.; Furthmüller, J. *Comput. Mater. Sci.* **1996**, *6*, 15–50.

(18) Kresse, G.; Furthmüller, J. *Phys. Rev. B* **1996**, *54*, 11169–11186.

(19) Perdew, J. P.; Burke, K.; Ernzerhof, M. *Phys. Rev. Lett.* **1996**, *77*, 3865–3868.

(20) Grimme, S.; Antony, J.; Ehrlich, S.; Krieg, H. *J. Chem. Phys.* **2010**, *132*, 154104.

(21) Blöchl, P. E. *Phys. Rev. B* **1994**, *50*, 17953–17979.

(22) Kresse, G.; Joubert, D. *Phys. Rev. B* **1999**, *59*, 1758–1775.

(23) Monkhorst, H. J.; Pack, J. D. *Phys. Rev. B* **1976**, *13*, 5188–5192.

(24) Mills, G.; Jónsson, H.; Schenter, G. K. *Surf. Sci.* **1995**, *324*, 305–337.

(25) Jónsson, H.; Mills, G.; Jacobsen, K. W. Nudged elastic band method for finding minimum energy paths of transitions, in Classical and Quantum Dynamics in Condensed Phase Simulations, ed. B. J. Berne, G. Ciccotti and D. F. Coker (World Scientific, 1998).

(26) Pätzmann, U.; Brockner, W. *Z. Naturforsch. A* **1987**, *42*, 593–596.

(27) Dietrich, C.; Sadowski, M.; Sicolo, S.; Weber, D. A.; Sedlmaier, S. J.; Weldert, K. S.; Indris, S.; Albe, K.; Janek, J.; Zeier, W. G. *Chem. Mater.* **2016**, *28*, 8764–8773.

(28) Becker, R.; Brockner, W.; Wibbelmann, C. *Z. Naturforsch. A* **1983**, *38*, 555–558.

(29) Kuhn, A.; Duppel, V.; Lotsch, B. V. *Energy Environ. Sci.* **2013**, *6*, 3548–3552.

(30) Barsoukov, E.; Macdonald, J. R., *Impedance Spectroscopy Theory, Experiment, and Applications*; JohnWiley & Sons, Inc.: Hoboken, NJ: 2005, p 15.

(31) Brug, G. J.; van den Eeden, A. L. G.; Sluyters-Rehbach, M.; Sluyters, J. H. *J. Electroanal. Chem. Interfacial Electrochem.* **1984**, *176*, 275–295.

(32) Maier, J. In *Physical Chemistry of Ionic Materials*; John Wiley & Sons, Ltd.: 2005; Chapter 7, pp 399–499.

(33) Dawson, J. A.; Canepa, P.; Clarke, M. J.; Famprikis, T.; Ghosh, D.; Islam, M. S. *Chem. Mater.* **2019**, *31*, 5296–5304.

(34) Krauskopf, T.; Culver, S. P.; Zeier, W. G. *Inorg. Chem.* **2018**, *57*, 4739–4744.

APPENDIX C

Supporting information for "Superionic conduction in the plastic crystal polymorph of $Na_4P_2S_6$"

Appendix C contains supporting information for Chapter 6.

Contents of Appendix C

C.1 Variable temperature powder X-Ray diffraction

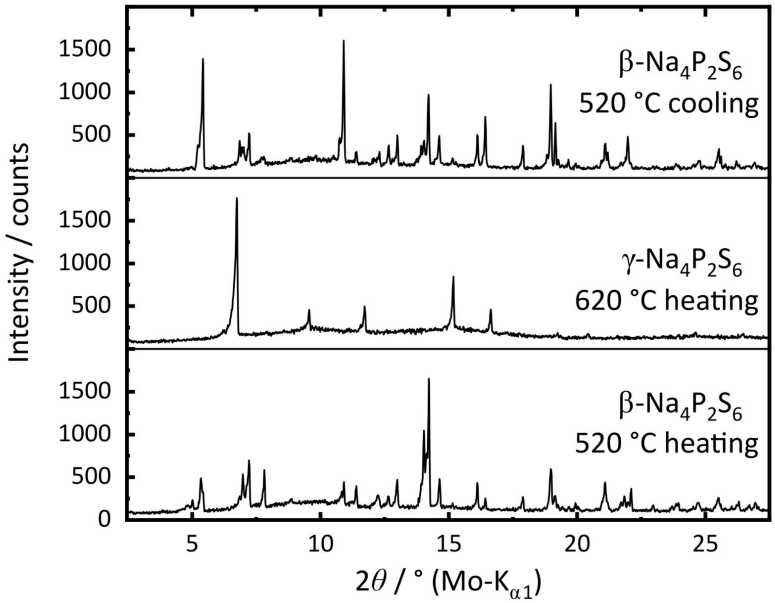

Figure C.1: Powder X-Ray diffraction pattern of β-$Na_4P_2S_6$ at 520 °C upon heating and cooling, and of γ-$Na_4P_2S_6$ at 620 °C. The patterns were extracted from the measurement depicted in Figure C.1. One hour measurement time per pattern; about 51 hours in total.

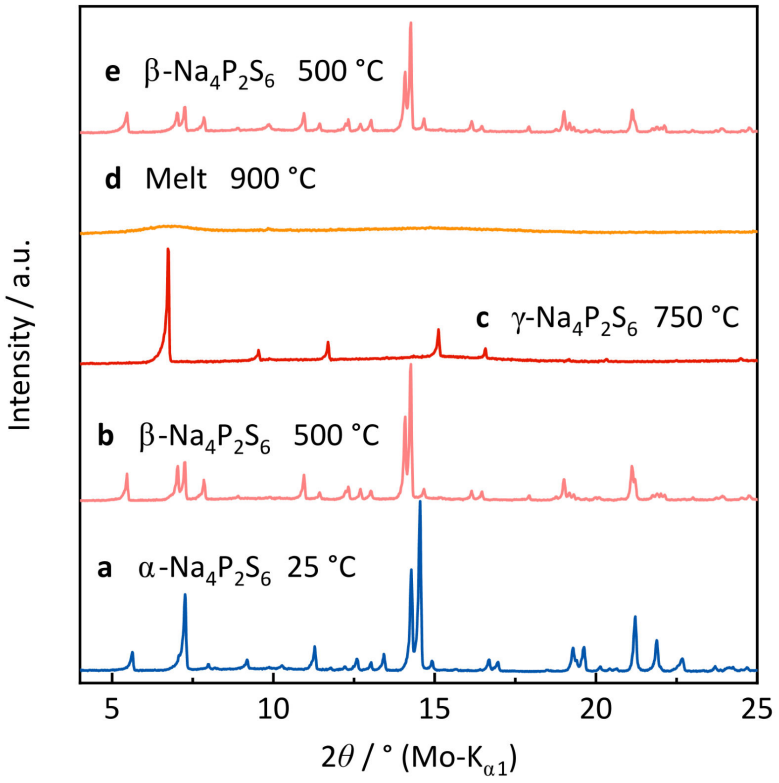

Figure C.2: Powder X-Ray diffraction pattern of (a) α-$Na_4P_2S_6$ at 25 °C, (b) β-$Na_4P_2S_6$ at 500 °C, (c) γ-$Na_4P_2S_6$ at 700 °C, (d) molten $Na_4P_2S_6$ at 900 °C, and (e) β-$Na_4P_2S_6$ at 500 °C after crystallizing from the melt. One hour measurement time per pattern; about 6 hours in total.

Table C.1: Crystallographic data and refinement details. Estimated standard deviations as obtained from the Rietveld refinements are given in parentheses.

	γ-$Na_4P_2S_6$
Temperature ϑ (°C)	650
Formula weight M ($g\,mol^{-1}$)	692.593
Crystal system	cubic
Space group	$Im\bar{3}m$ (no. 229)
Lattice parameter a (Å)	8.4851(5)
Volume V (Å^3)	610.91(10)
Formula units Z	2
Crystallographic density ρ ($g\,cm^{-3}$)	1.8826(3)
X-ray radiation	Ag $K_{\alpha 1}$
2θ range (°)	4–28
No. of refined parameters	37
R_{exp} (%)	1.90
R_p (%)	2.10
R_{wp} (%)	2.77
R_{Bragg} (%)	0.36

Table C.2: Atomic positions and displacement parameters of γ-$Na_4P_2S_6$ at 650 °C. Estimated standard deviations as obtained from the Rietveld refinement are given in parentheses.

Atom	Wyckoff position	x	y	z	Occupancy	B_{iso} (Å^2)
Na1	96l	0.729(4)	0.271(4)	0.151(4)	1/24	6(2)
Na2	96l	0.731(6)	0.455(6)	0.140(2)	1/24	6(2)
P1	96l	–0.090(6)	0.057(5)	–0.079(5)	1/48	11.5(4)
P2	96l	0.090(6)	–0.057(5)	0.079(5)	1/48	11.5(4)
S1	96l	–0.099(11)	0.287(4)	–0.016(16)	1/48	11.5(4)
S2	96l	–0.011(16)	0.026(16)	–0.3024(15)	1/48	11.5(4)
S3	96l	–0.2956(17)	–0.058(11)	–0.038(15)	1/48	11.5(4)
S4	96l	0.011(16)	–0.026(16)	0.3024(15)	1/48	11.5(4)
S5	96l	0.099(11)	–0.287(4)	0.016(16)	1/48	11.5(4)
S6	96l	0.2956(17)	0.058(11)	0.038(15)	1/48	11.5(4)

C.2 Raman spectroscopy

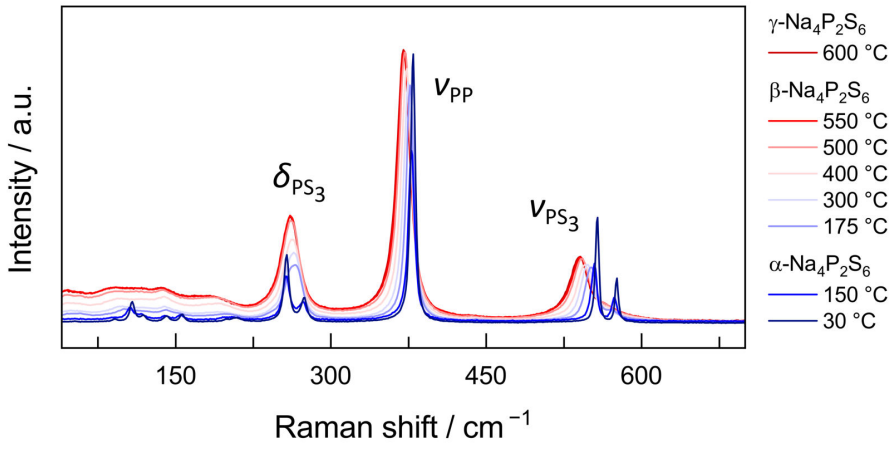

Figure C.3: Raman spectra of α-, β-, and γ-$Na_4P_2S_6$.

C.3 Pair distribution function analysis

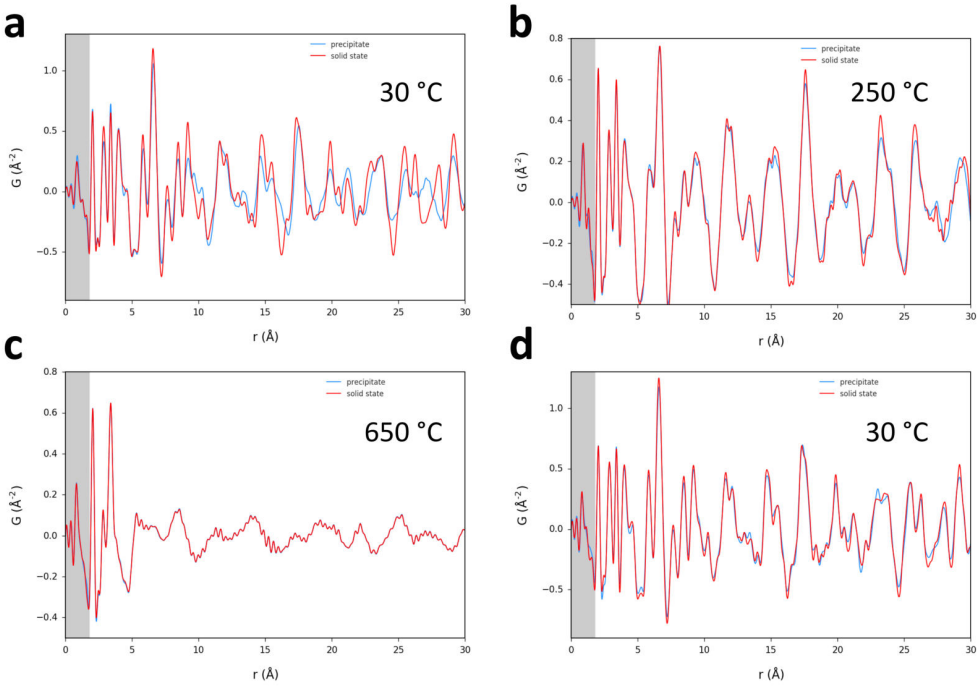

Figure C.4: PDFs of solid-state synthesized and precipitated $Na_4P_2S_6$ measured (a) on the pristine samples at 30 °C, (b) in the β-phase regime at 250 °C, (c) in the γ-phase regime at 650 °C, and after the high temperature measurements at 30 °C. The gray shaded region represents the unphysical interatomic distance range that is more highly affected by systematic errors from data processing.

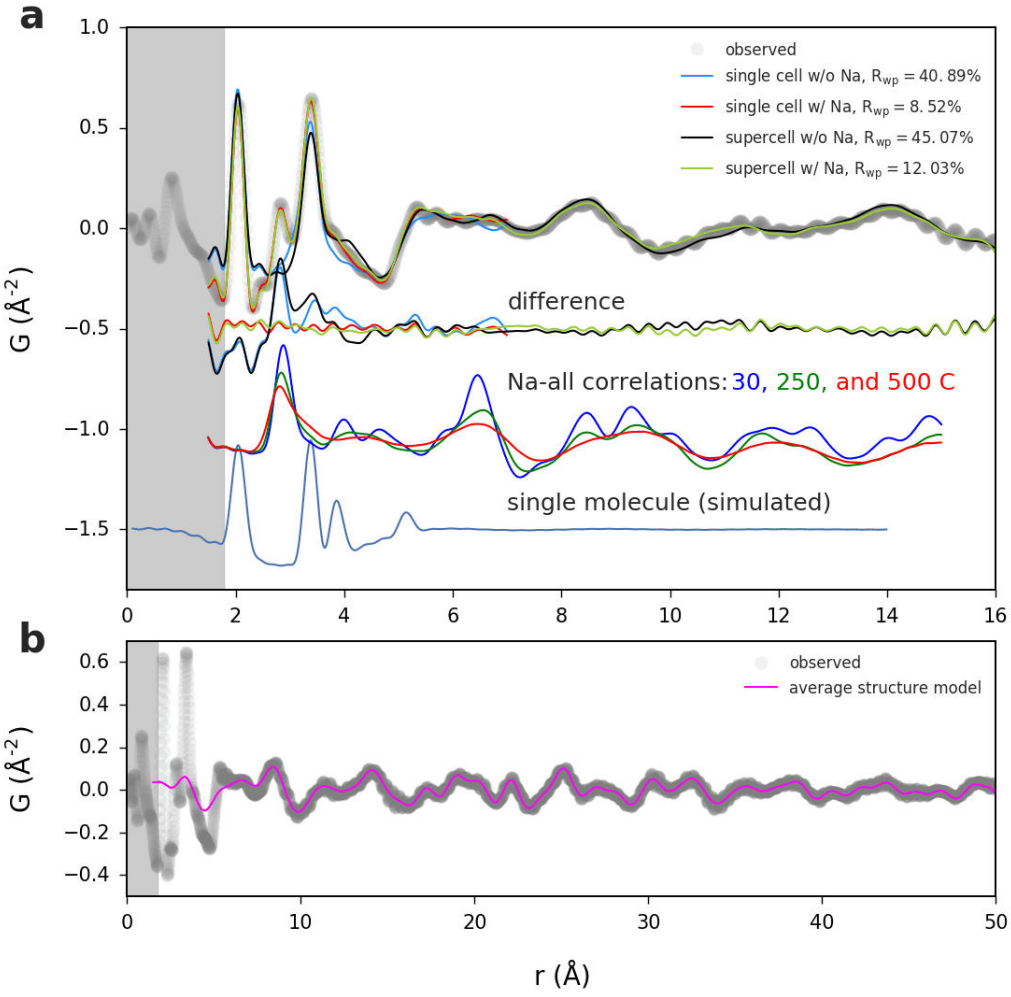

Figure C.5: (a) Comparison of the measured and fitted PDFs of the single cell and super-cell structure models of γ-$Na_4P_2S_6$ (constructed with $P1$ symmetry), with and without sodium contribution. For reference, the partial PDFs between Na and all other atoms were extracted from fits to the lower temperature data to index the Na-S distances around ~ 3 Å. The PDF simulated for a single $P_2S_6^{4-}$ anion is also shown. (b) A fit of the average structure with overlapping anion orientations ($Im\bar{3}m$) obtained from Rietveld refinement to the high-r region of the PDF. The gray shaded region represents the unphysical interatomic distance range that is more highly affected by systematic errors from data processing.

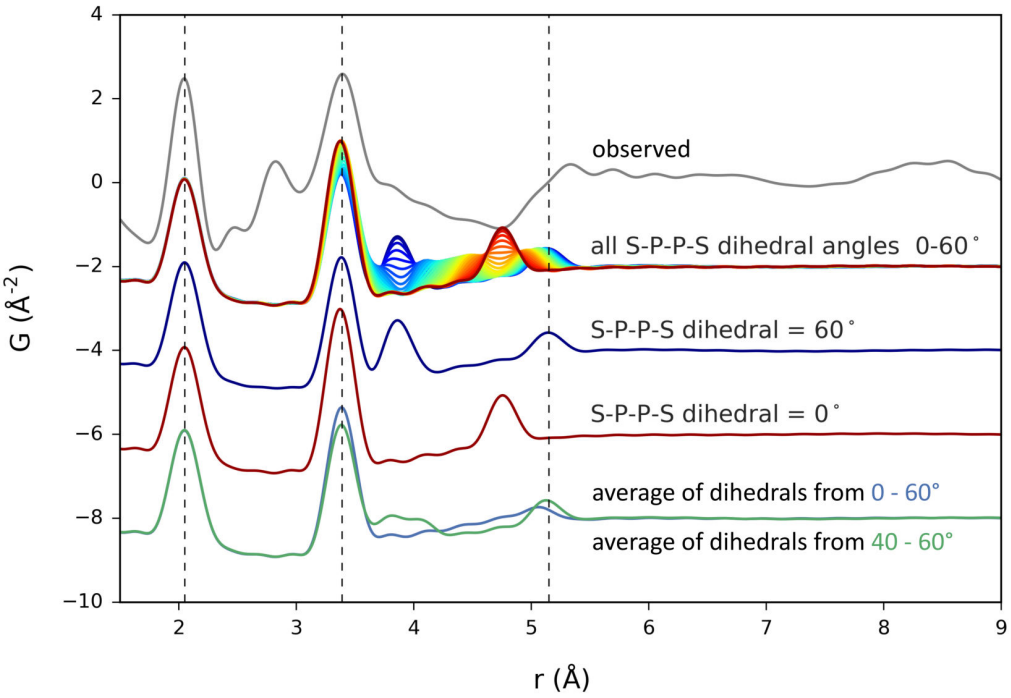

Figure C.6: Analysis of the effect of S-P-P-S dihedral angle on the intramolecular PDF signal for a $P_2S_6^{4-}$ anion. The PDFs for staggered (60°) and eclipsed (0°) conformations are shown for comparison, along with an overlay of PDFs for all conformations. The lack of the short S–(P–P)–S pair correlation just under 4 Å suggests the possibility for some distribution of the dihedral angles. We show that this peak can be washed out by averaging all possible conformations, but also more simply, by averaging conformations over a range of just 20° around the preferred, staggered conformation. The long S–(P–P)–S peak cannot be distinctly resolved to help further disambiguate these cases.

C.4 Impedance spectroscopy

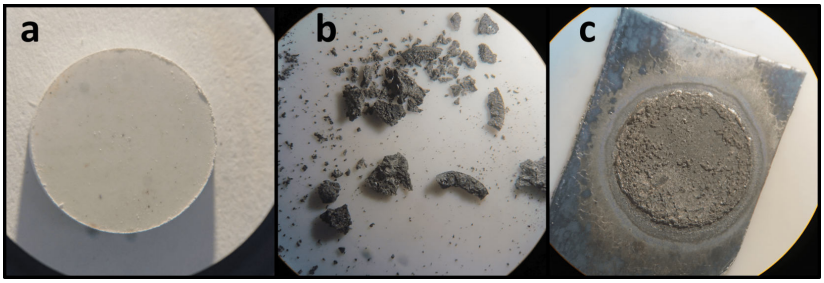

Figure C.7: Images of (a) pristine $Na_4P_2S_6$ pellet, (b) broken pieces of a $Na_4P_2S_6$ pellet after high-temperature impedance measurement, and (c) the Platinum electrode after being in contact with $Na_4P_2S_6$ at 640 °C.

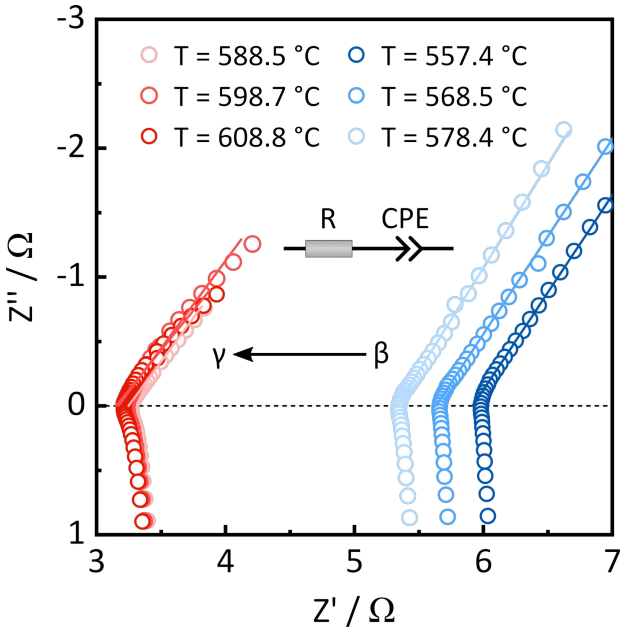

Figure C.8: Exemplary Nyquist plots of high temperature impedance measurements (hollow circles) and equivalent circuits fits (lines) at six selected temperatures.

C.5 Experimental difficulties and aggressive nature of $Na_4P_2S_6$

In this section we discuss the experimental difficulties we faced while characterizing γ-$Na_4P_2S_6$ with high-temperature diffraction, DSC and impedance spectroscopy. The following points summarize the experiments in which we noticed the chemically aggressive nature of γ-$Na_4P_2S_6$ and describe the visual changes we observed:

- High-temperature diffraction: Starting with white to light-gray powder, we noticed a darkening to gray in every HT (diffraction) experiment we performed. The color change was often accompanied with increasing issues in the mechanical stability of the capillary with increasing measurement time. Longer experiments resulted in capillaries that were difficult to unload from the furnace. Hair-cracks probably formed over time and resulted in a not airtight seal of the capillary. Sulfur loss and/or decomposition could be the cause of the extreme brittleness of the glass capillary. Shorter experiments were less affected.

- Preferred orientation: In some longer HT PXRD experiments we noticed a change of the reflection intensities before and after heating to the γ-phase (see Figure C.1). Another, shorter HT PXRD experiment does not show any of this change (compare Figure C.2b and e). We suspect the before mentioned capillary issue to be one possible explanation of this effect. Another explanation could the the formation of preferred orientation of crystallites during a rather slow cool-down. We fitted the HT PXRD data with higher order spherical harmonics to correct for preferred orientation. However, form fitting, we could not tell if preferred orientation or a compositional change by sulfur loss and/or decomposition leads to the change in intensity. It is plausible that both effects contribute to the observation.

- Differential scanning calorimetry: To test the thermal stability of $Na_4P_2S_6$ pellets, we performed a simple thermogravimetric experiment. We observed a slow, monotonic mass loss at 650 °C (12 hours). At the top of the furnace sulfur vapor condensed. Thus, we suspect that $Na_4P_2S_6$ slowly, but constantly, evaporates sulfur if the material is not contained in a closed vessel. Additionally, we noticed that the Al_2O_3 crucibles started to become porous and allowed $Na_4P_2S_6$ to leak and consequently corrode the platinum wires of the thermocouple.

- High-temperature impedance spectroscopy: As shown in image C.7c, the platinum electrodes severely suffered from corrosion. After the experiment the electrodes needed to be replaced and the connecting wire had to be cut to a shorter length, since they started to corrode at the jointed end. We suspect that sulfur vapor attacks the platinum components of the setup and consequently forms PtS or PtS_2, materials with a small bandgaps of 0.471 eV and 1.444 eV.[1]

C.6 Additional information on the $P_2S_6^{4-}$ dynamic disorder

The individual $P_2S_6^{4-}$ anions were placed into a reference frame with one P atom fixed to the origin of a Cartesian coordinate system that aligns with the unit cell axes at all times (see Figure 6.5a, top left). Then, the orientations were expressed in terms of polar coordinates as a function of azimuthal (ϕ) and polar (θ) angles. Visually, the chosen origin divides the possible orientations into eight octants as depicted in Figure 6.5a. Because the anions rotate about their center of mass, rather than the P atom fixed at the origin of the reference frame, octants related by inversion signify the same orientation of the P–P handle with respect to the crystal lattice (but with inverted P atoms). Note that with each simulation frame (*i.e.* reorientational motion of the $P_2S_6^{4-}$ anion), the reference frame origin changes with respect to the crystal lattice, such that the center of mass of the P–P handle remains translationally fixed. Thus, the ensuing population of these initially empty octants indicates that significant reorientation of individual anions occurs.

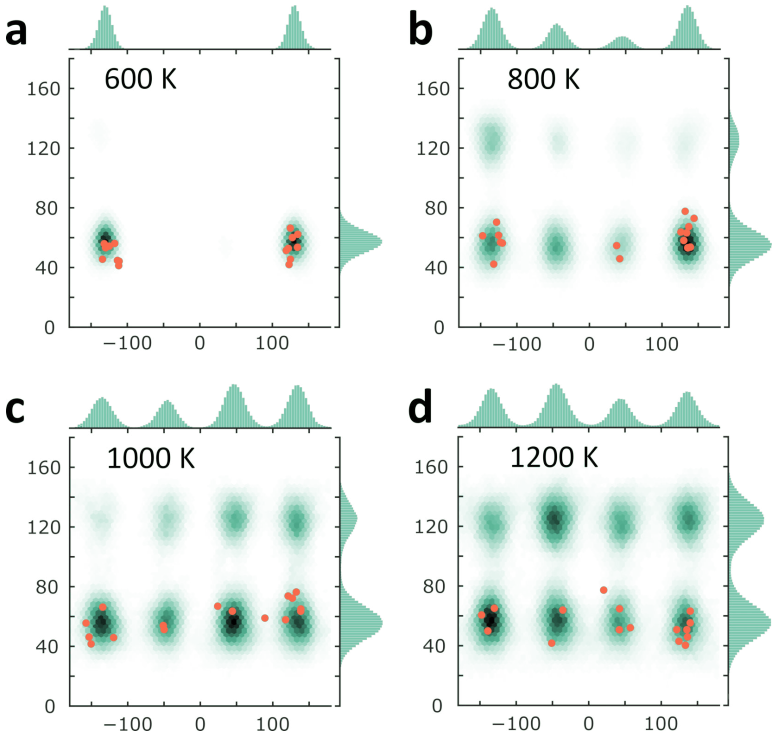

Figure C.9: Orientation heatmap of all $P_2S_6^{4-}$ in a $2 \times 2 \times 2$ supercell at (a) 600 K, (b) 800 K (both 600 ps calculations), (c) 1000 K, and (d) 1200 K (both 300 ps calculations). Initial positions are depicted in orange.

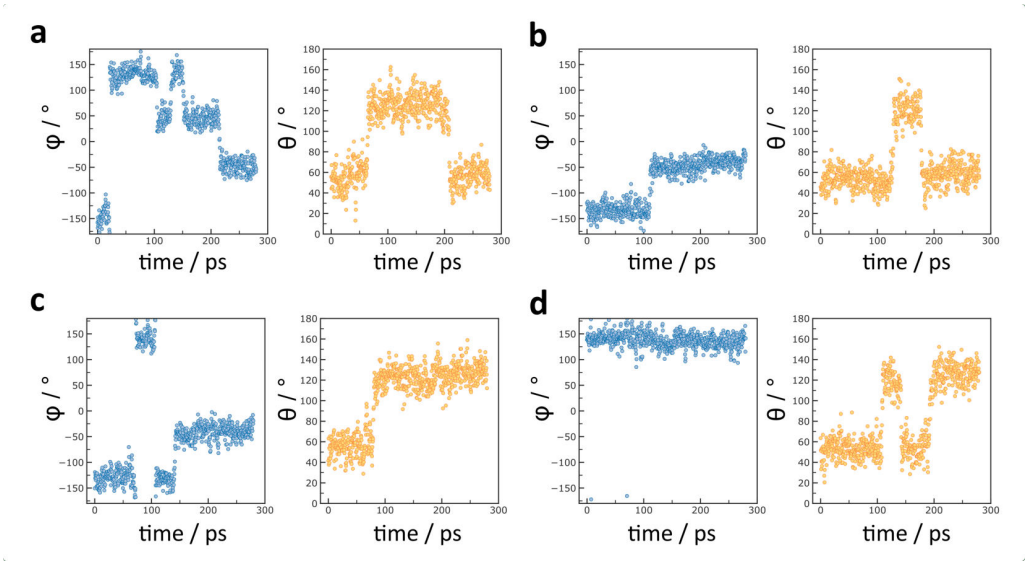

Figure C.10: Azimuthal angle (ϕ) and polar angle (θ) as a function of time of four $P_2S_6^{4-}$ at 1000 K.

C.7 Analysis of the S–P–P–S dihedral angle dynamics

The conformational freedom of the $P_2S_6^{4-}$ anions was investigated. Rotation around the PS_3–PS_3 bond is possible (see Figure C.11). The initial anions had a *gauche* conformation ($|\sphericalangle| = 60°$) as observed in the α and β crystal structures. To capture the evolution of the $P_2S_6^{4-}$ dihedral angle for the ensemble of anions, we counted the number of dihedral angles for different time scales. The histogram plots depicted in Figure C.11b, c, e, and f show an increase in the *anti* ($|\sphericalangle| = 180°$), and Figure C.12 show the time evolution of the dihedral angle of three randomly chosen S–P–P–S units. Although rotations around the P–P axis are observed, some anions showed no conformational reorientation on the 300 ps time scale. The likelihood for rotation around the P–P bond of the anions is supported by the lack of sharp correlations between the S–P–P–S atom-pairs in the experimental PDF and the corresponding need for significantly broadening these contributions in fitting the model.

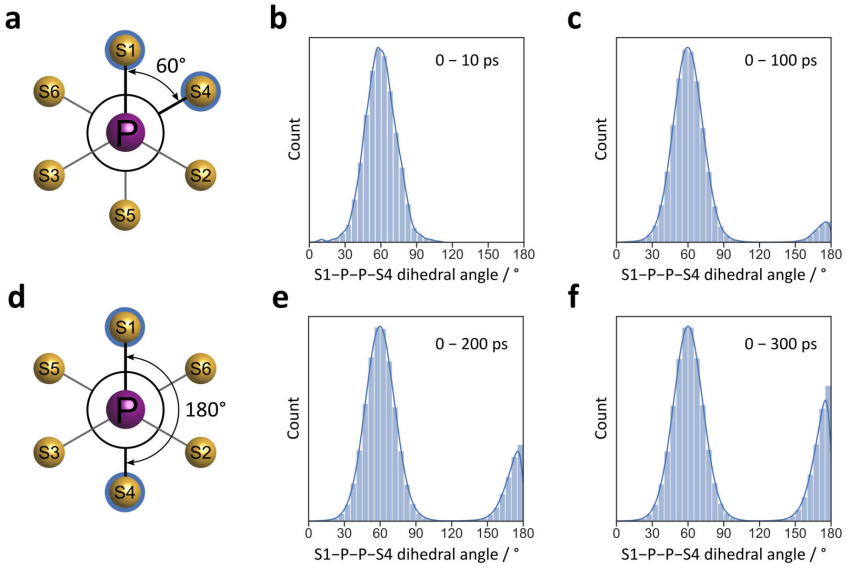

Figure C.11: Newman projection of the $P_2S_6^{4-}$ anion in the staggered conformation with a dihedral angle of (a) 60° and (d) 180°. Histograms of the dihedral angles of the $P_2S_6^{4-}$ anions (defined by two planes spanned by S1–P–P–S4) after the simulation time of (b) 10 ps, (c) 100 ps, (e) 200 ps and (f) 300 ps has elapsed.

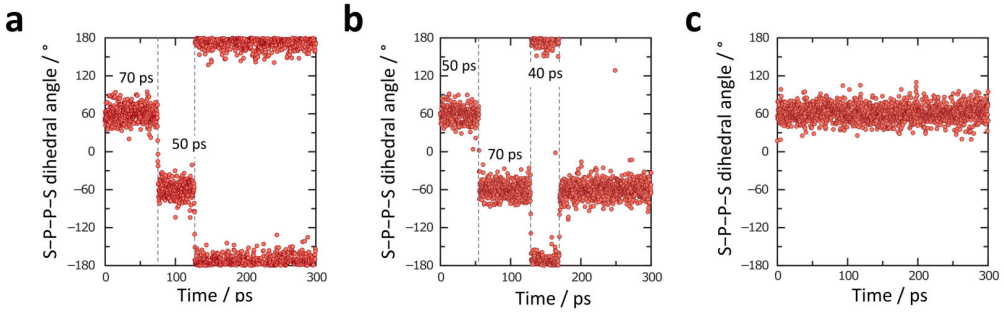

Figure C.12: Dihedral angles (S1–P–P–S4, as defined in Figure C.11) of three $P_2S_6^{4-}$ anions, randomly chosen from the $2 \times 2 \times 2$ supercell, as a function of time (in ps). (a) and (b) depict the diheral rotation of one PS_3 group around the P–P bond, whereas in (c) no rotation is observed in the simulation time of 300 ps (1000 K).

C.8 Short-ranged Na^+ hopping time analysis

Na^+ short-ranged hopping time was evaluated by analyzing the Na^+ trajectory from AIMD. The simulation cell was divided into $4 \times 4 \times 4$ identical cubic units each with a volume of ~ 76.34 Å^3. A hopping event happens when Na^+ crosses a boundary of these units. The hopping time for each Na^+ starts to count from 0, and it is checked every dt ($dt = 10$ fs in this study) to see whether there is a hopping event. If there is a hopping event, the total hopping time will be recorded and reset to 0. If there is no hopping event within dt, the hopping time of this Na^+ will keep on accumulating until it crosses a boundary. Finally, the hopping time was averaged over all hopping events as well as over all Na^+ at each temperature, which is shown in Figure C.13.

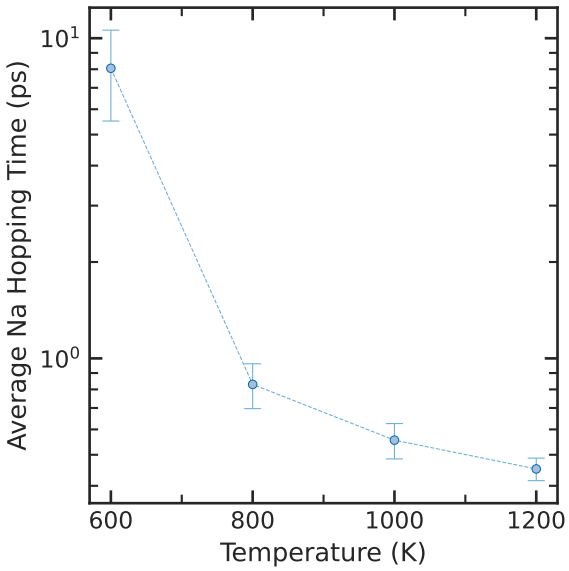

Figure C.13: Averaged short-ranged hopping time (in ps) of Na^+ as a function of temperature (in K). Error bar shows the standard deviation between different Na^+.

References

(1) Jain, A.; Ong, S. P.; Hautier, G.; Chen, W.; Richards, W. D.; Dacek, S.; Cholia, S.; Gunter, D.; Skinner, D.; Ceder, G.; Persson, K. a. *APL Materials* **2013**, *1*, 011002.

APPENDIX D

Supporting Information for "Impact of hydration on ion transport in $Li_2Sn_2S_5 \cdot xH_2O$"

Appendix D contains supporting information for Chapter 7.

Contents of Appendix D

D.1 Experimental

D.1.1 Sample preparation

$Li_2Sn_2S_5$ was synthesized from SnS_2 (precursor synthesized by heating a stoichiometric amount of Sn (99.8%, Acros) and S_8 (99.998%, Sigma Aldrich) with a slight excess of sulfur to 680 °C (12 h, 2 K min^{-1}) and Li_2S (99.9%, Alfa Aesar). A small amount of excess sulfur was added to the stoichiometric mixture to ensure a sulfur-rich atmosphere during the reaction. The mixture was manually ground and mixed in a mortar and pestle, pressed into pellets, and transferred into a glassy carbon crucible inside a quartz ampoule. The ampoule (17 mm diameter, 12 cm length) was flame sealed under low vacuum and annealed (650 °C, 48 h, 2 K min^{-1}). A shiny violet powder was obtained. During cooling, residual sulfur condensed at the cold end of the ampoule and was discarded. Samples of $Li_2Sn_2S_5 \cdot xH_2O$ with specific values of x were prepared by sealing anhydrous $Li_2Sn_2S_5$ powder in a glass container next to (but not in contact with) the desired amount of deionized water. The system was then allowed to equilibrate at 25 or 50 °C for at least 1–2 days. An additional synthesis was performed in the second TGA system described below. Another preparation method employed saturated salt solutions for humidification. Samples were placed in a custom-built desiccator containing the solution, a small fan as well as a sensor (SHT35, Sensirion AG) to measure both humidity and temperature. The samples were kept in the humid atmosphere for sufficiently long time to ensure equilibration at the respective humidities. Compacts of the anhydrous material were prepared by uniaxial pressing (5 mm diameter, 10–20 kN (5–10 kbar), 1–5 min, 25 °C). In one case a 5 mm square die was used. The resulting pellets had thicknesses in the range 0.5–7.3 mm and were about 87% dense as determined by mass and volume measurements. In order to further densify samples of $Li_2Sn_2S_5 \cdot xH_2O$ ($x = 0$) different heat treatments were conducted:

Pressed 300 °C:
Pellet pressed with 10 kN (5 kbar), heated to 300 °C with 5 K min^{-1}, dwelled for 0.3 h, cooled to room temperature with 5 K/min; relative density of 92.5%

Pressed 25 °C, sintered 400 °C:
Pellet pressed at 25 °C with 10 kN (5 kbar), heated to 400 °C with 1 K min^{-1} in a S_8 flux, dwelled for 72 h, heated to 520 °C with 1 K min^{-1}, dwelled for 3 h, cooled to room temperature with 5 K min^{-1}; relative density of 86.7%

Pressed 25 °C, sintered 700 °C:
Pellet pressed at 25 °C with 15 kN (7.5 kbar), heated to 700 °C with 2 K min^{-1} in a S_8 rich atmosphere, dwelled for 48 h, cooled to room temperature with 1 K min^{-1} (similar to synthesis conditions); relative density of 87.8%

The sintering was done under vacuum either in Al_2O_3 or glassy-C crucibles inside quartz ampoules. Compacts of the hydrated material were similarly prepared by uniaxial pressing (5 or 12 mm diameter, 0.1–1 min, 25 °C, 1.0–2.9 mm thickness). The material became softer with increasing water content, so the pressing force was decreased to 7–10 kN (3.5–5 kbar) for $0 < x \lesssim 3.0$ and about 0.1–1 kN (0.05–0.1 kbar) for $x \gtrsim 4.0$. For samples with $x \gtrsim 4.0$, pressing forces above this range were avoided, since they seemed to squeeze water out of the material. The relative density of the resulting compacts was estimated to be at least 79% for $0 < x \lesssim 3.0$, at least 72% for $x \approx 4.0$, and at least 61% for $x \approx 8.0$.

D.1.2 Thermogravimetricanalysis

The TGA set-up used for synthesis employed a balance (Mettler AT20) magnetically coupled (Rubotherm) to a quartz glass crucible containing the sample powder. The sample chamber (double-walled brass container) was connected to a transfer stage, which was directly attached to a humidifier (double-walled glass container). The sample chamber, humidifier and transfer stage were temperature controlled within an accuracy of ± 0.05 K. To ensure sufficient water feeding for the humidifier, it was connected with a 4 L storage vessel positioned higher than the water level of the humidifier. The storage vessel was connected to a wobble piston pump, which would dropwise feed enough water into the humidifier. Water spill-over was controlled by an installed overflow drain positioned at half height and attached with a bubbler to prevent the humidified gas of escaping through the overflow drain. N_2 was used as protective and carrier gas (< 10 ppm H_2O including trace leaks, $50\,\mathrm{mL\,min^{-1}}$) and the humidified gas after passing the sample would escape through a heated (180 °C) capillary-exhaust at the top of the sample chamber. The recorded weight gain was corrected using a two-dimensional (T and p_{H_2O}) buoyancy correction parameterized for the empty crucible.

D.1.3 X-Ray powder diffraction

Powder samples were sealed under dry inert gas in a polycarbonate dome (PANalytical). From previous experiments it was confirmed that the sample holder provides sufficient protection from atmosphere for ∼ 24 h. XRPD patterns were measured at room temperature (PANalytical Empyrean Series 2 diffractometer, Bragg-Brentano configuration, Cu-K_α, PIXcel 3D detector). The data were analyzed using HighScore Plus 3.0e (PANalytical).

D.1.4 Pulsed-field gradient nuclear magnetic resonance

The magnetization data were fit by the following equations:

$$M(G) = M(0) \cdot \exp\left(-\gamma_i^2 D^*_{xy}(i) \cdot I(G)\right) \int_0^1 \exp\left(\zeta\chi^2\right) d\chi \tag{D.1}$$

$$I(G) = G^2\delta^2\left(\Delta - \frac{\delta}{3}\right) \text{ for a rectangular gradient pulse} \tag{D.2}$$

$$\zeta = \left(D^*_{xy}(i) - D^*_z(i)\right)\gamma_i^2 \cdot I(G) \tag{D.3}$$

$$D^*_{eff}(i) = \frac{2}{3}D^*_{xy}(i) + \frac{1}{3}D^*_z(i) \tag{D.4}$$

In the above equations, $M(G)$ and $M(0)$ are the area of the Fourier transformed attenuating spin-echo signal of the measured and maximum value; γ_i is the gyromagnetic ratio of nucleus i; G and δ are the gradient strength and length of the pulse; Δ is the diffusion time; $I(G)$ is a double integral which can be represented with negligible error by the approximation in Equation D.2; χ is an integration variable; and $D^*_{xy}(i)$, $D^*_z(i)$, and $D^*_{eff}(i)$ are the tracer diffusivities of species i in the xy and z directions as well as the overall effective tracer diffusivity. The fits were performed using the *nlinfit* function in Matlab (*Mathworks*, Version R2017a). The resulting fit curves were visually satisfactory, with a reasonable goodness of fit (typically $\chi^2 < 1.5$) and relatively small confidence intervals. Alternative models for data fitting were also tested which we will briefly discuss here (also see Figure D.6). The first one was based on free, isotropic (3D) diffusion of ions with one mobile species (Stejskal and Tanner equation; $M(G) = M(0) \cdot \exp\left(-\gamma_i^2 G^2 D^*_{iso}(i)\delta^2\left(\Delta - \frac{\delta}{3}\right)\right)$).[1] This model yielded visually unsatisfactory fits with larger goodness of fit and confidence intervals and was consequently discarded. The second model described 3D diffusion with two mobile species. This model was often as good if not superior to the one from Ref. [2], however, this could be attributed to the extra fitting parameter, and given that this model lacked in physical meaning, it was judged to be unsuited. The last alternative model was the same as in Ref. [2] yet allowing for out-of-plane diffusion ($D^*_z(i) \neq 0$). Similar to the second model, due to the additional parameter the fitting was often superior, but again it repeatedly produced unphysical results, and was therefore also dismissed. In principle, the non-linearity of the attenuation signals obtained in this work could also be partly caused by geometric confinement of the diffusing species, e.g., due to grain boundaries. However, based on the high fit quality for the 2D model, the degree of attenuation and the layered crystal structure, we judge that confinement effects have only a small impact on the observed signal, as discussed in Chapter 7. The 2D model yielded values for both the in-plane diffusivity $D^*_{xy}(Li^+)$ and the out-of-plane diffusivity $D^*_z(Li^+)$. The latter was found to be far smaller than the former, and the variance in $D^*_z(Li^+)$ was of the same order of magnitude as $D^*_z(Li^+)$ itself. In light of this large variance, $D^*_z(Li^+)$ could not be precisely determined, but we conclude that $D^*_z(Li^+)$ is at least one order of magnitude smaller than $D^*_{xy}(Li^+)$ for allconditions and water contents. The effective Li^+ diffusivity of the entire polycrystalline sample, $D^*_{eff}(Li^+)$, was calculated from an average over all possible orientations, according to the relation $D^*_{eff}(Li^+) = \frac{2}{3}D^*_{xy}(Li^+) + \frac{1}{3}D^*_z(Li^+) \approx \frac{2}{3}D^*_{xy}(Li^+)$.[2]

D.1.5 Electrochemical measurements

For impedance measurements, compacts with $x < 3.0$ were contacted on both sides by ∼400 nm thick ruthenium electrodes (99.95%, Lesker) applied by DC sputtering (Emitech K575X, 100 mA current, either 4 or 2 min sputter time) in a glovebox. A mask was used to prevent metal deposition on the sides of each sample. During sputtering

the samples were exposed to high vacuum for several minutes, and the temperature increased to $\sim 50\,°C$ as measured by an adjacent thermocouple. This process caused a slight amount of water loss, which was accounted for by weighing. Typically, x decreased by ~ 0.5. For compacts with $x \gtrsim 4.0$, electrical contact was sufficient without adding metal electrodes,so the sputtering step was omitted. All measurement cells and chambers were leak-checked in advance using a helium leak detector (UL 200 dry, Oerlikon Leybold Vacuum). Anhydrous compacts ($x = 0$) were installed next to a thermocouple in an enclosed quartz holder in a tube furnace. Samples were heated to various temperatures under flowing inert gas (Ar or N_2, $100\,ml\,min^{-1}$), and after a 1 h dwell, impedance spectra were acquired. Typically, two spectra were acquired at each condition to confirm reproducibility. Additional measurements were acquired at -133 to $27\,°C$ by installing a compact in a cryostat (LH Fluke Appliance, He cooling) under high vacuum. Hydrated samples ($x > 0$) were installed in a Teflon-lined tube fitting (Swagelok) and contacted by two rods that sealed to the fitting using Teflon ferrules. This cell was installed in a quartz tube, and measurements were performed as described above, except with a 0.5 h dwell between steps. Additional measurements at -69 to $27\,°C$ were acquired by immersing the quartz tube containing the Swagelok cell in a thermostat-controlled silicone oil bath (thermostat FP90, silicone oil Thermal HY, Julabo). For comparison, another setup (TSC Battery closed, rhd instruments) was employed in which powder samples were contacted directly by steel electrodes under a constant pressure of 30 kPa in a Microcell HC cell stand (1 h equilibration time). The results from this setup are shown as Dataset 2 in Figure D.11.

D.1.6 Inductively coupled plasma optical emission spectroscopy (ICP-OES)

Samples for ICP-OES were prepared by solubilizing fine ground powder in HNO_3 (65%) for 25 min at $185\,°C$ with a microwave-assisted digestion system (Discover-SP-D). ICP-OES was performed with a Vista Pro Spectrometer (Varian/Agilent Technologies) with an axial plasma, Echelle grating polychromator, and a CCD-detector system. Data evaluation was performed with the software ICP-Expert.

D.1.7 Scanning electron microscopy and single crystal diffraction

Prior to SEM imaging, samples were placed on carbon tape and coated with $\sim$2–3 nm carbon (ACE600, Leica). Micrographs were then acquired by a Zeiss microscope (Merlin) using SE2 (Everhart-Thomley type) and/or in-lens detectors. The transfer steps were performed under high vacuum and inert gas, with no air exposure. For single crystal measurements, a suitable, transparent crystal ($\sim 10 \times 10 \times 5\ \mu m^3$) was picked in grease (Dow Corning) under a microscope in a glovebox. The crystal was mounted using grease on a 0.3 mm capillary (Hilgenberg, glass no. 14), inserted in a 0.5 mm capillary, and sealed with a hot wire under argon. Diffraction data were then collected at room temperature (Bruker AXS diffractometer, graphite-monochromated Mo-K_α, SMART-APEX-II detector) and analyzed (Bruker Suite software, precession module).[3]

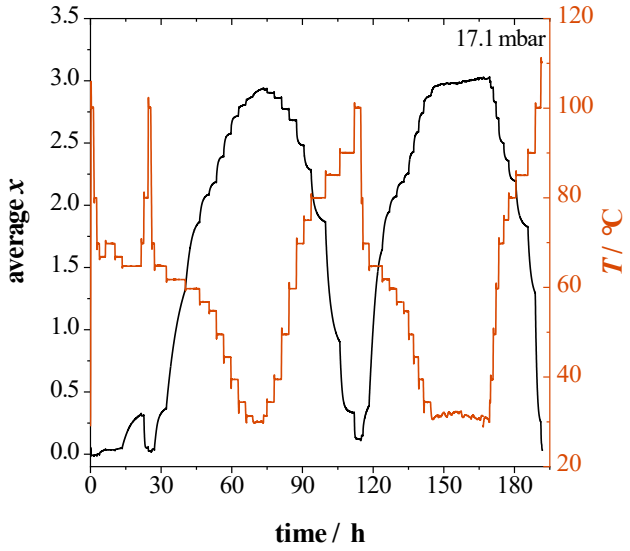

Figure D.1: Typical TGA measurement of $Li_2Sn_2S_5 \cdot xH_2O$ at various temperatures and constant p_{H_2O} of 17.1 mbar.

D.2 Thermogravimetric analysis

The mass change during hydration was found to be initially proportional to time (Figure D.4b).[4] It is unclear if this dependence arises from bulk- or surface-limited behavior, since the water diffusivity strongly increases with increasing water content. We think the kinetics are probably bulk-limited, as discussed in Chapter 7. However, if the kinetics are surface-limited, then the surface exchange constant $\overline{k}$ can be estimated from the relation $\overline{k} = 0.5 \cdot (L_{1/2}/t_{1/2})$, where $L_{1/2}$ is the particle radius ($\sim 25\,\mu m$) and $t_{1/2}$ is the time at which the mass uptake is halfway finished.[4] For example, a value of $1.3 \cdot 10^{-7}\,cm\,s^{-1}$ at 39 °C is obtained.

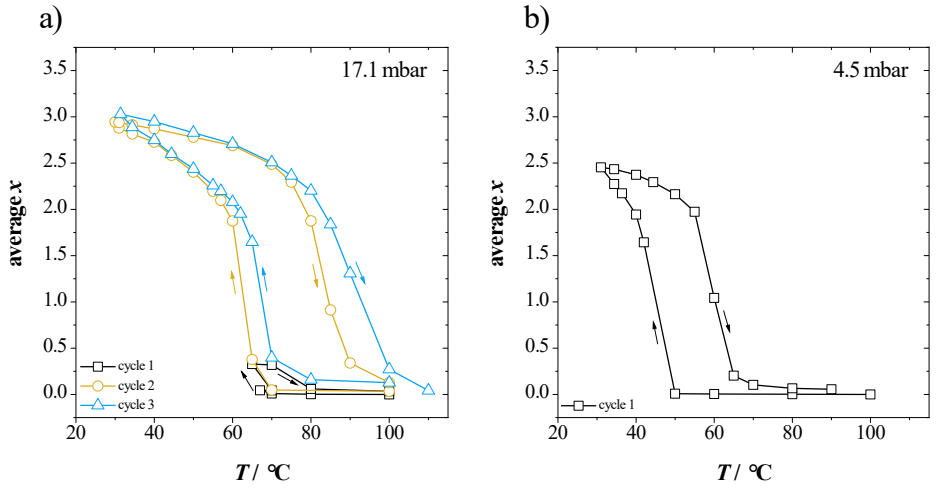

Figure D.2: Degree of hydration x as a function of temperature T showing the hysteresis behavior of $Li_2Sn_2S_5 \cdot xH_2O$ at different isobaric conditions; (a) 17.1 mbar; (b) 4.5 mbar. For each measurement, freshly prepared anhydrous $Li_2Sn_2S_5$ was used as starting material.

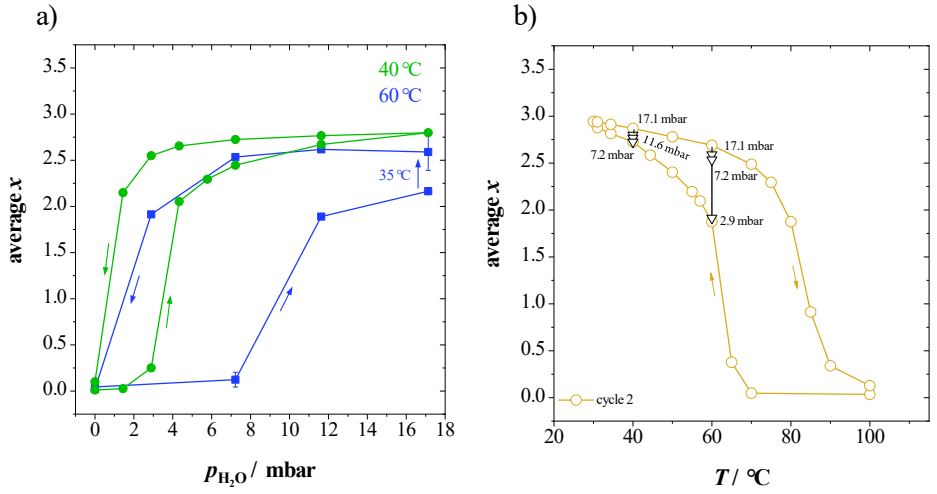

Figure D.3: (a) Degree of hydration x as a function of partial pressure of water p_{H_2O} showing the hysteresis behavior of $Li_2Sn_2S_5 \cdot xH_2O$ at the isothermal conditions for 40 °C and 60 °C. For each measurement, freshly prepared anhydrous $Li_2Sn_2S_5$ was used as starting material. (b) Isobaric measurement of $Li_2Sn_2S_5 \cdot xH_2O$ at 17.1 mbar shown in Figure D.2 with inserted data points from the isothermal measurement.

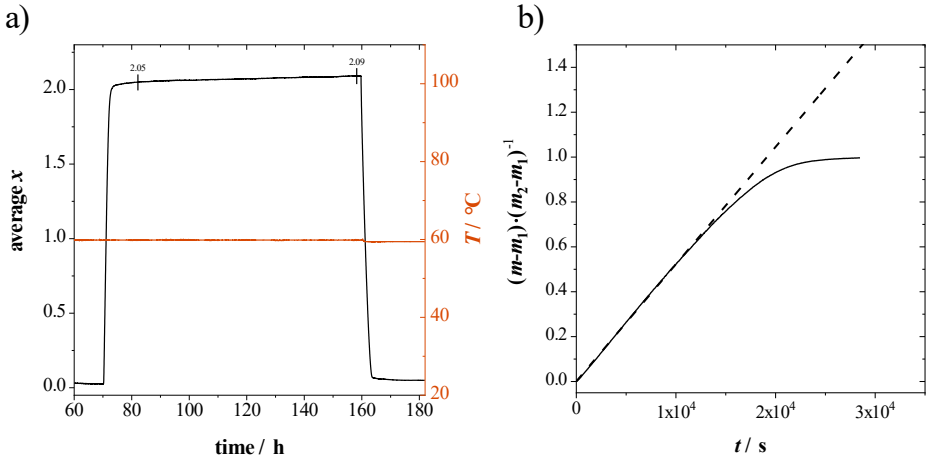

Figure D.4: Long-time TGA measurement of $Li_2Sn_2S_5 \cdot xH_2O$ at constant p_{H_2O} (17.1 mbar) and temperature (60 °C); (b) Normalized mass change for the measurement in Figure 7.1a; here m, m_1, and m_2 are the mass at time t, the initial mass, and the mass at equilibration.

D.3 Pulsed-field gradient nuclear magnetic resonance

Figure D.5 shows the effective diffusivity as a function of diffusion time for three values of the water content, as well as at different temperatures for $x \approx 8.0$. It is evident that the obtained value of $D^*_{\text{eff}}(Li^+)$ decreases slightly (by a factor of 1.5–3) when the diffusion time is increased from 10 to 100 ms. This behavior can be attributed to slightly slower transport at grain boundaries, as discussed previously.[5] If so, then to be precise, the in-plane diffusivity within a single grain is best estimated by $D^*_{\text{xy}}(Li^+)$ measured at a shorter diffusion time, although the true value in the absence of all boundaries may be slightly higher. The effective diffusivity across a randomly oriented polycrystalline sample is best estimated by $D^*_{\text{eff}}(Li^+)$ measured at a longer diffusion time, although the true DC value when all boundaries are accounted for may be slightly lower.

D.3.1 Solid-state nuclear magnetic resonance

Anhydrous $Li_2Sn_2S_5$ was measured by ssNMR to record both its relaxation time T_1 and the full width at half maximum (FWHM) of the peaks (Figure D.7). Using the equation $(T_1)^{-1} = F \times (\tau_c^\circ)^{-1} \exp\left(\frac{-E_A^{LT}}{k_B T}\right)$; where F is a constant, τ_c° is the correlation time of the Larmor frequency, E_A^{LT} is the activation energy at low temperatures and k_B is the Boltzmann constant;[6] one can estimate E_A^{LT} from linearly fitting the low temperature branch, yielding 0.05 eV for anhydrous $Li_2Sn_2S_5$. This very low activation energy, however, does not correspond to the long-range migration enthalpy recorded by PFG NMR and impedance, and rather reflects a local hopping of ions. The recorded FWHM can be analyzed with the empirical expression $E_A = 1.617 \cdot 10^{-3} \cdot T_c K^{-1}$, where T_c is the onset temperature of motional narrowing.[7,8] The resulting activation energy is 0.56 eV for high

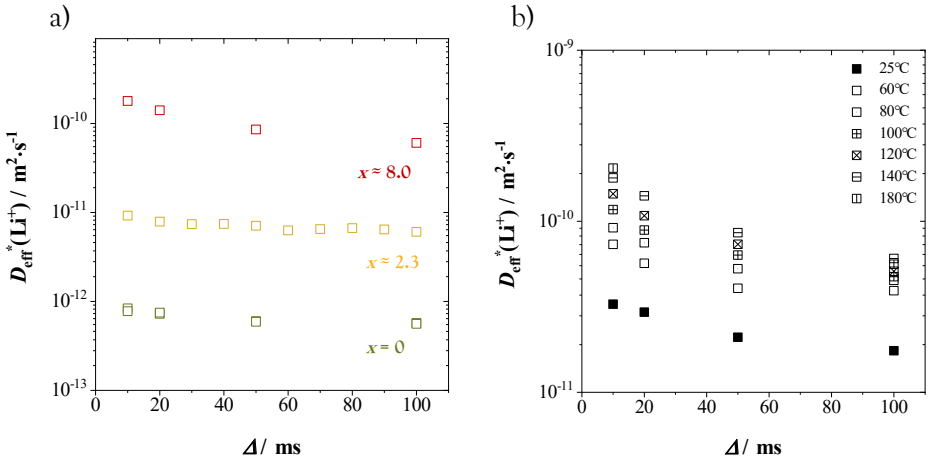

Figure D.5: Effective Li+ tracer diffusivity extracted from 7Li PFG NMR measurements with various diffusion times using the 2D diffusion model: (a) $x = 0$ (140 °C), $x \approx 2.3$ (180 °C) and $x \approx 8.0$ (140 °C); (b) $x \approx 8.0$ at various temperatures.

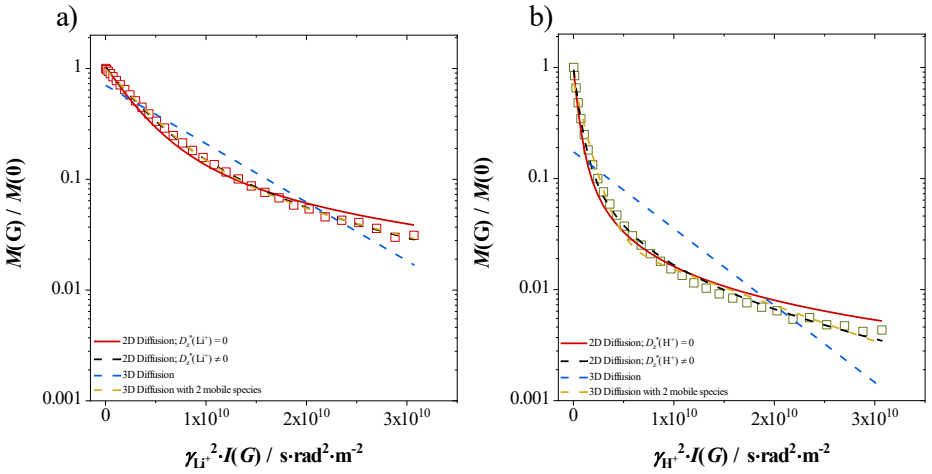

Figure D.6: Comparison of PFG NMR fits in $Li_2Sn_2S_5 \cdot xH_2O$ ($x \approx 8.0$, 170 °C) using different diffusion models; (a) Li^+ diffusion, (b) H^+ diffusion.

temperatures. Even though this value is not far from the ones measured by PFG NMR and impedance, one should keep in mind the empirical nature of this method.

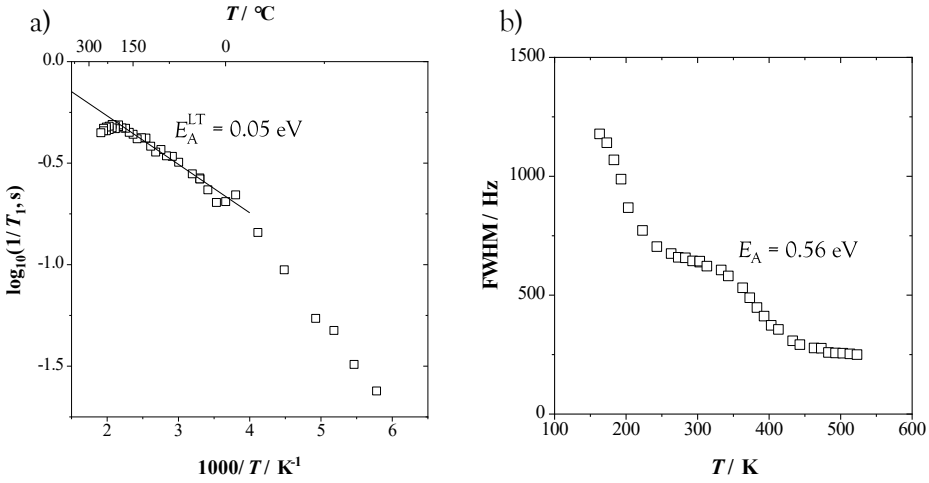

Figure D.7: (a) NMR relaxometry measurement of $Li_2Sn_2S_5 \cdot xH_2O$ ($x = 0$) at different temperatures. The low temperature regime is fitted linearly to yield a low activation energy of $E_A^{LT} = 0.05$ eV; (b) Plot showing the Full Width at Half Maximum (FWHM), also referred to as motional narrowing, of $Li_2Sn_2S_5 \cdot xH_2O$ ($x = 0$) at different temperatures. The onset temperature yields an activation energy of $E_A = 0.56$ eV.[8]

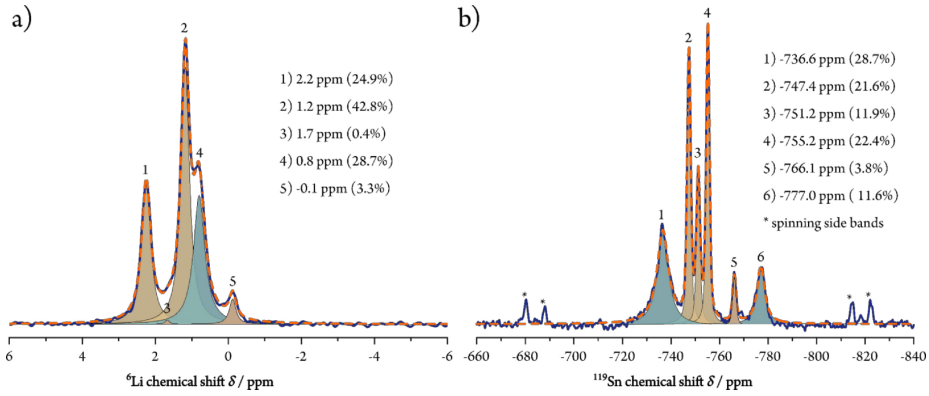

Figure D.8: ^{6}Li and (b) ^{119}Sn MAS NMR spectra of anhydrous $Li_2Sn_2S_5$ (single batch). Brown colored signals correspond to crystalline material, while turquoise colored signals are broader and are attributed to a disordered side phase and/or stacking faults. Signals 3 and 5 in the ^{6}Li and signal 5 in the ^{119}Sn spectrum are assigned to Li_2SnS_3. Slight batch-to-batch variations were observed in the ^{6}Li spectra.

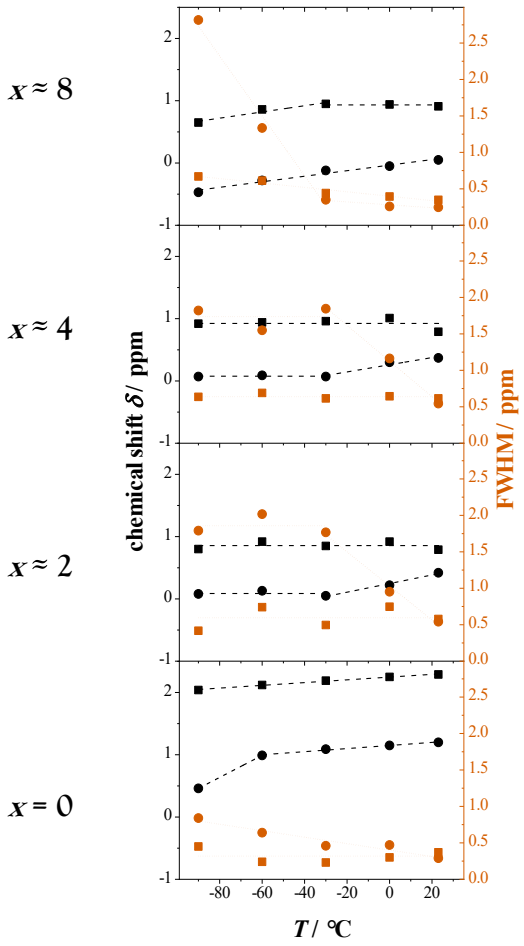

Figure D.9: Chemical shifts δ (black) and full widths at half-maximum FWHM (red) for signal 1 (squares) and signal 2 (circles) in the ^{6}Li NMR spectra in Figure 7.5. Dashed and dotted lines are guides for the eye. Although motional narrowing is theoretically accompanied by a transition from a Gaussian to a Lorentzian line shape, for simplicity a Lorentzian line shape was used in all fits.

D.4 Electrochemical measurements

To convert the by PFG NMR measured diffusivities into conductivity with the Nernst-Einstein relation (see equation (7.2) in Chapter 7), the lithium ion concentration $[Li^+]$ was estimated with:

$$[Li^+] = \frac{d_0}{d_x} \cdot \frac{Z_{Li}}{V_{UC}} \tag{D.5}$$

where d_0 and d_x are the interlayer spacing for $x = 0$ and $x > 0$ (see Figure 7.2), Z_{Li} and V_{UC} are the number of Li atoms (3.78) and volume (438.8 Å^3) per unit cell for $x = 0$. Note that the here estimated concentration is an upper bound, since, at least for $x = 0$, it is unclear how crystallinity affects the ionic transport (referring to the less crystalline content seen in Figure 7.5).

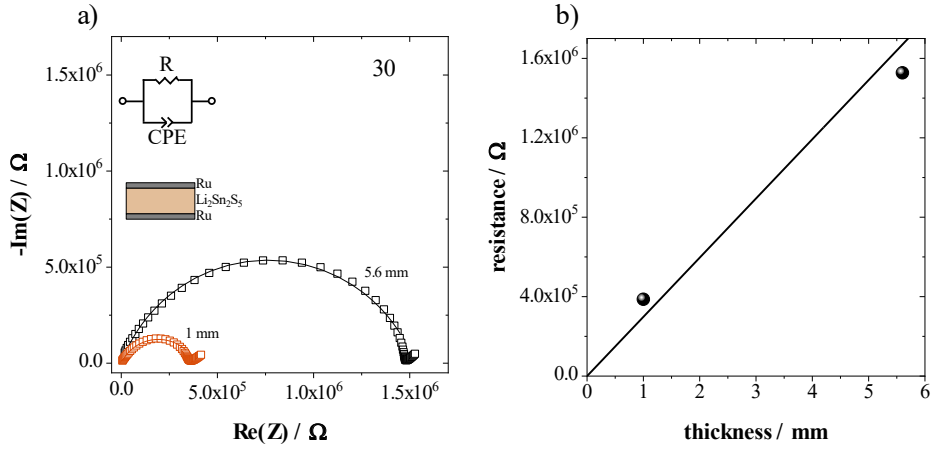

Figure D.10: Impedance measurements of $Li_2Sn_2S_5 \cdot xH_2O$ ($x = 0$) with different sample thicknesses showing (a) the impedance spectra and (b) the linear scaling of the resistance with thickness. The line is a linear fit going through 0.

Electromotive force (EMF) and conductivity measurements were performed with Li^+ reversible electrodes, for which anhydrous compacts were sandwiched between Li (99.9%, Alfa Aesar) and LiAl (> 99.5%, ELSAindustries SAS) electrodes (Figure D.13). LiAl powder was co-pressed with $Li_2Sn_2S_5$ powder, while slabs of Li were applied directly to the compacts. The Li^+ reversible electrodes themselves were contacted by either stainless steel rods or disks of molybdenum to avoid alloying of the metals. The measurement conditions were the same as described for the Li^+ blocking electrodes in Chapter 7. The measured EMF was 0.32 V initially, close to the Nernst voltage expected for these electrodes.[9] Over tens of hours it decreased to below 0.05 V, while the conductivity increased gradually to $\sim 10^{-4}$ S cm^{-1} and the dielectric constant ϵ_r increased from ~ 100 to ~ 4000. If instead noble metal electrodes are used, DC polarization experiments indicate pure ionic conduction,[5] as does the blocking impedance arc at low frequencies observed in this study. Taken together, these observations indicate that $Li_2Sn_2S_5$ is a predominant ion conductor, which however reacts in contact with Li alloy electrodes to

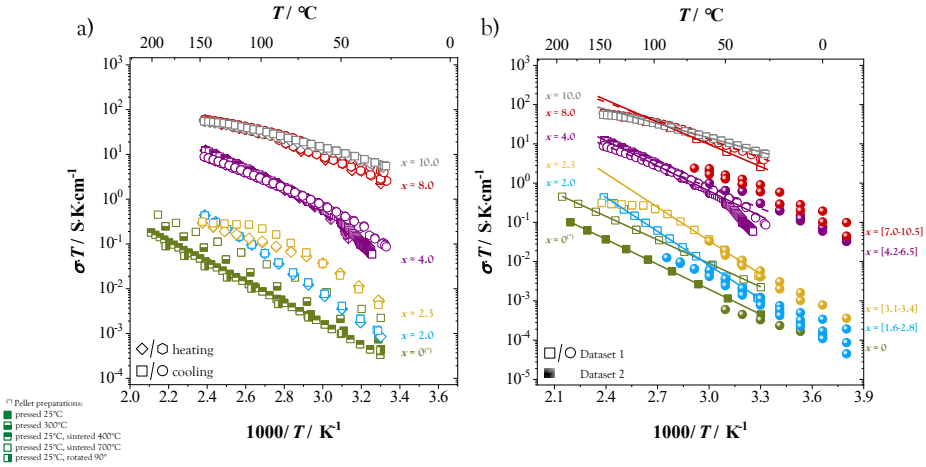

Figure D.11: Temperature dependence of the conductivity measured from $Li_2Sn_2S_5 \cdot xH_2O$ by impedance spectroscopy showing different sample preparation methods for $x = 0$ as well as heating and cooling runs for $x > 0$. (b) Comparison of impedance data of $Li_2Sn_2S_5 \cdot xH_2O$ collected at two different experimental set-ups. Solid lines are linear fits.

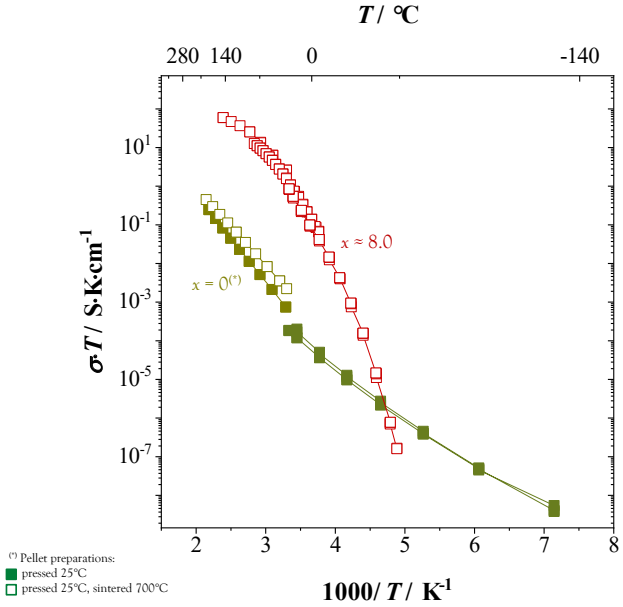

Figure D.12: Transport data for $Li_2Sn_2S_5 \cdot xH_2O$ ($x = 0$ and $x \approx 8.0$) measured above and below room temperature. For $x = 0$, two datasets are shown: pellet pressed at 25 °C (closed squares); pellet pressed at 25 °C, sintered at 700 °C (open squares

yield a phase with substantial electronic conductivity.

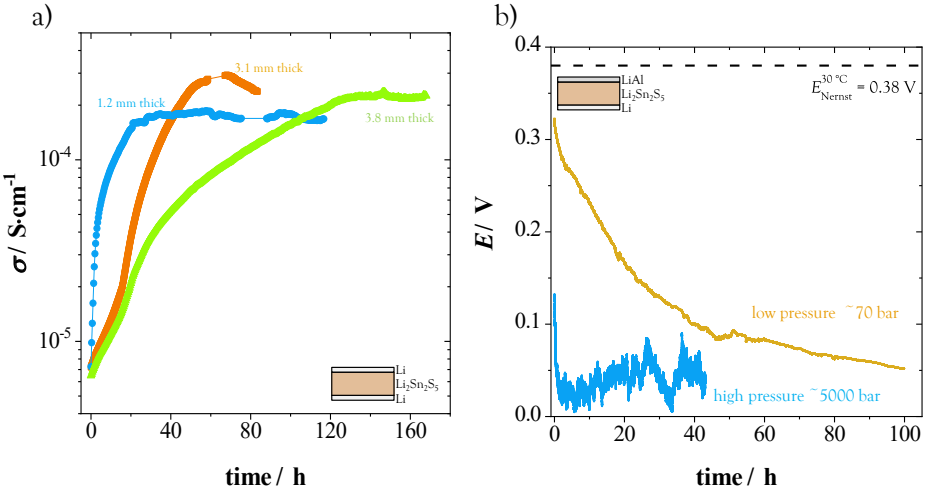

Figure D.13: Conductivity of anhydrous $Li_2Sn_2S_5$ after being contacted by Li metal electrodes. (b) EMF measurement of $Li_2Sn_2S_5$ at 30 °C with Li and LiAl as electrodes under high and low pressure. The Nernst voltage for this cell is 0.38 V.[9]

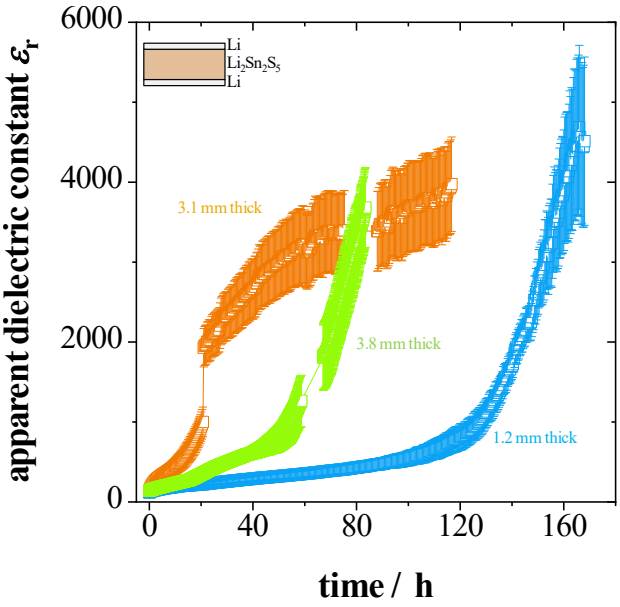

Figure D.14: Apparent dielectric constant ϵ_r of anhydrous $Li_2Sn_2S_5$ corresponding to the data shown in Figure D.13a

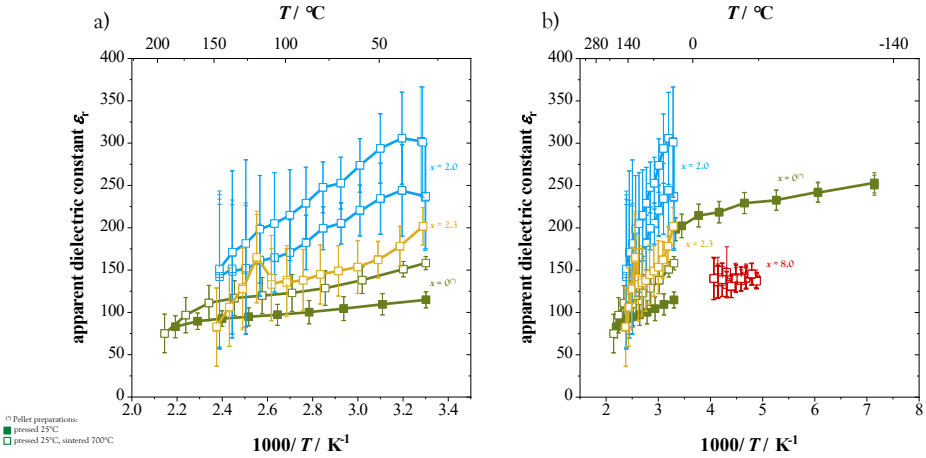

Figure D.15: Apparent dielectric constant ϵ_r of $Li_2Sn_2S_5 \cdot xH_2O$ over the temperature ranges shown. For $x = 0$, two datasets are shown: pellet pressed at 25 °C (closed squares); pellet pressed at 25 °C, sintered at 700 °C (open squares). For comparison, the dielectric constant of pure liquid water in the kHz range is 80 at 20 °C.[10]

D.5 Inductively coupled plasma optical emission spectroscopy (ICP-OES)

Table D.1: ICP-OES results from three samples of anhydrous $Li_2Sn_2S_5$ prepared in separate batches. The last column shows the Li:Sn molar ratio.

$Li_2Sn_2S_5$ ($x = 0$)	wt.% Li	wt.% sn	Li:Sn
Sample 1	3.49	56.82	1.05
Sample 2	3.44	57.71	1.02
Sample 3	3.35	58.43	0.98

D.6 Scanning electron microscopy and single crystal diffraction

Hydrolysis of $Li_2Sn_2S_5$ was ruled out by studying its electron micrographs. The particle morphologies are virtually unchanged by hydration and subsequent dehydration (Figure D.16). However, a few lamellar cracks are visible after dehydration, which is to be expected since other layered hydrates such as Li_3InCl_6 also show similar behavior.[11] The extent of cracking probably becomes slowly more severe over repeated hydration and dehydration cycles, or if particles are hydrated to a higher x value (cf. Figure 3 in ref. [12]). In fact, the covalent bonding in the defective SnS_2 layers of $Li_2Sn_2S_5$ is sufficiently strong that the layers remain intact even after being exfoliated,[12] however, some degree of hydrolysis is observed upon complete immersion in water. The resilience against hydrolysis of lithium tin sulfides is also shown by the compositions Li_2SnS_3 and Li_4SnS_4 (including derivatives), which are stable in humid atmosphere.[13–19] It must be mentioned that a faint H_2S smell was noticed when $Li_2Sn_2S_5$ powder was exposed to ambient air, indicating only minor hydrolysis owing to the enormous sensitivity of the human nose with respect to H_2S.[20] Finally, a TGA measurement performed while switching from argon to pure oxygen observed no change in mass, suggesting that anhydrous $Li_2Sn_2S_5$ is stable towards oxygen as well.

As shown in Chapter 7, the incorporation of water causes an expansion of the unit cell volume. Naturally, the water will coordinate to Li^+ in the structure, meaning that H_2O molecules will predominantly reside in-between the $(Li_\perp,Sn)S_2$-sheets. Figure D.17 shows a schematic representation how the structure would change upon the incorporation of water molecules, related to the observed behavior from XRD, SEM as well as the change in mechanical properties. The proposed coordination chemistry in $Li_2Sn_2S_5 \cdot xH_2O$ between Li^+ and H_2O is in line with findings for the layered mineral vermiculite,[21–23] in which the water would accommodate between sheets of tetrahedrally coordinated Si/Al cations (units of Si_3AlO_{10}) and coordinate to an ion exchanged metal cation M (M = Li, Na, Mg, Ca, Ni, Cu).

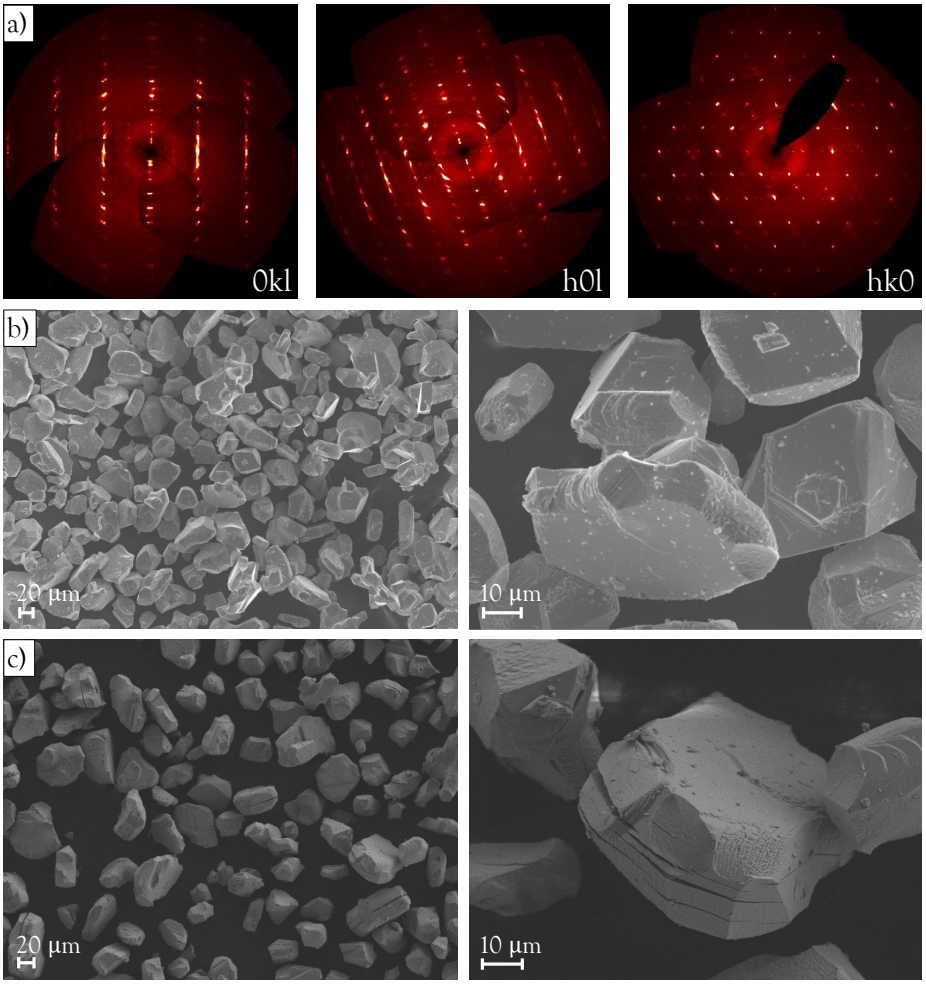

.

Figure D.16: (a) Single crystal diffraction images in reciprocal space of $Li_2Sn_2S_5 \cdot xH_2O$ ($x = 0$) of all three net planes. Scanning electron micrographs of $Li_2Sn_2S_5 \cdot xH_2O$; (b) $x = 0$; (c) $x \approx 2.7$. In the SEM the sample was exposed to high vacuum (> 1 h), meaning the images in (c) depict (partially) dehydrated grains

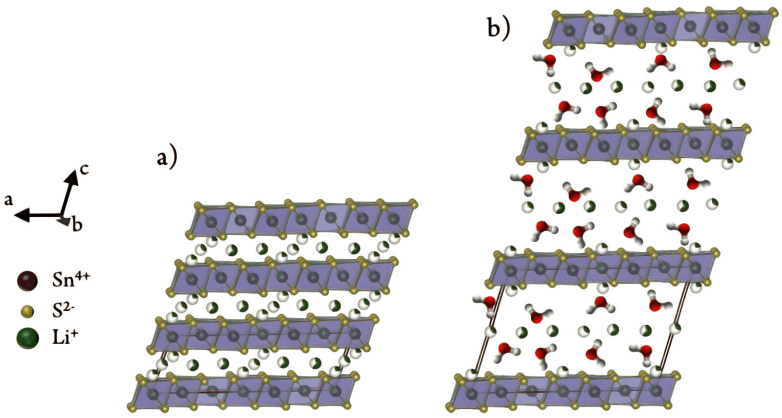

Figure D.17: (a) Crystal structure of anhydrous $Li_2Sn_2S_5$; (b) schematic structure of $Li_2Sn_2S_5 \cdot xH_2O$

D.7 Unpublished data

This section contains unpublished data from the project "Impact of hydration on ion transport in $Li_2Sn_2S_5 \cdot xH_2O$" presented in Chapter 7. The data include a brief discussion of synthetic routes for $Li_2Sn_2S_5$.

D.7.1 Literature synthesis of $Li_2Sn_2S_5$

The synthesis of $Li_2Sn_2S_5$ was first reported by Kuhn *et al.*,[12] and later by Holzmann *et al.*[5] Three different synthesis routes have been propoesed:

$$Li_2S + 2\,Sn + 4\,S \longrightarrow Li_2Sn_2S_5 \tag{D.6}$$

$$2\,Li_2CO_3 + 2\,SnS_2 + S \longrightarrow Li_2Sn_2S_5 + "CO_2" \tag{D.7}$$

$$Li_2S + 2\,SnS_2 + S \longrightarrow Li_2Sn_2S_5 \tag{D.8}$$

In all three reactions, excess sulfur was used to ensure complete oxidation of Sn by creating an oxidizing atmosphere at elevated temperature. Upon cooling, the excess sulfur solidifies at the cold end of the ampoule. For the reaction D.6, Holzmann reported the formation of an amorphous side phase observed by NMR.[5] However, a NMR spectrum showing the amorphous side phase or information on the chemical shift of the side phase peaks was not reported. In the other reactions, a crystalline product is reported to form without any side phases.

D.7.2 Synthesis approaches

The following synthetic routes were investigated after unknown NMR peaks were identified in the "Impact of hydration on ion transport in $Li_2Sn_2S_5 \cdot xH_2O$" project presented in Chapter 7.

$$Li_2S + 2\,SnS_2 \longrightarrow Li_2Sn_2S_5 \qquad SnS_2 \text{ prepared from } Sn + 2\,S \tag{D.9}$$

$$Li_2S + 2\,SnS_2 \longrightarrow Li_2Sn_2S_5 \qquad SnS_2 \text{ from Johnson Matthey} \tag{D.10}$$

$$2\,Li + 2\,Sn + 5\,S \longrightarrow Li_2Sn_2S_5 \tag{D.11}$$

$$Li_2CO_3 + 2\,Sn + 5\,S \longrightarrow Li_2Sn_2S_5 + "CO_2" \tag{D.12}$$

$$Li_2CO_3 + 2\,SnS_2 + S \longrightarrow Li_2Sn_2S_5 + "CO_2" \qquad SnS_2 \text{ prepared from } Sn + 2\,S \tag{D.13}$$

For reactions D.9, D.10, D.12, and D.13, the powdered starting materials were mixed in a mortar until a visually homogeneous mixture was obtained. For D.11, a homogeneous Sn/S was prepared in the same way as for the other reactions and then metallic Li was added to the mixture. The reaction mixtures were transferred to glassy carbon crucibles and sealed under vacuum in fused silica ampoules. The ampoules were heated in a round tube furnace to 700 °C at a heating rate of 120 K/min. The ampoules were

heat treated for 24 h (D.10), 48 h (D.9), or 72 h (D.11, D.12, D.13) and then cooled to room temperature at a rate of 120 K/min (D.9, D.10), or 180 K/min (D.11, D.12, D.13). The heating and cooling rates as well as the synthesis temperature are in accordance with the literature (120 K/min heating, 700 °C dwelling for 72 h, 180 K/min cooling)..[5] Previous synthesis experiments have shown that for the reaction D.9 the dwelling time can be reduced to 24 h, which is also confirmed by NMR and PXRD of the synthesis product of D.9 and D.10. After cooling, the ampoules were opened in an argon-filled glovebox and the reaction product was ground to a fine powder in a mortar. Significant depressurization was observed when the ampoules of D.12 and D.13 were opened, while the other ampoules remained evacuated after heat treatment, indicating gas evolution during heat treatment of approach D.12 andD.13.

Holzmann *et al.* synthesized $Li_2Sn_2S_5$ from commercial Li_2S and SnS_2. While Li_2S was still available from Alfa Aesar, Johnson Matthey ceased production of SnS_2. Therefore, and due to the small amount left from Johnson Matthey, for the project "Impact of hydration on ion transport in $Li_2Sn_2S_5 \cdot xH_2O$", SnS_2 was prepared from the elements and used as a precursor (see above). To compare commercially available (from Johnson Matthey) and self-prepared SnS_2, D.9 and D.10 reactions were performed.

D.7.3 Characterization

Solid-state NMR

Figure D.18 presents ^{6}Li and ^{119}Sn solid-state MAS NMR spectra of the synthesis approaches D.9, D.10, D.11, D.12, and D.13. The solid-state MAS NMR spectra of the five investigated synthesis approaches can be roughly divided into two groups ($1 + 2 + 3$ and $4 + 5$ in Figure D.18).
The reactions D.9 (1), D.10 (2), and D.11 (3) yield similar ^{6}Li and ^{119}Sn spectra, differing only in the amount of Li_2SnS_3 side phase (purple peaks) and unknown phase (turquoise peak). The ^{6}Li and ^{119}Sn peaks assigned to $Li_2Sn_2S_5$ are nearly identical in terms of their chemical shift, peak broadening, and peak integrals.
The reactions D.12 (4) and D.13 (5) give different NMR spectra compared to group 1/2/3. There, the unknown phase (turquoise peak) and the Li_2SnS_3 peaks[5] are missing. However, the ^{6}Li peaks associated with $Li_2Sn_2S_5$[5] are much more asymmetric and are best fitted with a broader, downshifted shoulder peak. The ^{6}Li peak at about 2.4 ppm could be assigned to unreacted Li_2S (2.4 ppm[24]), at least based on the chemical shift. For D.13, at least two peaks at 0.25 ppm and −0.65 ppm are observed in the ^{6}Li spectrum. The peak at 0.25 ppm can be assigned to Li_2O_2 or Li_2CO_3, but the literature on ^{6}Li chemical shifts for Li_2O_2 (−0.1 ppm,[24] 0 ppm,[25] 0.21 ppm,[26] 0.33 ppm[27]) and Li_2CO_3 (0.18 ppm,[25] 0.11 ppm[27]) does not allow a clear assignment. Given the low decomposition temperature of 195 °C,[28] it seems unlikely that Li_2O_2 would remain as a side phase after dwelling at a reaction temperature of 700 °C for 72 h. The ^{6}Li chemical shift of Li_2O (2.8 ppm,[24,25] 2.9 ppm[26,27]) does not match any of the observed peaks. In the ^{119}Sn spectra of the D.12 and D.13 reactions, additional peaks (shown in black and red) are observed that are not assigned to $Li_2Sn_2S_5$. The (black shaded) peak at −759 ppm could be assigned to unreacted SnS_2 (−764 ppm[29]), stacking faults, or highly distorted SnS_6 polyhedra in $Li_2Sn_2S_5$.[5] The (red shaded) peak at about −795 ppm remains undetermined because the literature does not provide a suitable chemical shift for any literature known Sn(IV) compound at −795 ppm.

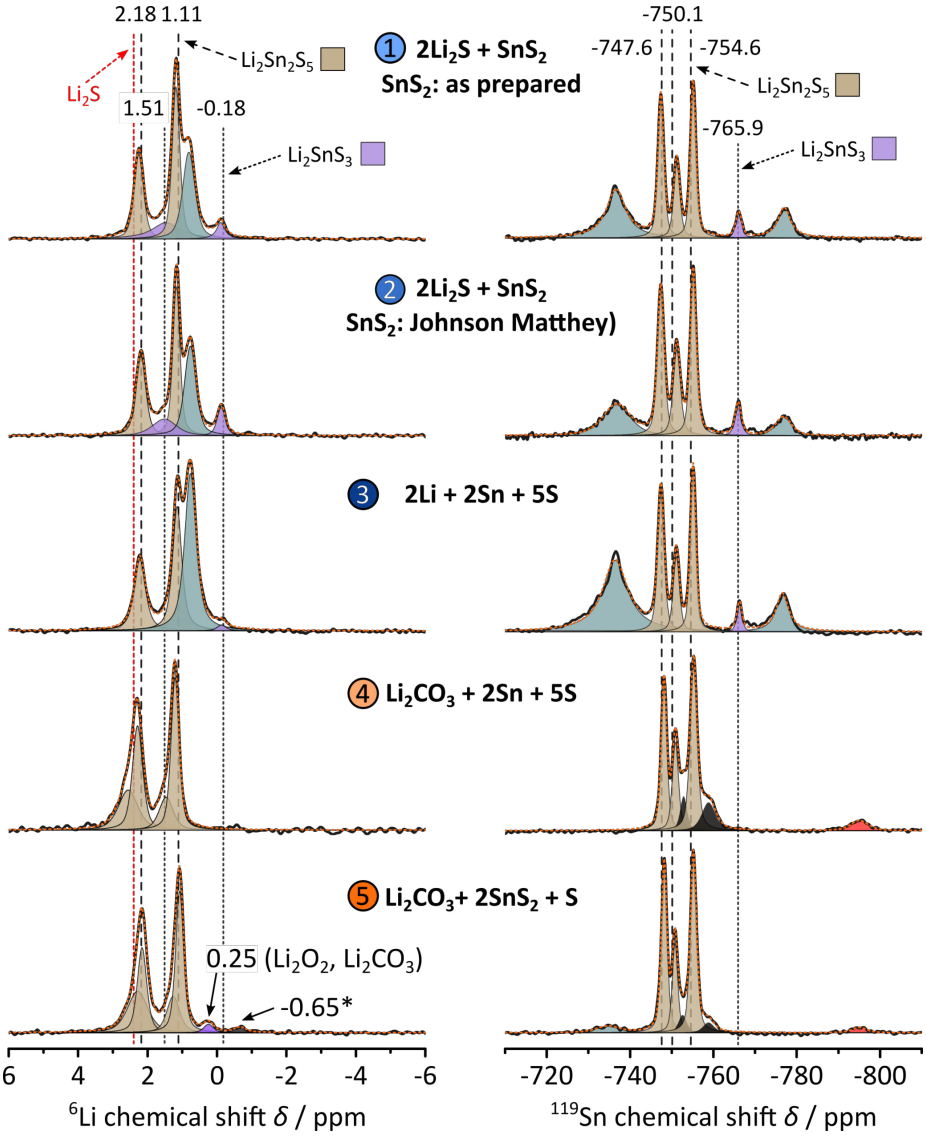

Figure D.18: ^{6}Li and ^{119}Sn MAS-NMR spectra of $Li_2Sn_2S_5$ samples prepared from different starting materials. Reference chemical shifts of Li_2S,[24] Li_2SnS_3,[5] and $Li_2Sn_2S_5$[5] are depicted a dashed and dotted vertical lines. Peaks assigned to known phases are color-coded or directly labeled.

PXRD

Figure D.19 corresponds to the PXRD pattern of D.9, D.10, D.11, D.12, and D.13. As with the solid-state NMR spectra, the PXRD pattern can be divided into two groups based on similar reflection patterns. Reactions with Li_2S or metallic Li as lithium source $(1 + 2 + 3)$ give a different pattern than reactions with Li_2CO_3 $(4 + 5)$. While the first group $(1 + 2 + 3)$ shows a higher number of reflexes compared to the later group $(4 + 5)$, all approaches give more reflexes than from the published[5] monoclinic $Li_2Sn_2S_5$ structure. A qualitative phase analysis by comparing the obtained pattern with the pattern of the used starting materials or possible side phases did not give a clear agreement of the additional peaks. Since $Li_2Sn_2S_5$ is a layered material, stacking faults or turbostratic disorder must be considered for the deviation of the reported and observed PXRD pattern. Superstructure reflections could also contribute to the observed reflections.

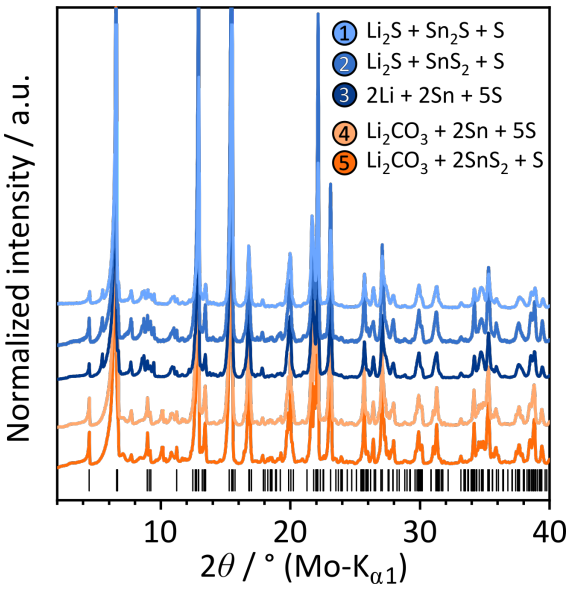

Figure D.19: XRD pattern of $Li_2Sn_2S_5$ samples prepared from different starting materials. Reference Bragg peak positions of $Li_2Sn_2S_5$[5] are depicted a vertical lines.

Elemental analysis

Elemental analysis by inductively coupled plasma optical emission spectroscopy (ICP-OES) was performed for all five reaction mixtures. The results are listed in table D.2. The Li/Sn ratio of $Li_2Sn_2S_5$ is ideally one, but all synthesis methods give higher Li/Sn ratios. Possible explanations for this are: (i) weighting errors of the Li-containing starting material, (ii) sublimation of volatile Sn-containing compounds during heat treatment, or (iii) compositional flexibility of the underlying Li_2S-SnS_2 solid-solution. Since SnS_2 can be sublimed at the reaction temperature of 700 °C and the formation of small amounts of SnS_2 single crystals is almost always observed at the top (colder) end of the ampoule, it stands to reason that Sn escapes from the reaction crucible in the form of a volatile compound. The synthesis approaches tested differ in the Li/Sn ratio. While the synthesis with Li_2S and SnS_2 gives a Li/Sn ratio close to 1, all other tested reactions show much higher Li/Sn ratios, which cannot be explained by the chosen starting materials alone, indicating a compositional flexibility of the aimed product. Moreover, the reactions using Li_2CO_3 as the starting material are contaminated with O- and C-containing compounds, as shown by the elemental analysis. This supports the results of possible, but low contamination of Li_2CO_3 observed in the solid-state NMR spectra of D.12 and D.13.

Table D.2: Results of ICP-OES measurements and O/C elemental analysis for different $Li_2Sn_2S_5$ synthesis approaches.

Reaction equation	Li/Sn ratio	O / wt%	C / wt%
$Li_2S + 2\,SnS_2 \longrightarrow Li_2Sn_2S_5$	1.018	—	—
$2\,Li + 2\,Sn + 5\,S \longrightarrow Li_2Sn_2S_5$	1.103	—	—
$Li_2CO_3 + 2\,Sn + 5\,S \longrightarrow Li_2Sn_2S_5 + "CO_2"$	1.104	$3,45 \pm 0,11$	$0,88 \pm 0,01$
$Li_2CO_3 + 2\,SnS_2 + S \longrightarrow Li_2Sn_2S_5 + "CO_2"$	1.090	$3,30 \pm 0,05$	$0,82 \pm 0,01$

D.7.4 Conclusion

The published synthesis approaches as well as the reflections calculated from the published crystal structure show some discrepancies with the results presented in this section. This could be due to the influence of the experimenter or the different quality of the starting material, ultimately leading to a different product. Although it was not possible to reproduce the literature compound of Holzmann *et al.*, this section has provided insight into the difficult synthesis of $Li_2Sn_2S_5$ by testing different approaches. For future projects dealing with $Li_2Sn_2S_5$, it is of utmost importance to further optimize the synthesis and reduce the amount of side phases and even refine the structure, including stacking faults and turbostratic disorder.[30] The results presented in this section can serve as a starting point for this and help to compare other synthesis approaches with those presented in this work.

References

(1) Price, W. S. *Concepts Magn. Reson.* **1997**, *9*, 299–336.

(2) Kimmerle, F.; Majer, G.; Kaess, U.; Maeland, A. J.; Conradi, M. S.; McDowell, A. F. *J. Alloys Compd.* **1998**, *264*, 63–70.

(3) Bruker Suite, Version 2019.1. Bruker AXS Inc., Madison, WI, USA, 2019.

(4) Maier, J., *Physical Chemistry of Ionic Materials*; John Wiley & Sons: Chichester, 2004, pp 419–462.

(5) Holzmann, T.; Schoop, L. M.; Ali, M. N.; Moudrakovski, I.; Gregori, G.; Maier, J.; Cava, R. J.; Lotsch, B. V. *Energy Environ. Sci* **2016**, *9*, 2578–2585.

(6) L. Sudmeier, J.; E. Anderson, S.; S. Frye, J. *Concepts Magn. Reson.* **1990**, *2*, 197–212.

(7) Kuhn, A.; Narayanan, S.; Spencer, L.; Goward, G.; Thangadurai, V.; Wilkening, M. *Phys. Rev. B* **2011**, *83*, DOI: 10.1103/physrevb.83.094302.

(8) Waugh J.; Fedin, E. *Sov. Physics-Solid State* **1963**, *4*, 1633–1636.

(9) Wen, C. J.; Boukamp, B. A.; Huggins, R. A.; Weppner, W. *J. Electrochem. Soc.* **1979**, *126*, 2258–2266.

(10) Francis Weston Sears Mark Waldo Zemansky, H. D. Y., *University physics*, 6th ed.; Reading, Mass. : Addison-Wesley Pub. Co.: 1982.

(11) Sacci, R. L.; Bennett, T. H.; Drews, A. R.; Anandan, V.; Kirkham, M. J.; Daemen, L. L.; Nanda, J. *J. Mater. Chem. A* **2021**, *9*, 990–996.

(12) Kuhn, A.; Holzmann, T.; Nuss, J.; Lotsch, B. V. *J. Mater. Chem. A* **2014**, *2*, 6100–6106.

(13) Kaib, T.; Haddadpour, S.; Kapitein, M.; Bron, P.; Schröder, C.; Eckert, H.; Roling, B.; Dehnen, S. *Chem. Mater.* **2012**, *24*, 2211–2219.

(14) MacNeil, J. H.; Massi, D. M.; Zhang, J.-H.; Rosmus, K. A.; Brunetta, C. D.; Gentile, T. A.; Aitken, J. A. *J. Alloys Compd.* **2014**, *586*, 736–744.

(15) Sahu, G.; Lin, Z.; Li, J.; Liu, Z.; Dudney, N.; Liang, C. *Energy Environ. Sci.* **2014**, *7*, 1053–1058.

(16) Brant, J. A.; Massi, D. M.; Holzwarth, N. A. W.; Macneil, J. H.; Douvalis, A. P.; Bakas, T.; Martin, S. W.; Gross, M. D.; Aitken, J. A. *Chem. Mater.* **2015**, *27*, 189–196.

(17) Park, K. H.; Oh, D. Y.; Choi, Y. E.; Nam, Y. J.; Han, L.; Kim, J.-Y.; Xin, H.; Lin, F.; Oh, S. M.; Jung, Y. S. *Adv. Mater* **2016**, *28*, 1874–1883.

(18) Choi, Y. E.; Park, K. H.; Kim, D. H.; Oh, D. Y.; Kwak, H. R.; Lee, Y.-G.; Jung, Y. S. *ChemSusChem* **2017**, *10*, 2605–2611.

(19) Kwak, H.; Park, K. H.; Han, D.; Nam, K.-W.; Kim, H.; Jung, Y. S. *J. Power Sources* **2020**, *446*, 227338.

(20) Leonardos, G.; Kendall, D.; Barnard, N. *J. Air Waste Manag. Assoc.* **1969**, *19*, 91–95.

(21) Whittingham, M. S. *Solid State Ion.* **1987**, *25*, 295–300.

(22) Stanley Whittingham, M. *Solid State Ion.* **1989**, *32-33*, 344–349.

(23) Whittingham, M. S. *Solid State Ion.* **2004**, *168*, 255–263.

(24) Wan, C.; Xu, S.; Hu, M. Y.; Cao, R.; Qian, J.; Qin, Z.; Liu, J.; Mueller, K. T.; Zhang, J.-G.; Hu, J. Z. *ACS Appl. Mater. Interfaces* **2017**, *9*, 14741–14748.

(25) Xiao, J.; Hu, J.; Wang, D.; Hu, D.; Xu, W.; Graff, G. L.; Nie, Z.; Liu, J.; Zhang, J.-G. *J. Power Sources* **2011**, *196*, 5674–5678.

(26) Zhu, Z.; Kushima, A.; Yin, Z.; Qi, L.; Amine, K.; Lu, J.; Li, J. *Nat. Energy* **2016**, *1*, 16111.

(27) Huff, L. A.; Rapp, J. L.; Zhu, L.; Gewirth, A. A. *J. Power Sources* **2013**, *235*, 87–94.

(28) Wiberg, N., *Lehrbuch der Anorganischen Chemie*; De Gruyter: 2008.

(29) Pietrass, T.; Taulelle, F. *Magn. Reson. Chem.* **1997**, *35*, 363–366.

(30) Hatz, A.-K.; Moudrakovski, I.; Bette, S.; Terban, M. W.; Etter, M.; Joos, M.; Vargas-Barbosa, N. M.; Dinnebier, R. E.; Lotsch, B. V. *Chem. Mater.* **2021**, *33*, 7337–7349.

APPENDIX E

Supporting Information for "Effect of particle size and pressure on the transport properties of the fast in conductor t-Li_7SiPS_8"

Appendix E contains supporting information for Chapter 8.

Contents of Appendix E

E.1 Crystallite size of pristine Li_7SiPS_8

The primary particle size, i.e. the crystallite size, can be estimated from the peak broadening observed in X-ray diffraction experiments. Peak broadening is affected by the domain size and instrumental broadening (size broadening), as well as broadening by lattice strain (defects). We measured powder X-ray diffraction (see Figure E.1) to compare the Bragg peak broadening of the <50 µm and >50 µm PSD fractions. The peaks of the

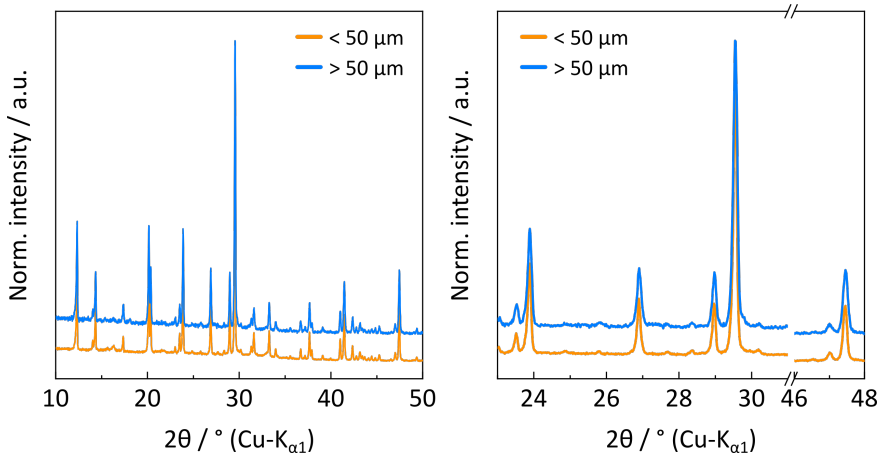

Figure E.1: (a) XRD pattern of t-Li_7SiPS_8 for the <50 µm and >50 µm fractions measured in Debye-Scherrer (capillary) geometry. (b) Zoomed-in XRD pattern.

<50 µm sample are slightly broader compared to the >50 µm sample, which is reflected in the FWHM and integral breadth of the five selected single peaks shown in Figure E.1b. According to the Scherrer equation, a lower FMHM or integral breadth translates to a larger crystallite size. However, one needs to account for instrumental broadening, which for the used lab diffractometer (STOE StadiP) is almost on the same order as the FWHM or integral breadth of the t-Li_7SiPS_8 sample. As a reference for instrumental broadening, a Si standard (NIST 640d) was measured using the same instrument parameters. Although, a precise domain size determination by XRD is not feasible, the slightly larger FWHM of the <50 µm sample indicates slightly smaller domain sizes compared to the >50 µm sample.

E.2 Process of SEM image analysis using ImageJ

This section describes the workflow for analyzing gray-scale images acquired using scanning electron microscopy (SEM). SEM images can contain different information depending on the type of detector used to generate the image. While secondary electron (SE) detectors provide topographic information, back-scattered electron (BSE) detectors resolve compositional details by displaying heavier atoms brighter than lighter elements. Since the subject of this study, the solid electrolyte *t*-Li_7SiPS_8, is homogeneous in composition, SE images were used to analyze particle morphology and size distribution. However, for composites such as catholytes—a mixture of solid electrolyte, cathode active material, binder, and conductive additive—BSE images can help distinguish between the individual components of the mixture. Combining the analysis of SE and BSE images can improve segmentation.

The flowchart of the analysis of SEM images to determine the particle size distribution and morphology parameters is shown in Figure E.2. In the following, important parts of the process and possible sources of error are described in more detail. These mainly concern the decisions that the user must make and depend on the user's experience. Since SEM images consist of individual pixels, each with a gray-scale value, the intensity of the pixel, such as brightness, can be used to determine whether a pixel belongs to the foreground or the background. For this method, the background should have a homogeneous gray value without artifacts, such as individual "high spots" (bright pixels/noise) or "shadows". Overexposure of the background can be corrected by applying a filter, such as a Gaussian blur, to the image (see Figure E.3b). While this process smooths the image and reduces noise, it has the disadvantage of losing detail and blurring the boundaries between the background and particles. Therefore, the user should be careful in this processing step and try different smoothing algorithms to find the best one for the task. After preparing the image, a mask must be created to separate the background from the region of interest (ROI) by choosing an appropriate threshold (see Figure E.3c). Here, only the ROI is analyzed while the background is ignored. For the analysis of particles, they must be separated. This can be done either by physical separation before image acquisition or by image processing. Although we finely dispersed *t*-Li_7SiPS_8 powder on the SEM sample holder, we visually observed larger agglomerates of touching particles. To digitally separate the agglomerates, the distance-transformed watershed algorithm was used as part of the MorphoLibJ[1] plugin. This algorithm is a combination of Euclidean distance map and watershed segmentation that together results in good segmentation without oversegmentation of particles. The segmented particles are separated by either a 4-fold (pixels sharing an edge) or 8-fold (pixels sharing an edge or vertex) connected line. The type of connection can affect the roundness of objects, especially for smaller objects. It can also be a source of error for later analysis, as some algorithms interpret diagonally (8-fold connectivity) separated particles as not separated. Once the agglomerates are resolved and the remaining holes are filled, the ROI can be analyzed (see Figure E.3d). Several particle counting and particle morphology algorithms are available either as a built-in function or as part of a ImageJ plugin. For this study, the plugin *morphology* by G. Landini[2] and the built-in particle analysis tool of ImageJ were used. After analyzing the ROI, the overlaid gray-scale mask that distinguishes individual particles can be converted to a randomly colored mask (see Figure E.3e), which can be

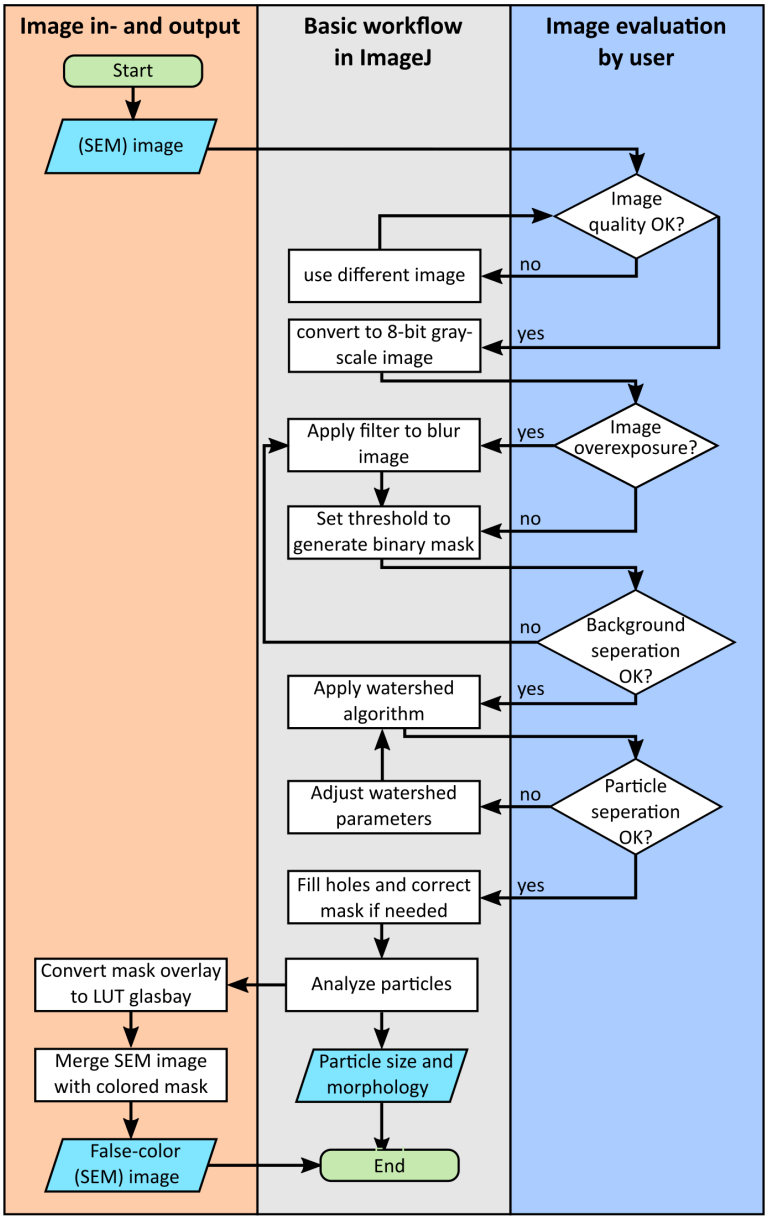

Figure E.2: Flowchart of particle size and morphology analysis used in this study. Processes are displayed as rectangular boxes, decisions as diamond boxes.

used to create false-color SEM images (see Figure E.3f), as shown in this paper.

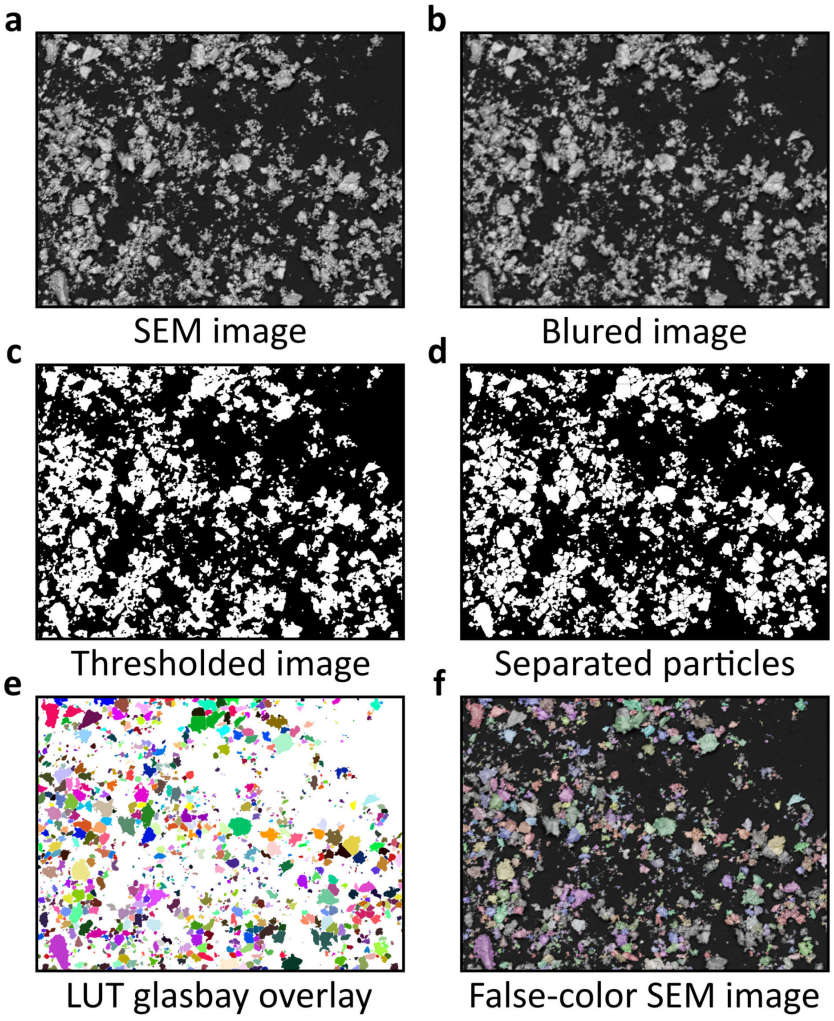

Figure E.3: (a) Original SEM image, (b) after applying Gaussian blur filter, (c) binary mask after thresholding. Black and white parts denote the background and ROI. (d) Separated particles after applying distance transform watershed algorithm, (e) Colored mask showing the individual particles, and (f) False-color SEM image by merging (a) and (e).

E.3 Particle size distribution of t-Li_7SiPS_8

Figure E.4a-c and E.5a-e show SEM images with a false-color overlay used to analyze the particle sizes and shapes of the two screened size fractions. The PSD, as shown in this work, is truncated at smaller particle sizes, as a consequence of the chosen image magnification. This effect is more pronounced for the >50 µm sample, because a lower SEM image magnification was needed for this sample in order to have good count statistics while still resolving small particles compared to the respective largest ones.

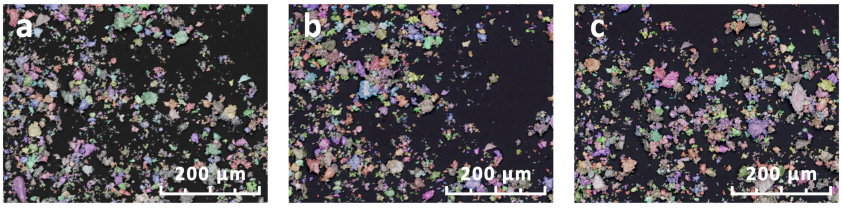

Figure E.4: (a)–(c) False-color SEM images of < 50 µm t-Li_7SiPS_8 particles. A total number of 3475 particles were measured.

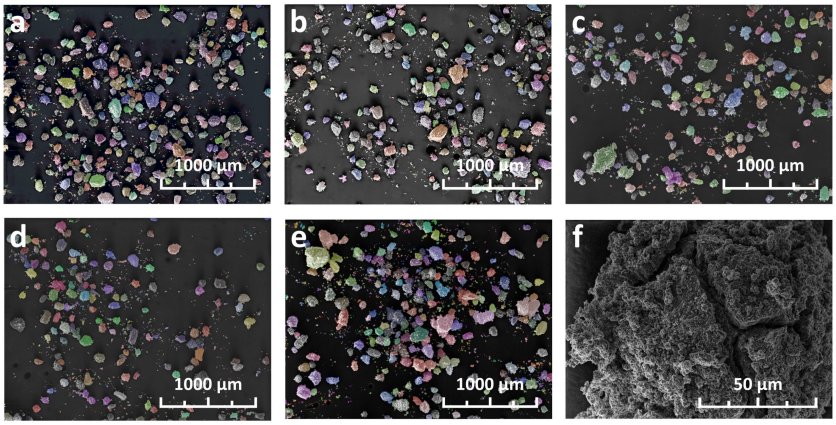

Figure E.5: (a)–(e) False-color SEM images of > 50 µm t-Li_7SiPS_8 particles. (f) SEM image of a t-Li_7SiPS_8 particle showing the rough surface morphology observed on large particles. A total number of 5118 particles were measured.

In addition to the number-based particle size distribution measured by SEM image analysis, we used sedimentation analysis in a centrifugal field (LUMiSizer, LUM GmbH) to measure the volume-based PSD of t-Li_7SiPS_8. For this purpose, some powder was dispersed in a solution of p-xylene and 4.5 wt.% HNBR, the latter being added to adjust the viscosity. During centrifuging with increasing speed from 300 to 4000 rpm, the samples were illuminated with an 870 nm laser beam. The PSD could be calculated from the measured sedimentation velocity distribution based on known material properties such as

viscosity and density. The PSD from sedimentation analysis (LumiSizer) and SEM image analysis is shown in Figure E.6.

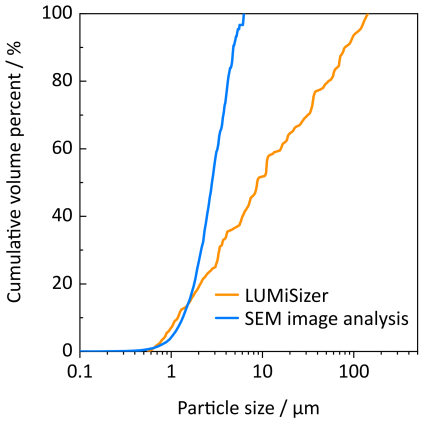

Figure E.6: Cumulative volume percent as a function of particle size for the <50 µm sieving fraction of *t*-Li_7SiPS_8. The distribution curve for the SEM image analysis is calculated from the number-based distribution of Feret diameters.

The particle size parameters D_{10}, D_{50}, and D_{90}, given in table E.1 and E.2, describe the particle size (Feret diameter) at which 10%, 50%, and 90% of the volume- and number-based size distribution are smaller than the given value.

Table E.1: Volume based size distribution parameters for *t*-Li_7SiPS_8 particle size fractions obtained by sieving. The volume based distribution was calculated from the Feret diameter.

Parameter	<50 µm	>50 µm
D_{10} / µm	17	89
D_{50} / µm	35	138
D_{90} / µm	60	240

Table E.2: Number based size distribution parameters for *t*-Li_7SiPS_8 particle size fractions obtained by sieving.

Parameter	<50 µm	>50 µm
D_{10} / µm	3	9
D_{50} / µm	11	17
D_{90} / µm	27	98

Morphology of t-Li_7SiPS_8 particles

Parameters describing the (2D) shape of a particle must meet certain criteria.[3] Based on these criteria, many shape descriptors have been proposed and used by researchers in different research areas. In this study, we have used some of the most popular shape descriptors, namely convexity, sphericity, circularity, and solidity. The dimensional and derived dimensionless parameters extracted from SEM image analysis using ImageJ are shown in Table E.3 and Table E.4, respectively.

Figure E.7a shows the particle shape parameters convexity, solidity, and sphericity in a 2D scatter plot for the <50 µm particle size fraction. Most particles have quite high values of convexity and solidity, but sphericity is quite low. While sphericity correlates negatively with bumps (small inscribed circle) and positively with spikes (large circumscribed circle), solidity and convexity are more robust to star-like patterns. The 2D representations of four different particles shown in Figure E.7 help to understand the concepts of convexity, solidity, and sphericity. Convexity is sensitive to the outline because it is the ratio between the perimeter of the shape and the perimeter of the smallest enclosing polygon (convex hull). It is 1 for shapes such as rectangles, spheres, or triangles, while it is close to 0 for stars. Solidity, on the other hand, is sensitive to area, as it is the ratio between the particle area and the area of the convex hull. A comparison of particles 1 and 2 from Figure E.7a shows that the two dents in particle 1 caused by the elongated part result in lower solidity, while the convexity in 1 and 2 is almost identical. When the outline of the particle is more irregular and thus the circumference is longer, as in particle 3, the convexity is lower compared to particles with regular outline like 1. In this case, the solidity is not strongly affected by the irregularity in the particle outline. Particle 2 has a higher sphericity than particles 1, 3 and 4. Since sphericity describes the ratio between the radii of the inscribed and circumscribed circles, dents, grooves, or peaks directly affect these circles and thus reduces sphericity. Therefore, sphericity is a good measure of how close a 2D object is to a circle. From Figure E.7a, it can be seen that t-Li_7SiPS_8 particles with higher convexity and solidity also have higher sphericity values, with the latter correlating more strongly with solidity than with convexity.

The corresponding figure for the >50 µm particle size fraction is shown in Figure E.8. It is evident, that the larger PSD sample also shows a broader distribution of convexity and solidity values, with values as low as 0.6 for convexity and 0.5 for solidity. However, the majority of particles have convexity and solidity values close to unity. The sphericity only shows a clear correlation with solidity but not with convexity. This trend was not observed as pronounced for the smaller PSD sample. Additionally, more particles have low sphericity as in the smaller PSD sample.

Since particle shape analysis is based on 2D representations consisting of pixels, the size of the particles, expressed here as the Feret diameter, can affect the calculation of dimensional parameters such as area and perimeter. Generally, smaller particles are more prone to artifacts because they appear “blockier” than they are. Higher magnification can mitigate this problem, but at the cost of increasing surface roughness artifacts and generally lower count statistics (see section above). Here, Feret diameter correlates negatively with convexity, a parameter sensitive to circumference (see Figure E.7b). Smaller particles have lower resolution of their respective roughness and therefore tend to have higher convexity. However, this artifact is less pronounced for solidity. Nevertheless,

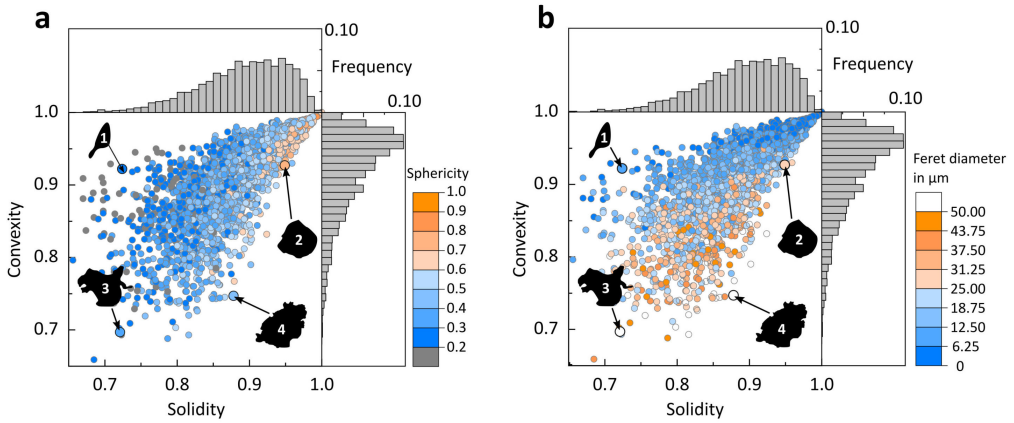

Figure E.7: 2D scatterplot of particle shape, convexity and solidity, with respective marginal histograms to show the data marker density. The associated sphericity (a) and Feret diameter (b) is represented by a color code as the marker infill color. 2D-representations of four particles are depicted as filled outlines. The data was measured on the <50 µm sieving fraction.

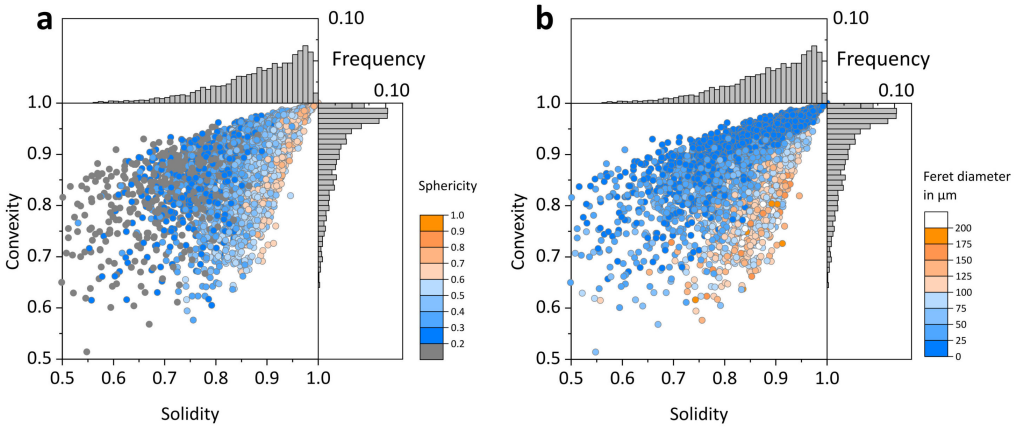

Figure E.8: 2D scatterplot of particle shape, convexity and solidity, with respective marginal histograms to show the data marker density. The associated sphericity (a) and Feret diameter (b) is represented by a color code as the marker infill color. 2D-representations of four particles are depicted as filled outlines. The data was measured on the >50 µm sieving fraction.

when analyzing particle size and shape, the magnification and resolution of the image are of great importance to the quality of the analysis. Therefore, the user should be aware of this effect and check the robustness of the morphology parameters to resolution and magnification.

Table E.3: Dimensional parameters from SEM image analysis using the Morphology[2] plugin *particles8* for ImageJ.

Parameter	Symbol	Unit	Short description
Area	A	px^2	Object's area defined by outline
Perimeter	p	px	Calculated from the boundary pixel's centers
Feret	D_{Feret}	px	Maximal distance of two parallel tangents (caliper diameter)
Breadth	D_{Breadth}	px	Largest diameter perpendicular to Feret
Circumscribed circle	R_{max}	px	radius of the circumscribing circle
Inscribed circle	R_{min}	px	radius of the inscribing circle
Convex hull	p_{hull}	px	Perimeter calculated from the convex hull pixel's centers
Convex area	A_{hull}	px^2	Area defined by convex hull outline

Table E.4: Dimensionless parameters[4] from SEM image analysis using the Morphology[2] plugin *particles8* for ImageJ.

Parameter	Formula	Comment
Aspect Ratio (AR)	$\frac{D_{\text{Feret}}}{D_{\text{Breadth}}}$	A simple measure of elongation. Not varying with surface irregularities.
Circularity	$\frac{4\pi A}{p^2}$	Synonymous to *form factor*. Varies with surface irregularities.
Solidity	$\frac{A}{A_{\text{hull}}}$	Measure of how dense an object is. Objects with holes or a highly irregular boundary appear to have a low solidity.
Convexity	$\frac{p_{\text{hull}}}{p}$	Relative amount that an object differs from a concave object. Measure of how irregular an object is.
Sphericity	$\frac{R_{\text{min}}}{R_{\text{max}}}$	Measure of the degree to which an object approaches a circle. Equal to unity for a circle and close to zero for extreme star-like shapes.
Compactness	$\frac{\sqrt{\frac{4}{\pi}A}}{D_{\text{Feret}}}$	Ratio of an object's area to the area of a circle of the same perimeter. Elliptical objects or those with irregular boundaries have a low compactness.

E.4 Pellet densification of t-Li_7SiPS_8

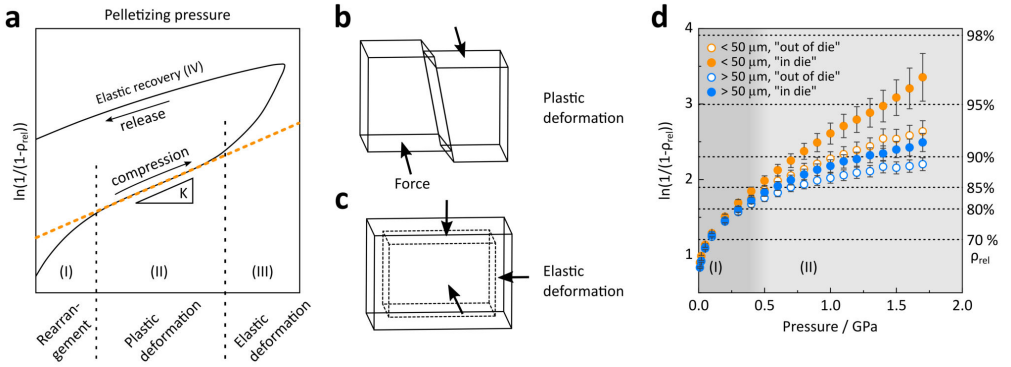

Figure E.9: (a) Schematic Heckel plot with the 4 distinctive regimes dominated by particle rearrangement (I), particle plastic deformation (II), compact elastic deformation (III), and compact elastic recovery (IV). The orange, dotted line represents the linear regime of the Heckel plot. (b) Scheme of irreversible plastic deformation by shifting along a (lattice) plane. (c) Scheme of reversible elastic deformation by compressing the unit cell. (d) Heckel plots of $< 50\,\mu m$ (orange) and $> 50\,\mu m$ (blue) t-Li_7SiPS_8 samples. Hollow and filled data markers represent "out of die" and "in die" data, respectively. "Out of die" data was extracted from stack (constant) pressure experiments at 10 MPa, "in die" data was extracted at pelletizing (variable) pressure.

If the compaction of a granular powder exhibits rearrangement and/or fragmentation of the particles, a deviation from the linear Heckel plot can be observed, as indicated in region (I) in Figure E.9a. The models of Cooper and Eaton,[5] and Wünsch[6] *et al.* attempt to provide a two-term model, including the initial (low pressure) regime of particle rearrangement/fragmentation, as well as the solid compressibility of the compact.

Comment on pellet recovery

Upon pressure release, the cracks, observed in E.10, may be introduced, which could increase the tortuosity for ion conduction. In the process of pellet recovery, we have experienced that the mechanical stability of the sample is sensitive to the previously applied pressure. Since the die limits the expansion of the pellet in the axial direction, it is likely that some stress builds up on the walls of the die as the pressure is released. To press the pellet out of the mold, the friction between the die wall and the pellet must be overcome. The stress on the walls can increase the friction, possibly leading to mechanical failure of the pellet when it is released from the die. The abrupt movement of the press bars resulted in the breaking of the pellet edges at best, but most often the pellet broke into many pieces. Taking the pellet out more slowly helped solve this problem in some cases. Notably, we observed that for some solid ion conductors (other than thiophosphates) a lower compaction pressure yielded a more stable pellet, while

higher pressures led to mechanical failure of the pellet during recovery from the die. This might be caused by a large elastic recovery of some materials building up internal stress.

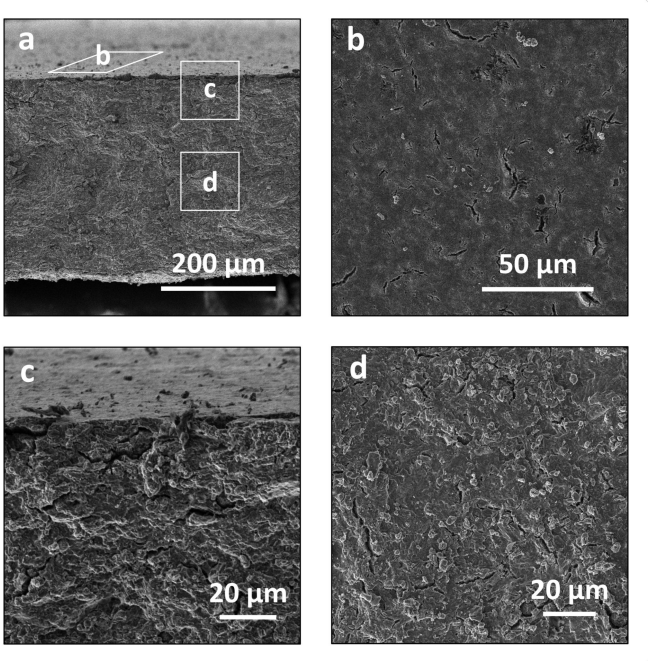

Figure E.10: SEM images of *t*-Li_7SiPS_8. (a) Broken cross-section of the pellet, (b) surface of the pellet, (c) broken cross-section close to the pellet's surface and (d) in the middle of the pellet.

Nyquist plots

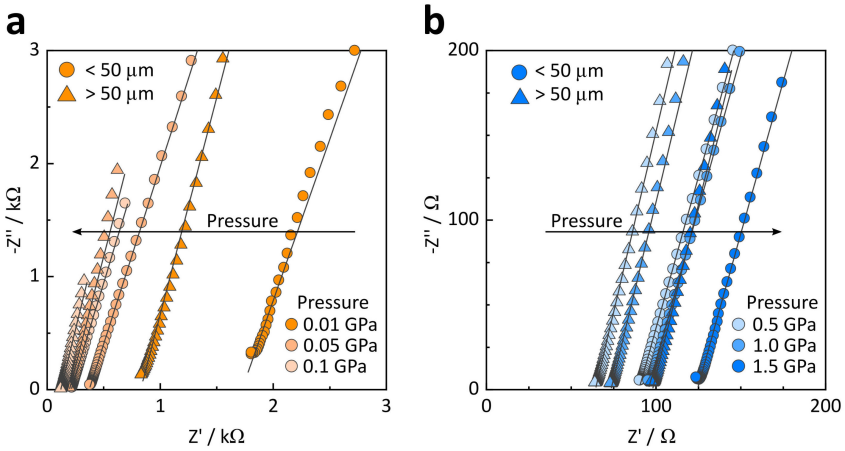

Figure E.11: Nyquist plots of t-Li_7SiPS_8 at low (a) and high (b) pelleting pressures. The circle and triangle data markers represent the < 50 and > 50 µm particle size fractions, while the fill color represents the pelleting pressure.

Derivation of activation volume

Similar to the effect of temperature on diffusion, which is a temperature-activated process following an Arrhenius law, thermodynamic laws allow the definition of an activation volume ΔV. Here, we briefly review the thermodynamics of ion diffusion and the definition of the activation volume. The ionic conductivity of solids can be described as a thermally activated process following an Arrhenius behavior:

$$\sigma T = \sigma_0 e^{\frac{-\Delta G}{k_B T}} \tag{E.1}$$

During diffusion, mobile ions must overcome the Gibbs free energy ΔG to jump from one lattice site to an adjacent one. Solving equation (E.1) for ΔG and assuming a closed system with the number of particles N of chemical potential i ($N_i = \text{const.}$) at a constant temperature ($T = \text{const.}$), we obtain:

$$\Delta G = k_B T \left(\ln(\sigma_0)_{T,N_i} - \ln(\sigma)_{T,N_i} \right). \tag{E.2}$$

Equation (E.1) includes the pre-exponential factor σ_0, that is defined as:

$$\sigma_0 = \frac{gnq^2r^2\nu_0}{k_B}, \tag{E.3}$$

with g, n, q, r, and ν_0 being a geometrical factor, the number of charge carriers per unit volume, the charge (*e.g.* for Li^+ $q = 1$), the "jump" distance between two neighboring

sites, and the attempt frequency, respectively.
Assuming z, n, and q to not change with pressure, equation (E.2) can be written as:

$$\Delta G = k_\mathrm{B} T \left(\ln(r)_{T,N_i} + \ln(\nu_0)_{T,N_i} - \ln(\sigma)_{T,N_i} \right) \tag{E.4}$$

It follows, that the Gibbs free energy ΔG depends on the jump distance, the attempt frequency and the conductivity. The partial derivative of ΔG with pressure is defined as the activation volume ΔV:

$$\left(\frac{\partial \Delta G}{\partial p} \right)_{T,N_i} = \Delta V \tag{E.5}$$

Combining equation (E.2) and (E.5) gives:

$$\Delta V = k_\mathrm{B} T \left(\left(\frac{\partial \ln(\sigma_0)}{\partial p} \right)_{T,N_i} - \left(\frac{\partial \ln(\sigma)}{\partial p} \right)_{T,N_i} \right) \tag{E.6}$$

While the variation of conductivity with pressure is readily available through experimentation, it is much more difficult to obtain information on the pressure variance of the jump distance and attempt frequency that contribute to the pre-exponential factor. Some approximations and simplifications can be found in the literature. In a cubic crystal system, for example, this correction term can be estimated by the compressibility β and the Grüneisen constant γ:[7–10]

$$\Delta V = k_\mathrm{B} T \left(\beta \left(\gamma - \frac{2}{3} \right) - \left(\frac{\partial \ln(\sigma)}{\partial p} \right)_{T,N_i} \right) \tag{E.7}$$

^{31}P-NMR of pristine and pressed t-Li_7SiPS_8

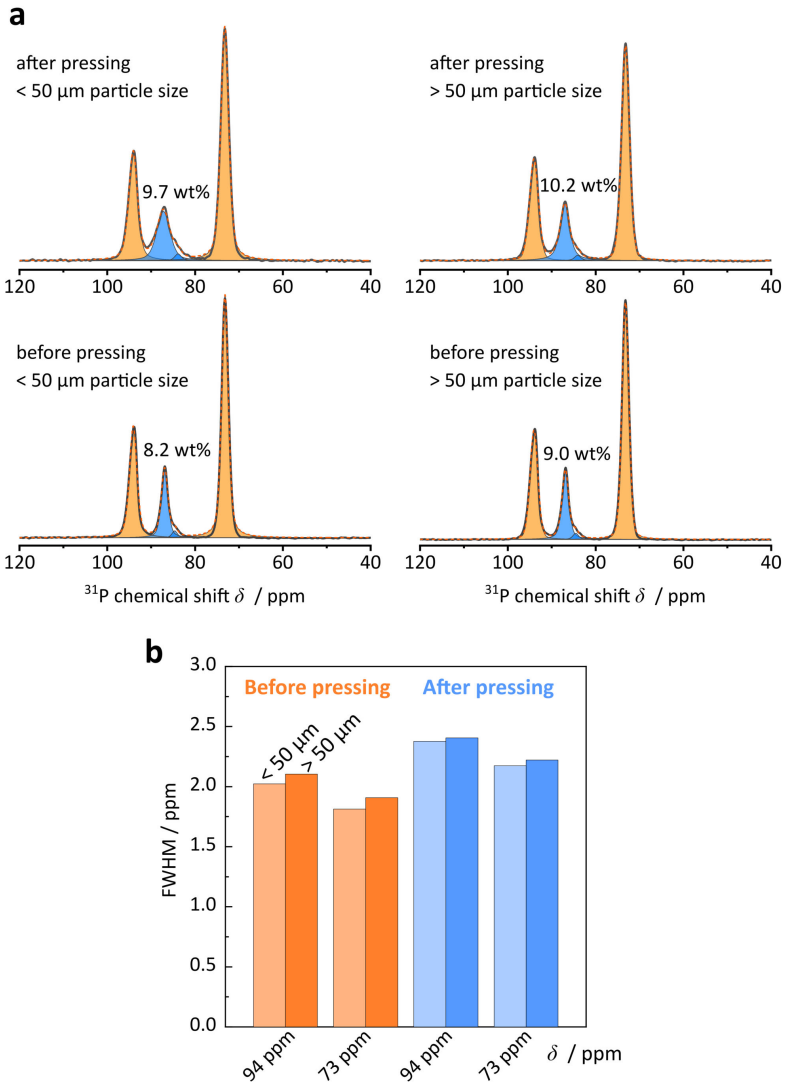

Figure E.12: (a) ^{31}P MAS NMR spectra of pristine and pressed t-Li_7SiPS_8 of different particle size fractions. Peaks attributed to crystalline t-Li_7SiPS_8 and to the amorphous side phase are depicted in orange and blue, respectively. The fit is displayed as an orange, dashed line. The measured data is depicted as a dark gray line. (b) Full width half maximum (FWHM) of ^{31}P MAS NMR t-Li_7SiPS_8 peaks.

Discrete element method simulation

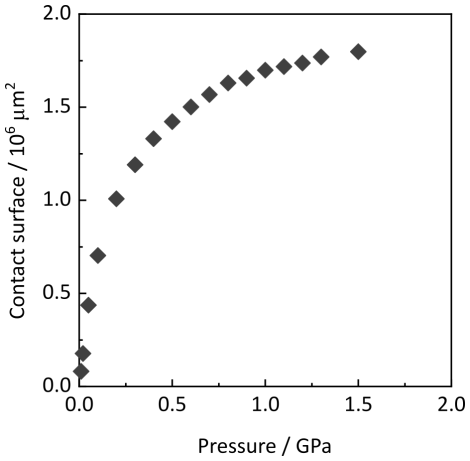

Figure E.13: Contact surface as a function of the pelletizing pressure.

In the DEM simulation the compaction of perfect spheres attributed with friction effects, form the pellet. The solid electrolyte powder, however, consists of particles that are far from spherical. They rather have various morphological features, such as holes, jags, dips, and bulges, which contribute to surface roughness (see for example Figure E.7). This can increase friction by causing the particles to coalesce into larger agglomerates that require higher stress to break up. Additionally, surface roughness can introduce current constriction effects[11–13] at the inter-particle contacts, especially, when the particles are not allowed to connect at low pressure. Fleig has shown that a larger number of inter-particle contact spots give rise to a smaller current constriction effect and thus a smaller grain-boundary resistance.[11] At a higher compression stage, the number of contact surface increases, as shown in Figure E.13.

E.5 Methods

E.5.1 Synthesis and sample preparation

Tetragonal Li_7SiPS_8 (t-Li_7SiPS_8) was prepared from a stoichiometric mixture of Li_2S (Sigma Aldirch, 99.98%), red phosphorus (Merck, 99%) and sulfur (sublimed). An excess of 5 wt% sulfur was added to the mixture to ensure an oxidizing reaction atmosphere during the synthesis. The starting mixture (10 g) was ball-milled using a Retsch PM 200 ball mill with 50 mL ZrO_2 jar and 10 ZrO_2 balls of 10 mm diameter. The ball mill was programmed to mill for 24 h at 500 rpm, with 5 min milling and 1 min cooling down pause. The homogenized mixture was placed in glassy carbon crucibles and subsequently sealed in quartz glass ampules under vacuum. The ampules were transferred to a tube furnace and heated to 525 °C at a rate of 50 K min^{-1}, annealed for 100 h, and naturally cooled down by switching of the furnace. The crystalline powder is pale-yellow colored and sensitive to moisture. The samples and cells were thus prepared and stored in an Argon filled glovebox ($(p(O_2)/p < 5$ ppm, $p(H_2O)/p < 5$ ppm). Pristine t-Li_7SiPS_8 powder was sieved using a 50 µm mesh size sieve to yield particle fraction, one with particle sized smaller than 50 µm and one with particles larger than 50 µm. The sieve was placed on a vortex mixer to facilitate the powder sieving by vibration. This was done until visually no more powder accumulated at the bottom of the sieving pan. The powder that passed the 50 µm mesh size sieve is denoted the < 50 µm fraction, while powder that remained in the sieve after the sieving process is denoted the > 50 µm fraction. Although the > 50 µm fraction has a greater number of particles below 50 µm, the volume of the sample is dominated by particles larger than 50 µm.

E.5.2 Scanning electron microscopy

Scanning electron microscopy images were taken with a VEGA TS 5130 MM microscope (equipped with an *Oxford* X-MaxN 20 (SDD) detector) or a TESCAN VEGA4 LMU microscope. The samples were prepared by scattering little amounts of t-Li_7SiPS_8 powder on a sticky carbon tape. Images were taken of areas at which individual particles were evenly spread out to ensure better image analysis. The particles were analyzed using the software *ImageJ*[14] and the plugins *MorphoLibJ*[1] and *Morphology*[2] by G. Landini. A more detailed description of the particle segmentation and size analysis can be found in the electronic supporting information (see above).

E.5.3 Gas pycnometer

The true density of t-Li_7SiPS_8 was measured with a *micromeritics* AccuPyc II 1340 gas pycnometer using Helium gas. A weighed amount of t-Li_7SiPS_8 powder was placed in an aluminum crucible and subsequently transferred to the gas pycnometer. The analysis chamber was purged 10 times with Helium prior to the measurement. The accessible analysis chamber volume was measured 10 times (10 s of equilibration time) per sample and the mean density of the sample was calculated from the volume displacement and the sample weight. An average of four samples was used as the reference density for the calculation of relative pellet density. The density of t-Li_7SiPS_8 powder was measured to be 2.008(6) g cm^{-3}, while the reported crystallographic density is 1.923(9) g cm^{-3}.[15]

The experimentally determined density is by 4.4 % larger that the reported one. This difference is small and might originate from measurement and weighting uncertainties.

E.5.4 Nuclear magnetic resonance

^{31}P solid-state NMR measurements were performed on a Bruker Avance-III wide bore spectrometer in a magnetic field of 9.4 T. The powder sample was loaded into a pyrex MAS insert (Wilmad Glass, product # DWGSK2576-1), flame sealed and subsequently transferred into a 4 mm ZrO_2 rotor. The ^{31}P spectra (Larmor frequency 161.9 MHz) were recorded using a Bruker BL4 MAS probe at a spinning speed of 10 kHz. A simple Bloch Decay excitation scheme with a total of 512–4096 accumulations in each experiment was used. The relaxation delay was chosen long enough to allow for complete relaxation of the magnetization and to ensure a quantitative measurement. The spectra are referenced against the external signal of 85 %H_3PO_4[16] and were fitted using the Dmfit[17] software.

E.5.5 Variable pressure measurements

For the variable pressure measurements, CompreCell cells (RHD INSTRUMENTS) were used. The cells are comprised of an electrically insulating Al_2O_3 cylinder in a stainless steel liner. Hard metal pistons of 6 mm diameter apply the uniaxial force onto the sample, while also serving as the electrodes. The cell was loaded with 50 mg of sieved *t*-Li_7SiPS_8 powder. A double O-ring design ensures an air-tight seal for inert atmosphere conditions during the experiments. The cell was inserted into a CompreDrive press (RHD INSTRUMENTS) and connected to a potentiostat in a two-electrode configuration. The CompreDrive system allows for constantly monitoring the applied force and actively controlling the pressure. The information about the motor position can be used to calculate the displacement of the hard metal piston at each pressure step and thus the pellet thickness. A reference run without sample was performed prior to the compaction experiment to later subtract the influence of setup deformation during the high pressure experiment. The temperature was controlled using a Julabo Presto A40 thermostat connected to heating/cooling mantle housing the cell.

E.5.6 Electrochemical impedance measurements

Prior to measuring the electrochemical impedance of *t*-Li_7SiPS_8, the potentiostat was calibrated using a load-short (100 Ω-shorted cell) calibration. The impedance spectra were recorded at 25 °C in a frequency range of 1 MHz to 100 Hz and with an applied voltage of V_{RMS} = 10 mV. The spectra interpretation was performed using the RHD INSTRUMENTS software package RelaxIS 3. Kramers-Kronig relation tests were performed prior to fitting to check for the reliability of the measured data. All data points were proportionally weighted during the fitting process to an equivalent circuit. The spectra were mostly fitted in the frequency range of 1 MHz to 1 kHz, however, depending on the pressure, adjustments had to be made to avoid unmeaningful fits. Error bars originate from error propagation calculated from uncertainties in pellet thickness and fitting error. The spectra were fitted using an equivalent circuit composed of a resistor in series with a

constant phase element, accounting for the ionic resistance and the polarization spike at lower frequencies.

E.5.7 DEM and FV Simulation

As already discussed in the introduction, we expect the mesostructural compaction of the powder to be the dominant effect in the low pressure regime. The discrete element method (DEM) is a common tool to model such effects as it enables to incorporate the crucial phenomena of powder compaction, i.e. the particle-particle and particle-wall interactions. Thus, we decided to employ DEM simulations to verify the hypothesis that powder compaction is indeed the dominant effect in this pressure regime.

The applied model is based on our previous work in the field of additive manufacturing.[18,19] It is premised on the DEM, as proposed by Cundall and Strack,[20] where the particles are described as rigid spheres. Therefore, the kinematics of each particle are completely described by the position vector of the center of gravity $\boldsymbol{r}_\mathrm{G}$ as well as the angular velocity vector $\boldsymbol{\omega}$. To mathematically describe the position and rotation we incorporate the balance of linear and angular momentum of an individual particle i:

$$(m\ddot{\boldsymbol{r}}_\mathrm{G})^i = m^i\boldsymbol{g} + \sum_j \left(\boldsymbol{f}^{ij}_\mathrm{CN} + \boldsymbol{f}^{ij}_\mathrm{CT}\right), \tag{E.8}$$

$$(I_\mathrm{G}\dot{\boldsymbol{\omega}})^i = \sum_j \left(\boldsymbol{r}^{ij}_\mathrm{CG} \times \boldsymbol{f}^{ij}_\mathrm{CT}\right), \tag{E.9}$$

where the particle mass is defined as $m = 4/3\pi r^3\rho$, and the moment of inertia with respect to the center of gravity of the particle is denoted by $I_\mathrm{G} = 0.4mr^2$. Additionally, $\boldsymbol{g}$ represents the gravitational acceleration, $\boldsymbol{f}^{ij}_\mathrm{CN}$, and $\boldsymbol{f}^{ij}_\mathrm{CT}$ symbolize the interaction forces of particles i and j in normal, and tangential direction, respectively. Finally, the vector from the centroid of particle i to the contact point with particle j is delineated as $\boldsymbol{r}^{ij}_\mathrm{CG} = \boldsymbol{r}^{ij}_\mathrm{C} - \boldsymbol{r}^{i}_\mathrm{G}$. Additionally, we need to define the contact laws to model the interaction between particles.

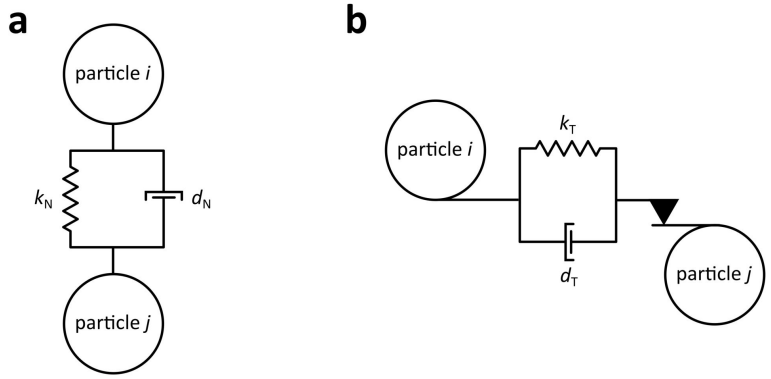

Figure E.14: Sketches of normal as well as tangential contact laws applied to the particle pair i, j. (a) Schematic of the spring-dashpot model applied as normal contact law. (b) Schematic of Coulomb's law of friction applied as tangential contact law.

Figure E.14 shows sketches of the applied contact laws in both normal and tangential directions. In normal direction a typical spring-dashpot model is employed:

$$\boldsymbol{f}_{\mathrm{CN}}^{ij} = \begin{cases} \min\left(0, k_{\mathrm{N}} g_{\mathrm{N}} + d_{\mathrm{N}} \dot{g}_{\mathrm{N}}\right) \boldsymbol{n}, & g_{\mathrm{N}} \leq 0 \\ \boldsymbol{0}, & g_{\mathrm{N}} > 0, \end{cases} \tag{E.10}$$

with the normal gap between the contacting particles $g_{\mathrm{N}} = ||\boldsymbol{r}_{\mathrm{G}}^{j} - \boldsymbol{r}_{\mathrm{G}}^{i}|| - \left(r^{j} + r^{i}\right)$ and the corresponding unit normal vector $\boldsymbol{n} = \left(\boldsymbol{r}_{\mathrm{G}}^{j} - \boldsymbol{r}_{\mathrm{G}}^{i}\right) / ||\boldsymbol{r}_{\mathrm{G}}^{j} - \boldsymbol{r}_{\mathrm{G}}^{i}||$.[21,22] The case distinction in (E.10) ensures that contact forces are only applied if a pair of particles i, j is in contact ($g_{\mathrm{N}} \leq 0$). Furthermore, k_{N} denotes the elastic normal contact stiffness and d_{N} the damping constant in normal direction. The latter calculates as:

$$d_{\mathrm{N}} = 2 \left|\ln\left(c_{\mathrm{COR}}\right)\right| \sqrt{\frac{k_{\mathrm{N}}\, m_{\mathrm{eff}}}{\ln\left(c_{\mathrm{COR}}\right)^{2} + \pi^{2}}}, \tag{E.11}$$

where c_{COR} represents the coefficient of restitution and $m_{\mathrm{eff}} = m^{i} m^{j} / \left(m^{i} + m^{j}\right)$ denotes an effective mass of the contacting particle pair.
Finally, the tangential contact law is based on Coulomb's law of friction:

$$\boldsymbol{f}_{\mathrm{CT}}^{ij} = \begin{cases} \min\left(\mu ||\boldsymbol{f}_{\mathrm{CN}}^{ij}||, ||k_{\mathrm{T}} \boldsymbol{g}_{\mathrm{T}} + d_{\mathrm{T}} \dot{\boldsymbol{g}}_{\mathrm{T}}||\right) \boldsymbol{t}_{\mathrm{T}}, & g_{\mathrm{N}} \leq 0 \\ \boldsymbol{0}, & g_{\mathrm{N}} > 0, \end{cases} \tag{E.12}$$

with the friction coefficient μ as well as the constants for tangential contact $d_{\mathrm{T}} = d_{\mathrm{N}}$ and $k_{\mathrm{T}} = (1-\nu)/(1-0.5\nu) k_{\mathrm{N}}$ using Poisson's ratio ν. Moreover, the time derivative of the tangential gap vector is defined as:

$$\dot{\boldsymbol{g}}_{\mathrm{T}} = \left(\boldsymbol{I} - \boldsymbol{n} \otimes \boldsymbol{n}^{T}\right) \left(\boldsymbol{v}_{\mathrm{G}}^{i} - \boldsymbol{v}_{\mathrm{G}}^{j}\right) + \omega^{i} \times \boldsymbol{r}_{\mathrm{CG}}^{ij} - \omega^{j} \times \boldsymbol{r}_{\mathrm{CG}}^{ji}, \tag{E.13}$$

where $\boldsymbol{I}$ denotes the identity tensor. Please note that the tangential gap vector $\boldsymbol{g}_{\mathrm{T}}$ is not uniquely defined by the geometric configuration. Instead, it is computed by numerical integration of (E.13). Furthermore, the unit tangent vector $\boldsymbol{t}_{\mathrm{T}}$ is calculated as:

$$\boldsymbol{t}_{\mathrm{T}} = -\frac{k_{\mathrm{T}} \boldsymbol{g}_{\mathrm{T}} + d_{\mathrm{T}} \dot{\boldsymbol{g}}_{\mathrm{T}}}{||k_{\mathrm{T}} \boldsymbol{g}_{\mathrm{T}} + d_{\mathrm{T}} \dot{\boldsymbol{g}}_{\mathrm{T}}||}. \tag{E.14}$$

The parameters listed in E.5 have been used to perform the DEM simulations.

Table E.5: Parameters used for the DEM simulations.

Symbol	Value	Unit	Short description	Source / Comment
ρ	1980.0	$\frac{\mathrm{kg}}{\mathrm{m}^3}$	Density	Averaged value from four batches (see section 'Gas Pycnometer')
ν	0.3	–	Poisson's ratio	Typical value for argyrodite and LGPS-type thiophosphates (see Table E.7)
k_N	0.01	$\frac{\mathrm{N}}{\mathrm{m}}$	Normal contact stiffness	In DEM simulations it is common not to use the original Young's modulus as a basis for the particle stiffness, but to reduce the value for reasons of numerical efficiency.[18, 23–25] We follow the same approach here, justified by the fact that we are not interested in the resulting global reaction force, but only in the resulting particle morphology. However, this is not affected by the exact value of the stiffness.
c_cor	0.1	–	Coefficient of restitution	Since we are only interested in the static equilibrium after compression, i.e., the final pellet morphology, the value has negligible effect on the solution. It was chosen non-zero to dissipate energy in addition to the friction effects to save computational resources.
μ	1.0	–	Friction coefficient	Typical friction coefficients are in the range of 0.05-2.0 depending on the material pairing.[26] Since we do not have further information on that we used a value from the middle of the range.
$\boldsymbol{g}$	$(0,0,0)^T$	$\frac{\mathrm{m}}{\mathrm{s}^2}$	Gravitational acceleration	Neglected since influence is several orders of magnitude lower compared to that of the compression as proven in a brief calculation. 50 mg of powder in a cylindrical shape of 6 mm diameter results in the following pressure due to gravity: $\frac{m_\mathrm{Smaple}}{A_\mathrm{Smaple}} \cdot g = \frac{50\,\mathrm{mg}\cdot 4}{(6\,\mathrm{mm})^2\pi} \cdot 9.81\,\frac{\mathrm{N}}{\mathrm{kg}} = 17.3\,\mathrm{Pa}$ In comparison to at least 0.01 GPa external pressure this is negligible.
a	1.944	–	Gamma distribution parameter a	Fit to experimental data (see Fig. 8.6a)
b	1.944	–	Gamma distribution parameter b	Fit to experimental data (see Fig. 8.6a)

Based on the results from the DEM-simulations, finite volume (FV) simulations were conducted on the particle microstructures to determine the effective ionic conductivities of the compressed electrolyte pellets. First, from the known particle positions and diameters in the compressed samples, voxel-based microstructures with a voxel size of 1 µm were generated. Then, the simulation environment BEST (Battery and Electrochemistry Simulation Tool)[27,28] was used to calculate the effective conductivity of the pellets by simulating the steady state current j for an applied voltage difference of $U = 1\,\mathrm{V}$. Essentially solving the Poisson equation for the electrolyte phase allows to evaluate the mean current density at the boundary of the computational domain. For an electrolyte pellet with the thickness l_i, the effective conductivity can be calculated according to equation (E.15):

$$\sigma_{\mathrm{eff,i}} = l_i \cdot \frac{j}{U} \tag{E.15}$$

To allow for a comparison of calculated and measured conductivities, the calculated conductivities were normalized to the maximum value $\sigma_{\mathrm{eff,max}}$.
In order to consider the atomistic effect of the activation volume, the bulk conductivity of the electrolyte was reduced with increasing pressure. For each pressure level p_i corresponding to a certain pellet thickness, the bulk conductivity σ_i can be calculated from a reference state according to equation (E.16), which was derived from the simplified expression of the activation volume (equation (8.3) in Chapter 8). However, due to the normalization of the simulated conductivities, the values in Figure 8.6b in Chapter 8 do not depend on the assumed bulk conductivity but only on the geometric properties of the pellet microstructure.

$$\sigma_i = e^{\ln \sigma_{\mathrm{ref}} - \frac{\Delta V}{k_{\mathrm{B}} T}(p_i - p_{\mathrm{ref}})} \tag{E.16}$$

In the FV-simulations the electrolyte material was treated as a homogeneous phase without any additional grain boundary resistances between individual particles.

E.5.8 DFT and AIMD Simulations

Density functional theory (DFT) and *ab initio* molecular dynamics (AIMD) simulations have been performed using the The Vienna Ab initio Simulation Package (VASP).[29–32] The PBE exchange-correlation functional[33] and projector augmented wave pseudopotentials[34,35] as shipped with VASP have been used. Total energy calculations and structural relaxations were performed with a k-spacing of $0.25\,\text{Å}^{-1}$ and an energy cutoff of the plane-wave basis set of 600 eV until the electronic structure and forces were converged within $10 \cdot 10^{-6}$ eV and $0.01\,\text{eV}\,\text{Å}^{-1}$, respectively. For the determination of elastic constants, the cutoff energy was increased to 900 eV. *Ab initio* molecular dynamics simulations were performed in the NVT ensemble using the default cutoff energy of 499 eV, only including the gamma-point, with time steps of 1 fs, and using the Nosé-Hoover thermostat. Based on the slope of the mean-squared-displacements (MSD) of Li ions, tracer diffusion coefficients D have been determined.
2×2×1 supercells (12 formula units) of t-Li_7SiPS_8 have been used in all simulations and the supercell program[36] was utilized to first occupy the shared Si/P sites, from which seven explicit arrangements were considered (see Figure E.15). Next, Li was distributed among its partially occupied sites in several steps and the structure with the lowest electrostatic energy was used as basis for the next step. After merging pairs of Li1-Li1 sites (fully occupied), the supercell program was used to occupy 87.5% and 62.5% of the Li2 and Li4 sites simultaneously. Finally, 87.5% of the Li3 sites were occupied.

Structural models for DFT/AIMD simulations

Molecular dynamics simulation

For LGPS, the structural archetype to t-Li_7SiPS_8, AIMD[37] and single crystal impedance spectroscopy[38] hint for a weak anisotopic conductivity, while PFG-NMR points more to isotropic ion conduction. Based on the reported crystal structure[15] (see Figure 8.4a), we have calculated an activation barrier based on the bond valence sum approach[39–41] of 0.22 eV for 1D ion migration along the c direction and 0.28 eV for 3D migration. Additionally, we performed AIMD simulations of several explicit arrangements of the PS_4^{3-}/SiS_4^{4-} anions to calculate tracer diffusion coefficients of lithium via an analysis of the MSD. The diffusivity of lithium along c is on average four times higher than in the a/b direction (see Figure E.17). This finding agrees well with the four times higher conductivity in [001] direction compared to [110] measured with single crystal impedance spectroscopy.[38] This anisotropy is also reflected in a higher activation barrier of about 155 meV in the a/b, compared to 127(13) meV in the c direction (see Figure E.18). The activation barrier derived from the total MSD amounts to 136(13) meV, fitting to the trend of the bond valence sum results. The AIMD activation barriers are lower than measured barriers in other sulfide solid electrolytes and we attribute this discrepancy to the shortcomings of extracting activation barriers from AIMD simulations at high temperatures.[42] Moreover, the simulations represent the single crystal properties and do not consider grain boundaries or (amorphous) side phases.

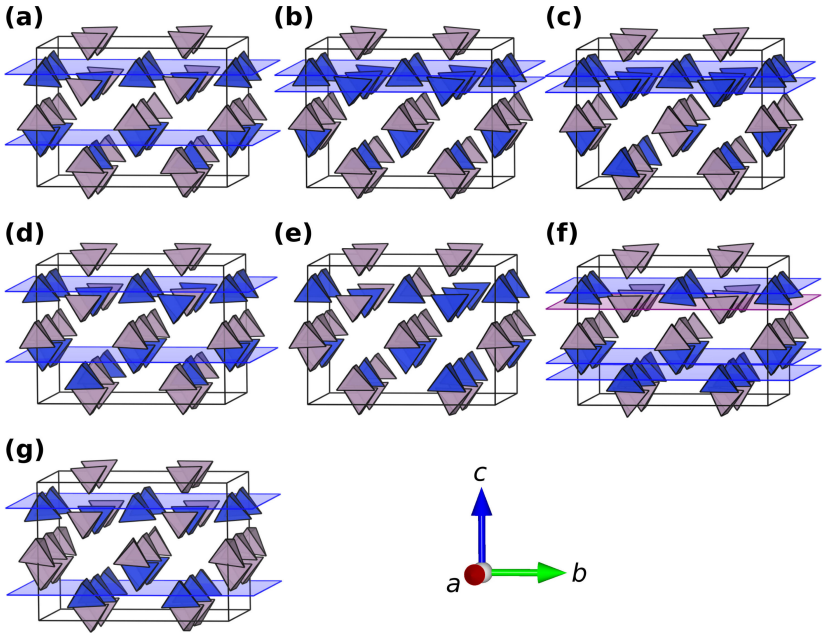

Figure E.15: Structural models of *t*-Li_7SiPS_8 that have been used for DFT and AIMD simulations. For clarity, only PS_4^{3-} (purple) and SiS_4^{4-} (blue) tetrahedra are shown. Planes have been added as a guide to the eyes and indicate layers that are occupied by the same type of tetrahedra.

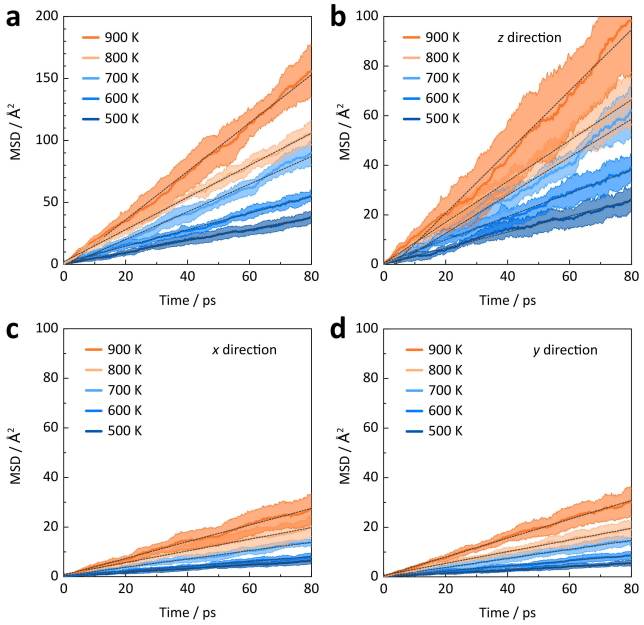

Figure E.16: (a) Averaged total Mean squared displacement (MSD) of lithium from AIMD simulations at different temperatures, in comparison to the individual spatial contributions of the (b) z, (c) x, and (d) y directions. The x, y, and z directions align with the crystallographic a, b, and c direction.

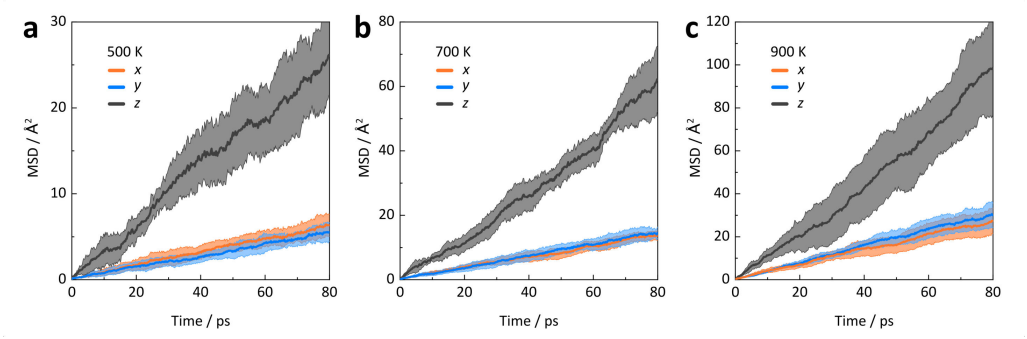

Figure E.17: Mean squared displacement (MSD) of lithium at MD simulation temperatures of (a) 500 K, (b) 700 K, and (c) 900 K. The x, y, and z directions align with the crystallographic a, b, and c direction.

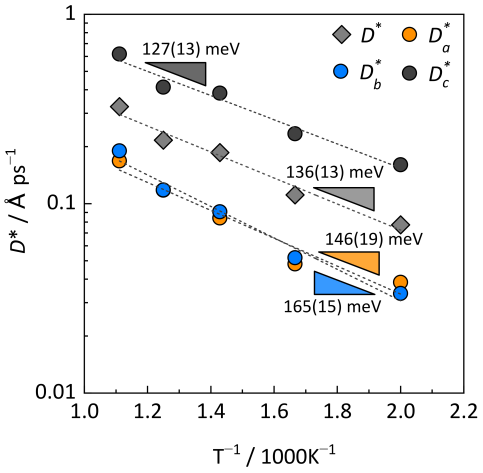

Figure E.18: Arrhenius plot of the total lithium tracer diffusion coefficient (diamond, light gray), and its individual contributions along the crystallographic a, b and c directions.

Elastic properties

We calculated the volume-energy curves for the different structural models and fitted them to the Birch-Murnaghan equation of state.[43,44] An average bulk modulus of 22.8 GPa is obtained. Additionally, the full elastic tensor of t-Li_7SiPS_8 was calculated (see Table E.6) and a bulk modulus of 23.5 GPa within the Reuss-Voigt-Hill approach[45] is obtained. Comparable bulk moduli have been calculated for $Li_{10}MP_2S_{12}$ (M = Si, Ge, Sn) and Li_6PS_5X (X = Cl, Br, I) (see Table E.7).

Table E.6: Averaged stiffness tensor C_{ij} (all entries in GPa) of *t*-Li_7SiPS_8, obtained from the stiffness tensors of four structural models of *t*-Li_7SiPS_8 with different PS_4^{3-}/SiS_4^{4-} arrangements. With partially occupied sites, the space group of *t*-Li_7SiPS_8 is $P42/nmc$.[15] Hence, the entries of C_{ij} that are put in brackets are expected to vanish. The explicit distribution of PS_4^{3-}/SiS_4^{4-} tetrahedra as well as the distribution of Li ions, however, formally lower the symmetry of the structural models in almost all cases. As a result, several entries in C_{ij} become non-zero. These entries, however, are all below 1 GPa and therefore negligibly low compared to the proper entries of a tetragonal system with $P42/nmc$ space group.

$$C_{ij} = \begin{bmatrix} \mathbf{38.5} & \mathbf{26.4} & \mathbf{13.5} & (0.7) & (-0.4) & (0.2) \\ \mathbf{26.4} & \mathbf{41.7} & \mathbf{15.4} & (-0.1) & (-0.4) & (0.3) \\ \mathbf{13.5} & \mathbf{15.4} & \mathbf{40.5} & (0.9) & (0.1) & (-0.2) \\ (0.7) & (-0.1) & (0.9) & \mathbf{11.4} & (0.3) & (0.2) \\ (-0.4) & (-0.4) & (0.1) & (0.3) & \mathbf{9.6} & (0.7) \\ (0.2) & (0.3) & (-0.2) & (0.2) & (0.7) & \mathbf{17.8} \end{bmatrix}$$

Table E.7: Calculated bulk modulus (B), Young's modulus (E), shear modulus (G), Poisson's ration (ν), and Pugh's ratio (G/B) of selected argyrodite and LGPS-type thiophosphate ion conductors based on the Reuss-Voigt-Hill approach. The values are taken from the references in column *Ref.* †The value in brackets was obtained from fitting energy-volume curves to the Birch-Murnaghan equation of state.

Compound	B / GPa	E / GPa	G / GPa	ν	G/B	Ref.
t-Li_7SiPS_8	23.5 (22.8)†	29.5	11.4	0.29	0.49	this work
$Li_{10}GeP_2S_{12}$	30.36	37.19	14.35	0.30	0.47	[46]
$Li_{10}GeP_2S_{12}$	27.3	21.7	7.9	0.37	0.29	[47]
$Li_{10}SiP_2S_{12}$	27.8	24.8	9.2	0.35	0.33	[47]
$Li_{10}SnP_2S_{12}$	23.5	29.1	11.2	0.29	0.48	[47]
Li_6PS_5Cl	28.7	22.1	8.1	0.37	0.28	[47]
Li_6PS_5Br	29.0	25.3	9.3	0.35	0.32	[47]
Li_6PS_5I	29.9	30.0	11.3	0.33	0.38	[47]

E.5.9 Densities of pressed argyrodite pellets - a metadata analysis

Although the importance of pellet density and preparation pressure is well known, few studies have addressed the influence of these two factors on the conductivity of thiophosphate-based solid electrolytes. Recently, Ohno and others published a laboratory comparative study that included such metadata. However, they focused only on the effects on ionic conductivity and activation energy. Figure E.19 shows the relative pellet densities as a function of the pelletizing pressure. While intuition suggests higher pellet density

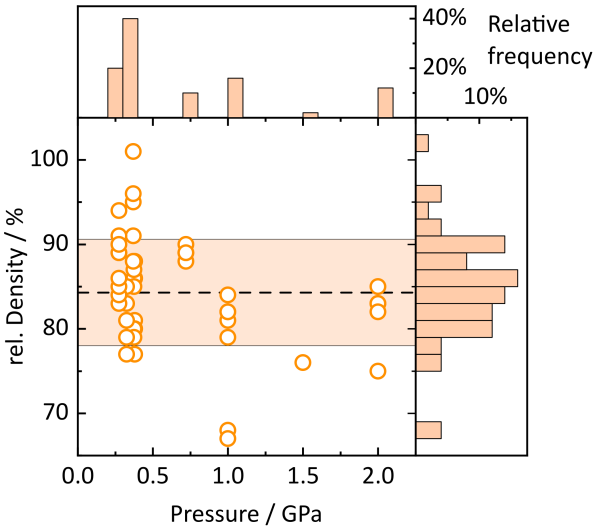

Figure E.19: Relative density of pellets prepared from $Li_{6.6}P_{0.4}Ge_{0.6}PS_5I$, Li_6PS_5Cl, $Li_6PS_5Br_{0.75}I_{0.25}$, $Li_6PS_5Br_{0.25}I_{0.75}$, and Li_6PS_5I at different pressures. The data was extracted from the ESI of Ohno *et al.*[48] The average density and the standard deviation is shown as a horizontal dashed line and light orange region, respectively.

with pressure, the data presented in Figure E.19 do not show a positive trend in pellet density with pelletizing pressure. In fact, pellet density fluctuates around an average value of about 85%, with outliers $> 100\%$ (nonphysical value) and $< 70\%$. This metadata analysis indicates that applied pelletizing pressure is not an appropriate descriptor of the achievable pellet density. However, for some materials used in the study by Ohno *et. al.*, ionic conductivity shows a positive trend with increasing pellet density, while no such trend is observed for pelletizing pressure.

Since the bulk (B) and elastic (E) modulus, as well as the G/B ratio of aryrodites, such as Li_6PS_5Cl, and the *t*-Li_7SiPS_8 prototype, $Li_{10}GeP_2S_{12}$, is comparable (see Table E.7), we expect similar high pressure densification behavior of the two classes of materials. Both materials meet Pugh's criterion for a ductile material ($B/G < 0.5$),[49] undergoing plastic deformation rather than fragmentation under stress.

References

(1) Legland, D.; Arganda-Carreras, I.; Andrey, P. *Bioinformatics* **2016**, btw413.

(2) Landini, G. Novel context-based segmentation algorithms for intelligent microscopy, Web Page, accessed: 11.04.2022.

(3) Clark, M. W. *J. Int. Assoc. Math. Geol.* **1981**, *13*, 303–320.

(4) Russ, J., *The Image Processing Handbook*, 4th ed.; CRC Press: Boca Raton, FL, 2002.

(5) Cooper, A. R.; Eaton, L. E. *J. Am. Ceram. Soc.* **1962**, *45*, 97–101.

(6) Wünsch, I.; Finke, J.; John, E.; Juhnke, M.; Kwade, A. *Pharmaceutics* **2019**, *11*, 121.

(7) Famprikis, T. et al. *J. Am. Chem. Soc.* **2020**, *142*, 18422–18436.

(8) Jeffery, R. N.; Lazarus, D. *J. Appl. Phys.* **1970**, *41*, 3186–3187.

(9) Allen, P. C.; Lazarus, D. *Phys. Rev. B* **1978**, *17*, 1913–1927.

(10) Samara, G. A. In *Solid State Phys.* Elsevier: 1984, pp 1–80.

(11) Fleig, J. *Solid State Ion* **2000**, *131*, 117–127.

(12) Fleig, J.; Maier, J. *J. Am. Ceram. Soc.* **2004**, *82*, 3485–3493.

(13) Dankat, G. G.; Dumitran, L. M. *Materials* **2022**, *15*, 2056.

(14) Schneider, C. A.; Rasband, W. S.; Eliceiri, K. W. *Nat. Methods* **2012**, *9*, 671–675.

(15) Harm, S.; Hatz, A.-K.; Moudrakovski, I.; Eger, R.; Kuhn, A.; Hoch, C.; Lotsch, B. V. *Chem. Mater.* **2019**, *31*, 1280–1288.

(16) Harris, R. K.; Becker, E. D.; de Menezes, S. M. C.; Goodfellow, R.; Granger, P. *Solid State Nucl. Magn. Reson.* **2002**, *22(4)*, 458–483.

(17) Massiot, D.; Fayon, F.; Capron, M.; King, I.; Le Calvé, S.; Alonso, B.; Durand, J.-O.; Bujoli, B.; Gan, Z.; Hoatson, G. *Magn. Reson. Chem.* **2002**, *40*, 70–76.

(18) Meier, C.; Weissbach, R.; Weinberg, J.; Wall, W. A.; Hart, A. J. *Powder Technol.* **2019**, *343*, 855–866.

(19) Meier, C.; Weissbach, R.; Weinberg, J.; Wall, W. A.; Hart, A. J. *J. Mater. Process. Technol.* **2019**, *266*, 484–501.

(20) Cundall, P. A.; Strack, O. D. L. *Géotechnique* **1979**, *29*, 47–65.

(21) Luding, S. *Behavior of granular media* **2006**, *9*, 137–147.

(22) Luding, S. *Granul. Matter* **2008**, *10*, 235–246.

(23) Parteli, E. J. R.; Pöschel, T. *Powder Technol.* **2016**, *288*, 96–102.

(24) Nan, W.; Pasha, M.; Ghadiri, M. *Powder Technol.* **2020**, *364*, 811–821.

(25) Tsuji, Y.; Kawaguchi, T.; Tanaka, T. *Powder Technol.* **1993**, *77*, 79–87.

(26) Blau, P., *Friction Science and Technology: From Concepts to Applications, Second Edition*; Mechanical Engineering; CRC Press: 2008.

(27) Latz, A.; Zausch, J. *J. Power Sources* **2011**, *196*, 3296–3302.

(28) Danner, T.; Singh, M.; Hein, S.; Kaiser, J.; Hahn, H.; Latz, A. *J. Power Sources* **2016**, *334*, 191–201.

(29) Kresse, G.; Hafner, J. *Phys. Rev. B* **1994**, *49*, 14251–14269.

(30) Kresse, G. *J. Non Cryst. Solids* **1995**, *192-193*, 222–229.

(31) Kresse, G.; Furthmüller, J. *Comput. Mater. Sci.* **1996**, *6*, 15–50.

(32) Kresse, G.; Furthmüller, J. *Phys. Rev. B* **1996**, *54*, 11169–11186.

(33) Perdew, J. P.; Burke, K.; Ernzerhof, M. *Phys. Rev. Lett.* **1996**, *77*, 3865–3868.

(34) Blöchl, P. E. *Phys. Rev. B* **1994**, *50*, 17953–17979.

(35) Kresse, G.; Joubert, D. *Phys. Rev. B* **1999**, *59*, 1758–1775.

(36) Okhotnikov, K.; Charpentier, T.; Cadars, S. *J. Cheminform.* **2016**, *8*, 17.

(37) Fu, Z.-H.; Chen, X.; Zhao, C.-Z.; Yuan, H.; Zhang, R.; Shen, X.; Ma, X.-X.; Lu, Y.; Liu, Q.-B.; Fan, L.-Z.; Zhang, Q. *Energy Fuels* **2021**, *35*, 10210–10218.

(38) Iwasaki, R.; Hori, S.; Kanno, R.; Yajima, T.; Hirai, D.; Kato, Y.; Hiroi, Z. *Chem. Mater.* **2019**, *31*, 3694–3699.

(39) Chen, H.; Adams, S. *IUCrJ* **2017**, *4*, 614–625.

(40) Chen, H.; Wong, L. L.; Adams, S. *Acta Cryst. B* **2019**, *75*, 18–33.

(41) Wong, L. L.; Phuah, K. C.; Dai, R.; Chen, H.; Chew, W. S.; Adams, S. *Chem. Mater.* **2021**, *33*, 625–641.

(42) Qi, J.; Banerjee, S.; Zuo, Y.; Chen, C.; Zhu, Z.; Holekevi Chandrappa, M. L.; Li, X.; Ong, S. P. *Mater. Today Phys.* **2021**, *21*, 100463.

(43) Murnaghan, F. D. *Proc. Natl. Acad. Sci.* **1944**, *30*, 244–247.

(44) Birch, F. *Phys. Rev.* **1947**, *71*, 809–824.

(45) Toonder, J. M. J. d.; Dommelen, J. A. W. v.; Baaijens, F. P. T. *Model. Simul. Ma.t Sci. Eng.* **1999**, *7*, 909–928.

(46) Wang, Z.-Q.; Wu, M.; Liu, G.; Lei, X.; Xu, B.; Ouyang, C. *Int. J. Electrochem. Sci.* **2014**, *9*, 562–568.

(47) Deng, Z.; Wang, Z.; Chu, I.-H.; Luo, J.; Ong, S. P. *J. Electrochem. Soc.* **2016**, *163*, A67–A74.

(48) Ohno, S. et al. *ACS Energy Lett.* **2020**, *5*, 910–915.

(49) Pugh, S. *London Edinburgh Philos. Mag. J. Sci.* **1954**, *45*, 823–843.

APPENDIX F

List of publications and author contributions

Publications that are part of this thesis

1. **Title:** Synthesis and Characterization of Three New Lithium-Scandium Hexathiohypodiphosphates: $Li_{4-3x}Sc_xP_2S_6$ ($x = 0.358$), m-$LiScP_2S_6$, and t-$LiScP_2S_6$
Authors: Leslie Mareike Schoop, Roland Eger, Florian Pielnhofer, Christian Schneider, Jürgen Nuss, Bettina V. Lotsch
Published in: *Zeitschrift für Anorganische und Allgemeine Chemie* **2018**, *644*, 1854-1862.
Author contributions: LMS, RE and BVL conceived and designed the study. RE synthesized the samples, measured the Raman and EDX spectra, and collected the PXRD data. JN measured the SCXRD data and solved the crystal structure with RE. FP performed the DFT calculations. CS performed the electrochemical measurements and calculated the BVEL. LS, RE, FP, and CS wrote the manuscript. All authors discussed and revised the work.

2. **Title:** Phase formation through synthetic control: polymorphism in the sodium-ion solid electrolyte $Na_4P_2S_6$
Authors: Tanja Scholz*, Christian Schneider*, Roland Eger, Viola Duppel, Igor Moudrakovski, Armin Schulz, Jürgen Nuss and Bettina Valeska Lotsch
*Equal contribution to this work
Published in: *Journal of Materials Chemistry A* **2021**, *9*, 8692-8703.
Author contributions: TS, CS, and BVL conceived and designed the study. RE, TS and CS synthesized the samples. CS collected the PXRD data, JN collected the SCXRD data. TS and JN performed the Rietveld refinements. VD performed the TEM measurements; VD, TS, and CS interpreted the TEM images. CS performed the DSC and TGA measurements. IM measured ssNMR; CS interpreted the NMR data. AS measured the Raman spectra; CS interpreted the Raman spectra. CS calculated the BVEL; TS performed the DFT and NEB calculations. CS measured and analyzed the EIS data. TS and CS wrote the manuscript. TS, CS, RE, JN and BVL discussed and revised the work.

3. **Title:** Impact of hydration on ion transport in $Li_2Sn_2S_5 \cdot xH_2O$
Authors: Markus Joos, Christian Schneider, Andreas Münchinger, Igor Moudrakovski, Robert Usiskin, Joachim Maier and Bettina V. Lotsch
Published in: *Journal of Materials Chemistry A* **2021**, *9*, 16532-16544.
Author contributions: MJ, CS, RU, JM and BVL conceived and designed the study. CS synthesized the samples. MJ and RU performed the TGA measurements. CS collected the PXRD data. IM and AM collected the ssNMR and PFG-NMR data. MJ and CS interpreted the NMR data. MJ and CS collected and interpreted the EIS data. MJ, RU, and CS wrote the manuscript. All authors discussed and revised the work.

4. **Title:** Superionic Conduction in the Plastic Crystal Polymorph of $Na_4P_2S_6$
   Authors: Tanja Scholz*, Christian Schneider*, Maxwell W. Terban, Zeyu Deng, Roland Eger, Martin Etter, Robert E. Dinnebier, Pieremanuele Canepa, and Bettina V. Lotsch
   *Equal contribution to this work
   Published in: *ACS Energy Letters* **2022**, *7*, *4*, 1403–1411.
   Author contributions: TS, CS, MWT and BVL conceived and designed the study. RE, TS and CS synthesized the samples. CS collected the HT-XRD data; TS and MWT performed the Rietveld refinements. ME collected the total scattering data; MWT performed the PDF refinements; CS performed the DSC measurements. CS and TS interpreted the Raman spectra. CS and TS calculated the BVEL; ZD performed the DFT and AIMD calculations; TS, CS, and ZD interpreted the AIMD results. CS measured and analyzed the HT-EIS data. TS, CS, MWT, and DZ wrote the manuscript. All authors discussed and revised the work.

5. **Title: Effect of particle size and pressure on the transport properties of the fast ion conductor *t*-Li_7SiPS_8**
   Authors: Christian Schneider, Christoph P. Schmidt, Anton Neumann, Moritz Clausnitzer, Marcel Sadowski, Sascha Harm, Christoph Meier, Timo Danner, Karsten Albe, Anrulf Latz, Wolfgang A. Wall, and Bettina V. Lotsch
   Published in: *Advanced Energy Materials*, **2023**, 2203873.
   Author contributions: CSchn, CSchm, AN, and BVL conceived and designed the study. SH and CSchn synthesized and prepared the samples. CSchn measured the particle size distribution. CSchn interpreted the ssNMR data. CSchn perfomrmed and interpreted the high-*p* EIS measurements. CSchm and CM performend the DEM simuation; AN, MC, and TD performed the FE analysis. MS performed the AIMD simulations. CSchn wrote the manuscript. CSchn, CSchm, AN, MC, MS, CM, and TD analyzed the data. All authors discussed and revised the work.

Publications that are not part of this thesis

1. **Title:** Finding the right blend: Interplay between structure and sodium ion conductivity in the system Na_5AlS_4 – Na_4SiS_4
   Authors: Sascha Harm, Anna-Katharina Hatz, Christian Schneider, Carla Hoefer, Constantin Hoch, Bettina V. Lotsch
   Published in: *Frontiers in Chemistry* **2020**, *8*
   Author contributions: SH, AKH and BVL concieved and designed the study. SH, AKH and BVL conceived and designed this study. SH and CaH synthesized the samples. SH, AKH and CaH measured SCXRD, PXRD, NMR and EIS. SH with help of CoH solved and interpreted the crytsal structure. CS calculated and interpreted the BVEL data. CS designed the structure images. AKH analysed the EIS data. SH, AKH and CS wrote the manuscript. All authors discussed and revised the work.

2. **Title: Dissolution and recrystallization behavior of Li_3PS_4 in different organic solvents**
   Authors: Kerstin Wissel, Luise Riegger, Christian Schneider, Aamir I. Waidha, Theodosios Famprikis, Yuji Ikeda, Blazej Grabowskie, Robert E. Dinnebier, Bettina V. Lotsch, Jürgen Janek, Wolfgang Ensinger and Oliver Clemens
   Published on: arXiv:2209.13955
   Author contributions: KW and OC conceived and designed the study. KW prepared the samples. LR measured and analysed the XPS data. KW and LR performed the EIS, and interpreted the data together with AW. TF measured neutron diffraction. CS measured and analyzed TGA and EGA. YI performed the DFT calculations. KW wrote the manuscript. All authors discussed and revised the work.

APPENDIX G

List of presentations

Oral presentations

1. **Title:** Development of a humidity tolerant lithium superionic conductor
   Authors: Christian Schneider, Tanja Holzmann, Leslie. M. Schoop, Igor Moudrakovski, Robert J. Cava, and Bettina V. Lotsch
   Occasion: Bunsenkolloquium, Solid-State-Batteries III, Frankfurt am Main, Germany 14.11.2018

2. **Title:** Bond Valence Sum - A valid Approach to Lithium Ion Diffusion Pathways?
   Authors: , Christian Schneider, Maximilian A. Plaß
   Occasion: FestBatt-Seminar: Theory meets Experiment, onsite, Kloster Höchst, Germany 30.10.2019

3. **Title:** Virtual Industry Day
   Authors: Christian Schneider, Simon Burkhardt, Michael Ghidiu, Michael Grube, and Nella Vargas-Barbosa
   Occasion: Digitaler Industrietag - FestBatt Meeting, digital, 09.06.2020

4. **Title:** Schwefelbasierte Festkörperleiter
   Authors: Christian Schneider, Sascha Harm, Markus Joos, Anna-K. Hatz, Igor Moudrakovski, Andreas Münchinger, Roland Eger, Alexander Kuhn, Tanja Schneider, Robert Usiskin, Constantin Hoch, Joachim Maier, Bettina V. Lotsch
   Occasion: Batterieforum, onsite, Berlin, Germany 24.01.2020

5. **Title:** Polymorphism in the Solid Electrolyte $Na_4P_2S_6$: Phase Formation through Synthetic Control and Superionic Sodium-Ion Conduction
   Authors: Christian Schneider, Tanja Scholz, Maxwell W. Terban, Zeyu Deng, Roland Eger, Viola Duppel, Igor Moudrakovski, Martin Etter, Armin Schulz , Jürgen Nuss, Pieremanuele Canepa, Bettina Valeska Lotsch
   Occasion: Materials Reserach Society - Fall Meeting, onsite, Boston, USA, 30.11.2021

6. **Title:** Zellplattform Thiophosphate - FB2-Thio
   Authors: Christian Schneider, Robert Calaminus, Lucas Balzat, Duc Hien Nguyen, Nina Philipp, Bettina V. Lotsch
   Occasion: FestBatt2 - 2. Clustermeeting, onsite, Frankfurt am Main, Germany, 19.05.2022

Poster presentations

1. **Title:** Development of a humidity tolerant lithium superionic conductor
   Authors: Christian Schneider, Tanja Holzmann, Leslie. M. Schoop, Igor Moudrakovski, Mazhar N. Ali, Robert J. Cava, and Bettina V. Lotsch
   Occasion: International Symposium on the Reactivity of Solids, onsite, Bayreuth, Germany, 15.–18.07.2018

2. **Title:** Development of a humidity tolerant lithium superionic conductor
   Authors: Christian Schneider, Tanja Holzmann, Leslie. M. Schoop, Igor Moudrakovski, Robert J. Cava, and Bettina V. Lotsch
   Occasion: Bunsenkolloquium, Solid-state–Batteries III, onsite, Frankfurt am Main, Germany 14.11.–16.11.2018

3. **Title:** Structure and Electrochemistry of Superionic Thiophosphate and Sulfide-based Lithium Solid Electrolytes
   Authors: Christian Schneider, Anna-Katharina Hatz, Sascha Harm, Igor Moudrakovski, Luzia German, Roland Eger, Bettina V. Lotsch
   Occasion: Scientific advisory board meeting - MPI-FKF, onsite, Stuttgart, Germany, 12.11.–14.11.2018

4. **Title:** New Insights into the Chemistry and Ionic Transport Properties of Sulfide-based Lithium Solid Electrolytes
   Authors: Christian Schneider, Sascha Harm, Anna-Katharina Hatz, Markus Joos, Andreas Münchinger, Igor Moudrakovski, Roland Eger, Alex Kuhn, Tanja Schneider, Robert Usiskin, Constantin Hoch, Joachim Maier, Bettina V. Lotsch
   Occasion: Batterieforum, onsite, Berlin, Germany 22.01.–24.01.2020

5. **Title:** Delving into the Rich Polymorphism of the Sodium Ion Conductor $Na_4P_2S_6$
   Authors: Christian Schneider, Tanja Scholz, Maxwell W. Terban, Zeyu Deng, Roland Eger, Viola Duppel, Igor Moudrakovski, Martin Etter, Armin Schulz, Jürgen Nuss, Pieremanuele Canepa, Robert E. Dinnebier, and Bettina V. Lotsch
   Occasion: Scientific advisory board meeting - MPI-FKF, onsite, Stuttgart, Germany, 08.11.–10.11.2021